Kinetics of Electronic Excitations in the Light-Harvesting Complexes of the Purple Bacterium
Marichromatium purpuratum

von

Inga Elvers

aus Giessen
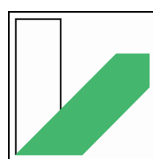
UNIVERSITÄT BAYREUTH

Fakultät für Mathematik, Physik und Informatik

What is a scientist after all?
It is a curious man looking through a keyhole,
the keyhole of nature, trying to know what's going on.

Jacques-Yves Cousteau

Science is fun.
Science is curiosity.
We all have natural curiosity.
Science is a process of investigating.
It's posing questions and coming up with a method.
It's delving in.

Sally Ride

Abstract

Detergent-isolated LH2 complexes of the purple bacterium *Marichromatium purpuratum* (*Mch. purpuratum*) were studied in detergent solution (20 mM HEPES, 0.1% LDAO, pH 7.8) by time-resolved spectroscopy as a function of the excitation parameters, such as the excitation fluence and the laser repetition rate. Both, excitation of the incorporated bacteriochlorophyll pigments as well as excitation of carotenoid pigments was investigated. The fluorescence transients for each of the different combinations of the excitation fluence and the laser repetition rate were analyzed using the phasor approach.

The phasor approach, originally formulated for fluorescence lifetime measurements in the frequency domain, was now adapted to lifetime measurements in the time domain. Recognizing the specific features of the fluorescence transients that were extracted from time-resolved measurements, here, a procedure for the calculation of the phasor coordinates was developed including all necessary corrections, such as background correction and correction for the influence of the instrument response (IRF) function. The special strength of the phasor approach is, that it allows for the analysis of the fluorescence kinetics without any *a priori* knowledge or assumption. Thus, the phasor approach allows for both a qualitative as well as a quantitative analysis of the observed fluorescence transients taking only into account the measured data and without making any assumption of the underlying kinetics as it is done for the 'traditional' fitting approach often seen in literature.

A detailed analysis using the phasor approach revealed a multiexponential kinetics for all measured fluorescence transients of the isolated LH2 complexes of *Mch. purpuratum*. For excitation of bacteriochlorophyll pigments in the near-infrared (NIR) wavelength range, a global biexponential kinetics with lifetime components of 730 ps and 50 ps was revealed. In addition a third lifetime component of about 500 ps was observed in phasor analysis for high excitation den-

sities, corresponding to the combination of high excitation fluence and high laser repetition rate. Upon excitation of the carotenoid pigments in the visible wavelength (VIS) range a biexponential kinetics featuring one lifetime component in the order of 750 ps and one faster lifetime of or below 100 ps was identified, hence showing almost the same biexponential kinetics as for bacteriochlorophyll excitation. Notably, no third lifetime component was observed for excitation of the carotenoid pigments.

The long fluorescence lifetime component in the order of 750 ps observed in the experiments is significantly quenched with respect to the usually reported fluorescence lifetime in the order of 1 ns for isolated LH2 complexes of various species of purple bacteria [1, 2, 3, 4]. Nonetheless, this lifetime component is attributed to the fluorosceen emission of the B830 bacteriochlorophyll pigments within the LH2 complex of *Mch. prupuratum*. The fast lifetime component of below 100 ps which is observed for all excitation conditions is tentatively attributed to the occurrence of a yet not known or resolved mixed exciton charge-transfer (CT) state within the B830 LH2 complex of *Mch. purpuratum*. The occurrence of such mixed exciton CT states in bacterial LH2 complexes is under discussion since years [5, 6, 7] and is in accordance with the observed shortening of B830 fluorescence lifetime [8]. The third lifetime component observed exclusively for excitation of bacteriochlorophyll pigment at high excitation densities is attributed tot the occurrence of singlet-triplet annihilation (STA) processes.

The identification of the different lifetime components in the multiexponential kinetics finally allowed for the evolution and proposal of an energy level scheme for the B830 LH2 complex of *Mch. purpuratum*. Based on this energy level scheme, the origin of the difference in the observed fluorescence kinetics upon excitation of bacteriochlorophylls or carotenoids was discussed. The different flow of energy within the LH2 complex upon excitation of the different pigments results in fundamental different situations of electronic excitations and it is reasonable presented that likely the occurrence of triplet-triplet annihilation results in the difference of the observed fluorescence kinetics.

In order to test the proposed energy level scheme for the LH2 complex of *Mch. purpuratum* numerical simulations using a dynamic Monte Carlo algorithm were performed, using on a rate model that is based on that energy level scheme.

A comparison of the fluorescence transients obtained experimentally and those resulting from the simulations showed an overall good agreement. Phasor analysis of the simulated fluorescence transients revealed that the multiexponential kinetics was reproduced correctly with respect to the up to three lifetime components seen in the experiments. Also the fractional contributions of the distinct lifetime components were well reproduced, with the only exception for high laser repetition rates. There, although the lifetime components were reproduced correctly, the fractional contribution did not reproduce the experimental data.

Overall, based on the experiments for investigation of the kinetics of electronic excitations within the B830 LH2 complex of *Mch. purpuratum* a detailed model for its electronic structure is presented.

Kurzusammenfassung

Isolierte LH2 Lichtsammelkomplexe des Purpurbakteriums *Marichromatium purpuratum* (*Mch. purpuratum*) in Lösung (20 mM HEPES, 0.1% LDAO, pH 7.8) wurden mittels zeitaufgelöster Spektroskopie in Abhängigkeit der Anregungsparameter, Wiederholrate des Anregungslasers sowie Photonenanregungsfluenz, untersucht. Es wurden Experimente sowohl bei Anregung der Bakteriochlorophyll-Pigmente als auch der Karotenoid-Moleküle durchgeführt. Die Fluoreszzerfallkurven für jede gemessene Kombination der Anregungsparameter wurden mit Hilfe des Phasor-Ansatzes ausgewertet. Der Phasor-Ansatz wurde ursprünglich für Fluoreszenzlebenszeitmessungen in der Frequenzdomäne formuliert und wurde nun für Lebenszeitmessung in der Zeitdomäne adaptiert. Unter Berücksichtigung der speziellen Eigenschaften der Fluoreszenzzerfallkurven als Folge der zeitaufgelösten Messungen wurde im Rahmen dieser Arbeit ein Verfahren zur Berechnung der Phasorkoordinaten entwickelt, welches alle notwendigen Korrekturen, wie eine Korrektur der Untergrundfluoreszenz sowie eine Korrektur des Einflusses der Apparatefunktion (eng. instrument response function, IRF) beinhaltet. Die besondere Stärke des Phasor-Ansatzes zur Analyse von Fluoreszenzlebenszeitkurven liegt darin, dass er die Analyse der Fluoreszenzkinetik ohne eine *a priori* Annahme oder jedwedes Wissen über die jeweilige Probe erlaubt. Dabei ist mit dem Phasor-Ansatz sowohl eine qualitative als auch eine quantitative Analyse der Fluoreszenzlebenszeitkurven möglich. Als Grundlage dienen dabei lediglich die gemessenen Daten. Eine Vorabannahme hinsichtlich der den Fluoreszenzkurven zugrunde liegenden Fluoreszenzkinetik, wie dies beim in der Literatur häufig beschriebenen traditionellen Ansatz des 'Fittens' von Fluoreszenzkurven der Fall ist, ist nicht notwendig.

Eine detailierte Phasoranalyse ergab eine multiexponentielle Fluoreszenzkinetik für alle gemessenen Fluoreszenzlebensdauermessungen der isolierten LH2 Lichtsammelkomplexe von *Mch. purpuratum*. Bei Anregung der Bakteriochlorophyll-Pigmente in nahen Infrarotbereich (eng. near infrared, NIR) konnte eine bi-

exponentielle Kinetik mit Lebenszeitkomponenten von 730 ps und 50 ps für alle Kombinationen der Anregungsparameter identifiziert werden. Zusätzlich wurde für hohe Anregungsdichten, welche der Kombination aus hoher Laserwiederholrate und hoher Photonenanregungsfluenz entsprechen, eine dritte Lebenszeitkomponent von etwa 500 ps festgestellt werden. Bei Anregung der Karotenoid-Pigmente im sichtbaren Wellenlängenbereich (VIS) wurde eine globale biexponentielle Kinetik mit einer Lebenszeitkomponente von etwa 750 ps sowie einer kleineren Lebenszeitkomponente < 100 ps identifiziert, was in der Größenordung der biexponentiellen Kinetik entspricht, die bei Anregung der Bakteriochlorophylle beobachtet wurde. Eine dritte Lebenszeitkomponente konnte bei Anregung der Karotenoide nicht festgestellt werden.

Die größte in den Experimenten beobachtbare Lebenszeitkomponente von etwa 750 ps is deutlich kleiner als die üblicherweise berichtete Lebensdauer von etwa 1 ns für isolierte Lichtsammelkomplexe unterschiedlicher Spezies von Purpurbakterien [1, 2, 3, 4]. Da sie dennoch in der gleichen Größenordnung ist, kann diese Lebenszeitkomponente der Fluoreszenzemission der B830 Bakteriochlorophyll-Pigmente im LH2 von *Mch. purpuratum* zugeschrieben werden. Die kleine Lebnsdauerkomponente von weniger als 100 ps, die für alle Anregungssituationen beobachtbar ist, wird vorläufig dem Auftreten eines bislang unbekannten oder nicht auflösbaren exzitonischen Zustandes mit Charge-Transfer Charakter (eng, mixed exciton charge-transfer state, CT) in der elektronischen Struktur des B830 LH2 Komplexes von *Mch. purpuratum* zugeschrieben. Das Vorkommen solcher gemischter Exziton-CT Zustände in bakteriellen Lichtsammelkomplexen werden seit Jahren diskutiert [5, 6, 7] und sind in Übereinstimmung mit der beobachteten, kleineren Lebenszeit der B830 Pigmente [8]. Die dritte Lebenszeitkomponent, die ausschließlich bei Anregung der Bakteriochlorophyll-Pigmente und für hohe Anregungsdichten beobachtet wurde, ist auf das Auftreten von Singulett-Triplett Annihilationsporzesse zurückzuführen (STA).

Die Zuordnung der unterschiedlichen Lebenszeiten in der multiexponentiellen Kinetik erlaubt den Entwurf und Vorschlag eines Energieniveauschemas für den B830 LH2 Komplexes von *Mch. purpuratum*. Basierend auf diesem Vorschlag wurde anschließend der Unterschied in der beobachteten Kinetik bei Anregung der beiden Pigmente, Bakteriochlorophylle oder Karotenoide, diskutiert. Für die Anregung der unterschiedlichen Pigmente ergibt sich ein unterschiedlicher

Fluss der Energie, welcher in einer fundamental unterschiedlichen Situation von elektronischen Anregungen im Lichtsammelkomplex resultiert. Basierend auf diesem Unterschied wurde nachvollziehbar dargelegt, dass wahrscheinlich das Aufteten von Triplett-Triplett-Annihilationsprozessen die Ursache für den Unterschied in der beobachteten Fluoreszenzkinetik darstellt.

Abschließend wurden numerische Simulationen auf Basis eines dynamischen Monte Carlo (DMC) Algorithmus durchgeführt um das vorgeschlagene Energieniveauschema zu testen. Dazu wurde auf Basis des vorgeschlagenen Energieniveauschemas ein Ratenmodell entiwckelt. Ein Vergleich der experimentellen Fluorezenzzerfallkurven und der simulierten Transienten zeigte eine gute Übereinstimmung für alle Anregungsparameter. Eine Phasor-Analyse der simulierten Fluoreszenzzerfallkurven ergab, dass die experimentell beobachtete, mutliexponentielle Kinetik hinsichtlich aller drei Lebenszeitkomponenten gut reproduziert wurde. Auch die anteiligen Intensitätsbeiträge (eng. fractional contributions) der einzelnen Lebenszeitkonponenten wurde durch die Simulationen insgesamt gut wiedergegeben. Lediglich bei hohen Laserwiederholraten waren Abweichungen hinsichtlich der Internsitätsbeiträge beobachtbar.

Insgesamt wurde, basierend auf den Experimenten zur Untersuchung der Kinetik elektronischer Anregungen im B830 LH2 Komplex von *Mch. purpuratum* ein detailliertes Modell für dessen elektronische Struktur präsentiert.

Contents

1. Introduction

Facing a rise of the worldwide energy consumption since decades [9] in combination with the growing public awareness that fossil energy resources are limited, gives scientists and researchers a major challenge for the 21st century. Among the alternatives for energy production based on fossil resources, such as coal, oil and natural gas, the usage of solar energy is a promising candidate. Via sunlight the energy of approximately 4.3×10^{20} J arrives at the Earth's surface within a single hour. This is almost the same amount of energy as the world wide total energy consumption in the year 2017 (4.1×10^{20} J) [9].

Although solar cells on roof tops for the production of electricity from sunlight are nowadays already part of our daily life, the improvement of the technology for the usage of solar energy is still in the focus of current research. Within this broad field of science, two main approaches are distinguished: The first focuses mostly on the improvement of already existing technologies, such as the solar cells mentioned above, ranging from technical improvements to the development of new materials [10, 11, 12]. The second approach focuses on the fundamental aspect for using solar energy, which is the capture of sunlight. This challenge of light-harvesting has already been faced by nature since millions of years either by plants or other organisms, such as algae and photosynthetic bacteria [13]. Thus, the second scientific approach follows the theme 'learning from nature' and focuses on the investigation of the natural light-harvesting apparatus to either apply the obtained knowledge on existing technologies or even create new technologies [14]. Within this field of research, the light-harvesting apparatus of purple bacteria is often studied as a model system [15][16]. This is reasonable as purple bacteria perform highly efficient light-harvesting within their antenna complexes [17, 18]. Moreover, the peripheral antenna complexes show a significant spectral heterogeneity in their absorption properties which indicates that purple bacteria are adapted to a broad range of illumination conditions while maintaining the high efficiency of capturing sunlight.

In purple bacteria the capture of sunlight is performed by specialized antenna complexes. In general, these complexes are ring shaped pigment-pigment protein complexes consisting of a protein scaffold, formed by an outer and an inner ring of apoproteins, that sandwiches the absorbing pigments for light-harvesting and holds them in place. A general building principle of these rings can be assumed from atomic force microscopy [19, 20] and electron microscopy [21]. However, from X-ray crystallization analysis the molecular structure of the peripheral light-harvesting complexes is only known for three species of purple bacteria at high resolution [22, 23, 24]. From biochemical analysis it is known that the peripheral light-harvesting complexes of these three species of purple bacteria have a homogeneous composition of apoproteins, such that within their ring structure only one type of apoprotein occurs [25, 26]. For other species of purple bacteria the growth of high quality crystals for X-ray diffraction analysis was not possible yet. Interestingly, for several species of purple bacteria a heterogeneous composition of apoproteins was reported [26], indicating that different types of apoproteins form the protein scaffold of the light-harvesting pigments within the light-harvesting complex. However, the geometrical structure of these complexes can be analyzed indirectly by investigating the electronic structure of the light-harvesting complexes. The electronic structure of the light-harvesting complexes depends on the underlying geometrical structure of the molecules and is accessible by means of optical spectroscopy.

This thesis follows the pathway of the second approach mentioned above and investigates the peripheral light-harvesting complex of the purple bacterium *Marichromatium purpuratum*. Time-resolved spectroscopy is applied on its peripheral light-harvesting complex to investigate the kinetics of the electronic excitations upon optical excitation and thus draw conclusions on the electronic structure of this complex. In the further course of this thesis, first an introduction into bacterial photosynthesis and light-harvesting will be given. In detail, the function and structure of bacterial light-harvesting complexes will be discussed. Then, the material and the methods for both, the sample preparation of the light- harvesting complexes as well as for the experiments of time-resolved spectroscopy are explained.
For the analysis of the obtained fluorescence transients the so-called phasor approach is used instead of the classical fitting approach [27]. The theory of the

phasor approach, which originates from studies performed in the frequency domain [28], is given in detail and is expanded to time-domain data. In addition to this formulation of the phasor approach for time-domain measurements, a technique for the evaluation of the resulting phasors and the interpretation and analysis of the underlying kinetics is developed. Finally, from phasor analysis of the observed fluorescence transients, the kinetics of the electronic excitations within the B830 LH2 complex is discussed and a model of the electronic structure of the LH2 complex of *Marichromatium purpuratum* is proposed.

2. Bacterial Photosynthesis and Light-Harvesting

Photosynthesis, which is mainly understood as the absorption of solar light for the energy supply of an organism, is well known for plants. Moreover, a lot of organisms, such as algae and phototrophic bacteria, perform photosynthesis by capturing solar energy for their metabolism since millions of years. In the following course of this chapter, a short introduction will be given to the bacterial photosynthesis of purple bacteria. Focusing especially on the fundamental step of light-harvesting, it is outlined how purple bacteria perform light-harvesting with very high efficiency in their light-harvesting apparatus via specially designed antenna complexes. In detail, the peripheral antenna complex, which is called light-harvesting complex 2 (LH2), and its photophysics are discussed. Finally, a detailed description of the LH2 complex of the purple bacterium *Marichromatium pupuratum* is given, which is investigated in this thesis.

2.1. Bacterial Photosynthesis

In general, photosynthesis can be divided into four single steps: First, absorption and capture of sun light has to be realized. Second, the transfer of the resulting electronic energy and then, the conversion of electronic energy into chemical energy has to be performed. This happens in a third step by oxidation of photoactive pigments which leads to charge separation within these pigments. Subsequently, this charge separated state is stabilized, in a fourth step, to allow for using the energy for the bacterial metabolism. In purple bacteria these single steps of photosynthesis, which are all together also referred to as 'light reaction', are realized by the photosynthetic apparatus. This apparatus consists of networks of different, specialized antenna complexes that perform the process of capturing sunlight as well as the subsequent transfer of energy towards so called reaction centers, where the electronic energy is converted into chemical energy

that can be used by the organism. This network of antenna complexes is located in the specialized intracellular membranes within the bacterium, also referred to as chromatophores. Depending on the species of purple bacteria these intracellular membranes, that host the bacterial photosynthetic apparatus, can have different geometric shapes, ranging from circular vesicles up to lamellar structures, see Fig. 2.1. Transmission electron micrograph (TEM) sections show the variation of morphologies of the intracellular membranes for different species of purple bacteria.
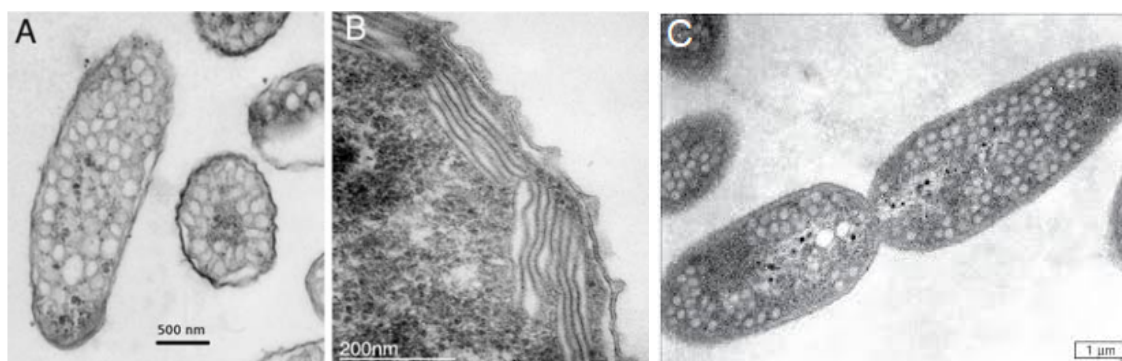
Figure 2.1.: The chromatophores of purple bacteria show a variation of morphologies : The intracellular membranes hosting the photosynthetic apparatus are shown by TEM sections of different purple bacteria: (A) Rhodospirillium rubrum, (B) Phaeospirillium molischianum and (C) Rhodobacter shaeroides. Whereas the chromatophores of Rhodospirillium rubrum (A) and Rhodobacter shaeroides (C) show circular membrane vesicles within the cytoplasma, Phaeospirillium molischianum forms stacked lamellar intracellular membranes (B). For details see text. (A) and (B) taken from [20]. (C) taken from [29].

The arrangement of the antenna complexes in networks within the intracellular membrane follows a general building principle for all purple bacteria. In Fig. 2.2 an atomic force microscopy (AFM) image shows the typical arrangement of the different ring-shaped antenna complexes [20]. Two types of light-harvesting complexes are distinguished by their function: The peripheral light-harvesting complexes, which correspond to the smaller rings in Fig. 2.2, act as antennas for capturing the sunlight and are called light-harvesting complexes 2 (LH2). In addition to the effective collection of sun light they also transfer the resulting electronic energy in the direction of the reaction center (RC), which is located within the ring of bigger diameter in Fig. 2.2. This transfer of energy can either occur via several other LH2 complexes until a light-harvesting complex that surrounds the reaction center is reached or by direct transfer to the other type

of light-harvesting complexes that surrounds the reaction center. This second type of light-harvesting complexes surrounding the reaction center are called light-harvesting complexes 1 (LH1) and appear as rings of bigger diameter in Fig. 2.2. The LH1 complex finally transfers the electronic energy to the reaction center where it is converted into chemical energy which can be used by the bacterium for metabolism. Due to their close contact with the reaction center LH1 complexes are referred to as RC-LH1 complexes.
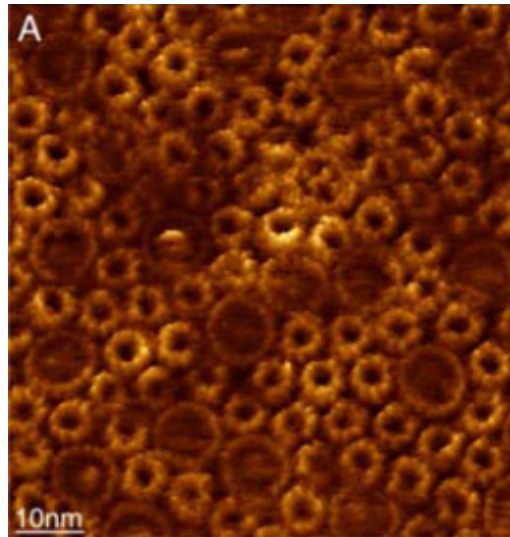
Figure 2.2.: Typical arrangement of the antenna complexes within the chromatophores: *An AFM image shows the typical structure of the light-harvesting apparatus for Rsp. photometricum. Antenna complexes of different functions are arranged within a dense network of antenna complexes to allow for the efficient capture of solar energy and subsequent energy transfer to the reaction centers. The smaller rings have been attributed to the peripheral light-harvesting complexes (LH2). The rings of bigger diameter have been identified as light-harvesting complexes 1 (LH1). Inside of the LH1 complexes the reaction center (RC) has been identified. For details see text. Taken from [20].*

A visualization of the process of light-harvesting and subsequent transfer of energy within the network of antenna complexes in purple bacteria is depicted in Fig. 2.3. The different types of light-harvesting complexes are shown schematically. The peripheral LH2 complexes are represented as green rings. The LH1 complex is visualized as a blue ring of bigger diameter which is filled by an orange sphere representing the reaction center (RC). Energy transfer processes are visualized by arrows. Sunlight, represented by the yellow flashes, is absorbed by the LH2 antenna complexes and the resulting electronic energy is subsequently transferred in the direction of the reaction center. The transfer of

energy between LH2 complexes, depicted as black arrows, occurs within 3 - 5 ps [30, 31, 32]. Subsequent transfer from a peripheral LH2 complex to an LH1 complex, grey arrows, happens on a similar timescale [30, 31, 32]. The final energy transfer step from the LH1 complex to the RC, visualized by the pale grey arrow, happens much slower within 35 ps [33, 34, 35].
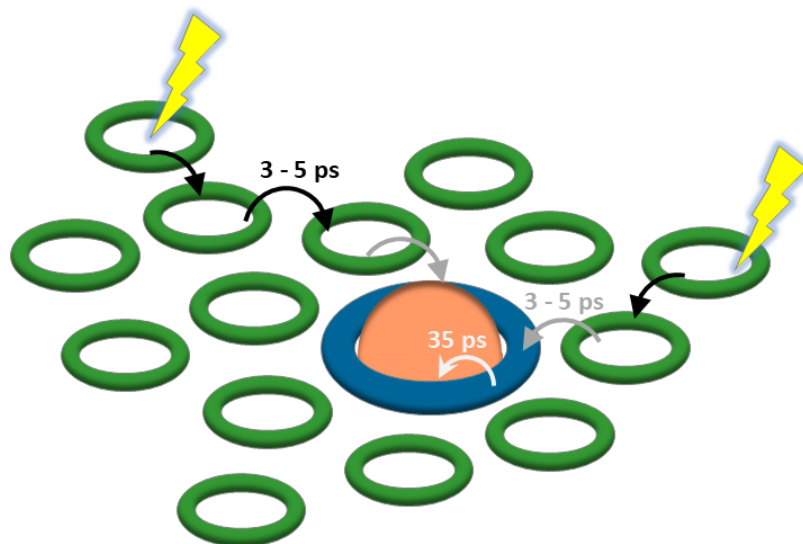
Figure 2.3.: Schematic drawing of the light-harvesting by a network of antenna complexes: *A network consisting of different light-harvesting complexes of purple bacteria is schematically shown. LH2 complexes are visualized by green rings, LH1 complexes appear as blue rings and the reaction center (RC) is visualized as an orange sphere within the LH1 complex. Incident sunlight is indicated by yellow flashes. Energy transfer processes are depicted by arrows. Black arrows correspond to LH2-LH2 transfer steps and grey arrows visualize the energy transfer from LH2 to LH1. The pale grey arrow represents the energy transfer from the LH1 ring to the RC. For details see text.*

In this thesis, the peripheral light-harvesting complex LH2 is in focus of investigation. Thus, a detailed description of the peripheral antenna complexes is given below.

2.2. Peripheral light-harvesting complexes (LH2) in purple bacteria

From atomic force microscopy [20], electron microscopy [21] as well as X-ray crystallography [22, 24, 23], it is known that the peripheral light-harvesting com-

plexes LH2 of purple bacteria have an elegant ring shape. Thus, although high resolution structural data is only available for the LH2 complex of two species, *Rhodopseudomonas (Rps.) acidophila* [22, 24] and *Rhodospirillium (Rsp.) molischianum* [23] until now, it is assumed that the cylindrical shape is a general feature of the LH2 complexes of purple bacteria and they all follow the same design principle.

The LH2 complex of *Rps. acidophila* is described below to give a detailed impression of the structure of such a peripheral light-harvesting complex. The absorbing pigments within the LH2 complex of *Rps. acidophila* are bacteriochlorophyll (BChl) *a* and the carotenoid (Car) rhodopin glucoside.

Bacteriochlorophyll *a* is a pigment that occurs in phototrophic bacteria for purpose of light-harvesting. The molecular structure of BChl *a* is shown on the left hand side of Fig. 2.4. The BChl *a* molecules consists of a tetrapyrrole ring hosting a central magnesium atom (Mg^{2+}) shown in pink and a long phytol chain tail. The pythol chain is oriented almost perpendicular to the bacteriochlorin macrocycle. Furthermore, the two transition-dipole moments of the tetrapyrrole ring are shown as red and blue arrows, respectively.
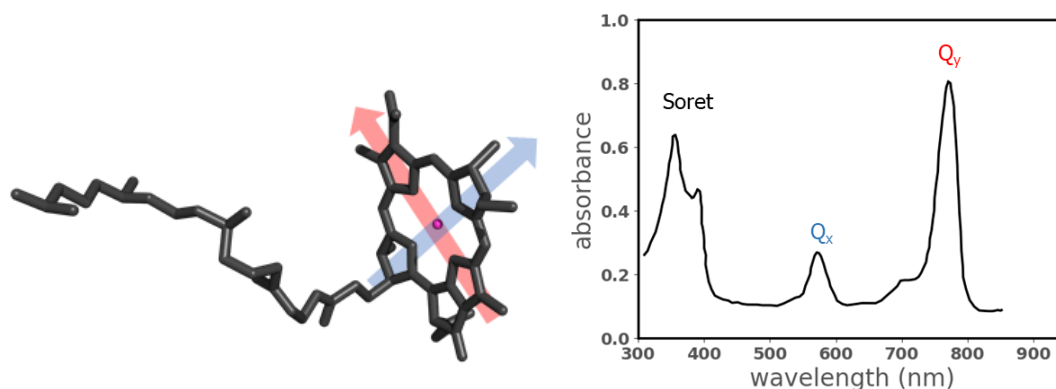
Figure 2.4.: Bacteriochlorophyll (BChl) a: On the left hand side the molecular structure of BChl a is visualized in grey. The central magnesium atom (Mg^{2+}) in the center of the bacterioclorin ring is highlighted in pink. The molecular structure was rendered with PyMOL (Schrödinger). On the right hand side the absorption spectrum of BChl a is shown. Data of the absorption spectrum is taken from [36]. For details see text.

On the right hand side of Fig. 2.4 the absorption spectrum of BChl *a* is shown. The intense absorption band at 770 nm in the near infrared (IR) and the absorption band located at 590 nm correspond to the transitions into the first and

second excited singlet state and are denoted as Q_y and Q_x, respectively. Their transition-dipole moments both originate in the perpendicular transition dipole moments of the bacteriochlorin ring (indicated by the red and blue arrow). The broad absorption band in the ultraviolet range (UV) between 300 nm and 400 nm corresponds to transitions into higher excited singlet states and is named Soret band.

The name carotenoids refers to a group of molecules that in principle all share the same general structure: A polyene chain with a length of 9 to 11 alternating double bonds. At both ends of the polyene chain terminating rings may appear. The molecular structure of the carotenoid rhodopin glucoside, that is incorporated in the LH2 complex of *Rps. acidophila*, is shown in green on the left hand side of Fig. 2.5. Both, the long polyene chain backbone as well as the terminal ring, are visualized. On the right hand side of Fig. 2.5 the absorption spectrum of rhodopin glucoside is shown. The broad absorption band is located around 500 nm in the visible (VIS) wavelength range. Thus, the carotenoid rhodopin glucoside allows for the absorption of light where BChl *a* shows nearly no absorption, compare right hand side of Fig. 2.4.
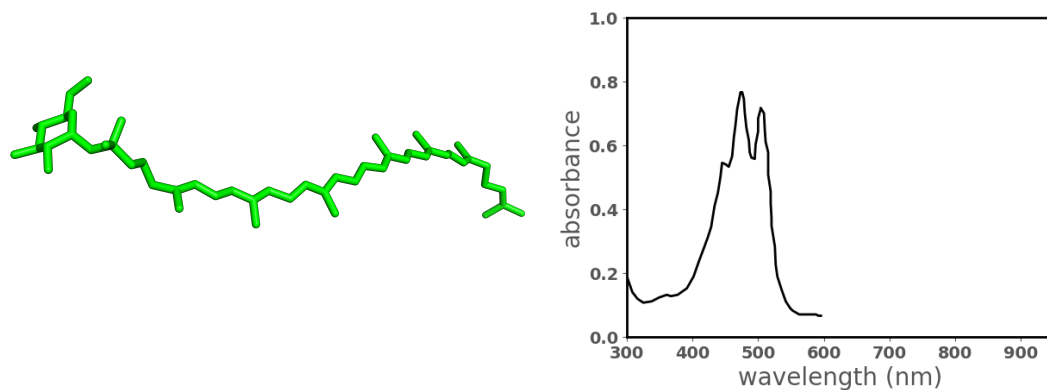
Figure 2.5.: The carotenoid rhodopin glucoside: *On the left hand side the molecular structure of the carotenoid rhodopin glucoside is visualized in green. The molecular structure was rendered with PyMOL (Schrödinger). On the right hand side the absorption spectrum of rhodopin glucoside is shown. Data of the absorption spectrum taken from [36]. For details see text.*

The LH2 complex of *Rps. acidophila* consists of nine identical subunits. Each of these basic building blocks comprises two apoproteins that act as scaffold for the absorbing pigments BChl *a* and the carotenoid rhodopin glucoside. In

each of the subunits the pair of apoproteins holds in place three bacteriochloro-
phyll *a* molecules and one rhodopin glucoside carotenoid molecule. A schematic
drawing of the basic building block of the LH2 complex of *Rps. acidophila* is
shown in Fig. 2.6. The two apoproteins are visualized as helices of light blue and
grey color, respectively. One of the BChl *a* molecules, shown in yellow, has its
tetrapyrrole ring oriented perpendicular to the symmetry axis of the two apopro-
teins. The other two BChl *a* molecules per subunit, both colored in red, are in
close contact to each other and the planes of their tetrapyrrole rings are oriented
parallel to the symmetry axis of the two apoproteins. The carotenoid molecule
of rhodopin glucoside, colored in green, winds along between the three BChl *a*
molecules and the apoprotein helices and lies almost diagonal within the basic
building block of the LH2 complex.

*(a) apoproteins plus
BChl a molecules*

*(b) apoproteins plus
BChl a and Car molecules*
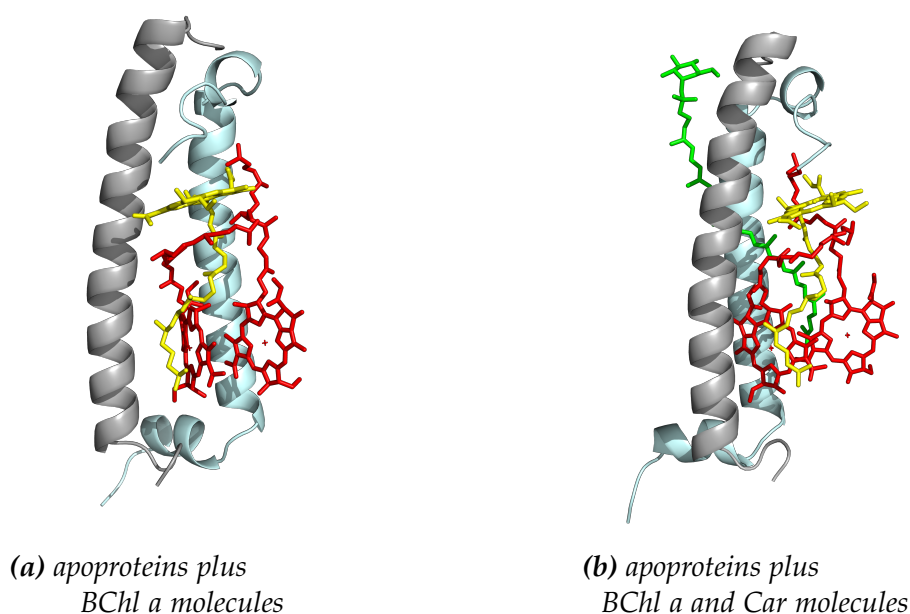
Figure 2.6.: The basic building block of the LH2 complex: *Two apoproteins (grey and
light blue helices, respectively) act as a protein scaffold for the absorbing pigments. The
positions of the three BChl a molecules is shown in **(a)**. One of the BChl a molecules has
its tetrapyrrole ring oriented perpendicular to the symmetry axis of the two apoproteins
(yellow). The other two BChl a molecules (red) are in close contact to each other and
the planes of their tetrapyrrole rings are oriented parallel to the symmetry axis of the
two apoprotein helices. In **(b)** additionally the Car molecule of rhodopin glucoside is
shown (green). Both graphics were rendered with PyMOL (Schrödinger). For detailed
description see text.*

Finally, the LH2 complex of *Rps. acidophila* is a ring formed by nine of such
subunits. Two views, one tilted view and one top view, of the complete LH2

complex *Rps. acidophila* are shown in Fig. 2.7. The apoproteins form two cylinders, one inner cylinder (light blue color) and one outer cylinder (grey color), that act as scaffold and hold in place the non-covalently bound pigments, 27 BChl *a* molecules and 9 Car molecules. Due to their almost diagonal position within the basic building block, the Car molecules of rhodopin glucoside stabilize the LH2 ring ranging from one subunit to the next. Thus, the Car has a stabilizing function within the LH2 complex and most species of purple bacteria cannot form LH2 complexes without Car pigments [37, 38]. Moreover, the dense packing of the absorbing pigments can be clearly seen in both views.

(a) tilted view   *(b) top view*
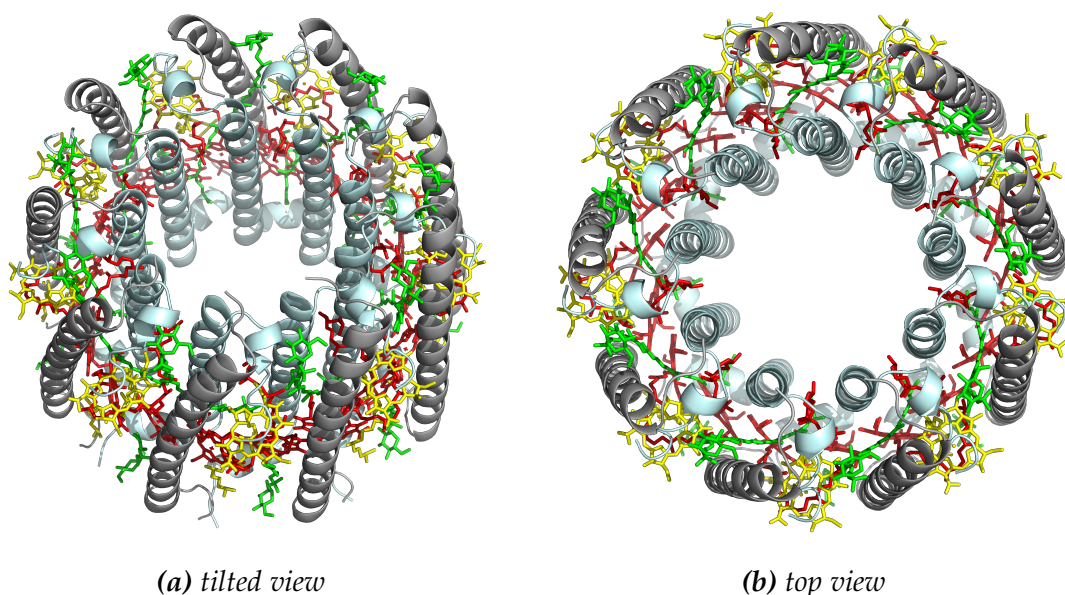
Figure 2.7.: The light harvesting complex 2 (LH2) of Rps. acidophila: *A tilted view (a) and a top view (b) of the LH2 complex is shown. The apoproteins that form the inner and the outer cylinder (grey and light blue color, respectively) that hold in place the non-covalently bound pigments are shown as helices. The two groups of BChl a molecules are shown in red and yellow, respectively, depending on how their bacteriochlorin rings are oriented with respect to the symmetry axis of the LH2 ring. Car molecules are shown in green. Both graphics were rendered with PyMOL (Schrödinger). For detailed description see text.*

The room temperature absorption spectrum of isolated LH2 complexes of *Rps. acidophila* in detergent solution is shown in Fig. 2.8(a). It clearly allows for identification of the contribution of the different pigments. In order to identify the different absorption bands, the absorption spectrum of the isolated LH2 complex is compared with the absorption spectra of the isolated pigments, see Fig. 2.4 and Fig. 2.5. Thus, the distinct absorption bands below 600 nm are easily identified.

The absorption bands at 400 nm and 600 nm originate in the BChl *a* pigment, whereas the three peaks in the range of 450 nm and 550 nm clearly correspond to the Car absorption spectrum. Thus, the combination of pigments allows the LH2 complex for absorption in a broad range over the VIS wavelength spectrum. The two intense absorption peaks located at 800 nm and 850 nm in the absorption spectrum of the LH2 complex are also attributed to the BChl *a* pigments within the LH2 complex. Two rings are formed by the BChl *a* molecules as visualized in Fig. 2.8(b). In analogy to the description of the basic building block of the LH2 complex above, these two groups of molecules are colored in yellow and red respectively, in order to visualize their distinction based on the different orientation of their BChl *a* molecules within the LH2 ring. The absorption band located at 800 nm originates from those 9 BChl *a* molecules, that have their tetrapyrrole rings oriented perpendicular to the symmetry axis of the LH2 ring and are shown in yellow. Thus, this group of BChl *a* molecules is also referred to as the B800 ring. The spectral shift of about 30 nm with respect to the Q_y absorption band of isolated BChl *a*, compare Fig. 2.4, is due to the non-covalent bonding with the surrounding apoproteins [39].

(a) Absorption spectrum

(b) BChl a rings: B800 and B850
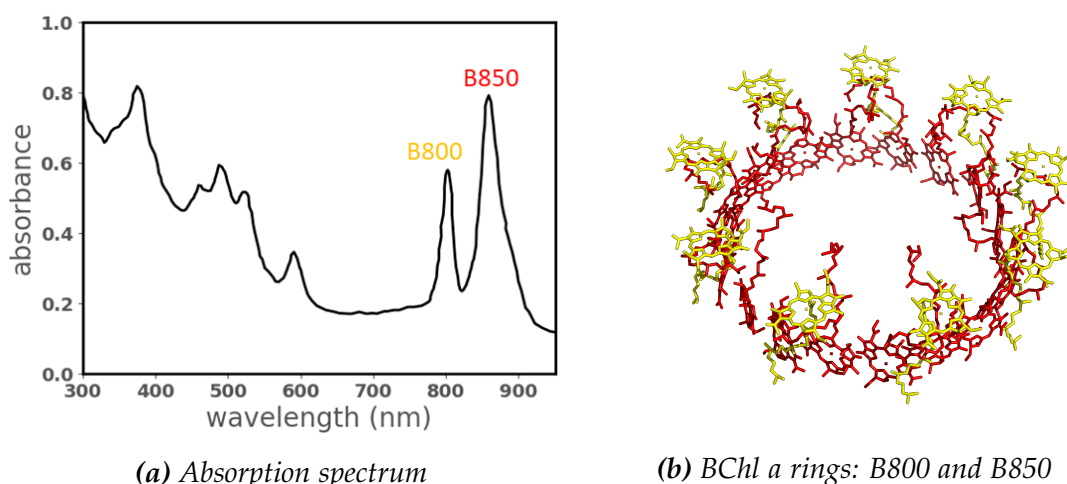
Figure 2.8.: The absorption spectrum of the LH2 complex of Rps. acidophila: *In* ***(a)*** *the absorption spectrum of the LH2 complex of Rps. acidophila in detergent solution (20 mM Tris-HCl, pH 8.0, 0.05% LDAO) is shown.* ***(b)*** *visualizes the two rings of BChl a molecules: the B800 ring is shown in yellow whereas the B850 ring is colored red. The molecular structure of the two rings was rendered with PyMOL (Schrödinger). Data of the absorption spectrum is taken from [39]. For detailed description see text.*

The strong absorption band located at 850 nm is attributed to the other group of 18 BChl *a* molecules, shown in red in Fig. 2.8b. This ring of BChl *a* molecules is

called B850 ring due to the location of the absorption band. All molecules within the B850 ring have oriented their tetrapyrrole rings parallel to the symmetry axis of the LH2 ring which leads to small intermolecular distances. This results in strong interaction of the transition moments of the single molecules within this ring. Thus, the pronounced shift of the absorption peak with respect to the Q_y absorption band of isolated BChl *a*, see Fig. 2.4, is mainly caused by excitonic effects resulting from the strong interaction of the single B850 BChl *a* molecules [40].

2.3. Photophysics of the LH2 complex: electronic structure and electronic excitations

The photophysics of LH2 complexes will be explained using the standard LH2 complex of *Rps. acidophila* as described above as an example.

The photophysics of an isolated LH2 complex is directly related to the incorporated pigments. Focusing on the strong absorption bands of the LH2 complex in the IR range, both rings of BChl *a* molecules, namely the B800 and the B850 ring, act as absorbing pigments. In Fig. 2.9 the two rings of BChl *a* molecules are visualized in red and yellow, respectively. Absorption of light results in the creation of singlet excitations on the BChl *a* molecules of the different rings. For the B800 ring, due to the relatively large distance between the BChl *a* molecules within the LH2 ring, there is only weak coupling observed and the electronic excitation is only slightly delocalized along the ring of molecules [36, 41, 42]. Thus, it is often approximated as rather localized on the individual pigments [43, 44] as indicated by the yellow clouds around the bacteriochlorin rings of the B800 molecules in Fig. 2.9. Subsequently, the excitation energy is either transferred to another, neighboring BChl *a* molecule by intra-band energy transfer within 1 ps [45, 46, 44] or alternatively transferred to the B850 ring on a similar timescale [44, 45, 47]. Both competing energy transfer processes are visualized in Fig. 2.9 by arrows between the B800 and B850 molecules, respectively.

In contrast to the B800 ring, the B850 ring of the LH2 complex shows strong coupling of the BChl *a* molecules due to the rather close arrangement of the individual molecules within the LH2 complex. As a result of this strong interac-

tion between the BChl *a* molecules, the electronic excitation within the B850 ring delocalizes over the entire ring forming excitons [48, 49, 50] immediately after creation and finally equilibrates on a few BChl *a* molecules within a few tens of femtoseconds (fs) [51, 1, 52]. A detailed theoretical and mathematical formulation and description of the delocalized excitons within the B850 ring can be found in detail in literature [36]. The delocalization of the electronic excitations along the B850 ring of the LH2 complex is visualized in Fig. 2.9 in pale red color. The transfer of energy between the BChl *a* molecules of the B850 ring happens extremely fast within a few hundred femtoseconds (fs) [45].
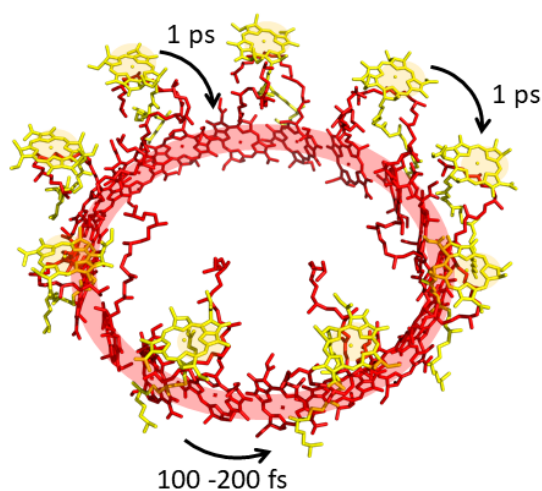
Figure 2.9.: Electronic excitations in the B800 and B850 ring of LH2: The BChl a molecules of the B800 and B850 rings within the LH2 complex are visualized in yellow and red, respectively. Electronic excitations created in the B800 ring are rather localized on the individual pigments, indicated by the yellow clouds around the bacteriochlorin rings of the B800 molecules. In contrast, electronic excitation of the B850 ring delocalizes immediately along the ring, as indicated in pale red color. Energy transfer processes between the BChl a molecules are depicted by arrows. The molecular structure of the two BChl a rings was rendered with PyMOL (Schrödinger). For details see text.

Neglecting the intra-band energy transfer processes within the B800 ring as well as for the B850 ring allows for approximation of the excited states of the two rings as single energy levels, respectively. Thus, the photophysics of the LH2 complex, which is closely related to its electronic structure, can be summarized in an energy level diagram as shown in Fig. 2.10.
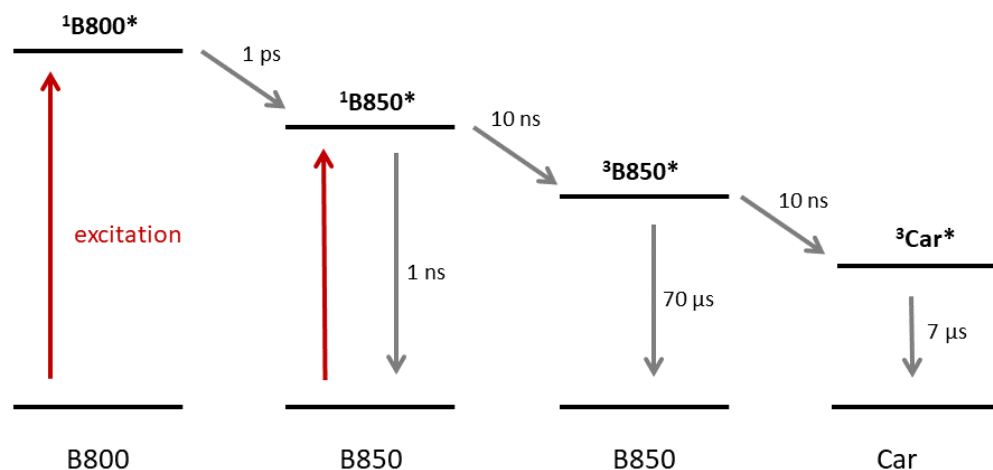
Figure 2.10.: Energy level scheme for the LH2 complex of Rps. acidophila: *The excited states of the three groups of pigments, the B800 BChl a molecules, the B850 BChl a molecules and the Car molecules, are shown as single energy levels. The singlet excitation levels of the B800 and the B850 ring are denoted as ^{1}B800* and ^{1}B850*, respectively. The triplet states of the B850 and Car molecules are referred to as ^{3}B850* and ^{3}Car*, respectively. Absorption of excitation light is depicted by red arrows, downhill transitions between the distinct energy levels are depicted as grey arrows. For details see text.*

Absorption of excitation light (depicted as red arrows) results in the formation of an excited singlet state ^{1}B800* and ^{1}B850* in the two rings of BChl *a* molecules depending on the excitation wavelength. Energy transfer from the B800 to the B850 ring occurs within 1 ps [44, 45, 47]. From the singlet excited state ^{1}B850* of the B850 ring, relaxation into the ground state occurs radiatively under emission of fluorescence within 1 ns [1, 2]. Alternatively, the energy of the ^{1}B850* state can be transferred to the triplet state ^{3}B850* via intersystem crossing (ISC) within 10 ns [53]. The population of the ^{3}B850* triplet state occurs predominantly under high illumination conditions. Relaxation from the ^{3}B850* triplet state into the ground state is observed on a timescale of about 70 μs [53, 54][1]. The ^{3}B850* triplet state is highly sensitive for singlet oxygen, which is extremely harmful for pigment-protein complexes such as the LH2 complex. Thus, the energy of this triplet can also be transferred to an adjacent carotenoid molecule for reasons of photoprotection [58, 59, 60]. The quenching of the ^{3}B850* triplet state by the carotenoid occurs via triplet-triplet energy transfer on a timescale of about 10 ns

---

[1]This value for the BChl triplet lifetime refers to LH2 complexes lacking carotenoids. For LH2 complexes containing carotenoid pigments a BChl triplet lifetime of about only 20 ns is reported, due to quenching by the highly efficient triplet-triplet energy transfer from bacteriochlorophyll to carotenoid [55, 56, 57].

[57]. The lifetime of the ^{3}Car* triplet state decay is reported to be in the range of $7\,\mu$s [57]. Thus, additionally to their structural function mentioned above, carotenoids are essential for photoprotection of the light-harvesting complex. Finally, recognizing their photoprotective role allows for the formulation of a simplified energy level scheme of the LH2 complex that disregards the ^{3}B850* triplet state, shown in Fig. 2.11.
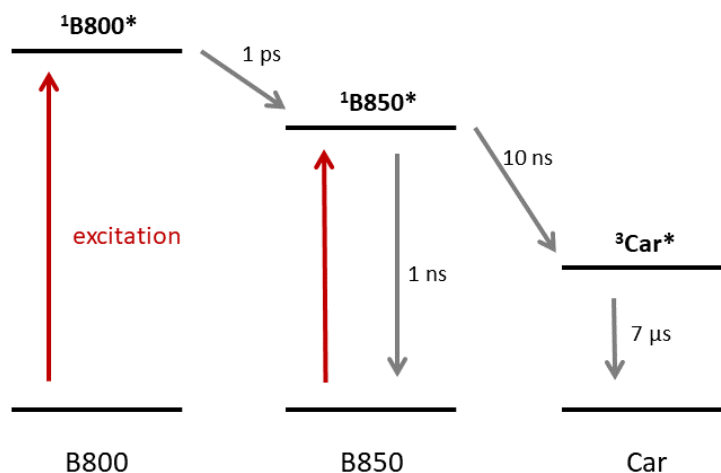
Figure 2.11.: Simplified energy level scheme for the LH2 complex of Rps. acidophila: The excited states of the three groups of pigments, the B800 BChl a molecules, the B850 BChl a molecules and the Car molecules, are approximated as single energy levels. The singlet excitation levels of the B800 and the B850 ring are denoted as ^{1}B800* and ^{1}B850*, respectively. The triplet state of the Car molecules is referred to as ^{3}Car*. Absorption of excitation light is depicted by red arrows, downhill transitions between the distinct energy levels are depicted as grey arrows. For details see text.

The electronic structure of the LH2 complex and the resulting kinetics of the electronic excitations can be studied by means of optical spectroscopy. Previous studies on isolated LH2 complexes reported the occurrence of excitation-excitation annihilation (EEA) processes as a function of the excitation conditions. For high illumination conditions, such as high excitation energies per pulse, the occurrence of multiple singlet excitations within the B850 ring of the LH2 complex was reported. Thus, singlet-singlet annihilation (SSA) was observed due to the high mobility of the delocalized excitons within the B850 ring [61]. From these findings a lower limit of the critical value for the onset of the occurrence of singlet-singlet annihilation processes in LH2 complexes was determined to $8 \cdot 10^{14}$ photons/(pulse·cm^2) [61]. Moreover, for the repetition rate of the excitation laser pulses, which determines the temporal distance between the laser

pulses, it was reported that values above 1 MHz may lead to an accumulation of triplet states within the LH2 ring [62]. Moreover, when an LH2 complex still carries a triplet excitation resulting from the previous pulse, the occurrence of singlet-triplet annihilation (STA) has to be considered. Although the triplet excitation within the LH2 complex is reported to be localized on one Car molecule and thus can be expected as immobile [63, 64, 65], due to the high mobility of the singlet excitation within the B850 ring singlet-triplet annihilation may occur. For the situation of high laser repetition rates in combination with high excitation power per pulse, even the occurrence of triplet-triplet annihilation (TTA) has to be taken into account [62].

All excitation-excitation annihilation (EEA) processes described above follow a general principle. A schematic drawing of this principle is shown in Fig. 2.12.

energy transfer

internal conversion

A*   B*   A   B**   A   B*
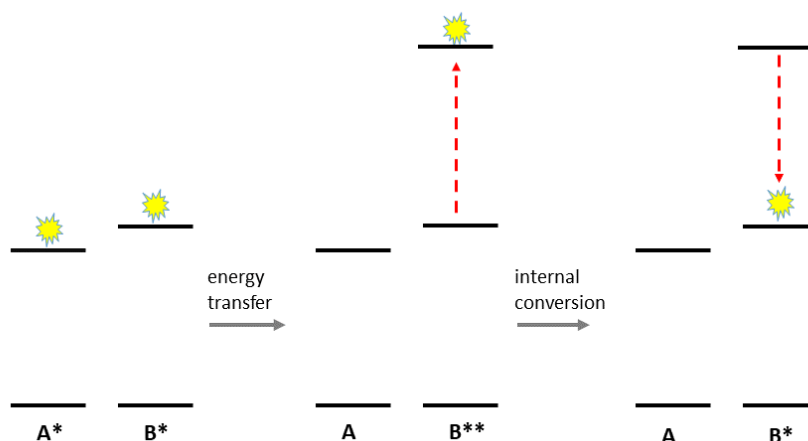
Figure 2.12.: Excitation-excitation annihilation (EEA) process: *The general principle of excitation-excitation annihilation is visualized. Two excitations are in close proximity to each other. Excitations are represented by stars. First energy transfer takes place such that one of the molecules relaxes to the ground state whereas the other is in a higher excited stated. The second step is internal conversion. Thus, one excitation was annihilated and only one molecule in the excited state is left. Visualization adapted from [66]. For details see text.*

Two excitations on two molecules, approximated as two level systems for simplicity, are in close proximity to each other. The two molecules are named A and B and the first excited state is denoted by a superscript *. In the first step the energy of one of the molecules is transferred to the other. Depending on the type of electronic excitation of the two molecules, the energy transfer mechanism

of this step is either mediated via dipole-dipole interaction (Förster-type [67]) or occurs via electron exchange (Dexter-type [68]) for singlet and triplet excitations, respectively. After this first step of energy transfer within the process of EEA, one molecule is in the ground state (A) whereas the other is now in a higher excited state, denoted as B**. Then, by internal conversion the excited molecule relaxes into the lowest excited state (B*), the same as before the annihilation occurred. A detailed review on the theory of excitation-excitation annihilation can be found in [66].

Although the single steps of energy transfer and internal conversion within the process of excitation-excitation annihilation will not be resolved by optical spectroscopy, the occurrence of annihilation processes can be observed. Thus, investigation of the kinetics of electronic excitations by variation of the excitation parameters is a well known principle of time-resolved spectroscopy [3, 69, 70].

2.3.1. The role of carotenoids in the photophysics of LH2 complexes

As already indicated in the previous section carotenoids play various roles within bacterial light-harvesting complexes. Besides their stabilizing, structural function for the entire geometry of the LH2 complex [37, 59, 38, 71], these pigment molecules serve at least two more fundamental functions within the photophysics of bacterial light-harvesting complexes: light harvesting as well as photoprotection [58, 59, 60].

The photoprotective role of carotenoids in LH2 complexes of purple bacteria has already been mentioned above when describing the energy level scheme of the LH2 complex of *Rps. acidophila*. By quenching of the bacteriochlorophyll (BChl) triplet excitation via triplet-triplet energy transfer to the carotenoid triplet state of an adjacent carotenoid molecule, the harmful reaction of the BChl triplet with molecular oxygen is prevented [58, 60]. Thus, due to their photoprotective characteristics carotenoids play an essential role for the integrity of the bacterial LH2 complex [72]. The light-harvesting function of carotenoids within LH2 complexes was slightly indicated before, when describing the building principle of peripheral bacterial light-harvesting complexes, LH2 complexes. The carotenoid pigments incorporated into the LH2 complex of purple bacteria result

in significant absorption peaks in the visible (VIS) region of the electromagnetic wavelength spectrum, mostly located between 450 nm and 550 nm, compare also Figures 2.5 and 2.8a. Thus, the incorporation of carotenoids within the LH2 complex allows for absorption of sun light which would otherwise not be accessible for the bacterial metabolism and expands the number of possible habitats of purple bacteria.

In order to illustrate the light-harvesting function of carotenoids within LH2 complexes, Fig. 2.13 shows a simplified[2] energy level scheme of the LH2 complex of *Rps. acidophila* in similar manner as before, but now considering excitation of the carotenoid molecules.
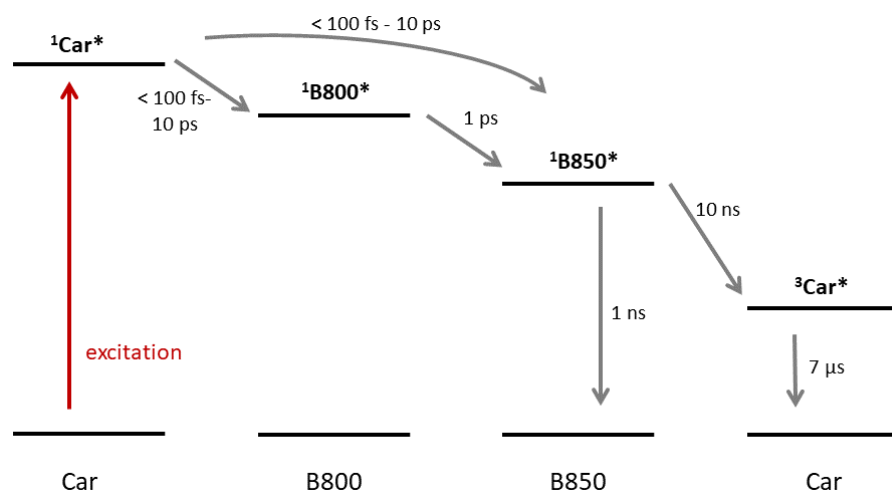
Figure 2.13.: Simplified energy level scheme for the LH2 complex of Rps. acidophila considering carotenoid excitation as well as carotenoid-to-bacteriochlorophyll energy transfer: The excited states of the three groups of pigments, the B800 BChl a molecules, the B850 BChl a molecules and the Car molecules, are approximated as single energy levels. The singlet excited state of the Car molecules, resulting from carotenoid excitation, is referred to as ^{1}Car*. The singlet excitation levels of the B800 and the B850 ring are denoted as ^{1}B800* and ^{1}B850*, respectively. The triplet state of the Car molecules is referred to as ^{3}Car*. Absorption of excitation light is depicted by red arrows, downhill transitions between the distinct energy levels are depicted as grey arrows. For details see text.

Absorption of sunlight by the carotenoid molecules incorporated within the LH2

---

[2]The photophysics of carotenoids themselves as well as when these molecules are incorporated in LH2 complexes is complex and still matter of investigations. Thus, here the focus lies on the essential aspects of carotenoids for baterial light-harvesting. An overview of the photophysics of carotenoids in general is given in Appendix A.

complex results in a singlet excitation of the absorbing carotenoid molecule[3]. By energy transfer of this singlet excitation from the carotenoid to an adjacent BChl *a* molecule in close proximity, the absorbed energy is fed into the downhill energy cascade of the LH2 complex as outlined before and known from the energy level scheme shown above, compare Figures 2.10 and 2.11. Thus, the excitation of carotenoid pigments within the LH2 complex can be considers as an 'alternative' excitation pathway of the bacteriochlorophyll molecules, resulting in approximately similar kinetics.

The energy transfer from the carotenoid is reported to occur to both groups of BChl *a* pigments within the LH2 complex, the B800 ring as well as the B850 ring [73, 74, 75, 71]. Both, the energy transfer efficiency as well as the transfer time of the carotenoid-to-bacteriochlorophyll energy transfer within the LH2 complex are reported to vary significantly for different species of purple bacteria. The energy transfer efficiency varies from 25% for LH2 of *Rps. palustris* up to almost 100% for LH2 of *Rba. sphaeroides* [76, 73, 63]. Regarding the energy transfer times of the carotenoid-to-bacteriochlorophyll energy transfer within LH2, time values ranging from below hundred fs up to 10 ps are reported [73, 77]. Thus, the incorporation of carotenoid molecules allows for highly efficient light-harvesting of bacterial LH2 complexes.

2.4. Spectral variation of LH2 complexes for different species of purple bacteria

The LH2 complex of *Rps. acidophila* featuring the characteristic absorption bands at 800 nm and 850 nm described above is often referred to as 'standard' LH2 complex. This is not only due to the fact that its structure was the first available at high resolution from X-ray crystallization [22]. Moreover, also the LH2 complex of *Phs. molischianum*, which corresponds to the other structure of an LH2 complex that is known at high resolution until now [23], exhibits a similar absorption spectrum. For low-light (LL) growth conditions a spectral shift of the B850 absorption band to 820 nm is observed for the LH2 complex of *Rps. acidophila*. As this LH2 complex is the third in the group of three, for which

---

[3]For simplicity this excitation of the carotenoid is only referred to as a singlet excitation for the moment without naming any details, neglecting the complex and yet not fully resolved photophysics of carotenoids as outlined in Appendix A.

the structure is known at high resolution at the moment, comparison with the 'standard' LH2 complex grown at high-light (HL) intensities allows for investigation of this phenomenon. Whereas both LH2 complexes of *Rps. acidophila* exhibit a nonameric symmetry of their LH2 ring, for the LH2 complex grown at LL intensities structural changes in the sequence of amino acids of the apoproteins were found [78]. As a result of this, different binding of the B850 BChl *a* molecules within the apoprotein scaffold occurs, and thus the absorption band is shifted to 820 nm for the LL LH2 complex [79].

Interestingly, in general, the LH2 complexes of various purple bacteria show a strong spectral variation of the absorption bands in the near infrared (IR) range. The absorption spectra of isolated LH2 complexes in detergent solution are shown in Fig. 2.14 for different species of purple bacteria.
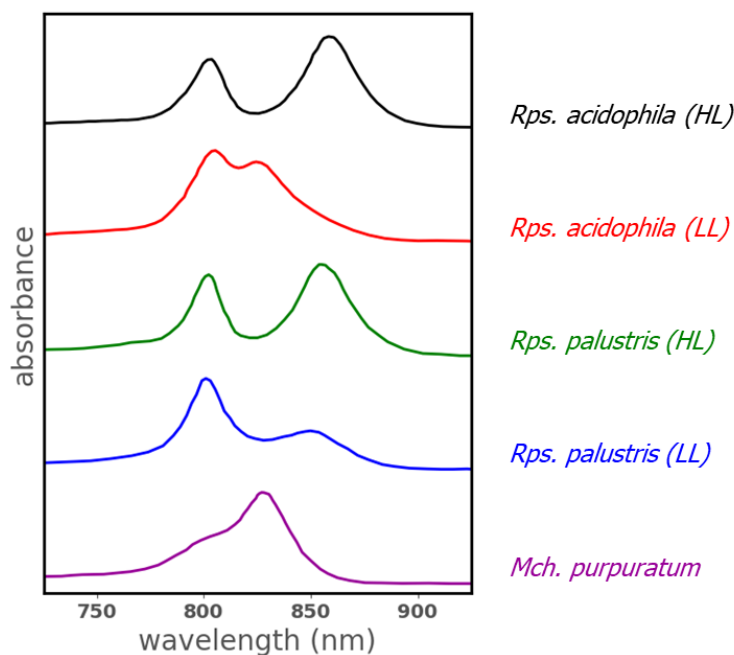
***Figure 2.14.: Spectral heterogeneity of LH2 complexes:** The absorption spectra of isolated LH2 complexes in detergent solution are shown for different species of purple bacteria. The absorption spectrum of the 'standard' LH2 complex of Rps. acidophila grown at high-light (HL) intensities is shown in black, the spectrum for LH2 complexes grown at low-light (LL) intensities is shown in red below. In green and blue the absorption spectra for LH2 complexes of Rps. palustris grown at HL and LL contitions are shown, respectively. At the bottom, the absorption spectrum of the B830 LH2 complex of Marichromatium purpuratum is shown in purple. Data for Rps. acidophila and Mch. purpuratum taken from [80]. Data for Rps. palustris taken from [36]. For details see text.*

At the top, the 'standard' absorption spectrum of the LH2 complex of *Rps. acidophila* grown at HL intensity as well as for the LH2 complex grown at LL intensities is shown in black and red, respectively. The influence of the grow conditions is clearly seen, as the B850 absorption band shifts to 820 nm for LL intensity growth conditions. Below, the absorption spectra of the LH2 complexes of *Rps. palustris* are illustrated for both, HL (green) and LL (blue) growth conditions. Whereas the HL LH2 complex of *Rps. palustris* exhibits similar positions of the absorption bands as the 'standard' absorption spectrum of *Rps. acidophila*, for LL growth conditions the B850 band nearly vanishes. At the bottom of Fig. 2.14, the unusual absorption characteristics of the B830 LH2 of *Marichromatium purpuratum* is shown. The absorption maximum is located at 830 nm such that the B800 absorption peak almost disappears and reduces to a shoulder of the broad absorption band.

The origin of the variation of the spectral positions is not only attributed to structural changes of the apoproteins resulting in different binding of the BChl *a* molecules [79], moreover for species exhibiting non-standard absorption spectra heterogeneous apoprotein compositions of the LH2 complexes are reported [81, 82, 25, 26]. This feature is strikingly different to the 'standard' LH2 complexes of *Rps. acidophila* described above, which have homogeneous apoprotein compositions [26]. The definition of a homogeneous or heterogeneous apoprotein composition refers to the composition of the apoproteins within one LH2 ring, forming the protein scaffold for the enclosed pigments, as illustrated in Fig. 2.15.

homogeneous   vs.   heterogeneous

apoprotein composition
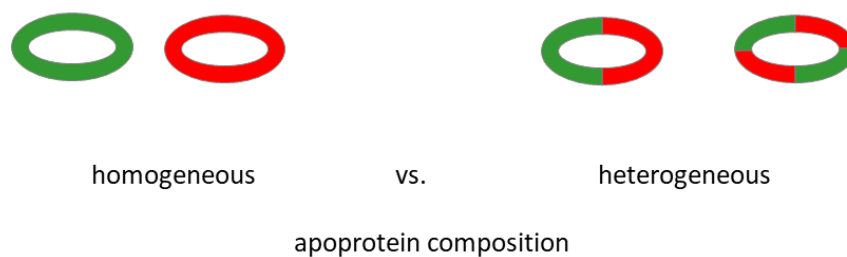
Figure 2.15.: Different apoprotein compositions of the LH2 ring: Whereas homogeneous apoprotein compositions suggest that within one LH2 ring only one type of apoprotein occurs, different LH2 complexes may have different apoproteins. In contrast, a heterogeneous apoprotein composition refers to the fact that one LH2 ring is formed by several types of apoproteins. Different types of apoproteins are visualized by different colors.

Whereas LH2 complexes of *Rps. acidophila* have a homogeneous apoprotein composition for both growth conditions, the apoproteins are different for HL and LL growth intensities [25]. In contrast, the LH2 complexes of most of the purple bacteria exhibiting non-standard absorption characteristics have a heterogeneous apoprotein composition such that within one ring different apoproteins appear [26].

As the growth of high-quality crystals for X-ray diffraction analysis is extremely difficult for non-standard LH2 complexes, the determination of their precise structure is still object of current research. However, the electronic structure of an LH2 complex is strongly correlated to its geometrical structure. In order to investigate the structure of an LH2 complex the comparison of spectra resulting from optical spectroscopy, which allows for probing the electronic structure of the LH2 complex, and spectra calculated and resulting from an assumed structural model of the respective LH2 complex, allows for indirect investigation of the geometrical structure of the LH2 complex. On basis of the agreement or mismatch of the compared spectra the structural model underlying the calculated spectra, proposing a geometric structure for the LH2 complex, can be either confirmed or not, giving rise to further refinements. Thus, optical spectroscopy is a powerful tool that allows for drawing conclusions on the geometrical structure of the LH2 complex, especially for single-molecule spectroscopy [83].

2.5. The peripheral B830 LH2 complex of *Marichromatium purpuratum*

The peripheral light-harvesting complex of the marine purple bacterium *Marichromatium (Mch.) purpuratum* was first described in 1990 [84] and prooven to be extremely stable, regarding high concentrations of salt, detergents and organic solvents [85]. Due to its unusual absorption characteristics, as shown in Fig. 2.16, it is often referred to as B830 LH2 complex. In contrast to the 'standard' LH2 of *Rps. acidophila* only one strong absorption band located at 830 nm appears, the expected B800 nm peak reduces to a small shoulder, compare also Fig. 2.14. The pigments within the B830 LH2 complex were identified as BChl *a* and the rather unusual keto-carotenoid carotenoid okenone [84].

Detailed biochemical analysis revealed that upon variation of growth conditions, such as high-light or low-light intensities, no spectral variation of the B830 LH2 complex was observed [85, 86, 87], which is in contrast to the LH2 complexes of many other species of purple bacteria [88, 89, 90, 91, 92, 93, 82]. Moreover, a heterogeneous apoprotein composition was found for the B830 LH2 complex of *Mch. purpuratum* [87, 85, 86]. Detailed analysis of the apoproteins even resulted in the hypothesis that one apoprotein pair, as the basic building block of the LH2 ring, might contain more than the usual three BChl *a* molecules due to the possibility of an additional BChl *a* binding site [85]. Additionally, a very strong interaction of the BChl *a* molecules and the carotenoid okenone was reported for the B830 LH2 complex of *Mch. purpuratum* [63].
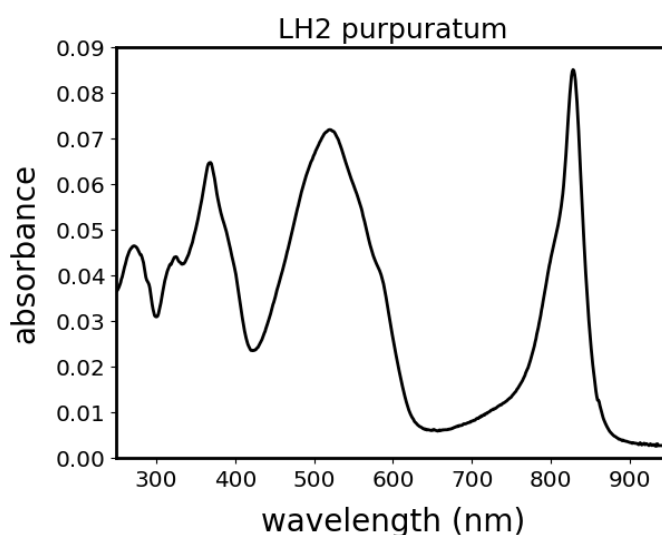
Figure 2.16.: Absorption spectrum of the B830 LH2 complex of Mch. purpuratum: The absorption spectrum of isolated B830 LH2 complexes in detergent solution (20 mM HEPES, 0.1% LDAO, pH 7.8) is shown. For details see text.

From preliminary X-ray analysis an octameric symmetry was proposed for the B830 LH2 complex [94]. Moreover, it was found that the apoproteins of the LH2 of *Mch. purpuratum*, which form the protein scaffold for the enclosed pigments, show a high degree of homology in their sequences of amino acids in comparison with those of the 'standard' LH2 of *Rps. acidophila* [94, 86]. Thus, the general assumption that the B830 LH2 complex of *Mch. purpuratum* follows the same modular building principle as the 'standard' LH2 complex of *Rps. acidophila* is reasonable [94].

2.5.1. The structure of the B830 LH2 complex of *Marichromatium purpuratum*

Very recently the structure of the B830 LH2 complex of *Mch. purpuratum* was resolved at high resolution by electron cryo-microscopy (cryo-EM) [95, 96]. The symmetry of the B830 LH2 complex was found to be heptameric, hosting three BChl *a* and two molecules of the caroteoid okenon per apoprotein pair. A tilted view and a top view of the structure of the LH2 complex of *Mch. purpuratum* are shown in Fig. 2.17.

(a) *tilted view*   **(b)** *top view*
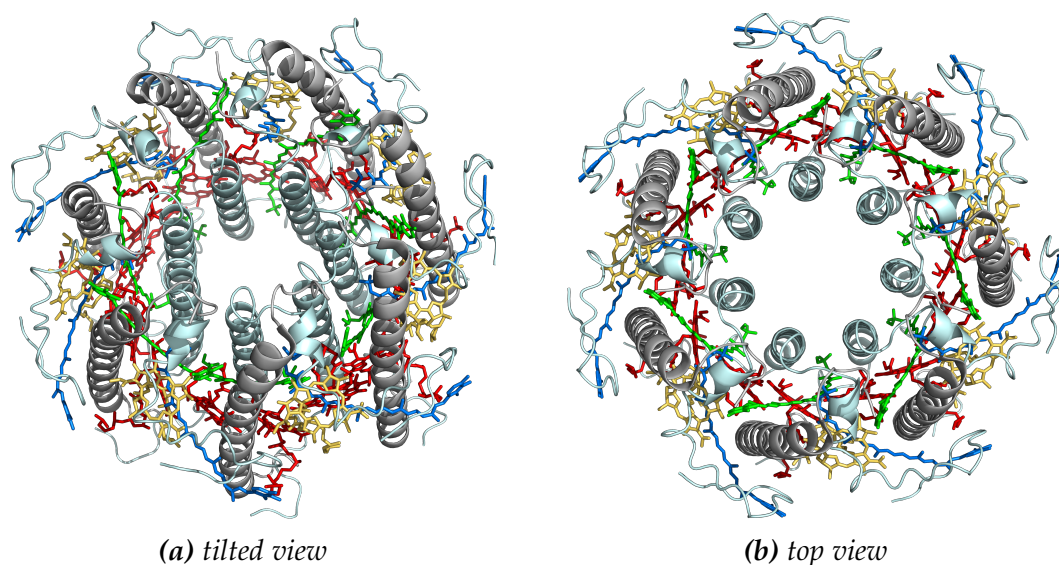
*Figure 2.17.: The B830 LH2 complex of Mch. purpuratum: A tilted view **(a)** and a top view **(b)** of the B830 LH2 complex is show. The apoproteins are visualized as helices of grey and pale cyan color corrsponding to the outer and inner apoproteins, respectively. The pigment Bchl a molecules of the two rings, the B800 ring and the B830 ring, are visualized in yellow and red color, respectively. The two carotenoid molecules of okenone are visualized in green and blue color. Both graphics were rendered with PyMOL (Schrödinger). For details see text.*

In order to allow for comparison with the previously shown structure of the 'standard' LH2 complex of *Rps. acidophila* the same color code was chosen for visualization of the distinct molecules. Thus, the inner and outer apoproteins holding in place the pigment molecules of the LH2 complex are visualized as helices of gray and pale cyan color, respectively. The BChl *a* pigment molecules are shown in yellow and red, representing the different orientations of their bacteriochlorin rings with respect to the symmetry axis of the apoprotein helices. The two carotenoid molecules of okenone are shown in green and blue color.

The BChl *a* molecules within the LH2 complex of *Mch. purpuratum* are organized in a similar manner as in the 'standard' LH2 complex of *Rps. acidophila* described before, forming two groups of molecules, the B800 and the B830 ring. Concerning the two carotenoid molecules of okenone per apoprotein pair, one of the carotenoid molecules is oriented similarly as in the 'standard' LH2 complex of *Rps. acidophila*, thus, running almost parallel to the apoprotein helices. This okenone molecule, also referred to as Car1 in the following, is visualized in green in Fig. 2.17. In contrast, the second carotenoid molecule of okenone, in the following also referred to as Car2, is oriented significantly different within the LH2 complex, lying at almost medium height of the LH2 complex and at right angles to apoprotein helices. In order to allow for visualization of this special pigment arrangement within the B830 LH2 complex a side view of the structure of the LH2 complex as well as a top view illustrating the pigment arrangement without the apoprotein helices are shown in Fig. 2.18.

(a) *side view*
with apoproteins

(b) *tilted view*
pigments only
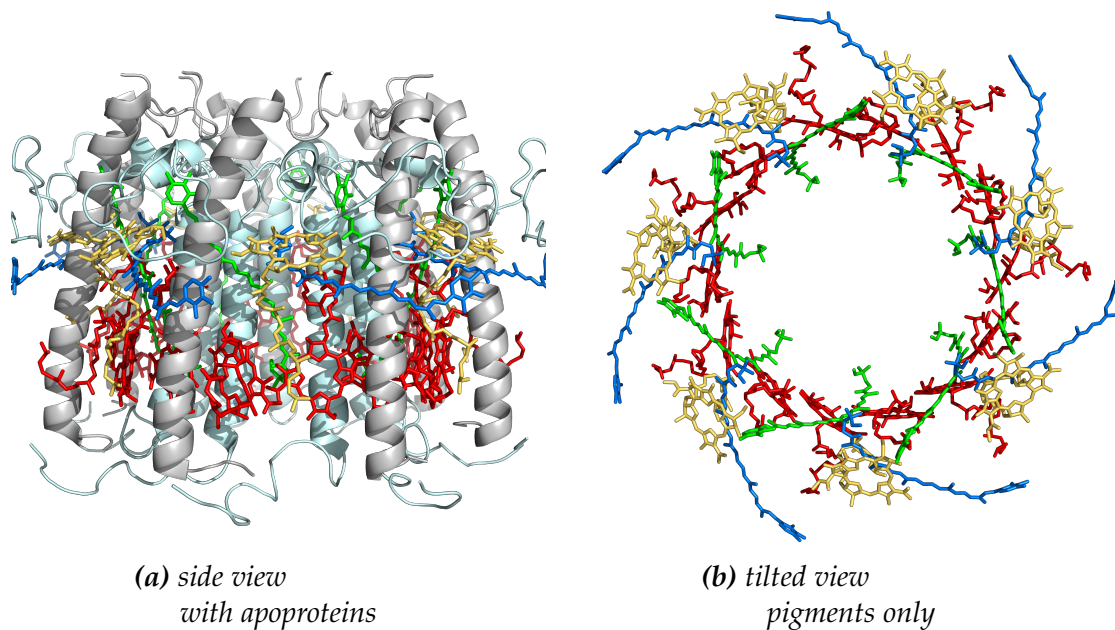
Figure 2.18.: The pigment arrangement within the B830 LH2 complex of Mch. purpuratum: *A side view **(a)** and a top view **(b)** of the B830 LH2 complex are show. Whereas the side view (a) includes the visualization of the apoproteins as helices of grey and pale cyan color, respectively, the top view on the right hand side (b) shows only the incorporated pigments. The Bchl a molecules of the two rings, the B800 ring and the B830 ring, are visualized in yellow and red color, respectively. The two carotenoid molecules of okenone, Car1 and Car2, are visualized in green and blue color, respectively, thus clearly illustrating their fundamental different orientation within the LH2 complex. Both graphics were rendered with PyMOL (Schrödinger). For details see text.*

The color code of this visualization was chosen as before, in order to allow for comparison between the different figures. The inner and outer apoproteins of the protein scaffold for the pigment molecules are visualized as helices of gray and pale cyan color, respectively. The BChl *a* pigments are shown in yellow and red, representing their assignment to the B800 and the B830 ring of BChl *a* molecules, respectively. The two carotenoid molecules of okenone are shown in green and blue color, in order to allow for distinction of the two molecule differing their fundamental different orientation within the B830 LH2 complex.

The two groups of carotenoid molecules within the B830 LH2 complex do not only differ in their position and arrangement within the LH2 complex but also appear in different molecular configuration of the okenone molecule, compare Fig. 2.19.

(a) chemical structure   *(b) molecular conformation*
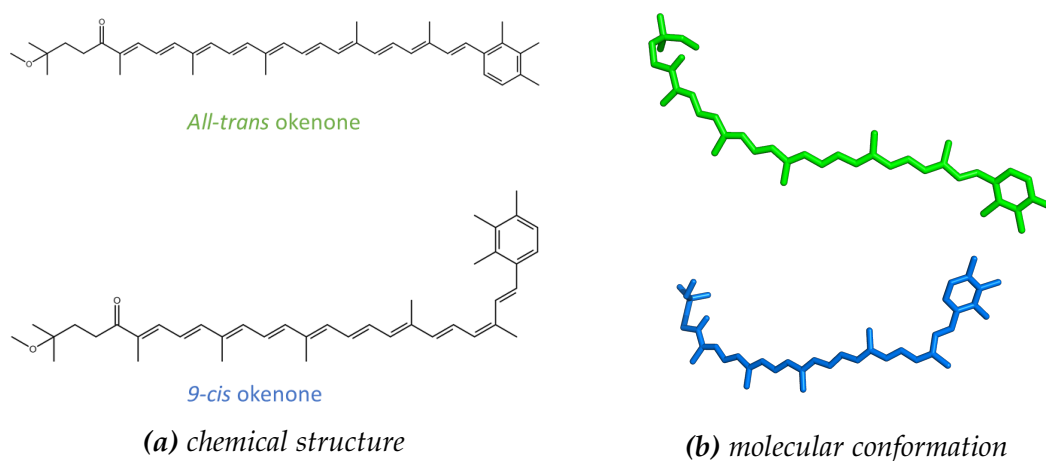
Figure 2.19.: Different molecular conformations of the carotenoid okenone within the B830 LH2 complex of Mch. purpuratum: *The chemical structures* **(a)** *as well as the corresponding molecular conformations of the Car1 and Car2 okenone molecules within the B830 LH2 complex are visualized. As before, Car1 adopting an* $all - trans$ *conformation is represented in green, wheres the Car2 okenone molecule that adopts a* $9 - cis$ *conformation is shown in blue. Both graphics in (b) were rendered with PyMOL (Schrödinger). For details see text.*

Whereas the Car1 okenone molecule adopts an $all - trans$ configuration, which is common for carotenoids incorporated in LH2 complexes of purple bacteria [59, 97, 72, 60], the newly identified second okenone molecule per apoprotein pair (Car2) adopts a $9 - cis$ configuration. This molecular conformation of carotenoid molecules is usually observed for carotenoids in RC-LH1 complexes and not in those peripheral LH2 complexes of the bacterial photosynthetic ap-

paratus [59, 97, 98, 60]. Although the chemical composition of the two okenone molecules is identical, their chemical structure and thus their molecular geometry is significantly different, as can be seen in Fig. 2.19.

Notably, both, the presence of a second carotenoid molecule per apoprotein pair as well as the fact that it adopts a $9 - cis$ conformation, are unique structural features of the B830 LH2 complex of *Mch. purpuratum* and have not been reported before [95, 96]. Neither, the LH2 complex of *Rps. acidophila* nor the LH2 complex of *Rhodospirillium (Rsp.) molischianum*, which are the only other two bacterial light harvesting complexes whose structures are known at high resolution, feature such a second carotenoid per apoprotein pair [22, 24, 23].

Although the LH2 complex of *Mch. purpuratum* was intensely studied by biochemical methods in the past [84, 87, 99, 85, 86] only a few experiments of optical spectroscopy were performed, focusing mainly on the photophysics of the enclosed carotenoid okenone [100, 101]. Thus, in this thesis the electronic structure and the resulting kinetics of the electronic excitations within the B830 LH2 complex of *Mch. purpuratum* will be investigated by time-resolved optical spectroscopy.

3. Material and Methods

In this chapter, first the preparation of the light harvesting complexes and the handling of the samples is described. Afterwards, the two experimental setups used for the optical experiments are described in detail. In particular the working principle and two important acquisition modes of the streak camera are explained.

3.1. Preparation of light harvesting complexes

The samples used for the experiments in this thesis were isolated LH2 complexes in solution, ready for use. They were provided by the groups of Prof. Richard Cogdell, University of Glasgow, and Prof. Neil Hunter, University of Sheffield, both United Kingdom.

3.1.1. Isolation of LH2 complexes from purple bacteria

The process of the purification of LH2 complexes from purple bacteria has been described in the literature in detail for *Marichromatium purpuratum* [84, 85, 94, 86] and several other species of purple bacteria [91, 80]. Nevertheless, in the following the basic principle of LH2 purification will be outlined schematically. Figure 3.1 shows a flow chart roughly visualizing the purification process.

In the first step of the process about three liters of LH2 containing bacteria cells are grown in a nutrient solution. After several days of growth those cells are broken by using a french press with an operating pressure of about 1.4 bar, see step 2 in Fig. 3.1. For better breaking of the cell membranes this step is repeated once. The next step, step 3 in Fig. 3.1, is the separation of the broken membranes and other solid parts from the liquid part of the solution. This is done by centrifugation at 15,000 rotations per minute (rpm) for 15 minutes. After centrifugation the centrifuge tube contains a highly viscous, dark purple

colored solution of broken cells at the bottom of the tube and on top a nearly transparent aqueous phase which can be removed easily.
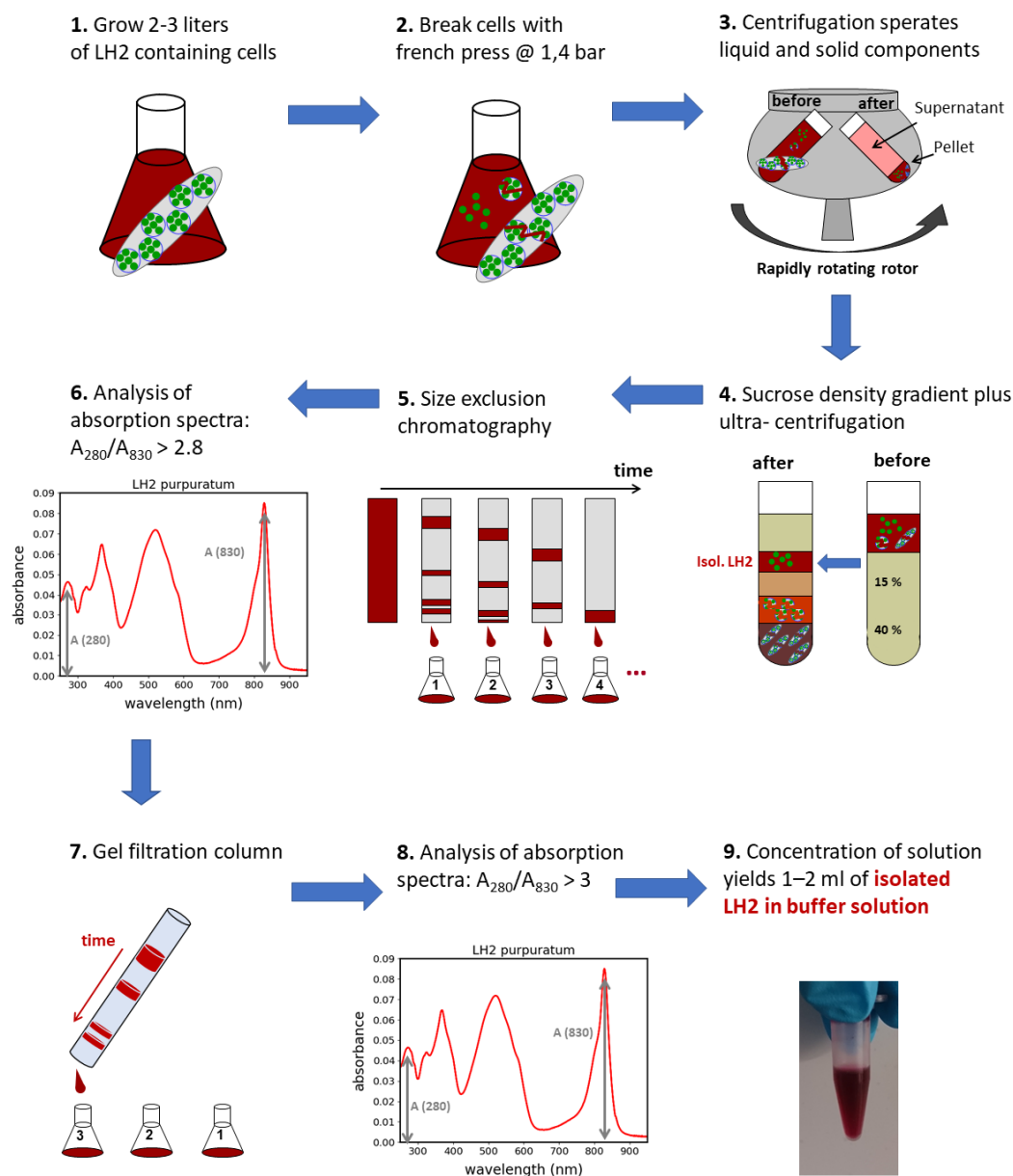
Figure 3.1.: Flow chart visualizing the LH2 purification process: *After growing and breaking of bacteria cells subsequent separation of components and analysis allows purification of LH2 complexes. For details see text.*

To further isolate the solid parts of the broken cells in the viscous phase a sucrose density gradient centrifugation is done with 27,000 rpm for 10 hours, step 4 in Fig. 3.1. After centrifugation the tube shows clearly separated and differ-

ently coloured layers. Whereas the big and heavy membrane segments of the lipid bilayer are found in the layers at the bottom of the tube, the LH2 complexes are found in higher lying layers of bright purple to dark red colour. Using a pasteur pipette allows withdrawal of the individual layers and separation of the layer of concentrated LH2 complexes, which is solubilised in a 20 mM pH 7.8 HEPES (4-(2-hydroxyethyl)-1-piperazineethanesulfonic acid, purchased from Sigma Aldrich) buffer solution containing the detergent LDAO (Dodecyldimethylaminoxid, purchased from Sigma Aldrich). The detergent is added to prevent aggregation of the LH2 complexes. The next step towards isolation is done by size exclusion chromatography which allows separation of particles by their size and molecular weight, step 5 in Fig. 3.1. After adding a resin containing buffer a gravity column is loaded with the concentrated LH2 solution. Washing the loaded column with an appropriate elution buffer several bands of bright purple color appear in the column, corresponding to different sizes and molecular weights of LH2 complexes. Further washing of the column leads to a movement of the bands to the bottom of the column, whereas the mutual separation of the bands is maintained. During all the washing of the column fractions of 20 ml are collected at the bottom of the column for further analysis. After washing the complete column absorption spectra are recorded for each of the collected 20 ml fractions, step 6 in Fig. 3.1. The spectra are analyzed by calculation of the absorption ratios at 850 nm and 280 nm and only fractions fullfilling the criterion of a A(850)/A(280) ratio higher than 2.8 are used for further purification. The selected fractions are collected and concentrated and run afterwards on a gel filtration column to further separate the LH2 complexes of different size, step 7 in Fig. 3.1. During gel filtration fractions of 5 ml are collected and again absorption spectra are taken. By calculation of the A(850)/A(280) ratio only fractions with ratios above 3 are selected for final concentration, step 8 in Fig. 3.1. Finally this gives about 1-2 ml of purified LH2 complexes in solution which are best stored in the dark and below 5°C in the refrigerator.

3.1.2. Handling of isolated LH2 complexes for optical measurements

Samples of isolated LH2 complexes in HEPES buffer (20 mM HEPES, 0.1% LDAO, pH 7.8) were obtained by the procedure outlined above in the United Kingdom and arrived at the University of Bayreuth ready for use. They were checked

for quality by taking an absorption spectrum with an UV-VIS absorption spectrometer (Lambda750, Perkin Elmer) using a 2 mm quarz cuvette. For optical measurements samples were diluted to an optical density of 0.04 OD at a wavelength of 790 nm, corresponding to a concentration of 140 μM of LH2 complexes. For dilution a HEPES buffer (20 mM HEPES, 0.1% LDAO, pH 7.8) was used and an enzymatic oxygen scavenger was added to prevent chemical damage due to contact with oxygen. The enzymatic oxygen scavenger buffer was prepared analogously to a previously published recipe [102]. The 0.1% volume concentration of the detergent LDAO corresponds to a molar concentration of about 4 mM, which is well above the critical micellar concentration (CMC) of 1-2 mM reported for LDAO [103]. Thus, aggregation of the LH2 complexes can be neglected and the LH2 complexes in detergent solution can be assumed as isolated and non-interacting.

3.2. Time-resolved spectroscopy

Time-resolved spectroscopy allows for the detection and resolution of the kinetics of a fluorescent sample which is otherwise hidden and not resolvable by static fluorescence spectroscopy. In general there are two methods of time-resolved spectroscopy: measurements in the frequency domain (FD) and measurements in the time domain (TD). The basic principle of temporal resolution is the detection of the transient information and subsequent data processing. Regarding measurements in the time domain the detection of the transient information resulting from repetitive excitation of a sample requires an appropriate detector and/or detection technique. In practice there are several ways of realization, such as gated detection, also called sampling technique, time-correlated single photon counting (TCSPC) or the use of a streak camera. Within this thesis time-resolved experiments using a streak camera as well as those using TCSPC were performed. The corresponding two experimental setups will be outlined below.

3.2.1. Time-resolved spectroscopy using a Streak-camera

In Fig. 3.2 a schematic drawing of the optical setup used for time-resolved spectroscopy employing a streak camera is shown. A picosecond (ps) pulsed titan-sapphire laser (Ti:Sa, Tsunami, Spectra Physis) with a pulse repetition rate of

80 MHz and a pulse width of 2 ps was used as light source operating at a wavelength of 790 nm. It was pumped by a 532 nm continuous wave (cw) 10 W Neodymium-doped yttrium orthovanadate laser (Nd:YVO4, Verdi G10, Coherent). A glass wedge allowed splitting off a beam of low intensity from the main excitation for inspection purposes. The inspection beam was directed towards an autocorrelator (PulseCheck, APE Berlin) for supervision of pulse shape and stability and into a trigger diode (PIN Diode Head C1808-03, Hamamatsu Photonics) which is needed for temporal synchronization of optical and electronic signals as described below in detail.
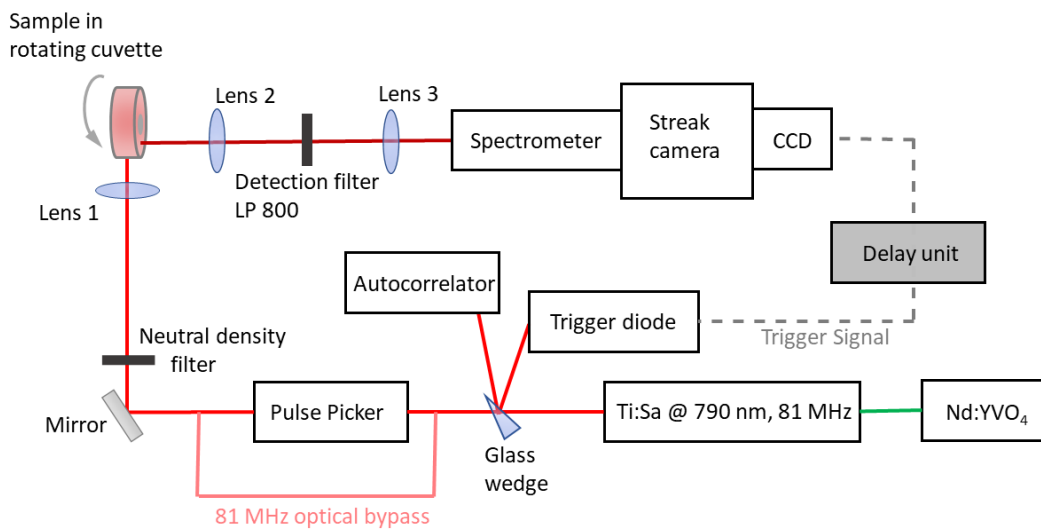
Figure 3.2.: Optical setup: *The schematic drawing visualizes the optical setup. Laser signals and detected fluorescence are shown as solid lines, electronic signals are shown as dashed lines. For details see text.*

The main excitation beam enters a pulse picker unit (Model 3980, Spectra Physics) which allows changes of the pulse repetition rate by use of an accusto-optical modulator (AOM) by factors of 10, 40, 160 and 1600 to repetition rates of 8 MHz, 2 MHz, 0.5 MHz and 0.05 MHz. For measurements at the fundamental repetition rate of 80 MHz of the Ti:Sa the excitation beam is directed around the pulse picker unit by an optical bypass. After leaving the pulse picker unit the excitation light passes a variable neutral density filter which allows variation of the excitation intensity. Finally a lens of focal length 30 mm focuses the excitation light onto the sample which is inside a home-built rotating cuvette to

prevent chemical damage of the sample due to strong illumination and to avoid bleaching effects. The rotation frequency of the cuvette was 6,6 Hz for all measurements.

A lense of focal length 100 mm collects the fluorescence emission of the sample in right angle geometry. A dielectric filter (LP 808, RazorEdge LP Edge Filter 808 RU, AHF) in the detection path allows for spectral selection of the fluorescence emission and removes any signal due to scattering of the excitation light. Finally a lense of 100 mm focal length focuses the signal into the spectrometer (Cromex 250 Imaging Spectrograph, Bruker Optics) just in front of the streak camera (Streak Camera C5680, Hamamtsu Photonics). The purpose and function of the delay unit (C10647 and C1097-05, both from Hahamatsu Photonics) and the CCD camera (CCD camera C4742-95-12ER, Hamamatsu Photonics) behind the streak camera are described in detail in the next section.

For optical experiments the excitation photon fluence, in the following for reasons of simplicity called fluence, is a parameter which is of special interest. It is defined as the number of photons which arrive at the sample per pulse and reference area, often approximated by the focal diameter. The fluence F can be calculated from the experimental parameters: the excitation laser wavelength λ and the laser pulse repetition rate RR. When additionally the continuous wave (cw) laser power P of the experiment is known, the fluence F can be calculated according to

$$F = \frac{P}{h\frac{c}{\lambda}} \frac{1}{RR} \frac{1}{A_{focus}}$$ (3.1)

with h as Planck constant, c as speed of light and A_{focus} as reference area such as the area of the focal spot.

Streak Camera: Working principle and acquisition modes

A streak camera is an electronic device that allows the detection of time-resolved information by converting it into spatial information for the time range of picoseconds (ps). Actually, the name camera is rather misleading as the streak camera is no camera in traditional sense. The working principle of a streak camera is shown in Fig. 3.3.
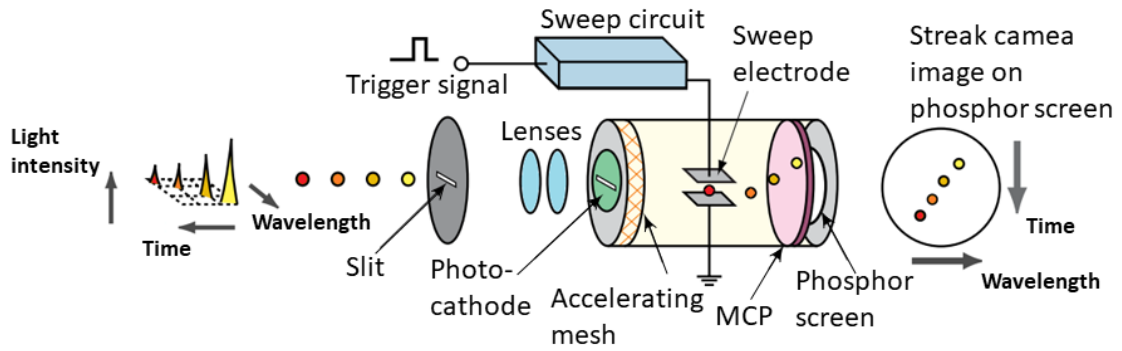
Figure 3.3.: Principle of the streak camera: *Photons of different wavelengths, intensities and temporal information enter the streak camera by passing a horizontal slit. A photocathode converts photons into electrons which are deflected within the deflection unit according to their arrival times. Electrons corresponding to photons arriving earlier are deflected less than electrons corresponding to photons arriving later. After signal enhancement by a multi channel plate a streak camera image is visible on the phosphor screen. For details see text. Adapted and modified from [104].*

Light of different intensities, wavelengths (spectral information) and at different times (temporal information) enters the streak camera through a horizontal slit of variable height. Lenses focus the incoming light onto a photocathode where photons are converted into electrons. These are accelerated into a deflection unit which is similar to a plate capacitor. The electronic deflection unit, which is triggered by the electronic signal from the trigger diode in the optical setup, allows the synchronization of optical signals (incoming photons) and the voltage applied to the deflection unit. Hence, electrons corresponding to photons arriving earlier at the deflection unit are deflected less as those that enter the streak camera later. The delay unit shown in the optical setup, Fig. 3.2, as a grey box is used for achieving the temporal synchronization just mentioned by applying an additional time shift. A scheme of the deflection mechanism is shown in Fig. 3.4.

Finally a multi-channel plate (MCP) enhances the deflected electrons which afterwards hit a phosphor screen. The phosphor screen converts the electrons into photons and shows a fluorescent image resulting from the electrons arriving at different times. Whereas spectral information (wavelength) of the photons remains unchanged their temporal information is made visible by the deflection mechanism of the streak camera. Thus, the image on the phosphor screen has two dimensions: spectral information along the horizontal axis and temporal information along the vertical axis. This fluorescent image on the phosphor screen

37

is finally captured by the CCD camera just behind the streak camera as shown in Fig. 3.2 and stored in computer memory. This final image, corresponding to a three dimensional histogram where each pixel contains spectral information, temporal information and the intensity, is called streak camera image.
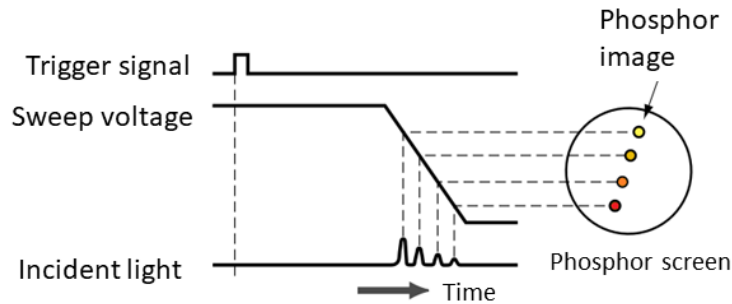
Figure 3.4.: Deflection mechanism inside the streak camera: A sweep voltage is applied to the deflection unit resulting in a deflection which increases the later the photons arrive in the streak camera. For details see text. Adapted and modified from [104].

Streak camera measurements always follow the general working principle just described. Depending on the acquisition mode in which the streak camera is operated, different signal processing is done and different information is accessible. In the following two acquisition modes, the *photon counting mode* and the *dynamic photon counting mode*, are described in detail.

Acquisition mode: Photon counting

This acquisition mode detects so-called single-photon-events. As already mentioned in the last section, photons entering the streak camera are converted to electrons with a ratio of one to one. In this mode of acquisition the MCP is operated at the maximum voltage which leads to a multiplication of the electrons by a factor of up to 10^4 resulting in the maximum sensitivity of the streak camera. Thus, the resulting avalanche of electrons appears at the phosphor screen as a smeared out, broad point instead of a single pixel. Streak camera measurements in the photon counting mode are performed by summing up a predefined number of CCD images each with a suitable acquisition time for signal accumulation at the phosphor screen. For all measurements in this thesis the acquisition time of one CCD image was 61 ms. The number of exposures, that were accumulated during the measurement of one streak camera image was chosen in order to obtain a streak image of good signal to noise ratio (SNR). In the photon counting

mode every single image of the CCD camera is processed by the software of the streak camera (HPDTA 9.3, Hamamatsu Photonics) according to the following three steps:

1. Signals resulting from the detection of a photon have to be discriminated from signals due to accumulation of noise. By performing a calibration measurement a threshold for the distinction of signals is determined. This threshold depends on the electronic components and the operation options of the streak camera, such as the MCP gain and the time range for example. The threshold should be determined before any measurements or when major changes of parameters haven been applied to the streak camera. Only signals which exceed the threshold are classified as detected single photons and are used for further signal processing. The basic principle of this distinction of signals is shown in Fig. 3.5.
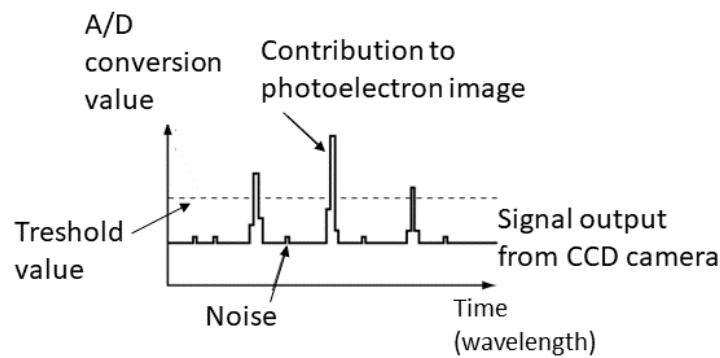
Figure 3.5.: Photon counting mode: Only signals exceeding the threshold value are recognized as single photon events. For details see text. Adapted and modified from [104].

2. Every detected signal exceeding the threshold is assigned to a photon count value equal to one.

3. For every detected signal the coordinates of the detected intensity is determined via calculation of the center of intensity. Then the photon count value of one is added at these coordinates.

Finally after adding a predefined number of exposures, each corresponding to a single image of the CCD camera and each following signal processing according to the three steps just described, one streak camera measurement results in one streak camera image. Two typical streak camera images are shown in Fig. 3.6.

(a) excitation laser   *(b) fluorescent sample*
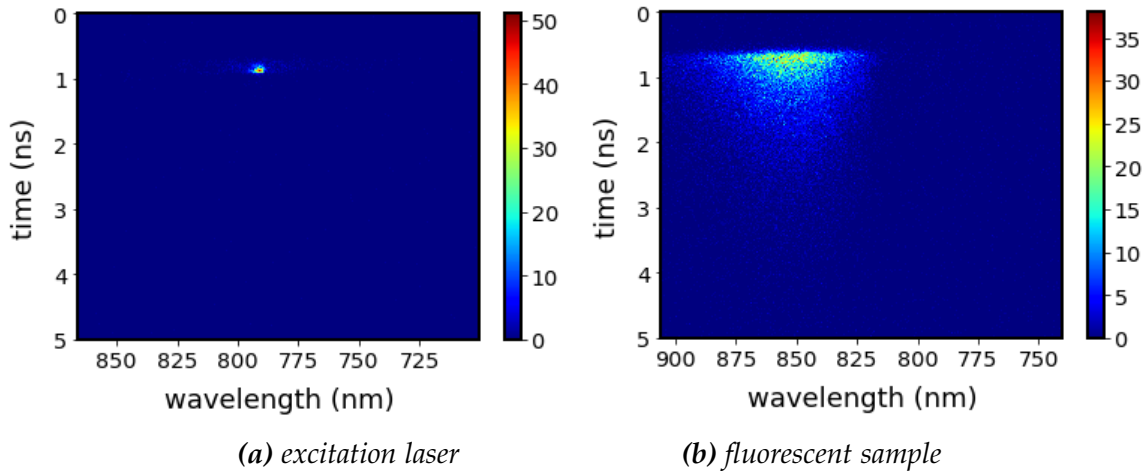
Figure 3.6.: Typical streak camera images: *Two streak camera images, **(a)** of the excitation laser and **(b)** a fluorescent sample are shown. The horizontal axis represents spectral information, the vertical axis temporal information. The intensity is shown color coded, ranging from zero to the maximum of photon counts, as shown in the color scale at the right hand side. For detailed description see text.*

The horizontal axis in the streak camera image corresponds to spectral information, covering a spectral window of fixed width around a center wavelength. The position of the center wavelength and thus, range covered by the spectral window, is chosen to cover the emission of the sample. In this thesis, the width of the spectral window is about 165 nm as a grating of 1000 lines per milimeter was used. Due to the relatively low signals of the detected emission, the slits of the spectrometer were set to 100 μm resulting in a spectral resolution of 8 nm. The vertical axis of the streak camera image corresponds to temporal information. The length of the temporal axis is determined by the time range chosen for the streak camera measurement, which is 5 ns for all measurements of this thesis. The intensity is shown in units of photon counts and is visualized by a color code ranging from black as lowest signal to red for highest photon counts. In Fig. 3.6a a streak camera image of the excitation laser light is shown. As the laser light corresponds to a series of short pulses (3 ps), the photons are deflected equally and result in a nearly circular light point on the streak camera image with fixed position along the temporal and the spectral axis. Analysis of this laser spot on the streak camera image allows for determination of the temporal resolution of a streak camera measurement. According to [104] a temporal resolution of down to 0.2 ps is possible under ideal experimental conditions. For a fluorescent sample the streak camera image looks different as shown in Fig. 3.6b. The fluorescence emission starts at the same time as the laser excitation pulse appears.

It is spread over broad spectral range, corresponding to a broad fluorescence emission spectrum, and spreads in time revealing the transient information of the fluorescence emission.

Acquisition mode: Dynamic photon counting

This acquisition mode is an expansion of the *photon counting mode* just described. In this mode an additional file, the so-called dynamic photon counting (dpc) file, is created in the computer before the streak camera measurement begins. The experiment itself is absolutely identical to the experiments in the photon counting mode: A fixed number of exposures, each having a fixed acquisition time, is added up as already described. The special feature of the dynamic photon counting mode is the additional recognition of the photon arrival times which are stored in the dpc file during the streak camera measurement. Hence, the dpc file contains the arrival times[1] of all detected photons together with their coordinates within the streak camera image.

Whereas the final streak camera image resulting from one streak camera measurement contains the information summed up over all the exposures, the dpc file gives access to information at any time during the complete measurement. It allows the creation of streak camera images from the dpc file by summation. Summation over the complete dpc file results in a streak camera image absolutely identical to the streak camera image resulting from normal photon counting mode. Thus, the special advantage of the dynamic photon counting mode is that it allows to create streak camera images from selected temporal windows during the streak camera measurement and therefore gives access to information that is otherwise hidden in the summation of exposures during normal acquisition in photon counting mode. For example, if 1000 exposures where added during one streak camera measurement resulting in a final streak camera image, the dpc mode allows to create five new streak camera images each corresponding to 200 exposures from the dpc file. These five streak camera images can then be analyzed in any context as for example the formation of additional emission bands or photobleaching of the sample. All measurements of this thesis where done in dpc mode.

---

[1]The coordinates of a detected photon are stored for each exposure of the streak camera measurement. Thus, the temporal resolution of the stored arrival times corresponds to the temporal integration time chosen for one exposure.

3.2.2. Data processing: From the Streak camera image to fluorescence emission decay and fluorescence emission spectrum

The three dimensional histogram of the streak camera image allows the extraction of both, the fluorescence emission spectrum as well as the fluorescence intensity decay. This is done by integration along the temporal or the spectral axis, which corresponds to a summation over photon counts to obtain the fluorescence emission spectrum and the fluorescence decay, respectively. A visualization of the integration along the temporal and the spectral axis is shown in Fig. 3.7. For the extraction of the fluorescence emission spectra and the fluorescence intensity decays from the streak camera images a script written in Python™ was developed within this thesis.
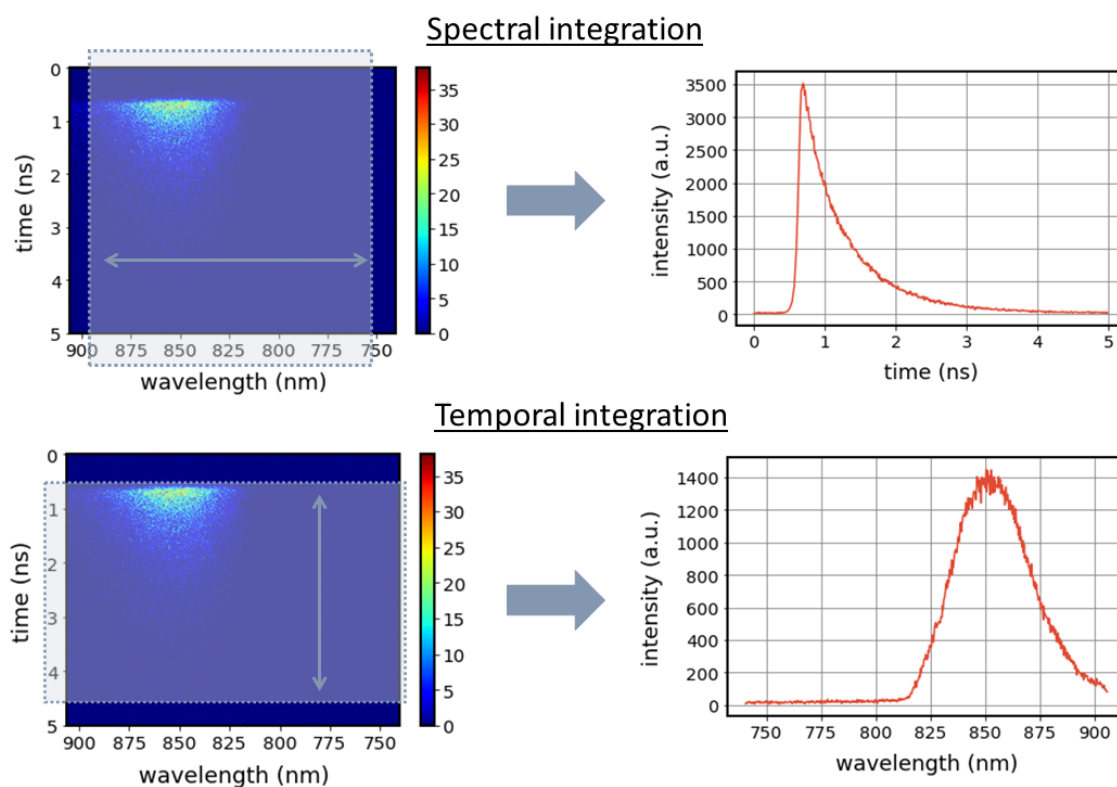
Figure 3.7.: Extraction of fluorescence emission spectrum and fluorescence intensity decay from a streak camera image: *Integration along the temporal and spectral axis yields the fluorescence emission spectrum and the fluorescence intensity decay, respectively. For details see text.*

The temporal resolution of a streak camera measurement is mainly influenced by the width of the horizontal entrance slit of the streak camera. The slit deter-

mines how much a short pulse entering the streak camera is smeared out due to the deflection in the streak camera measurement. Extraction of the fluorescence intensity decay from a streak camera image of the excitation laser, as shown in Fig. 3.6a, allows determination of the temporal resolution of a streak camera measurement. As the excitation laser pulses have a nearly gaussian shape, which is known from the autocorrelator in the experimental setup in Fig. 3.2, the extracted fluorescence intensity decay can be fitted well by a gaussian function. The resulting full-width-at-half-maximum (FWHM) is a good approximation of the temporal resolution of a streak camera measurement. In this thesis the temporal resolution of all measurements was in the range of 50 ps.

3.2.3. Time-resolved spectroscopy using Time-Correlated Single Photon Counting (TCSPC)

Time-resolved experiments employing the technique of time-correlated single photon counting (TCSPC) were performed on a a commercial confocal fluorescence microscope (MicroTime 200, PicoQuant). One drop of sample solution containing isolated LH2 complexes in detergent solution (see Chapter 3.1.2) was dripped on a glass cover slide that was positioned on the microscopes sample stage. Depending on the distinct experiment either a laser diode with a wavelength of 485 nm (LDH-D-C-485, PicoQuant) operated in pulsed mode at laser repetition rates of 40 MHz, 20 MHz, 8 MHz, 2 MHz and 0.5 MHz, or a laser diode with a wavelength of 560 nm (LHD-D-TA-560B, PicoQuant) operated in pulsed mode at laser repetition rates of 40 MHz, 20 MHz, 8 MHz, 2 MHz, 1 MHz and 0.5 MHz, respectively, was used as light source. The pulse width of the excitation laser pulses were 140 ps for a wavelength of 485 nm and 80 ps for a wavelength of 560 nm, respectively, according to laser diode specifications.

The excitation laser light was focused onto the sample with a water immersion objective (60x UPlanS APO UIS2, NA = 1.2, Olympus).The emission from the sample passed a dichroic beamsplitter (HC BS 801, AHF) and a suitable optical detection filter removing excitation laser light (LP808, RazorEdge LP Edge Filter 808 RU, AHF). The emission signal of the sample was then direct towards and focused on a single-photon counting avalanche diode (SPCM-AQRH-14-TR, Excelitas) and used for time-resolved data acquisition employing time-correlated single photon counting (TCSPC) (TCSPC TimeHarp 260 PICO Dual, PicoQuant).

All fluorescence transients were measured with a temporal binning of 25 ps and the accumulation time of the fluorescence signal for each transient was 120 s.

Optionally a beamsplitter cube in a ratio of 50/50 was positioned in the optical path before the avalanche photo diode in order to allow for simultaneous detection of the emission spectrum and the fluorescence intensity decay by splitting of the samples emission signal. Then one part of the emission signal was directed towards a spectrometer (Shamrock SR-163, grating 600 lines/mm blazed at 500 nm, spectral resolution 0.55 nm [105]) via an optical fiber and the emission spectrum was detected using an electron-multiplying charge-coupled device (EMCCD Newton 970, Andor).

The instrument response function (IRF) of the optical microscope was measured using the back reflection of an empty glass cover slip. Thus, the full-width-at-half-maximum (FWHM) values of the IRF were determined to 264 ps for the laser diode operated at 485 nm and to a value of 168 ps for the second laser diode operated at 560 nm, respectively. Both, intensity transients resulting from IRF measurements as well as sample fluorescence were exported as ASCII data from the software operating the commercial microscope commercial software (SymPhoTime 64, Picoquant).

The excitation fluence of the optical experiments using the TCSPC technique was calculated analogously as for streak camera measurements according to Equation 3.1.

The principle of time-correlated single photon counting (TCSPC)

The technique of time-correlated single photon counting (TCSPC) allows for detection of the fluorescence transient resulting from repetitive excitation of a fluorescent sample by using a single photon sensitive detector [106]. The basic principle of TCSPC is visualized in Fig. 3.8 schematically. Excitation of a fluorescent sample with a laser pulse results in a fluorescence intensity decay of the emission. The technique of TCSPC requires a single photon sensitive detector such as a photomultiplier tube (PMT), a micro channel plate (MCP), a single photon avalanche diode (SPAD) or a hybrid PMT for example [106].
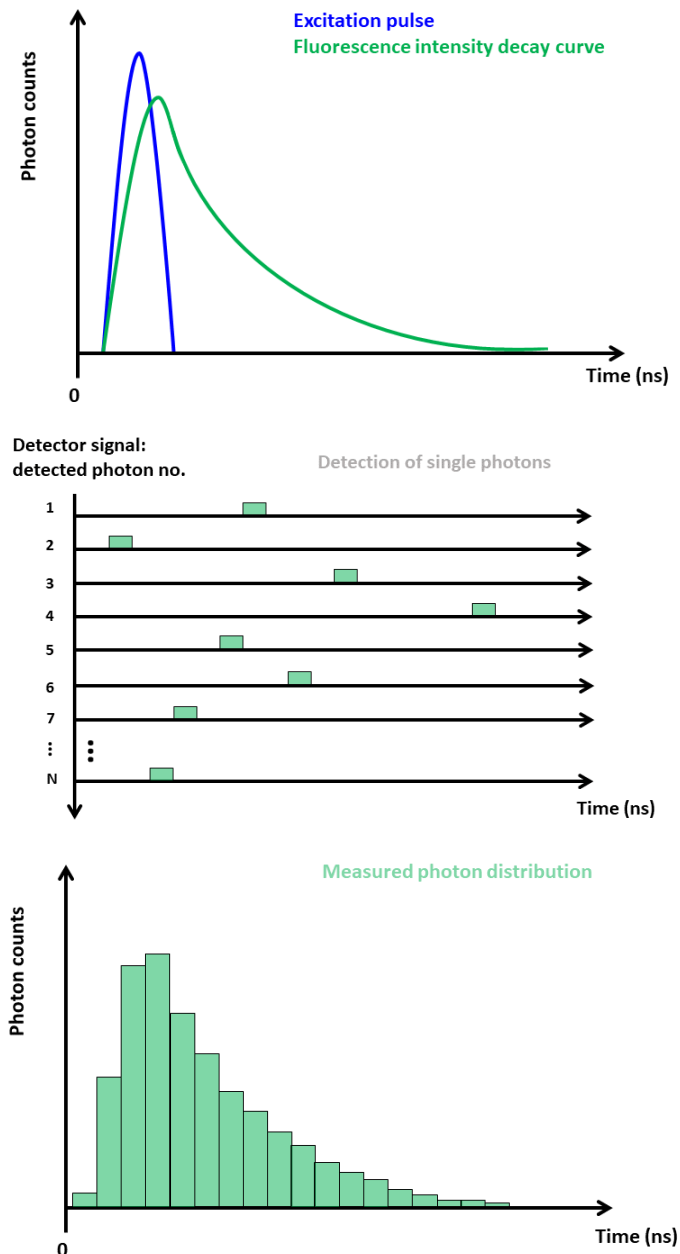
Figure 3.8.: The principle of time-correlated single photon counting (TCSPC): *Excitation of a fluorescent sample with an excitation laser pulse results in a fluorescence intensity decay. Using a single photon sensitive detector allows for detection of single photons of the fluorescence emission, each featuring a distinct arrival time at the detector. Thus, by using the excitation laser pulses as a master clock, a histogram of detected photons and their arrival times with respect to the excitation laser pulse is formed. This histogram resembles the fluorescence decay curve of the fluorescent sample. For details see text. Adapted from [107].*

Thus, using the excitation laser pulses as a master clock, starting a stop watch in the figurative sense, allows for the assignment of the arrival time of each

detected single photon with respect to the excitation laser pulse. Finally, the detection of a high number N of photons, usually $N \approx 10.000\text{-}100.000$ photons [106], allows for building up of a histogram of detected photons. This photon histogram resembles the fluorescence intensity decay curve of the fluorescent sample upon pulsed excitation and allows for determination of the fluorescence kinetics.

4. The Phasor Approach

The expression **phasor** is a linguistic blend of the words *phase* and *vector* [108, 109] and is in general the vectorial representation of a periodic function in the complex plane. Moreover, the complex number of the phasor has a precise position within the complex plane and is often used for analytical and graphical representation [110].

For analyzing fluorescence lifetime data a common and widely used method for measurements in the time domain is fitting the measured fluorescence decay curve by a sum of exponentials based on a predefined model. In this chapter an alternative approach of data evaluation without any a priori knowledge of the sample will be described: **the phasor approach**. Although originally defined for measurements in the frequency domain it can be adapted to time domain data offering a powerful tool for analyzing fluorescence lifetimes with high precision from raw data [111, 112]. In the following, the definition and the principle of the phasor approach will be outlined. Afterwards, the phasor approach will be adapted to fluorescence lifetime data measured with a streak camera.

4.1. The phasor approach to fluorescence lifetime measurements in the frequency domain

The principle of fluorescence lifetime measurements in the frequency domain, sometimes also called phase fluorometry [113] , is sketched in Fig. 4.1. Sinusoidally modulated excitation $E(t)$ leads to a delayed sinusoidally modulated emission $F(t)$ with a phase shift ϕ:

$$E(t) = E_0 + E \ sin(\omega t) \tag{4.1}$$

$$F(t) = F_0 + F \ sin(\omega t - \phi) \tag{4.2}$$

with ω as modulation frequency. The values E_0 and F_0 denote the static, unmodulated amplitudes of the excitation and emission respectively, whereas E and F denote the amplitudes of the modulated excitation and emission.
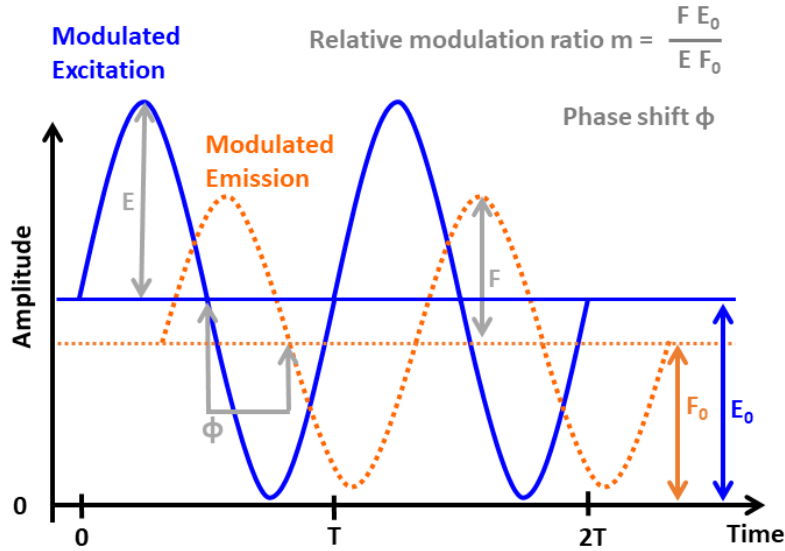
Figure 4.1.: Fluorescence lifetime measurements in the frequency domain: *Sinusoidally modulated excitation (blue) results in a delayed sinusoidally modulated emission (orange) with phase shift ϕ. The ratio of the amplitudes is called modulation ratio. For details see text. Adapted from [114].*

The quotient of the amplitude of the modulated excitation E and the static amplitude of excitation E_0 defines the modulation of the excitation as

$$m_E = \frac{E}{E_0} \tag{4.3}$$

Analogously the modulation of the emission is defined as

$$m_F = \frac{F}{F_0} \tag{4.4}$$

The quotient of those two modulations thus finally defines the relative modulation ratio m as

$$m = \frac{m_F}{m_E} = \frac{\frac{F}{F_0}}{\frac{E}{E_0}} = \frac{F \, E_0}{F_0 \, E} \tag{4.5}$$

A simple two-level system as shown in Fig. 4.2 represents a single exponential

fluorescence decay with lifetime τ.
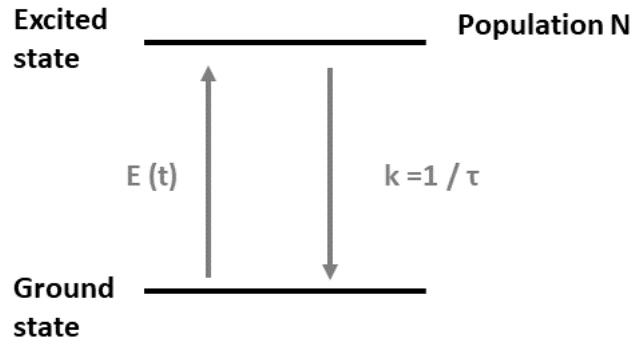
Figure 4.2.: Two-level system describes single exponential fluorescence decay: The excitation E(t) populates the excited state as a function of time. The population N of the excited stated relaxes into the ground state with a rate k inversely proportional to the characteristic lifetime of the relaxation (fluorescence decay).

Within this picture the population N of the excited state is described by the differential equation

$$\frac{dN}{dt} = -k \cdot N + E(t) = -\frac{1}{\tau} \cdot N + E(t) \tag{4.6}$$

As the fluorescence emission is proportional to the population of the excited state this equation is also valid for $F(t)$ instead of N. Using equations 4.1 and 4.2 for the modulated excitation and the modulated emission in the frequency domain plus some trigonometric identities[1] **the two basic relations of phase fluorometry** [113] are obtained:

$$\boxed{tan(\phi) = \omega\tau} \tag{4.7}$$

$$\boxed{m = cos(\phi) = \frac{1}{\sqrt{1 + \omega^2\tau^2}}} \tag{4.8}$$

For monoexponential fluorescence decays, as assumed by the two level system, they describe the relation of the measured phase shift ϕ and the modulation ratio m respectively to both, the experimental parameter ω and the fluorescence lifetime τ.

---

[1]The detailed calculation is shown in Appendix B.1.

Historically the first formulation of the phasor approach to fluorescence lifetime data was published by Gregorio Weber in 1981 [28]. Focusing on fluorescence lifetime measurements with modulated excitation light, also referred to as fluorescence lifetime measurements in the frequency domain (FD), he described a procedure for the determination of fluorescence lifetimes from the phase shift ϕ, between excitation and emission, and the relative amplitude modulation ratio m of the measured emission with respect to the excitation. According to this first formulation the phasor coordinates G and S are defined as:

$$G(\omega) = m \cdot cos(\phi) \tag{4.9}$$

$$S(\omega) = m \cdot sin(\phi) \tag{4.10}$$

They are in general a function of the modulation frequency ω as both, the phase shift ϕ and the modulation ratio m, are affected by the modulation frequency. Using the two basic relations of fluorometry, equations 4.7 and 4.8, allows formulation of the phasor coordinates G and S for monoexponential decays in relation to the modulation frequency ω and the fluorescence lifetime τ:

$$G(\omega) = \frac{1}{1 + \omega^2 \tau^2} \tag{4.11}$$

$$S(\omega) = \frac{\omega \tau}{1 + \omega^2 \tau^2} \tag{4.12}$$

In 1984 Jameson et al. [113] introduced a simple geometric representation of fluorescence lifetime data measured in the frequency domain using the phase shift ϕ and the modulation ratio m, defining a vector of length m making an angle ϕ with the x-axis, as shown in Fig. 4.3. Remembering the basic definition of the phasor coordinates by Weber [28] as $G = m \cdot cos(\phi)$ and $S = m \cdot sin(\phi)$ in equations 4.9 and 4.10 one recognizes that Jamesons diagram is simply a graphical representation of this formulation. Therefore plotting of the values G versus S in one diagram is known as the **phasor plot** since then. The semicircle shown in black in Fig. 4.3 is called the *universal semicircle* and is a special feature of the phasor plot, see Section 4.4.
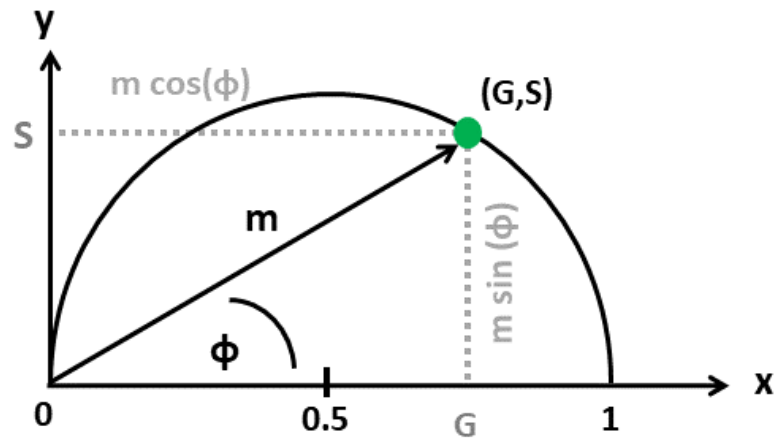
Figure 4.3.: The phasor plot: *Originally introduced by Jameson et al. [113] the phasor plot represents the position of the phasor in the phasor space by plotting the phasor coordinates G versus S. For details see text. Adapted from [113].*

The graphical representation in the phasor plot and the resulting intrinsic vectorial character of the phasor implies that the two basic relations of phase fluorometry formulated before, equations 4.7 and 4.8, can be rewritten in terms of the phasor coordinates G and S as

$$tan(\phi) = \frac{S}{G} \tag{4.13}$$

$$|m| = \sqrt{G^2 + S^2} \tag{4.14}$$

Thus, the modulation ratio m corresponds to the length of the vector m in the graphical representation and the phase shift ϕ can be calculated from the phasor coordinates when the position of the phasor is known.

4.2. The Phasor approach for time domain data

Fluorescence lifetime measurements in the time domain follow the scheme of detecting a time-resolved fluorescence emission signal I(t), also called fluorescence decay curve, as a fluorescence response after pulsed excitation. In Fig. 4.4 the fluorescence response resulting from excitation of a fluorescent sample with an excitation pulse is shown schematically.
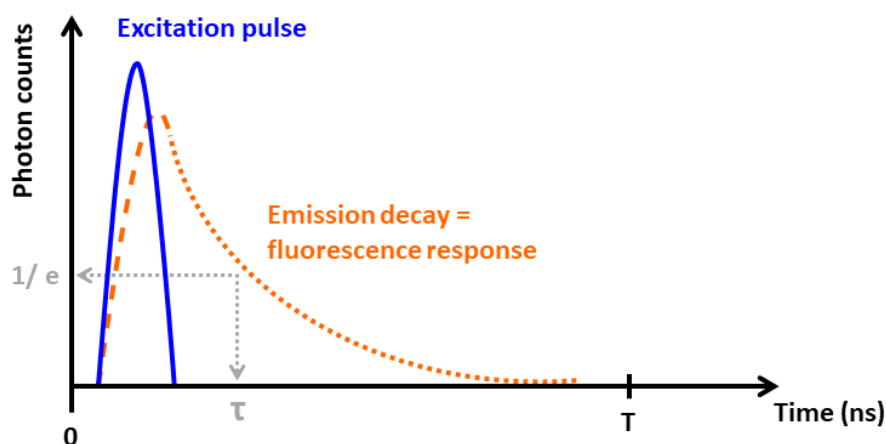
Figure 4.4.: Lifetime measurements in the time domain: *Pulsed excitation results in an emission decay as fluorescence response. For details see text. Adapted from [114].*

As data measured in the frequency domain and in the time domain are equivalent due to their connection via Fourier transformation, Weber already stated a general phasor definition for the time domain [28]. The phasor coordinates G and S are defined as

$$G(\omega) = \frac{\int_0^\infty I(t)\ cos(\omega t)dt}{\int_0^\infty I(t)\ dt} = \frac{Re\ (\ \mathcal{F}\{I(t)\}\ )}{\int_0^\infty I(t)\ dt} \tag{4.15}$$

$$S(\omega) = \frac{\int_0^\infty I(t)\ sin(\omega t)dt}{\int_0^\infty I(t)\ dt} = \frac{Im\ (\ \mathcal{F}\{I(t)\}\ )}{\int_0^\infty I(t)\ dt} \tag{4.16}$$

G and S are defined as the real and imaginary parts of the Fourier transform of the measured fluorescence decay I(t) performed at an arbitrarily chosen transformation frequency ω. The normalization by the area below the fluorescence decay curve in the denominators of equations 4.15 and 4.16 was initially not part of Webers general definition but was added later without loss of generality and for generalization of the phasor definition [115, 116, 117, 118, 119]. Plotting of the phasor coordinates G versus S yields the phasor plot as in the frequency domain. Due to the formulation of the phasor coordinates for time domain data in equations 4.15 and 4.16 the two axes of the phasor plot are often labeled as real axis ('Re') and imaginary axis ('Im').

4.3. Practical implications to time domain measurements

The general phasor formulation for lifetime measurements in the time domain given in the last section does not take into account any specific detection method. Due to the detection principle of the streak camera as well as the time-correlated single photon counting (TCSPC) technique used in this work, see Chapter 3.2, and for considering the characteristics of „real" measured data some changes have to be applied to the general formulation to obtain a phasor formulation for data from time domain measurements.

4.3.1. Binned detection

The fluorescence decay resulting from the time domain measurements is basically a histogram of photon arrival times, see Chapter 3.2. The resulting discrete character of the measured data has to be recognized when phasor coordinates are calculated. In detail, for time domain measurements this means taking into account the following aspects:

- **The finite width of the temporal detection window:**
  Both techniques of time-resolved measurements used within this thesis, the streak camera as well as TCSPC, measure the fluorescence decay curve only within a certain temporal range, the so called detection window. For streak camera measurements the temporal width of the detection window is determined by the time range at which the streak camera image was acquired, see Section 3.2.1. For TCSPC measurements the width of the detection window is chosen appropriately in a way that the measured fluorescence decay curve has safely dropped to zero or the background fluorescence value, respectively. In both cases the discrete sampling of the extracted fluorescence decay curve has to be taken into account for phasor calculation. Thus, for time domain data the transformation frequency ω for phasor calculation is defined inversely proportional to the finite temporal width T of the detection window [120, 121]

$$\omega = \frac{2\pi}{T} \tag{4.17}$$

53

- **The numerical integration of the measured data:**

  Due to its discrete character the measured fluorescence decay curve has to be integrated numerically for calculating the phasor coordinates. One of the most simple to calculate and mostly used methods is the mid-point approximation which approximates the fluorescence decay curve by a sum of rectangles [120, 121]. Each rectangle is calculated from the intensity measured within one bin, precisely the number of photons collected within this bin, multiplied by the temporal width of one bin. Thus, the measured fluorescence decay curve I(t) is approximated by a histogram of intensities. An illustration of this method of numerical integration a fluorescence decay curve is shown in Fig. 4.5.
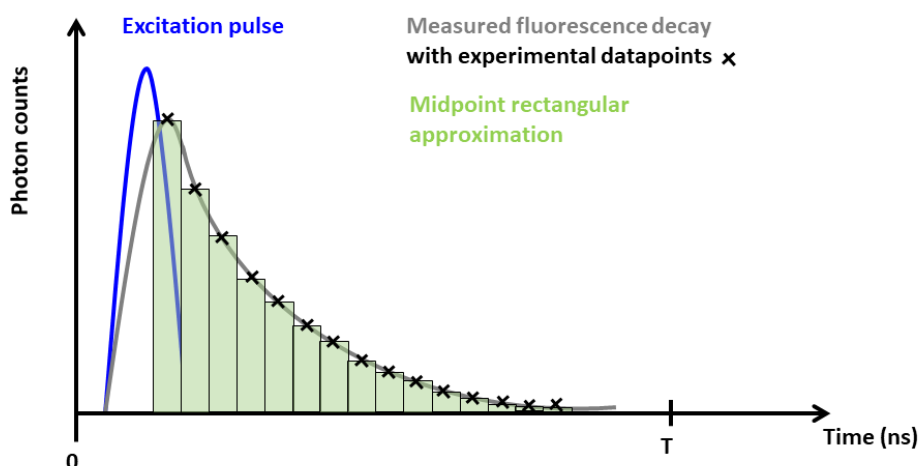
Figure 4.5.: Numerical integration of a fluorescence decay by midpoint approximation: The fluorescence decay is approximated by a sum of rectangles, each centered around the experimental data point corresponding to the measured intensity in units of photon counts, multiplied with the width of one temporal bin. For details see text. Adapted from [120].

Fereidouni et al. presented a modified phasor formulation for time-correlated single photon counting (TCSPC) data taking into account both aspects discussed above [121]. The Fourier transform integrals of the generalized phasor formulation in equations 4.15 and 4.16 transformed into sums in the modified formulation. By taking into account the finite temporal length of the detection window T, the total number of bins of the intensity histogram N_{bins} and the resulting

width of one bin $\Delta t = \frac{T}{N_{bins}}$, the discrete and normalized Fourier transform D_n of the intensity histogram that approximates the measured fluorescence decay curve I(t) has the shape of

$$D_{\mathrm{n}} = \frac{\sum_{k=0}^{N_{\mathrm{bins}}-1} N_k \ \exp^{i\,n\,\omega(k+\frac{1}{2})\frac{T}{N_{\mathrm{bins}}}}}{\sum_{k=0}^{N_{\mathrm{bins}}-1} N_k} \tag{4.18}$$

The transformation frequency ω is defined as

$$\omega = \frac{2\pi}{T} \tag{4.19}$$

and n is the harmonic number of the transformation. Summation runs over k counting the bins of the intensity histogram within the discrete Fourier transform and N_k is the fluorescence intensity for the kth bin of the histogram in units of photon counts.

Finally, the modified phasor approach defines the phasor coordinates G and S by

$$G(\omega) = Re(\ D_n\ ) \tag{4.20}$$

$$S(\omega) = Im(\ D_n\ ) \tag{4.21}$$

as the real and imaginary parts of the discrete and normalized Fourier transform D_n of the intensity histogram approximating the measured fluorescence decay curve I(t).

4.3.2. Background correction

The importance of background correction and its proper application has been intensively studied and discussed in Fereidouni et al. in 2017 [122]. Improper performed background correction can lead to incorrect phasor coordinates as exemplarily shown in Fig. 4.6. Phasors calculated from raw data[2], as shown in the blue box, have positions within universal semicircle in the phasor plot and do not represent the underlying fluorescence decay correctly due to influence

---

[2]For reasons of illustration a single exponential decay was chosen as raw data in [122] and phasors of single exponential decays are expected to lie on the universal semicircle, see Section 4.4.

of background fluorescence. When taking the background signal into account this leads to correct phasor positions on the universal semicircle as shown in the green box of Fig. 4.6. Both, overestimation by giving the background signal a too high weight as well as underestimation of the background fluorescence, leads to wrong phasor positions in the phasor plot as shown in the red box of this figure. Thus, phasor calculation is extremely sensitive to the influence of background fluorescence.
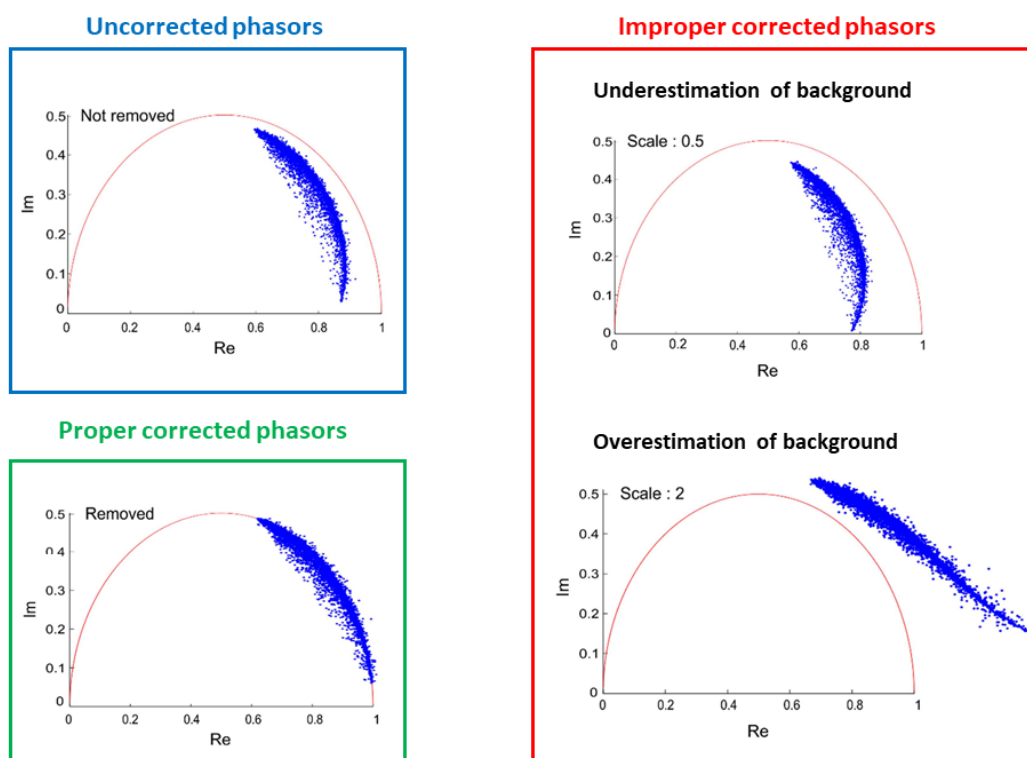
Figure 4.6.: Influence and importance of proper background correction for phasor calculation: *Performing phasor calculation of raw data without background correction may lead to wrong phasor positions. Properly performed background correction yields the correct phasor coordinates. For details see text. All phasor plots are taken from [122] and are rearranged for reasons of visualization and clarity.*

In order to take the influence of background fluorescence of the time-resolved measurements into account, for each fluorescence decay curve either extracted from a streak camera image or resulting from the time-correlated single photon counting (TCSPC), the background fluorescence intensity was calculated as the average intensity over the first 50 pixels prior to the increase of the fluorescence

decay curve[3]. The calculated average background intensity was then subtracted from the photon count of every pixel of the fluorescence decay curve. This background corrected fluorescence decay curve is then used for phasor calculation. Fore more details of the background correction in the phasor calculation see Section 4.3.4.

4.3.3. Correction for the instrument response function

Fluorescence decay curves measured in the time domain can be affected by the instrument response function (IRF). The IRF represents the finite response of the detection system to a finite pulse [120]. Hence it combines all influences of the experimental setup, including for example influences of the excitation light source, the optics along the optical path and the detection efficiency of the detector. In practice the IRF is often recorded using a fluorescent sample of known lifetime, such as laser dyes, or using a non-fluorescent scattering sample such as a diluted solution of colloidal silica or LUDOX in a cuvette. In the latter case the IRF is also referred to as a fluorescence decay with lifetime zero.

In mathematical terms the measured fluorescence decay $I(t)$ can be described as the convolution of the IRF with the pure fluorescence decay of the sample $F(t)$

$$I(t) = IRF * F(t) \tag{4.22}$$

In the „classical" fitting approach for analyzing fluorescence decay curves the influence of the IRF is taken into account by fitting the measured fluorescence decay by a convolution of the IRF with a sum of exponentials

$$I(t) = IRF(t) * \sum_i A_i \, exp^{-\frac{t+\Delta t}{\tau_i}} \tag{4.23}$$

with index i counting the number of exponentials chosen for the fit and Δt as temporal shift between the IRF and the measured decay.

Using the phasor approach for analysis of fluorescence kinetics the influence of

---

[3]This approach is justified as the background fluorescence within a streak camera image measured in photon counting mode is nearly homogeneous, which is clear from the working principle of this acquisition mode and can also be seen in Fig. 3.6. In similar manner also TCSPC measurements show an almost homogeneous fluorescence background signal.

the IRF has to be considered as well in order to obtain the phasor coordinates of the pure fluorescence decay, F, of the sample. The mathematical procedure for the correction of the IRF shown in the following was nicely introduced in detail by Martelo et al. [115].

The phasor coordinates of a measured fluorescence decay D, given by the convolution of the IRF and the pure decay F according to equation 4.22, are calculated with the basic definition of the phasor coordinates in the time domain, in equations 4.15 and 4.16, as real and imaginary parts of the Fourier transform of the measured decay D. For simplicity those phasor coordinates are named $G[D]$ and $S[D]$ in the following.

$$G[D] = Re(\ \mathcal{F}\{D\}\ ) = Re(\ \mathcal{F}\{IRF * F\}\ ) \qquad (4.24)$$

$$S[D] = Im(\ \mathcal{F}\{D\}\ ) = Im(\ \mathcal{F}\{IRF * F\}\ ) \qquad (4.25)$$

For clarity the measured decay D, the IRF and the pure decay F are regarded as time dependent and normalized for the moment. Performing the Fourier transform calculations in detail[4] results in

$$G[D] = G[IRF]\,G[F] - S[IRF]\,S[F] \qquad (4.26)$$

$$S[D] = S[IRF]\,G[F] + G[IRF]\,S[F] \qquad (4.27)$$

This gives the relation of the phasor coordinates $G[D]$ and $S[D]$ of the measured decay D as a function of the phasor coordinates of the IRF and the pure fluorescence decay F. Rewriting these two relations in matrix form yields

$$\begin{bmatrix} G[D] \\ S[D] \end{bmatrix} = \begin{bmatrix} G[IRF] & -S[IRF] \\ S[IRF] & G[IRF] \end{bmatrix} \begin{bmatrix} G[F] \\ S[F] \end{bmatrix} \qquad (4.28)$$

Remembering the basic definition of the phasor coordinates as $G = m \cdot cos(\phi)$ and $S = m \cdot sin(\phi)$ in equations 4.9 and 4.10, which also follows from the geometric definition by Jameson when introducing the phasor plot, we can rewrite

---

[4]The detailed calculation is shown in Appendix B.2

the 2x2 matrix as

$$\begin{bmatrix} G[D] \\ S[D] \end{bmatrix} = m_{IRF} \begin{bmatrix} cos(\phi_{IRF}) & -sin(\phi_{IRF}) \\ sin(\phi_{IRF}) & cos(\phi_{IRF}) \end{bmatrix} \begin{bmatrix} G[F] \\ S[F] \end{bmatrix} \tag{4.29}$$

with m_{IRF} and ϕ_{IRF} being the length and the phase of the phasor of the IRF, respectively.

Initially it was the aim to calculate the phasor of the pure decay F from the measured decay D and the IRF. This is now possible by reformulating equation 4.29 as

$$\begin{bmatrix} G[F] \\ S[F] \end{bmatrix} = \frac{1}{m_{IRF}} \begin{bmatrix} cos(\phi_{IRF}) & sin(\phi_{IRF}) \\ -sin(\phi_{IRF}) & cos(\phi_{IRF}) \end{bmatrix} \begin{bmatrix} G[D] \\ S[D] \end{bmatrix} \tag{4.30}$$

A closer view on equation 4.30 reveals that the square matrix corresponds to a canonical rotation matrix. Hence, for the phasor approach the correction of the influence of the IRF corresponds to a counterclockwise rotation of the phasor of the measured decay D and a radial stretching, see Fig. 4.7.
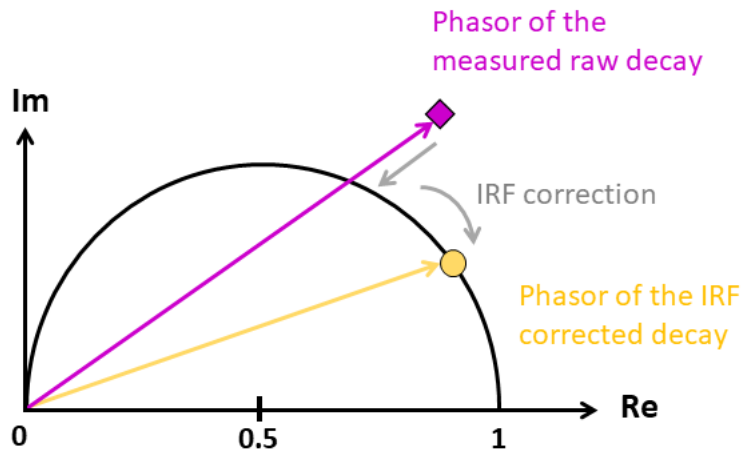
Figure 4.7.: Correction for the IRF in the phasor space: The correction of a measured phasor for the IRF corresponds to a stretching and rotation of the phasor. For details see text.

Using the basic definition of the phasor coordinates G and S as $G = m \cdot cos(\phi)$ and $S = m \cdot sin(\phi)$ in equations 4.9 and 4.10 together with trigonometic identi-

ties[5] allows reformulation of equation 4.30 as

$$G[F] = \frac{m_D}{m_{IRF}} \cdot cos(\phi_D - \phi_{IRF}) = m_F \cdot cos(\phi_F) \tag{4.31}$$

$$S[F] = \frac{m_D}{m_{IRF}} \cdot sin(\phi_D - \phi_{IRF}) = m_F \cdot sin(\phi_F) \tag{4.32}$$

with

$$m_F = \frac{m_D}{m_{IRF}} \tag{4.33}$$

and

$$\phi_F = \phi_D - \phi_{IRF} \tag{4.34}$$

Now the phasor coordinates of the pure fluorescence decay F can be calculated from the measured decay D and the IRF.

How to obtain the IRF

In practice the IRF is recognized by measuring the fluorescence decay of a fluorescent sample with known fluorescence lifetime[6]. Thus, the phasor of the IRF has to be calculated from this measured decay of the fluorescent sample. The detailed procedure will be outlined below. In order to avoid confusion with the previously used naming of F and D, in the following text the pure fluorescence decay of the fluorescent sample will be denoted as F^* and the corresponding measured decay of the fluorescent sample is denoted as D^*, when corresponding to the measured IRF.

The convolution in equation 4.24 is still valid, leading to the following relation of the pure fluorescence decay F^* and the measured decay D^*:

$$D^* = IRF * F^* \tag{4.35}$$

The commutative character of the convolution leads to a symmetric role of the IRF and the pure fluorescence decay F^*. Thus, equation 4.30 remains valid when

---

[5]The detailed calculation is shown in Appendix B.3
[6]When using a non-fluorescent scattering sample such as a diluted solution of colloidal silica or LUDOX in a cuvette this lifetime is assumed to be zero.

the labels F^* and IRF are exchanged:

$$\begin{bmatrix} G[IRF] \\ S[IRF] \end{bmatrix} = \frac{1}{m_{F^*}} \begin{bmatrix} cos(\phi_{F^*}) & sin(\phi_{F^*}) \\ -sin(\phi_{F^*}) & cos(\phi_{F^*}) \end{bmatrix} \begin{bmatrix} G[D^*] \\ S[D^*] \end{bmatrix} \tag{4.36}$$

This allows the calculation of the IRF phasor from the pure fluorescence decay F^* and the measured fluorescence decay D^*. By using the known lifetime of the fluorescent sample, the two basic relations of fluorometry in equations 4.7 and 4.8 allow the calculation of m_{F^*} and ϕ_{F^*}. By analogy to the considerations outlined above, see equations 4.31 and 4.32, it follows

$$G[IRF] = \frac{m_{D^*}}{m_{F^*}} \cdot cos(\phi_{D^*} - \phi_{F^*}) = m_{IRF} \cdot cos(\phi_{IRF}) \tag{4.37}$$

$$S[IRF] = \frac{m_{D^*}}{m_{F^*}} \cdot sin(\phi_{D^*} - \phi_{*F}) = m_{IRF} \cdot sin(\phi_{IRF}) \tag{4.38}$$

with

$$m_{IRF} = \frac{m_{D^*}}{m_{F^*}} \tag{4.39}$$

and

$$\phi_{IRF} = \phi_{D^*} - \phi_{F^*} \tag{4.40}$$

Thus, the length and the phase of the IRF phasor , m_{IRF} and ϕ_{IRF}, can be calculated from the measured decay of the fluorescent sample D^* used as IRF and the pure fluorescence decay F^* given by the known lifetime of this fluorescent sample.

Calculation of the phasor coordinates corrected for the IRF

Finally, combining all the considerations above, the calculation of the phasor coordinates $G[F]$ and $S[F]$ of the pure fluorescence decay of any sample F from the measured decay D of this sample is possible, including the correction of the influence of the IRF. A graphical summary of this calculation is given in Fig. 4.8.

Measured	Naming in calculations
Decay of a sample (e.g. LH2 in detergent solution)	**D**
IRF (e.g. reference sample such as a laser dye)	**D***
Known	
pure decay of the measured IRF (fluorescence lifetime value of the laser dye used for measuring the IRF)	**F***

Calculation of
pure fluorescence decay
of the measured sample   F

and **corresponding phasor**
coordinates
       G[F] and S[F]
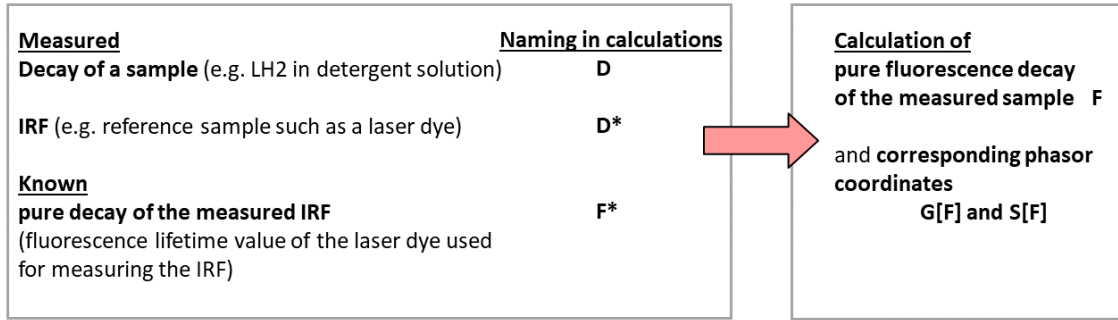
Figure 4.8.: Graphical summary of phasor calculation: *The phasor coordinates $G[F]$ and $S[F]$ of the pure fluorescence decay of a sample are calculated from a measured decay of that sample, a measured IRF and the known fluorescence lifetime value of the IRF. For details see text.*

As outlined above, the correction of the influence of the IRF is determined from a measured decay D^* of a fluorescent sample with known lifetime, giving the length m_{F*} and the phase ϕ_{F*} of the phasor F^*. Thus, by using the definitions of m_{IRF} and ϕ_{IRF} in equations 4.39 and 4.40 one obtains the following formulation of $G[F]$ and $S[F]$:

$$\begin{bmatrix} G[F] \\ S[F] \end{bmatrix} = \frac{1}{m_{IRF}} \begin{bmatrix} cos(\phi_{IRF}) & sin(\phi_{IRF}) \\ -sin(\phi_{IRF}) & cos(\phi_{IRF}) \end{bmatrix} \begin{bmatrix} G[D] \\ S[D] \end{bmatrix} \tag{4.41}$$

$$= \frac{m_{D*}}{m_{F*}} \begin{bmatrix} cos(\phi_{D*} - \phi_{F*}) & sin(\phi_{D*} - \phi_{F*}) \\ -sin(\phi_{D*} - \phi_{F*}) & cos(\phi_{D*} - \phi_{F*}) \end{bmatrix} \begin{bmatrix} G[D] \\ S[D] \end{bmatrix} \tag{4.42}$$

Splitting this into single components yields

$$G[F] = \frac{m_{D*}}{m_{F*}} \left(cos(\phi_{D*} - \phi_{F*}) \, G[D] + sin(\phi_{D*} - \phi_{F*}) \, S[D] \right) \tag{4.43}$$

$$S[F] = \frac{m_{D*}}{m_{F*}} \left(-sin(\phi_{D*} - \phi_{F*}) \, G[D] + cos(\phi_{D*} - \phi_{F*}) \, S[D] \right) \tag{4.44}$$

Now the final phasor coordinates $G[F]$ and $S[F]$ can be calculated from the measured decay of a sample and a measured IRF according to equations 4.43 and 4.44. The values of $G[D]$ and $S[D]$ can be calculated directly from a measured fluorescence decay D according to equations 4.18 - 4.21. Correction of the influence of the IRF is recognized by multiplicative factors resulting from a measured IRF decay D^* and their pure fluorescence decay F^*. The factors m_{F*} and ϕ_{F*} are

accessible by the two basic relations of phase fluorometry in equations 4.7 and 4.8 as the lifetime is known. For the factors correlated to the measured IRF decay D^* the calculation of m_{D*} and ϕ_{D*} has slightly more effort of calculation. First, the phasor of D^* has to be calculated similar to the one of D and afterwards the factors m_{D*} and ϕ_{D*} can be calculated from this phasor D^*.

Additionally to the influence of the IRF on the measured decay as just discussed, moreover the width of the IRF as well as the time shift between the IRF and the measured fluorescence decay D have to be taken into account during phasor calculation. Whereas the width of the IRF can be neglected for single exponential decays [120], in general it should be taken into account in the phasor calculation. The time shift between IRF and the measured decay D, also referred to as color shift [123], is an artifact of detection due to the fact that often the IRF is not detected at the same spectral position as the fluorescence emission and most detectors feature a wavelength-dependent detection yield. However, the time shift sensitively influences the phasor calculation especially for short lifetimes (in the same order of magnitude as the temporal width of the IRF) [115]. Thus, the time shift has to be considered in general within the calculation of the phasor coordinates for the pure fluorescence decay as well.

4.3.4. Phasor formulation for time domain measurements

Until now the procedure of phasor calculation for a measured fluorescence decay was discussed conceptually for any data measured in the time domain in the previous section. Now, this procedure is applied to the example of a measured fluorescence decay extracted from a streak camera measurement[7]. A visualization of this procedure is shown in the flow chart in Fig. 4.9.

The starting point for the procedure of phasor calculation are two streak camera images: one is the streak camera image resulting from a streak camera measurement of the fluorescence decay of the sample of interest, like the LH2 complexes in this thesis, and the other is a streak camera image resulting from a streak camera measurement of the IRF, which was a scattering solution of colloidal silica in

---

[7]For time domain data measured with the TCSPC technique the procedure of phasor calculation outlined in the following is in principle identical. Only for reasons of smoother reading and in order to consider that data resulting from streak camera measurements requires additional steps of data processing, the procedure is outlined here using this example.

this thesis.
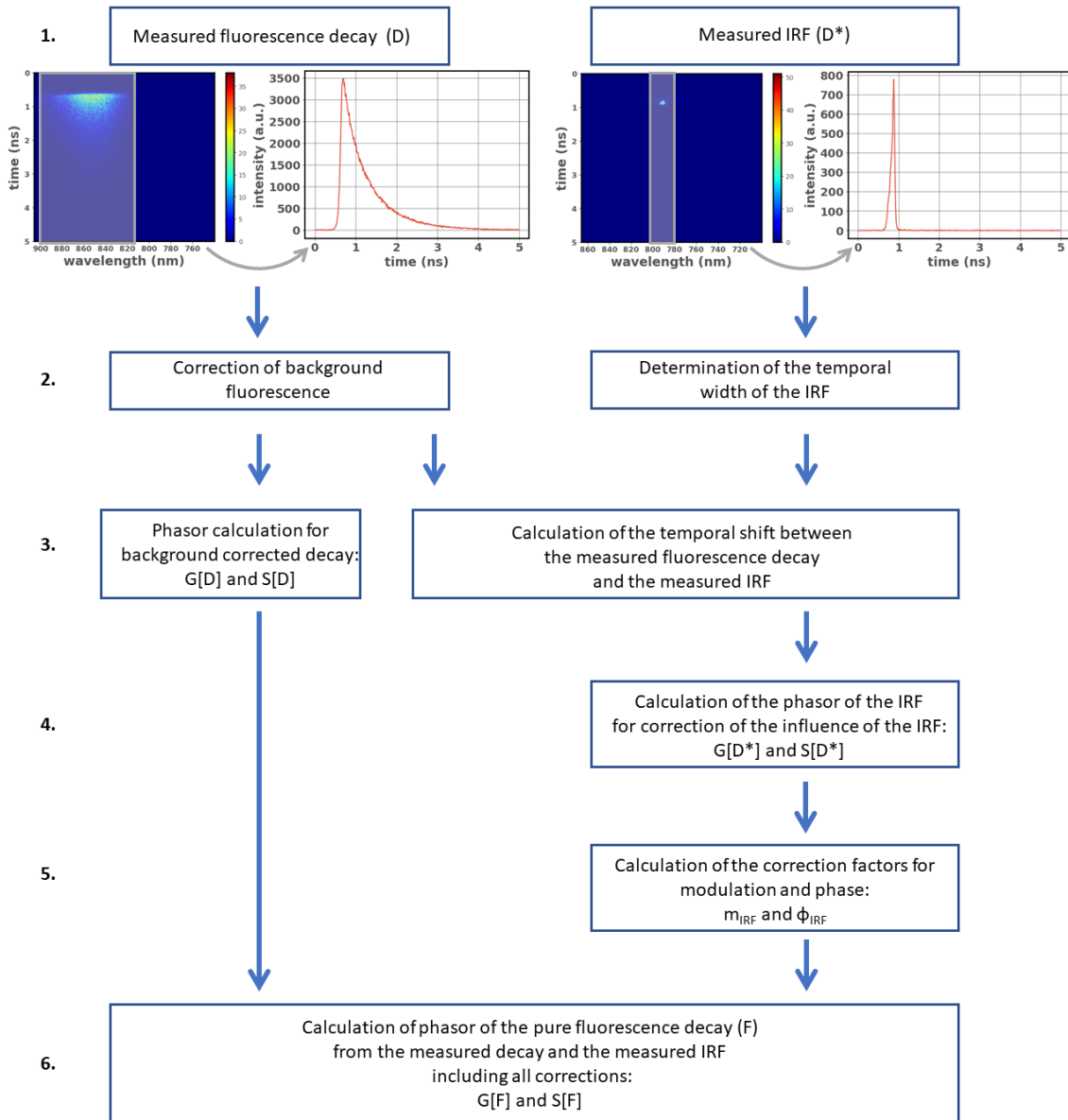
Figure 4.9.: Flow chart for visualization of the phasor calculation for streak camera measurements: *Starting with a measured fluorescence decay and a measured instrument response function (IRF) the single steps towards proper phasor calculation of the pure fluorescence decay F, including background correction and correction of the influence of the IRF, are shown. For details see text.*

In a first step, for both images the fluorescence intensity decay curves are extracted by integration along the spectral axis of the streak camera image as already outlined in Section 3.2.1. The fluorescence intensity curve extracted from the streak camera image of the measured decay shows an evident fluorescence

decay whereas the fluorescence intensity curve of the IRF only shows a small nearly delta-shaped pulse.[8]

As the steps during the procedure of phasor calculation are different for the measured decay, denoted as D, and the measured IRF, denoted as D^*, their pathways through the flow chart in Fig. 4.9 will be described separately. As most of the phasor calculation procedure focuses on the correction of the influence of the measured IRF, first the two steps resulting from the measured fluorescence decay are described before afterwards the single steps of phasor calculation using the measured IRF are discussed.

After generation of the fluorescence decay curve, the second step of phasor calculation for the measured decay D is determining the average background fluorescence intensity. This is done by averaging the fluorescence intensity over the first 50 pixels of the fluorescence decay, prior to the rise of fluorescence decay due to excitation, see Fig. 4.10. The resulting average intensity is then subtracted from the measured decay in every bin yielding the background corrected fluorescence decay curve.
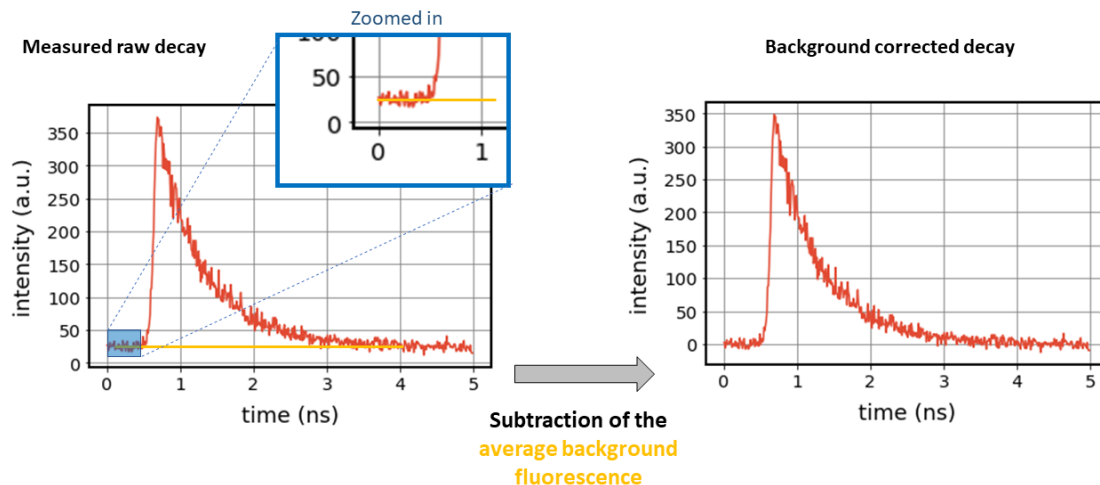
Figure 4.10.: Background correction of the measured raw decay: By calculating an average background fluorescence intensity over the first 50 pixels of the measured raw fluorescence decay a background correction is performed. For details see text.

Now, after background correction, the third step during the procedure of phasor

---

[8]From here on the outlined principle of phasor calculation can be directly adapted to measured time domain data resulting from TCSPC.

calculation for the measured fluorescence decay is calculating the phasor coordinates $G[D]$ and $S[D]$ of the background corrected, measured fluorescence decay according to equations 4.18 - 4.21. As already discussed, the transformation frequency ω is determined by the length of the temporal axis of the streak camera image, which is 5 ns for all measurements of this thesis.

Concerning the measured IRF the second step towards phasor calculation after extraction of the fluorescence intensity curve from the streak camera image is fitting the measured IRF by a gaussian function. This allows for determination of the temporal width of the IRF, which is about 50 ps for all streak camera measurements of this thesis. An example for the gaussian fit of one IRF for one of the streak camera measurements is shown in Fig. 4.11. As already outlined in the last section, in general the temporal width of the IRF has to be taken into account for phasor calculation. This is done by using the curve of the gaussian fit as the IRF from now on in the procedure of phasor calculation.
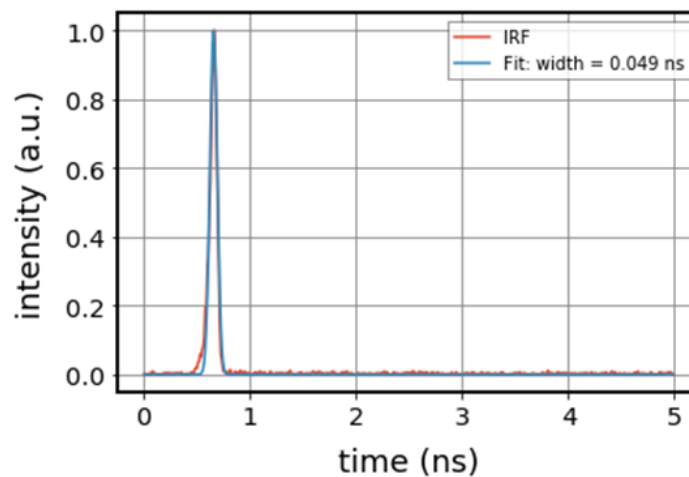
Figure 4.11.: Determination of the temporal width of the IRF: By performing a gaussian fit to the measured IRF the temporal width is determined by the full-width-at-half-maximum (FWHM).

The third step of the measured IRF within the procedure of phasor calculation is the determination of the temporal shift Δt between the measured IRF and the measured decay curve. This is done by performing a „traditional" multiexponential fit, according to equation 4.23, of the background corrected decay D and Δt being the only parameter of interest. This approach for the determination of Δt is a well known procedure [124]. Testing different numbers of exponents in

the multiexponential fitting showed only minor influence on the resulting time shift Δt and revealed that the time shift Δt can be determined with this approach with an accuracy of one time bin, corresponding to 9.7 ps for measurements of this thesis. After determination of Δt the IRF is shifted by this value for best temporal overlap with the measured decay curve.

Afterwards, in the fourth step within the flowchart shown in Fig. 4.9, the phasor coordinates $G[D^*]$ and $S[D^*]$ of this shifted IRF are calculated according to equations 4.18 - 4.21 analogously to the measured decay, as already described above. By assuming that the IRF is measured from a scattering solution, corresponding to a fluorescent sample of lifetime zero, the modulation and phase correction parameters, m_{IRF} and ϕ_{IRF}, respectively, are calculated according to the basic relations of phase fluorometry in equations 4.8 and 4.7 within the fifth step of the procedure of phasor calculation.

Finally, in the last step, the phasor coordinates $G[F]$ and $S[F]$ for the pure fluorescence decay, which were the aim of all our efforts, are calculated. This is done according to equations 4.43 and 4.44 and by using the calculated correction parameters of phase and modulation according to equations 4.39 and 4.40.
All phasors shown in the further course of this thesis are calculated and corrected as just described and schematically shown in the flow chart in Fig. 4.9.

4.4. Features of the phasor plot

The phasor plot introduced by Jameson [113] features some special intrinsic properties irrespective whether the data used for the calculation of the phasor coordinates has been aquired in the frequency or time domain. In the following, these features of the phasor plot will be discussed in detail.

- **The universal semicircle:**
  From the basic definition of the phasor coordinates by Weber [28], see Section 4.1, that have the shape of

$$G(\omega) = m \cdot cos(\phi)$$

$$S(\omega) = m \cdot sin(\phi)$$

and the first basic relation of phase fluorometry , also compare Section 4.1,

$$tan(\phi) = \omega\tau$$

it follows that phasors corresponding to single exponential decays always fall on a semicircle of radius 0.5 centered at the position (0.5,0) in the phasor plot as shown in Fig. 4.12. Consequently, the phasor coordinates G and S of phasors corresponding to monoexponential decays follow the relation[9]

$$S = \sqrt{G(1 - G)} \qquad (4.45)$$

This feature applies to all phasors from monoexponential decays irrespective of the discrete value of the corresponding lifetime or how the underlying fluorescence lifetime data was measured. The semicircle is therefore called *universal semicircle*.
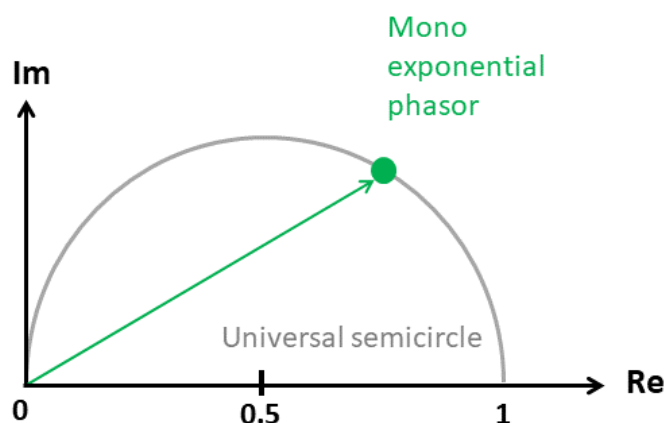
Figure 4.12.: The universal semicircle: *Phasors corresponding to a single exponential decay (green) fall onto the universal semicircle (grey).*

- **The lifetime-ruler along the universal semicircle:**
  The universal semicircle acts as a lifetime ruler. It indicates the lifetime of the underlying fluorescence decay by the position of the phasor. Phasors corresponding to short lifetimes are located close to the position (1,0). Phasors corresponding to longer lifetimes „move" along the semicircle counterclockwise with increasing lifetime as shown in Fig. 4.13.

---

[9]The equation of a circle of radius r that is centered at (x_0,y_0) is given by $(x - x_0)^2 + (y - y_0)^2 = r^2$.
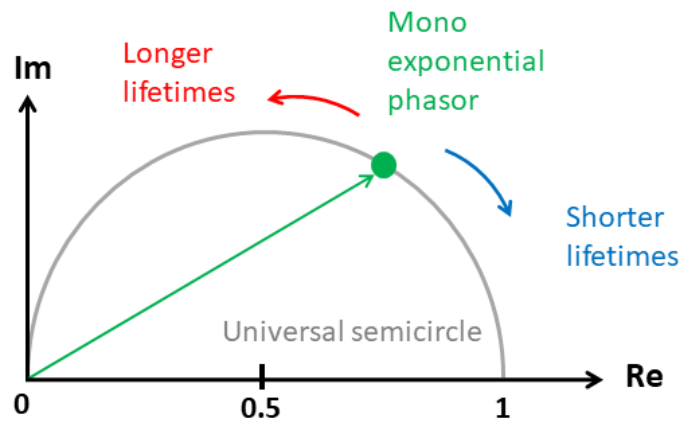
Figure 4.13.: The universal semicircle: A phasor corresponding to a single exponential decay (green) lies on the universal semicircle (grey). Phasors representing monoexponential decays move counterclockwise along the universal semicircle as their corresponding lifetimes increase. For details see text.

- **Scaling the lifetime ruler:**

  The scaling of the lifetime ruler along the universal semicircle is nonlinear and depends strongly on the transformation frequency and the harmonic number used for the Fourier transformation in the calculation of the phasor coordinates for time domain measurements[10]. Thus, by choosing the scaling of the lifetime ruler properly it is possible to resolve short time constants that would be hidden otherwise. Both, the influence of the different scaling of the lifetime ruler and the nonlinear scaling are shown in Fig. 4.14.

  The phasors corresponding to selected lifetimes ranging from 0 ns to 10 ns were calculated for different transformation frequencies and are shown as a function of the transformation frequency. The nonlinearity of the scaling is visible at first sight. Focusing in particular on the phasors of fluorescence lifetimes below 0.5 ns, it is obvious that for the transformation frequency ω the phasors corresponding to the lifetimes of 0 ns, 0.1 ns and 0.2 ns cannot be resolved whereas this is easily possible for higher transformation frequencies (3ω, 5ω). Thus, the transformation frequency has to be chosen properly for phasor calculation.

---

[10]For frequency domain measurements this is valid for the modulation frequency respectively.
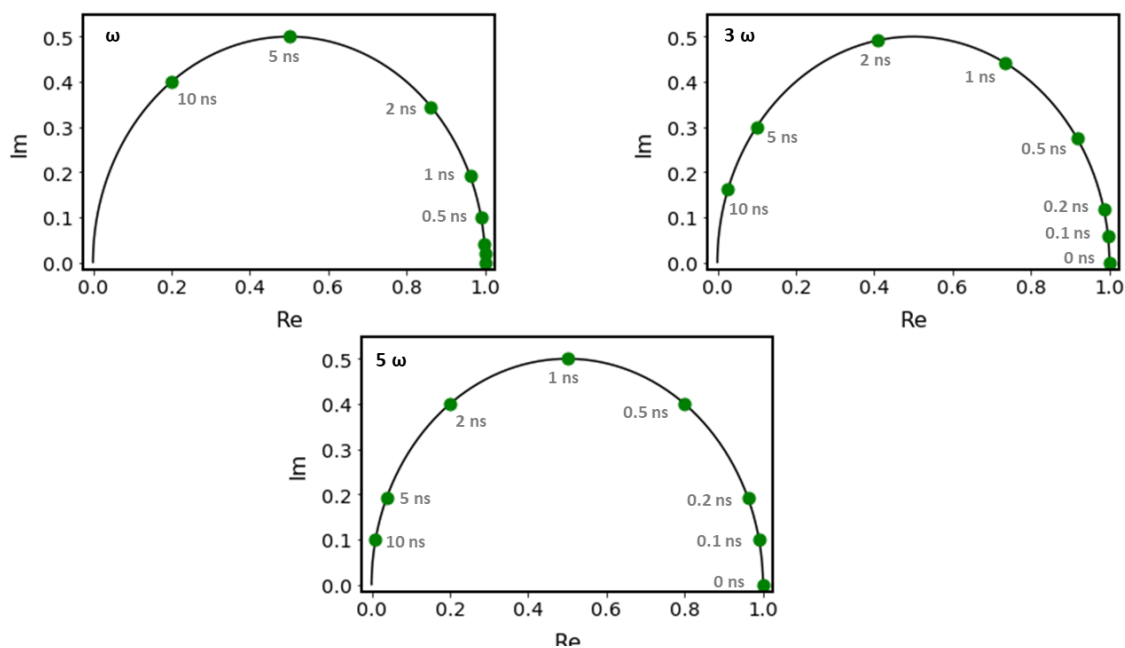
Figure 4.14.: Nonlinear scaling of the lifetime ruler: *Phasors corresponding to lifetimes in the range of 0 ns to 10 ns are shown, calculated for different transformation frequencies. Obviously different values of the transformation frequency correspond to different scaling factors of the lifetime ruler. For details see text.*

For time domain data the transformation frequency is determined by the temporal width of the detection window, compare Section 4.3.1, and thus a fixed value. It follows that proper scaling of the universal semicircle is realized by an increase of the harmonic number n of the transformation for time domain data.

- **The linearity of phasor addition:**
  By definition phasors are vectors and therefore follow vector algebra. This allows the identification of multiexponential decays easily. As just stated, phasors corresponding to single exponential fluorescence decays lie on the universal semicircle. Consequently, all phasors that do not lie on the universal semicircle are multiexponential. Phasors that are located inside the universal semicircle correspond to fluorescence decays consisting of a linear combination of single exponential decays. Reasonably, phasors of biexponential decays lie on a straight line between the phasors of the contributing lifetime components. For fluorescence decays with three contributing lifetimes the phasor lies within a triangle defined by the three contributing lifetime phasors. Both features are visualized in Fig. 4.15.

70
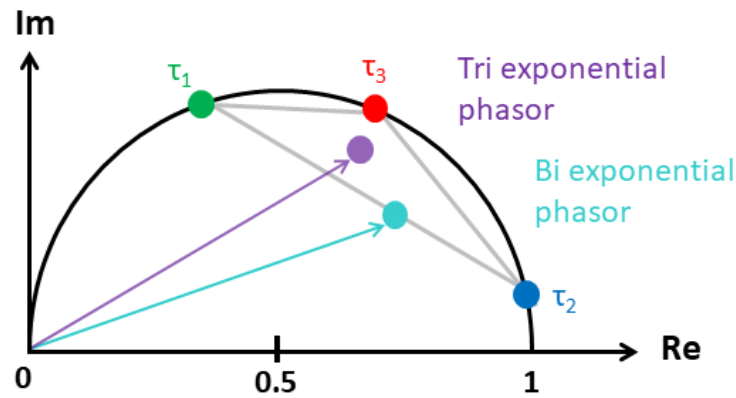
Figure 4.15.: The linearity of phasor addition: *Phasors corresponding to biexponential (cyan) decays lie on a straight line connecting the phasors of the contributing lifetimes τ_1 and τ_2, shown in green and blue respectively. For triexponential decays the corresponding phasor (purple) lies within a triangle defined by the three contributing lifetimes τ_1, τ_2 and τ_3 (shown in red).*

Although many publications that use the phasor approach neglect the possibility of phasors outside the universal semicircle, such locations are physically possible. For example excited state reactions [125] as well as components with negative amplitudes, also known as rising components, [126, 127] and photo-chemical bleaching effects [128, 129] have been identified to lead to phasor positions outside the universal semicircle.

4.5. Working with the phasor plot: Identifying lifetimes and amplitudes

After calculation of the phasor coordinates and plotting them in the phasor plot the analysis begins. Using the features of the phasor plot, as outlined in the last section, it can easily be identified whether the phasor of interest corresponds to a single or multiexponential decay. If the phasor lies on the universal semicircle, the lifetime of the single exponential decay follows from equations 4.11 and 4.12:

$$G(\omega) = \frac{1}{1 + \omega^2 \tau^2}$$

$$S(\omega) = \frac{\omega \tau}{1 + \omega^2 \tau^2}$$

For phasors that do not fall on the universal semicircle the determination of lifetimes is more complicated because these phasors correspond to multiexponential decays.

4.5.1. Biexponential decays

The simplest case of a multiexponential decay features two lifetimes τ_1 and τ_2, contributing to the total fluorescence intensity with different fractions f_1 and f_2, respectively. As outlined above, in general, phasors corresponding to biexponential decays lie inside the universal semicircle on a straight line connecting the phasors A and B of the two underlying lifetimes τ_1 and τ_2 as exemplarily shown in Fig. 4.16. As the phasors A and B correspond to the lifetime values τ_1 and τ_2, respectively, these phasors lie on the universal semicircle.
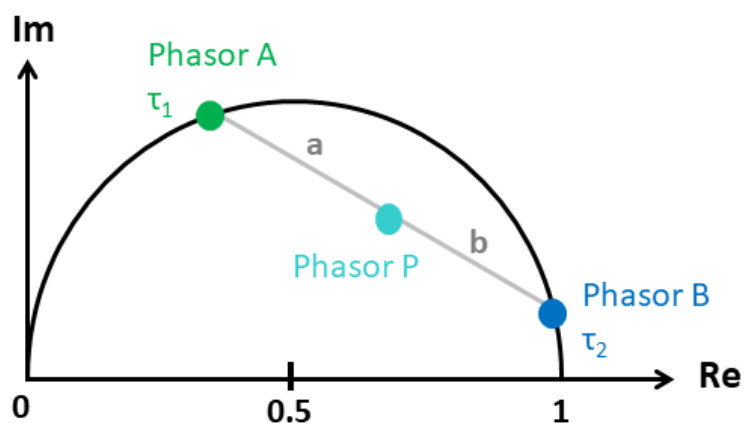
Figure 4.16.: Phasor position for a biexponential decay*: The phasor P (cyan) corresponds to a biexponential decay and lies on a straight line connecting the phasors A and B (green and blue) of the contributing lifetimes τ_1 and τ_2. The length of the line segments a and b corresponds to the fractional contributions of the two lifetime components to the total fluorescence intensity. The fractional contributions are calculated according to the lever rule. For details see text.*

The phasor P of the biexponential decay divides the distance between the phasors A and B into two parts of length a and b, respectively, see Fig. 4.16. The fractional contributions f_1 and f_2 of the two lifetimes τ_1 and τ_2 can be calculated analogously to the lever rule [130] known from phase diagrams in thermody-

namics as

$$f_1 = \frac{b}{|\overrightarrow{AB}|} = \frac{|\overrightarrow{PB}|}{|\overrightarrow{AB}|} \tag{4.46}$$

$$f_2 = \frac{a}{|\overrightarrow{AB}|} = \frac{|\overrightarrow{AP}|}{|\overrightarrow{AB}|} \tag{4.47}$$

Due to their vectorial character phasors allow the calculation of distances in the phasor plot as the length of vectors. For example $|\overrightarrow{AB}|$ is the length of the vector connecting the phasors A and B. As already mentioned above, the contributing lifetimes τ_1 and τ_2 can easily be calculated from the phasor coordinates.

In practice there is often no or only limited a priori knowledge about the underlying fluorescence decay of a phasor. In experiments usually the effect of changing one specific parameter on the fluorescence decay is of interest. In the case of a biexponential decay with changing fractional contributions of the two basic lifetime components this leads in the phasor plot to a cloud of phasors that „appears" along a straight line as a function of the parameter of interest, as shown in Fig. 4.17.
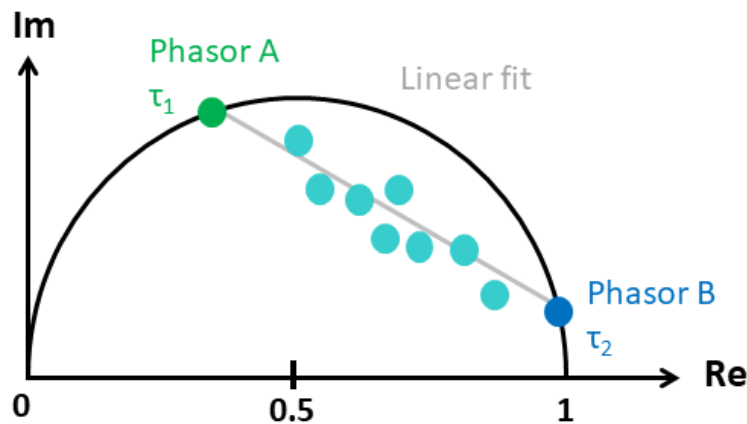
Figure 4.17.: Resolving a biexponential decay by linear fitting: By performing a linear fit through the cloud of measured phasors (cyan), the underlying biexponential decay can be resolved from a cloud of scattered phasors in the phasor space. The intersections of the linear fit with the universal semicircle yield the phasors A and B of the two contributing lifetimes τ_1 and τ_2. For details see text.

The movement of the phasors along the line indicates a biexponential decay having two contributing lifetimes τ_1 and τ_2 with changing fractional contributions for the different phasors. To determine the two contributing lifetimes of the

underlying biexponential decay a linear fit[11] is performed through the cloud of scattered phasors. The intersections of the linear fit and the universal semicircle reveal the phasors A and B of the two basic lifetimes τ_1 and τ_2, which can be calculated from their phasor coordinates as described before.

As the straight line, which leads to the identification of the two contributing lifetimes τ_1 and τ_2, is determined via linear fitting, in general the phasors in the „cloud of interest" do not fall directly on this line but have a small displacement. When calculating the fractional contributions of the two lifetime components for each phasor in the cloud of phasors, this displacement has to be taken into account. Fig. 4.18 shows an example for a distinct phasor P in the cloud of scattered phasors that has a small displacement from the fitted line.
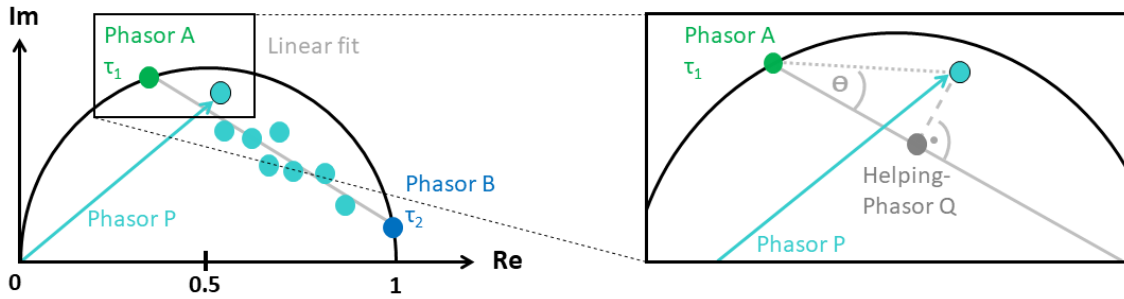
Figure 4.18.: Calculating the fractional contributions of the lifetime components of a biexponential decay from the linear fit through a cloud of phasors: The phasor P is one distinct phasor within the cloud of scattered phasors. On the right hand side a zoomed in view is shown to visualize the distance of the phasor P from the straight line of the linear fit. Scalar projection of the vector connecting the phasors A and P yields the helping phasor Q which lies on the fitted line and allows the calculation of the fractional contributions as already described. For details see text.

The relative contributions of the two contributing lifetimes can be calculated for this phasor P by using the vectorial character of the phasor. In order to take into account the small displacement of the phasor from the fitted line, a helping phasor Q is defined by performing a scalar projection. The scalar product known from vector algebra as

$$\overrightarrow{AP} \cdot \overrightarrow{AB} \;=\; |\overrightarrow{AP}||\overrightarrow{AB}|cos(\Theta) \tag{4.48}$$

---

[11]Although in general a least-square linear fit can be applied, considering the uncertainty of both phasor coordinates due to their calculation from measured data instead performing an orthogonal distance regression (ODR) linear fit is preferred [121, 131]. See also Appendix C.

allows calculation of the angle Θ between the vectors $\overrightarrow{AP}$ and $\overrightarrow{AB}$. Afterwards the scalar projection of the vector $\overrightarrow{AP}$ on $\overrightarrow{AB}$ can be calculated as

$$|\overrightarrow{AQ}| = |\overrightarrow{AP}| \, cos(\Theta) \tag{4.49}$$

defining the helping phasor Q. This helping phasor Q lies on the fitted line and allows to determine the two segments a and b needed for the calculation of the two fractional contributions f_1 and f_2 of the two basic lifetimes τ_1 and τ_2. Thus, f_2 can be calculated as

$$f_2 = \frac{a}{|\overrightarrow{AB}|} = \frac{|\overrightarrow{AQ}|}{|\overrightarrow{AB}|} = \frac{|\overrightarrow{AP}| \, cos(\Theta)}{|\overrightarrow{AB}|} \tag{4.50}$$

and f_1 can be calculated analogously or simply by subtraction of vector lengths

$$f_1 = |\overrightarrow{AB}| - a = |\overrightarrow{AB}| - |\overrightarrow{AQ}| \tag{4.51}$$

4.5.2. Triexponential decays

Although biexponential decays are the most common case of multiexponential decays in fluorescence kinetics, sometimes even triexponential decays occur. The analysis of the contributing lifetime components and their fractional contributions which was just described for two underlying exponentials can easily expanded to three exponentials as phasors follow vector algebra.

Phasors corresponding to triexponential decays are located inside a triangle in the phasor space which is spanned by the phasors of the three contributing lifetimes, as sketched in Fig. 4.19. A phasor P corresponding to a triexponential decay lies within the triangle of phasors spanned by the phasors A,B and C of the three contributing basic lifetimes τ_1, τ_2 and τ_3. As the phasors A,B and C each correspond to single lifetime values, these phasors lie on the universal semicircle. The phasor P splits the total area of the big triangle ABC into three segments, named α, β and γ, which are defined by the smaller triangles BCP, ACP and ABP, respectively. The calculation of the fractional contributions of the three lifetime components follows the same logic as for the biexponential decays. Whereas the analysis of biexponential decays follows the lever rule using linear segments of a straight line, this changes into using the areas of the smaller

triangles α, β and γ instead of the linear segments of a straight line.
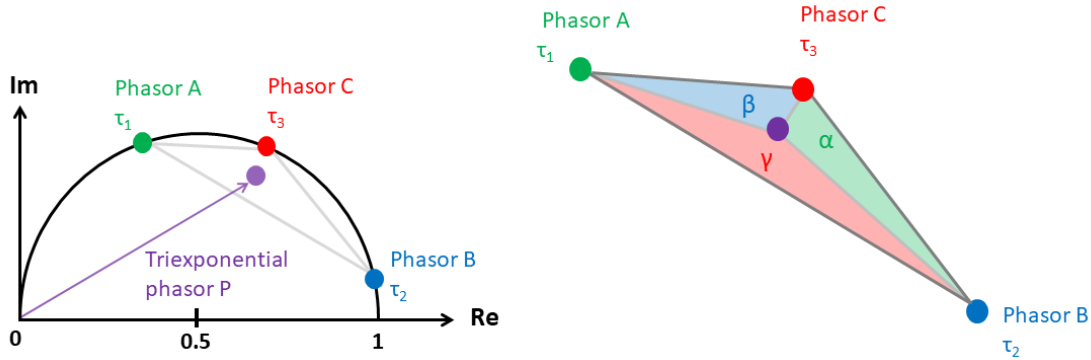
***Figure 4.19.: Phasor of a triexponential decay**: The phasor P corresponding to a triexponential decay lies within the triangle of phasors spanned by the phasors A,B and C of the three contributing basic lifetimes τ_1, τ_2 and τ_3. On the right hand side a zoomed view of the triangle of phasors is shown. The phasor P divides the total area of the triangle ABC in smaller triangles α, β and γ which are defined by the triangles BCP, ACP and ABP, respectively. For details see text.*

Thus, for a triexponetial decay the relative contributions f_1, f_2 and f_3 of the three lifetime components τ_1, τ_2 and τ_3 are given by

$$f_1 = \frac{A_\alpha}{A_{ABC}} \tag{4.52}$$

$$f_2 = \frac{A_\beta}{A_{ABC}} \tag{4.53}$$

$$f_3 = \frac{A_\gamma}{A_{ABC}} \tag{4.54}$$

The different parameters A denote the area of the triangle named in the subscript, respectively, such as A_α refers to the area of the triangle α, and so on.

The vectorial character of the phasors allows the calculation of the areas of the triangles α, β, γ and ABC by means of the cross product of vector algebra. As the cross product is only defined in three dimensions it is assumed for the moment that there is a third axis perpendicular to the plane of the phasor plot. Consequently, the phasors have a third component of value zero by assumption for the moment. Per definition the norm of the cross product $\vec{a} \times \vec{b}$ can be interpreted as the area of the parallelogram spanned by the vectors $\vec{a}$ and $\vec{b}$. For vectors with one component equal to zero the related cross product results

in a vector with only one component being different from zero. Thus, the area of the parallelogram spanned by the vectors $\vec{a}$ and $\vec{b}$ can easily be calculated as the norm of the cross product. The calculation of the norm of the cross product reduces to a simple multiplication and subtraction of the phasor coordinates as shown in equation 4.55:

$$
|\vec{a} \times \vec{b}| = \left| \begin{pmatrix} a_1 \\ a_2 \\ 0 \end{pmatrix} \times \begin{pmatrix} b_1 \\ b_2 \\ 0 \end{pmatrix} \right| = \left| \begin{pmatrix} 0 \\ 0 \\ a_1 b_2 - a_2 b_1 \end{pmatrix} \right| = a_1 b_2 - a_2 b_1 \tag{4.55}
$$

From basic mathematics it follows that a parallelogram is divided into two triangles of equal area by its diagonal. Thus, the area of the triangles α, β and γ and the big triangle ABC can easily be calculated using the cross product formulation in equation 4.55 and the phasor coordinates of the phasors spanning the different triangles. Finally, calculation of the three fractional contributions f_1, f_2 and f_3 is possible with the following equations:

$$
f_1 = \frac{A_\alpha}{A_{ABC}} = \frac{0.5\,|\overrightarrow{BC} \times \overrightarrow{BP}|}{0.5\,|\overrightarrow{AB} \times \overrightarrow{AC}|} = \frac{|\overrightarrow{BC} \times \overrightarrow{BP}|}{|\overrightarrow{AB} \times \overrightarrow{AC}|} \tag{4.56}
$$

$$
f_2 = \frac{A_\beta}{A_{ABC}} = \frac{0.5\,|\overrightarrow{AP} \times \overrightarrow{AC}|}{0.5\,|\overrightarrow{AB} \times \overrightarrow{AC}|} = \frac{|\overrightarrow{AP} \times \overrightarrow{AC}|}{|\overrightarrow{AB} \times \overrightarrow{AC}|} \tag{4.57}
$$

$$
f_3 = \frac{A_\gamma}{A_{ABC}} = \frac{0.5\,|\overrightarrow{AB} \times \overrightarrow{AP}|}{0.5\,|\overrightarrow{AB} \times \overrightarrow{AC}|} = \frac{|\overrightarrow{AB} \times \overrightarrow{AP}|}{|\overrightarrow{AB} \times \overrightarrow{AC}|} \tag{4.58}
$$

The notation of the vectors follows the geometry shown in Fig. 4.19. Thus, for example the vector $\overrightarrow{AB}$ connects the phasors A and B.

4.5.3. A special triexponential decay: Expanding a biexponential decay by adding a third component

In the previous section the general case of a triexponential decay with three known contributing lifetime components was discussed. Now we focus on a more complex situation when a biexponential decay is expanded to a triexponential decay by adding a third component. Fig. 4.20 illustrates this situation

exemplarily: On the left hand side of the figure a phasor P corresponding to a decay that is assumed to be biexponential is shown in purple color. It can be seen clearly that this phasor lies apart from the straight line (shown in grey) defining all possible locations of the biexponential decay with contributing lifetime components τ_1 and τ_2 represented by the phasors A and B, shown in green and blue respectively. Consequently, the purple colored phasor P cannot correspond to a biexponential decay and thus has to be described by a triexponential decay. As the purple colored phasor originally was expected to correspond to a biexponential decay, it can now be assumed that the two contributing lifetimes τ_1 and τ_2, as well as the ratio of their relative contributions is maintained in the observed triexponential decay. On the right hand side of Fig. 4.20 two possible locations of the phasor C, representing the third, yet unknown, contributing lifetime component τ_3, are shown as red circles. The corresponding big triangles ABC are illustrated by the dotted and dashed lines, respectively.
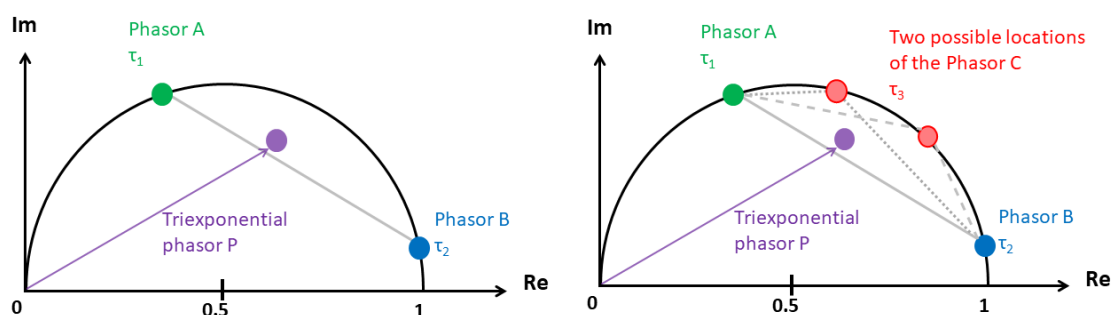
Figure 4.20.: Phasor of a triexponential decay expanded from a biexponential decay: *On the left hand side a purple colored phasor P clearly lies apart from the straight line (shown in grey) defining all possible locations of the biexponential decay with contributing lifetime components τ_1 and τ_2 represented by the phasors A and B, shown in green and blue, respectively. Thus, this phasor has to be described by a triexponential decay. On the right hand side two possible locations of the phasor C, representing the third, yet unknown contributing lifetime component τ_3, are illustrated in red. The triangles connecting the possible phasors C with the phasors A and B are illustrated as dotted and dashed lines, respectively. For detailed description see text.*

In order to determine the position of the phasor C and the corresponding third lifetime component τ_3 of this special triexponential decay, a procedure of calculation is developed: As outlined before, in general a phasor P corresponding to a triexponential decay lies within a triangle spanned by the phasors A, B and C of the contributing lifetime components τ_1, τ_2 and τ_3 as visualized in Fig. 4.21.
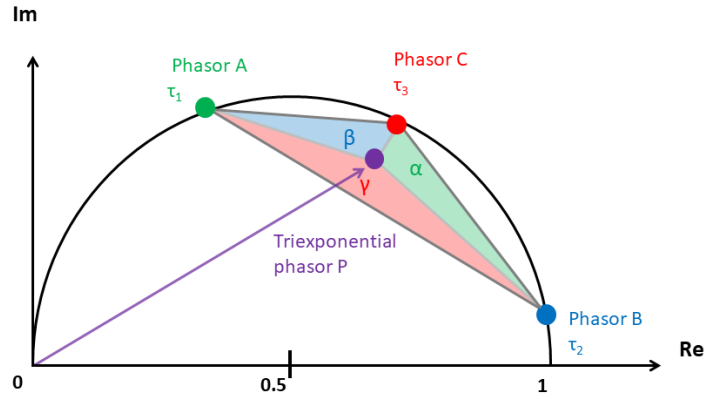
Figure 4.21.: Triexponential phasor lying within a triangle: *A phasor P (purple circle) corresponding to a triexponential decay lies within a triangle ABC. The triangle is spanned by the phasors A, B and C (green, blue and red colored circles, respectively) corresponding to the contributing lifetimes τ_1, τ_2 and τ_3. The phasor P divides the total area of the big triangle ABC into smaller triangles α, β and γ, colored in green, red and blue. For detailed description see text.*

The phasors A, B and C of the contributing lifetimes τ_1, τ_2 and τ_3 lie on the universal semicircle and thus, as stated before, their coordinates can be calculated by

$$G(\omega) = \frac{1}{1 + \omega^2 \tau^2}$$

$$S(\omega) = \frac{\omega \tau}{1 + \omega^2 \tau^2}$$

As phasors are vectors by definition, these two relations for the coordinates of a phasor representing a monoexponential decay can be expanded to the case of a multiexponential phasor [113, 115]. The phasor coordinates of a multiexponential decay in general fulfill the following relations:

$$G(\omega) = \sum_i f_i\, G_i(\omega) = \sum_i f_i \frac{1}{1 + \omega^2 \tau_i^2} \tag{4.59}$$

$$S(\omega) = \sum_i f_i\, S_i(\omega) = \sum_i f_i \frac{\omega \tau_i}{1 + \omega^2 \tau_i^2} \tag{4.60}$$

The index i is counting the number of exponentials. The coefficients f_i are the fractional contributions of the i-th exponential.

This general knowledge about phasors corresponding to multiexponential decays allows writing of the phasor coordinates G_P and S_P of the phasor P, cor-

responding to the triexponential decay in Fig. 4.20, as weighted sums of the coordinates of the phasors A, B and C:

$$G_P = f_A G_A + f_B G_B + f_C G_C \tag{4.61}$$

$$S_P = f_A S_A + f_B S_B + f_C S_C \tag{4.62}$$

The coefficients f_A, f_B and f_C are the fractional contributions of the basic lifetime components τ_1, τ_2 and τ_3 contributing to the triexponential decay. Thus, they are identical to the fractional contributions f_1, f_2 and f_3 discussed in the last section and follow the relations

$$f_A = \frac{A_\alpha}{A_{ABC}} \tag{4.63}$$

$$f_B = \frac{A_\beta}{A_{ABC}} \tag{4.64}$$

$$f_C = \frac{A_\gamma}{A_{ABC}} \tag{4.65}$$

The total area A_{ABC} of the big triangle ABC is given by the sum of the areas A_α, A_β and A_γ of the smaller triangles α, β and γ as visualized in Fig. 4.21

$$A_{ABC} = A_\alpha + A_\beta + A_\gamma \tag{4.66}$$

Using this relation allows reformulation of equation 4.62 as

$$A_{ABC} S_P = A_\alpha S_A + A_\beta S_B + A_\gamma S_C \tag{4.67}$$

Thus, the phasor coordinate S_C of the yet unknown phasor C, is accessible by

$$S_C = \frac{A_{ABC} S_P - A_\alpha S_A - A_\beta S_B}{A_\gamma} \tag{4.68}$$

As stated before, for the phasor P it is assumed that the two contributing lifetimes τ_1 and τ_2, as well as the ratio of their relative contributions, is maintained when expanding the expected biexponential to a triexponential decay. Thus, the phasor coordinates of the phasors A and B as well as the area A_γ of the small triangle γ are known.

$$A_\gamma = 0.5 \left| \overrightarrow{AB} \times \overrightarrow{AP} \right| = 0.5 \left(G_{BA} S_{PA} - S_{BA} G_{PA} \right) \tag{4.69}$$

The appearing values G_{BA}, S_{PA}, S_{BA} and G_{PA} are defined as the differences of the corresponding phasor coordinates, such as $G_{BA} = G_B - G_A$ for example.

Taking this assumption into account and recognizing moreover the fact, that the calculation of the areas of the triangles ABC, α, β and γ can be easily done by using the cross product, one obtains a quadratic equation for the phasor coordinate G_C which can be solved. Thus, one finally obtains[12] the following equation for calculation of the phasor coordinate G_C of the yet unknown phasor C:

$$G_{C_{1,2}} = \frac{-(-2u_1u_3 - u_2^2) \pm \sqrt{(-2u_1u_3 - u_2^2)^2 - 4\left(u_3^2 + u_2^2\right)u_1^2}}{2\left(u_3^2 + u_2^2\right)} \tag{4.70}$$

with u_0, u_1, u_2 and u_3 defined as

$$u_0 = \frac{R\,S_{PA} + S_{PB}}{0.5\,(G_{BA}\,S_{PA} - S_{BA}\,G_{PA})} \tag{4.71}$$

$$u_1 = -0.5\,G_{PA}\,S_A\,u_0 + 0.5\,S_{PA}\,G_A\,u_0 + S_P \tag{4.72}$$

$$u_2 = (1 - 0.5\,G_{PA}\,u_0) \tag{4.73}$$

$$u_3 = (0.5\,S_{PA}\,u_0) \tag{4.74}$$

and

$$R = \frac{A_\alpha}{A_\beta} \tag{4.75}$$

denoting the ratio of the fractional contributions of the lifetime components of the biexponential decay, given by the quotient of the areas of the smaller triangles α and β.

Calculation of the fluorescence lifetimes corresponding to the two solutions of G_C allows for the evaluation of the correct solution as τ_3 has to fulfill the constraint $\tau_2 < \tau_3 < \tau_1$, see Figures 4.19 and 4.21. Afterwards, the calculation of the other phasor coordinate S_C is easily possible.

---

[12]The detailed calculation is shown in Appendix B.4

4.6. The strength of phasor analysis

As outlined in the previous sections of this chapter it is a fundamental feature of the phasor approach that it is based only on the experimental data of the time-resolved measurements and does not require any *a priori* assumption of the underlying kinetics. The calculation of the phasor coordinates and their subsequent evaluation allows for identification of the measured kinetics simply from of the phasor positions in the phasor plot with respect to the universal semicircle. Thus, referring only to the measured data in the time-domain and giving direct access to the underlying kinetics allows for an intuitive analysis of that kinetics which is not interfered by any probably misleading *a priori* assumption. Moreover, the analysis of time-domain data using the phasor approach allows for the resolution of lifetime components contributing to the total kinetics which would otherwise not be resolved by the 'traditional ' fitting as there is no such indication from the shape of the fluorescence transient [132]. This special strength of the phasor approach is outlined in more detail in Appendix D.

4.7. Summary and Conclusion: The phasor approach to time domain measurements

The theory of the phasor approach has been introduced as a powerful tool for both, the visualization as well as the model-free analysis of fluorescence lifetime data. Although originally formulated for fluorescence lifetime measurements in the frequency domain, the basic formulation of the phasor approach for the time domain is now adapted to discrete fluorescence lifetime data extracted from streak camera measurements or alternatively resulting from time-correlated single photon counting (TCSPC).

A procedure for the calculation of the phasor coordinates was developed: In principle the calculation of the phasor coordinates is performed via Fourier transformation of the discrete fluorescence decay curve resulting from time domain measurements and additionally taking into account the length of the measured temporal window as well as the number of data points within this window. Furthermore, the correction of background fluorescence and the correction of the influence of a measured instrument response function (IRF) are taken into

account for the proposed procedure of phasor calculation. Moreover, the influence and importance of the transformation frequency and the harmonic number of the transformation have been discussed. The complete procedure of phasor calculation that is developed and outlined in this chapter and the subsequent analysis of lifetimes and their corresponding amplitudes has been implemented in a script written in Python™.

After calculation of the phasor coordinates, by plotting the phasors within a phasor plot the major strength of the phasor approach to fluorescence lifetime data is revealed: Fluorescence lifetimes and decay processes can be analyzed and identified by their phasors and their phasor positions within the phasor plot, respectively. Simple inspection of the plotted data by eye allows for a qualitative analysis of the data. The distinction of single exponential and multiexponential decays directly from the position of the phasors with respect to the universal semicircle is an intrinsic property of the phasor approach and the phasor plot. Moreover, the phasor approach also allows for quantitative analysis. The calculation of the contributing fluorescence lifetime components and their corresponding fractional contributions is described in detail for both, biexponential as well as triexponential kinetics.

In summary, the phasor approach allows for detailed investigation of the fluorescence kinetics of a sample based only on the measured data and giving access to both, qualitative as well as quantitative information of those kinetics. Moreover, phasor analysis allows for the resolution of the contributing lifetime components of a multiexponential kinetics that feature only a small fractional contribution, either resulting from a small value of the lifetime or a small relative amplitude or both. Such contributions to a multiexponential kinetics are mostly not accessible using the 'traditional' fitting approach.

5. Fluorescence kinetics of isolated B830 LH2 complexes of *Marichromatium purpuratum*

Isolated LH2 complexes of the purple bacterium *Marichromatium purpuratum* are studied in detergent solution (20 mM HEPES, 0.1% LDAO, pH 7.8) by time-resolved spectroscopy as outlined in Chapter 3.2. Upon excitation either into the higher energetic shoulder of the characteristic absorption spectrum in the NIR or excitation into the pronounced absorption band in the VIS, fluorescence emission is detected above 810 nm, as indicated by the red boxed region in Fig. 5.1.
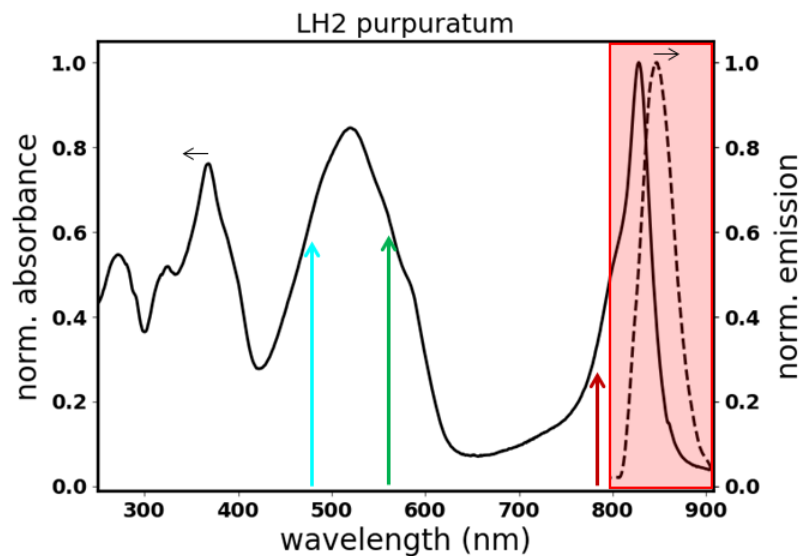
Figure 5.1.: Detection of the fluorescence emission upon excitation at different wavelengths: *The normalized absorption spectrum of the LH2 complex of Marichromatium purpuratum in detergent solution (20 mM HEPES, 0.1% LDAO, pH 7.8) is shown as solid line. The different excitation laser wavelengths of 485 nm, 560 nm and 790 nm are indicated by arrows of turquoise, green and red color, respectively. Fluorescence emission is detected above 810 nm as indicated by the red shaded region of the absorption spectrum. The normalized fluorescence emission spectrum is shown as dashed line. For details see text.*

Aim of the time-resolved experiments is to investigate the fluorescence kinetics of the light harvesting complexes and thus to obtain knowledge about its electronic structure. In the following, first the experimental parameters, such as the excitation fluence and the laser repetition rate, and the purpose of their variations are explained in detail. Next, the kinetics of the observed fluorescence transients are analyzed as a function experimental parameters using the phasor approach for each of the different excitation wavelength.

5.1. Experimental conditions for probing different situations of excitations

From previous studies on LH2 complexes of various species of purple bacteria it is known that all LH2 complexes studied so far follow a modular construction principle and have common features such as a ring-shaped arrangement of pigments, bacteriochlorophylls and carotenoids, hold in place by a protein scaffold, see Chapter 2. Besides the homology of apoprotein sequences for the B830 LH2 complex of *Mch. purpuratum* and the 'standard' LH2 complex of *Rps. acidophila*, reported before [94], the recently published structure of the B830 LH2 complex of *Mch. purpuratum* [96] confirms LH2 of *Mch. purpuratum* to fit into the generally accepted building scheme of LH2 complexes. Presumably, the electronic structure of the LH2 complex of *Rps. acidophila* can be used as a starting point for the investigation of the electronic structure of the B830 LH2 complex of *Mch. purpuratum*. Thus, for the following considerations the simplified energy level scheme of *Rps. acidophila* presented in Chapter 2 is adapted for the B830 LH2 complex of *Mch. purpuratum*.

The simplified energy level scheme that is expected for the B830 LH2 complex is shown in Fig. 5.2. As before, the excited states are shown as single energy levels, named ^{1}B800*, ^{1}B830* and ^{3}Car*. In analogy to the photophysics of LH2 of *Rps. acidophila* for the B830 LH2 complex of *Mch. purpuratum* it is assumed: Excitation laser light in the near-infrared, e.g. at a wavelength of 790 nm, is absorbed by the B800 bacteriochlorophyll *a* molecules.[1] Subsequently, the energy

---

[1]The possible excitation into the carotenoid absorption band of the LH2 complex is neglected for the moment. This simplification is valid due to the highly efficient carotenoid-to-bacteriochlorphyll energy transfer, resulting in excitation of the BChl *a* molecules within LH2 in similar manner as for direct excitation of BChl *a*, see Section 2.3.1. Thus, the considerations

is transferred to the excited ^{1}B830* state within approximately 1 ps [47]. Fluorescence emission occurs upon radiative relaxation to the B830 ground state within approximately 1 ns [1, 2]. Alternatively, the energy of the excited ^{1}B830* state can be transferred to the carotenoid triplet state ^{3}Car* via intersystem crossing within 10 ns [53, 76] and relaxes to the carotenoid ground state within 1.2 μs [57], which was reported as the lifetime value of the triplet state for the carotenoid okenon incorporated in the B830 LH2 complex of *Mch. purpuratum*.
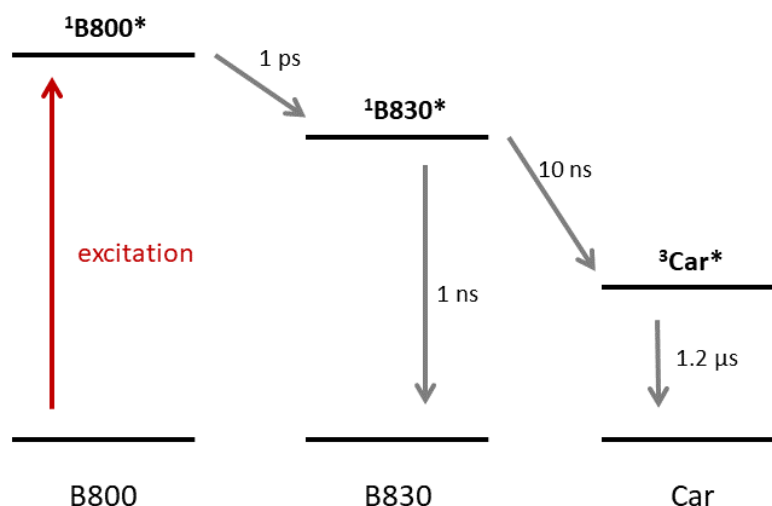
Figure 5.2.: Simplified energy level scheme of the B830 LH2 complex: *The excited states of the three groups of pigments, the B800 BChl a molecules, the B830 BChl a molecules and the Car molecules, are shown as single energy levels. The singlet excitation levels of the B800 and the B830 ring are denoted as ^{1}B800* and ^{1}B830*, respectively. The triplet state of the Car molecules is referred to as ^{3}Car*. Absorption of excitation light is depicted by the red arrow, downhill transitions between the distinct energy levels are depicted as grey arrows. For details see text and Chapter 2.*

Obviously, the energy transfer processes depicted in Fig. 5.2 occur on different timescales covering a range of several orders of magnitude. This allows for probing different situations of electronic excitations within the LH2 complex by choosing the excitation conditions properly. In this thesis the excitation conditions are determined by the variation of the excitation fluence and the variation of the laser repetition rate.

Variation of the excitation fluence, defined as the number of photons per pulse and area arriving at the sample, results in different numbers of excitations that

---

outlined next for excitation of BChl *a* is valid for excitation of carotenoids likewise.

are created in the LH2 complex. The created singlet excitations in the B830 bacteriochlorophylls delocalize over parts of the LH2 ring [51, 1, 48, 49, 50] and are known to be mobile along the ring. Thus, for high excitation fluences multiple singlet excitations within one LH2 ring can occur [61]. Due to their mobility, the singlet excitations can travel along the ring and meet each other. If this happens, singlet-singlet-annihilation (SSA) is possible to occur. Moreover, high excitation fluences can also lead to the formation of triplet excitations, see also Chapter 2. Those triplet excitations are reported to be almost immobile[2] and thus can be expected as localized on the carotenoid molecules. [63, 64, 65].

Variation of the laser repetition rate corresponds to different temporal separations between the excitation laser pulses. Hence, by increasing the laser repetition rate, which corresponds to shorter temporal separation between the pulses, the probability rises that an LH2 complex still carries an excitation resulting from the previous pulse. From the fast energy transfer processes within the LH2 complex and the carotenoid triplet lifetime in the order of microseconds it follows that these excitations resulting from a previous pulse must be triplet excitations. Thus, an increase of the laser repetition rate is expected to result in an increase of the probability for the occurrence of singlet-triplet-annihilation (STA) events. For the combination of high excitation fluences and high laser repetition rates, moreover, triplet-triplet-annihilation (TTA) might be possible when several triplet excitations occur within one LH2 ring.

Thus, experimental variation of the excitation photon fluence and the laser repetition rate allows to prepare several situations of electronic excitations within the LH2 complex and to probe various decay channels and annihilation processes. This principle is common practice for investigating the kinetics of electronic excitations [3, 69, 70] and should allow for detailed analysis of the electronic structure of the B830 LH2 complex of *Marichromatium purpuratum*.

---

[2]For triplet excitations the transfer of energy requires wavefunction overlap, hence triplet excitations are considered as rather immobile.

5.2. Excitation into the BChl *a* absorption band in the NIR (790 nm)

Experiments of time-resolved spectroscopy using a streak camera and an excitation laser wavelength of 790 nm are performed on isolated B830 LH2 complexes in detergent solution as a function of the excitation fluence and the laser repetition rate. For experimental details see Chapter 3: Materials and Methods.

For these experiments the excitation fluence is varied over more than one order of magnitude from $5 \cdot 10^{12}$, $1 \cdot 10^{13}$ to $1 \cdot 10^{14}$ photons/(pulse·cm²). In the further course of this thesis, sometimes these values for excitation fluences are denoted as '5E12', '1E13' and '1E14' without naming the units of photons per pulse and squared centimeters for reasons of abbreviation and smoother reading. The laser repetition rate is varied over three orders of magnitude ranging from 0.05 MHz, 0.5 MHz, 2 MHz, 8 MHz to 80 MHz, corresponding to temporal separations between two successive laser pulses of 20 μs, 2 μs, 500 ns, 125 ns and 12.5 ns, respectively. Table 5.1 shows the parameter combinations for which experiments with excitation wavelength of 790 nm are performed.

laser repetition	excitation fluence $\frac{photons}{pulse \cdot cm^2}$		
rate (MHz)	$5 \cdot 10^{12}$	$1 \cdot 10^{13}$	$1 \cdot 10^{14}$
0.05	-	-	+
0.5	-	+	+
2	o	+	+
8	o	+	+
80	+	+	+

***Table 5.1.: Variation of the excitation parameters for an excitation wavelength of 790 nm:** Time-resolved experiments are performed for all combinations of excitation parameters shown. For the different parameter situations the experiment gave a good signal (+), a weak signal (o) or no signal (-). For details see text.*

For excitation parameter combinations labeled with a minus sign in Table 5.1 no fluorescence emission is detectable as the fluorescence signal is too weak for the streak camera. Combinations marked with a neutral sign (o) indicate that a weak fluorescence emission is observed but no good signal-to-noise ratio is achieved for those experiments. For excitation parameter combinations labeled with a

plus sign, results with good signal-to-noise ratio are obtained. These parameter combinations are used to analyze the fluorescence kinetics of the isolated B830 LH2 complexes below.

5.2.1. Observed fluorescence kinetics

The fluorescence transients of isolated LH2 complexes of *Mch. purpuratum* resulting from excitation at 790 nm into the bacteriochlorophyll absorption band are shown as a function of the excitation parameters in Fig. 5.3. Only the fluorescence transients corresponding to those excitation parameter combinations labeled in green in Table 5.1 are shown. Each fluorescence transient is normalized to its maximum and plotted in semi-logarithmic scaling. Analogously to Table 5.1, the different columns in Fig. 5.3 correspond to different excitation fluences and different rows correspond to different laser repetition rates. Linear scaling on logarithmic scale reveals on first sight that all fluorescence transients have linear shapes thus indicating a monoexponential kinetics. In the literature monoexponential fluorescence kinetics are reported for isolated LH2 complexes of several other species of light harvesting purple bacteria [1, 2]. A more detailed quantitative analysis of the observed fluorescence transients is performed in the next section by using the phasor approach.
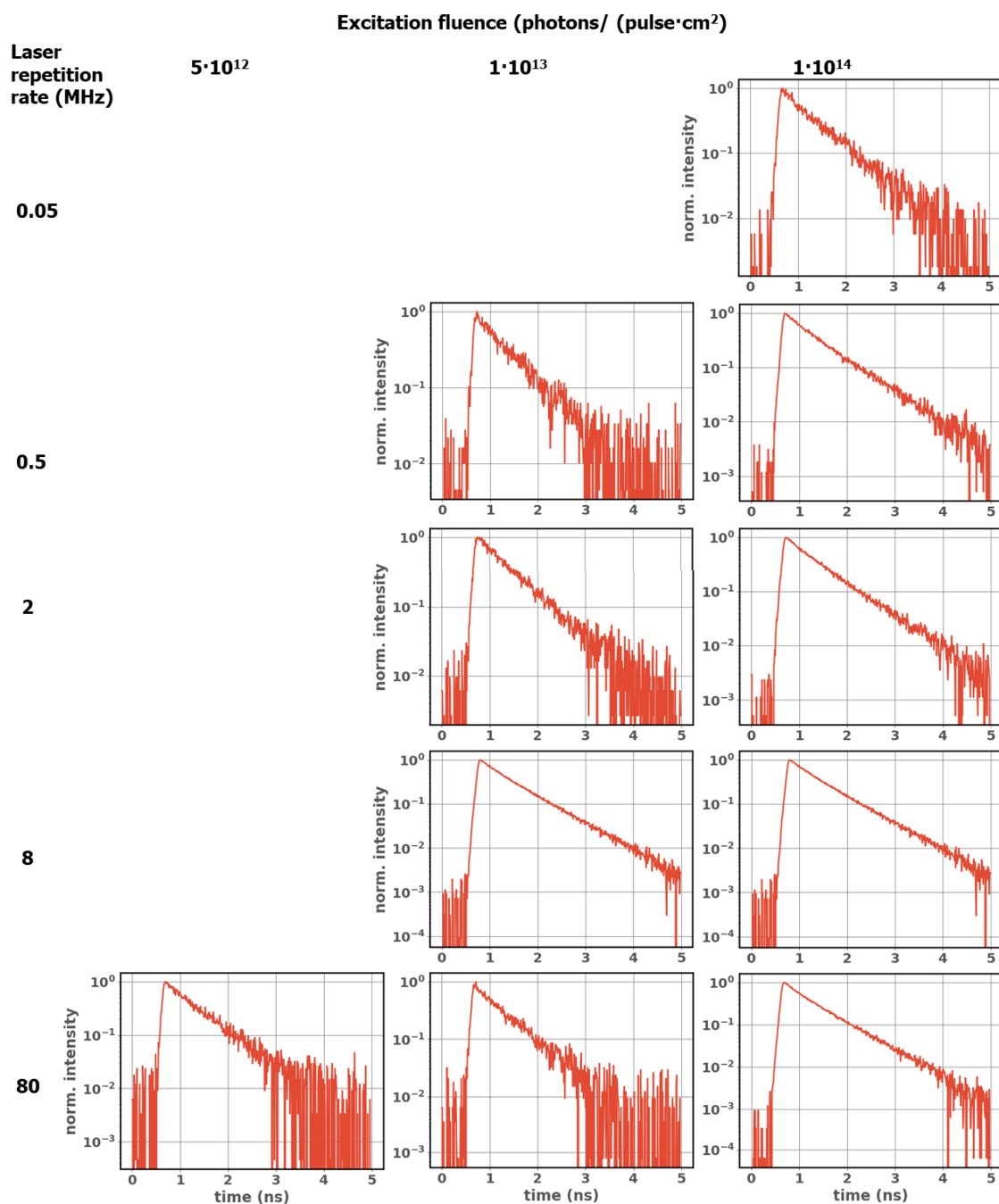
Figure 5.3.: Observed fluorescence transients of isolated B830 LH2 complexes upon excitation at 790 nm as a function of the excitation parameters: The normalized fluorescence transients of the isolated LH2 complexes of Mch. purpuratum are shown in semi-logarithmic scaling as a function of the excitation parameters. Different rows correspond to different laser repetition rates (increasing from top to bottom). Different columns correspond to different excitation fluences (increasing from left to right). For details see text.

91

5.2.2. Analysis of the observed fluorescence kinetics using the phasor approach

The phasor approach has been introduced and explained in detail in Chapter 4. The specific formulation for the time domain, that is developed there, is now applied on the measured fluorescence transients. All phasors shown in the following are calculated according to the procedure of phasor calculation visualized in the flow chart in Fig. 4.9. Thus, all phasors are already corrected for background fluorescence and the influence of the IRF. The harmonic number of the Fourier transformation used for the calculation of the phasor coordinates is chosen to $n = 5$ in order to achieve a reasonable scaling of the lifetime ruler along the universal semicircle as shown in Fig. 5.4. Choosing the harmonic number of the transformation to $n = 5$ corresponds to an effective increase of the transformation frequency of the Fourier transform[3].
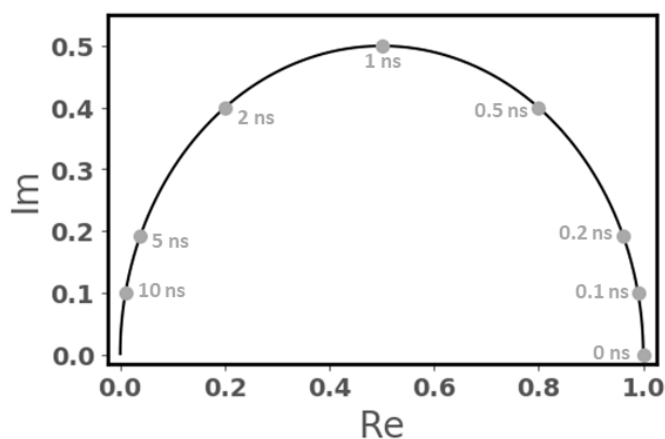
Figure 5.4.: Ruler of lifetimes: *Walking counterclockwise along the universal semicircle, the phasors corresponding to the lifetime values of 0 ns, 0.1 ns, 0.2 ns, 0.5 ns, 1 ns, 2 ns, 5 ns and 10 ns are shown.*

This ruler of lifetimes will be shown in all phasor plots from now on to allow for orientation within the phasor plot. For reasons of clarity only the grey dots will be shown, without labels.

---

[3]For time domain measurements the transformation frequency ω of the Fourier transform is in general a fixed value determined by the length of the temporal detection window, see also Section 4.3.1. A higher harmonic of the transformation corresponds to a transformation with an effective transformation frequency $\omega_{eff} = n \cdot \omega$.

The detailed analysis of the observed fluorescence transients given below focuses on different aspects: First, the situation corresponding to a low number of excitations within the LH2 complex is discussed. This situation occurs for low laser repetition rates, such as 0.05 MHz and 0.5 MHz. Next, the influence of an increase of the laser repetition rate is analyzed for moderate laser repetition rates (2 MHz and 8 MHz) and high laser repetition rates (80 MHz). Finally, the influence of a variation of the excitation fluence is discussed. Both, an increase of the laser repetition rate as well as an increase of the excitation fluence, correspond to situations with high numbers of electronic excitations within the LH2 complex.

Commentaries:

- All frequencies named in the following analysis of the fluorescence transient using the phasor approach and the accompanying figures refer to the laser repetition rates of the experiments and do <u>not</u> correspond to the transformation frequencies ω at which the phasor coordinates were calculated from the measured fluorescence transients.

- All phasors shown afterwards were calculated from the measured data as outlined above and thus are expected to have an uncertainty in their position within the phasor plot. Thus, phasors are shown with corresponding error bars when necessary. The estimation of uncertainties for the phasor positions within the phasor plot is given in detail in Appendix C.

Qualitative analysis of the calculated phasors

The phasor plots shown in Fig. 5.5 allow for a first qualitative analysis of the fluorescence kinetics of the B830 LH2 complex of *Marichromatium purpuratum*. The phasors that were calculated from the measured fluorescence transients are plotted in separate phasor plots for each of the categories of laser repetition rates, low, medium and high laser repetition rates, respectively. Whereas on the left hand side of Fig. 5.5 complete phasor plots are shown, on the right hand side a zoomed view allows for a more detailed inspection of the phasor positions. Evidently, the phasors corresponding to all measured fluorescence transients lie inside the universal semicircle. This clearly indicates a non-monoexponential kinetics for all excitation parameter combinations of the laser repetition rate and the excitation fluence.

93

Low laser repetition rates (0.05 MHz and 0.5 MHz)

Medium laser repetition rates (2 MHz and 8 MHz)

High laser repetition rate (80 MHz)
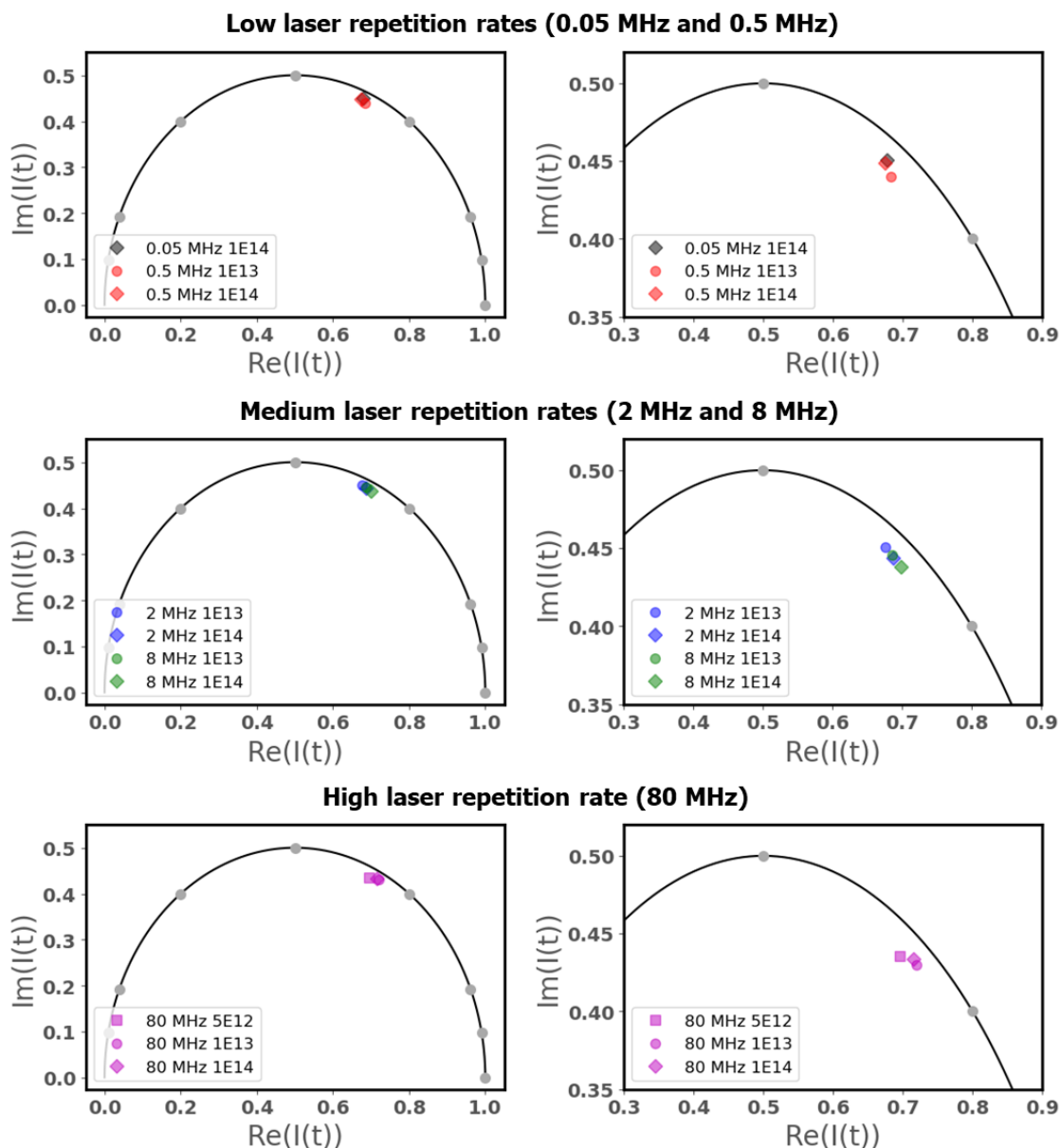
Figure 5.5.: Comparison of phasor positions in the phasor plot: *The calculated phasors corresponding to the measured fluorescence transients resulting from excitation at 790 nm are shown in single phasor plots for each of the different categories of laser repetition rates, low, medium and high repetition rates, respectively. On the left hand side the complete phasor plots are shown including a ruler of lifetimes (grey circles) counterclockwise corresponding to the lifetime values of 0 ns, 0.1 ns, 0.2 ns, 0.5 ns, 1 ns, 2 ns, 5 ns and 10 ns. On the right hand side zoomed views of the phasor plots allow for detailed inspection of the phasor positions. Different laser repetition rates are coded by color, different excitation fluences are coded by symbol. For details see text.*

Quantitative analysis

In Fig. 5.6 the phasors of all measured fluorescence transients of isolated LH2 complexes of *Marichromatium purpuratum* resulting from excitation at 790 nm are shown within one phasor plot in order to allow for comparison. For low laser repetition rates the phasors corresponding to the measured fluorescence transients show overlapping uncertainties of their phasor positions, whereas for increasing laser repetition rate and increasing excitation fluence a significant shift of the phasor positions is observed. Moreover, the phasors of the whole data set optically seem to align on a straight line, thus giving rise to the assumption of a biexponential decay, compare Section 4.5.1.
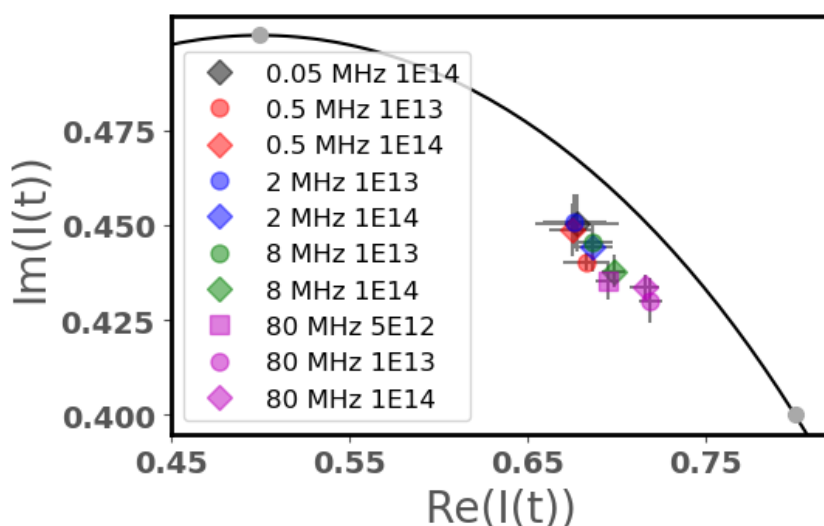
Figure 5.6.: Comparison of phasor positions in the phasor plot for excitation of BChl a: The calculated phasors corresponding to the measured fluorescence transients resulting from excitation at 790 nm are shown in one phasor plots together with their respective error bars to allow for comparison of the phasor positions. Different laser repetition rates are coded in color, different excitation fluences are coded by symbol. The two grey dots on the universal semicircle counterclockwise correspond to the values of 0.5 ns and 1 ns on the ruler of lifetimes. For details see text.

Although a first view on the phasors in Fig. 5.6 might indicate a biexponential kinetics for the measured fluorescence of the B830 LH2 complex, it has to be kept in mind that those phasors correspond to different situations of electronic excitations within the LH2 complex as their corresponding excitation parameter combinations differ significantly. This circumstance follows directly from the experimental approach of a well-aimed variation of the excitation parameters,

namely the excitation fluence and the laser repetition rate, in order to investigate the kinetics of electronic excitations within LH2, as outlined in detail in Section 5.1. Thus, assuming that the entire dataset of phasors follows one global biexponential kinetics, as one might identify by performing a linear fit to the group of phasors as outlined in Section 4.5.1, is not sufficient[4]. Rather, the experimental situation corresponding to a low number of electronic excitations within the LH2 complex, thus avoiding mostly any annihilation and quenching effects, can be used for determining the kinetics of the 'pure' and mostly undisturbed fluorescence response of the LH2 complex. This fluorescence kinetics can then be used as a starting point for the further analysis.

In order to allow for a consistent description of the entire dataset of the measured fluorescence transients of the B830 LH2 complexes upon excitation of BChl *a* a detailed analysis of the calculated phasors is performed below for the different categories of laser repetition rates. First, the biexponential kinetics for a low number of excitations within the LH2 complex is determined from the phasors corresponding to low laser repetition rates. For an excitation wavelength of 790 nm the situation of only a low number of electronic excitations within the LH2 corresponds to low laser repetition rates, which are 0.05 MHz and 0.5 MHz in this thesis. Next, this biexponential kinetics is kept fixed and for all other phasors it is checked if their phasor positions correspond to that biexponential kinetics or whether a third lifetime component is needed.

Low laser repetition rates: 0.05 MHz and 0.5 MHz

For low laser repetition rates, such as 0.05 MHz and 0.5 MHz, the temporal separation between the excitation laser pulses amounts to 20 μs and 2 μs, respectively. These temporal separations of the excitation laser pulses are larger than the timescales expected for the kinetics of the B830 LH2 complex of *Marichromatium purpuratum*, compare Section 5.1 and especially Fig. 5.2. Thus, for low laser repetition rates the measured fluorescence transients are expected to represent the fluorescence kinetics of the B830 LH2 complex corresponding to excitations resulting from only one excitation laser pulse.

---

[4]Moreover, a detailed global analysis of the phasors reveals an inhomogeneity within the dataset of phasors, thus showing that a consistent description using a global biexponential decay is not possible, see Appendix E.1.

In Fig. 5.7 the phasors corresponding to fluorescence transients measured at low laser repetition rates are shown in a phasor plot. Performing a linear fit reveals a biexponential decay with contributing lifetime components of 727 (+ 39/- 13) ps and 51 (+ 215/- 140) ps [5]. In the following these two lifetime components are referred to as 730 ps and 50 ps, which is valid with respect to the uncertainty interval. The biexponential decay is visualized as turquoise colored line in Fig. 5.7, contributing lifetime components are given by the intersections of the turquoise colored line with the universal semicircle.
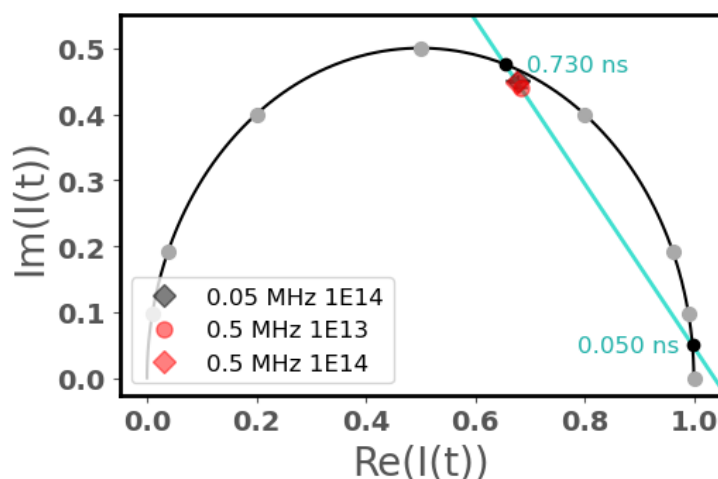
Figure 5.7.: Phasor plot of the biexponential kinetics at low laser repetition rates for excitation of BChl a: The phasors corresponding to the excitation parameter combinations 0.05 MHz and 1E14, 0.5 MHz and 1E13 and 0.5 MHz and 1E14 are shown. The laser repetition rate is coded by color (0.05 MHz: black, 0.5 MHz: red) and the excitation fluence is coded by different symbols (1E13: circle, 1E14: diamond). The turquoise colored line visualizes the biexponential kinetics resulting from the linear fit. The black circles correspond to their intersections with the universal semicircle and correspond to the two contributing lifetime components. A ruler of lifetimes is shown along the universal semicircle (grey circles). Counterclockwise the values 0 ns, 0.1 ns, 0.2 ns, 0.5 ns, 1 ns, 2 ns, 5 ns and 10 ns are shown. For details see text.

The fractional contributions of the two lifetime components are calculated by means of the lever rule, as outlined in Section 4.5.1, from the phasors corresponding to the measured fluorescence transients and the two phasors corresponding to the contributing lifetime components of the biexponential kinetics. The resulting values for the fractional contributions f_{730} and f_{50} are summarized in Table 5.2 as a function of the different excitation parameter combinations.

---

[5]The asymmetric values of the uncertainty of the lifetime components is due to the nonlinear scaling of the ruler of lifetimes along the universal semicircle, see also Appendix C.

excitation parameters	f_{730}	f_{50}
0.05 MHz and 1E14	0.94	0.06
0.5 MHz and 1E13	0.92	0.08
0.5 MHz and 1E14	0.94	0.06

Table 5.2.: Fractional contributions f_{730} and f_{50} of the biexponential fluorescence kinetics at low laser repetition rates

Evidently, at low laser repetition rates all excitation parameter combinations show a similar ratio of the fractional contributions of the two contributing lifetimes of the biexponential kinetics. On average the relative contributions the two lifetime components 730 ps and 50 ps amount to 0.93 and 0.07, respectively.

Medium laser repetition rates: 2 MHz and 8 MHz

For medium laser repetition rates of 2 MHz and 8 MHz the temporal separation between the excitation laser pulses is in the order of several hundreds of nanoseconds. As a consequence of the smaller temporal separation of the successive excitation laser pulses, a more complex situation of excitations within the B830 LH2 complex may appear. Namely, the probability that an LH2 complex carries an excitation resulting from a previous pulse increases with the excitation laser repetition rate, see also Section 5.1. Thus, for each fluorescence decay measured for medium laser repetition rates it is tested whether its corresponding phasor matches the biexponential kinetics found for low laser repetition rates within the limits of the uncertainties or not.

The phasors corresponding to the fluorescence transients detected for different excitation fluences and a laser repetition rate of 2 MHz are shown in Fig. 5.8 together with their error bars representing the uncertainties of the phasor positions. A zoomed view of the phasor plot is shown in order to compare the positions of the calculated phasors easily with the biexponential decay that was determined for low laser repetition rates in the last section. The biexponential kinetics with the contributing lifetimes of 730 ps and 50 ps obtained before for low laser repetition rates is visualized by the turquoise colored line, as before in Fig. 5.7. Additionally, as red and black lines the lines of minimum and maximum slope of the fitted parameters of the biexponential decay for low laser repetition rates are shown, respectively, to visualize the tolerance interval of the linear fit.

The grey circles on the universal semicircle are part of the ruler of lifetimes and show the phasors corresponding to the values 0.5 ns and 1 ns counterclockwise.

Figure 5.8.: Phasor plot for fluorescence transients measured at a laser repetition rate of 2 MHz: The phasors corresponding to the excitation parameter combinations 2 MHz and 1E13 and 2 MHz and 1E14 are shown. The excitation fluence is coded by different symbols (1E13: circle, 1E14: diamond). Additionally, the biexponential kinetics obtained for low laser repetition rates (compare Fig. 5.7) is shown as a straight line in turquoise color. In order to visualize the tolerance interval of the biexponential kinetics obtained for low laser repetition rates, in red and black color the lines with minimum and maximum slope within the uncertainty of the fit are shown. The grey circles correspond counterclockwise to the values 0.5 ns and 1 ns on the ruler of lifetimes. For detailed description see text.

The phasor corresponding to the excitation fluence of $1 \cdot 10^{13}$ photons/(pulse·cm^2), visualized by the blue circle symbol in Fig. 5.8, lies on the turquoise line representing the biexponential decay with the contributing lifetimes of 730 ps and 50 ps obtained for low laser repetition rates. Thus, the underlying kinetics is biexponential and features the same two contributing lifetimes. In contrast, the phasor corresponding to the parameter combination of an excitation fluence of $1 \cdot 10^{14}$ photons/(pulse·cm^2), visualized by the blue diamond symbol in Fig. 5.8, lies close to that turquoise colored straight line, but not exactly on that line. Nevertheless, its error bars overlap with the turquoise colored line as wells as the red line representing the tolerance interval of the biexponential kinetics obtained for low laser repetition rates. Thus, the underlying kinetics of the phasor corresponding to an excitation fluence of $1 \cdot 10^{14}$ photons/(pulse·cm^2) is also biexponential.

The fractional contributions of the two lifetime components of 730 ps and 50 ps as obtained for low laser repetition rates, are summarized in Table 5.3 for the different excitation fluences and a laser repetition rate of 2 MHz.

excitation parameters	f_{730}	f_{50}
2 MHz and 1E13	0.94	0.06
2 MHz and 1E14	0.92	0.08

Table 5.3.: Fractional contributions for the two lifetime components of 730 ps and 50 ps for the fluorescence kinetics at a laser repetition rate of 2 MHz

In addition to the experiments for a laser repetition rate of 2 MHz, experiments are also performed at a laser repetition rate of 8 MHz. The phasors corresponding to the measured fluorescence transients are shown with their corresponding error bars in Fig. 5.9 for different excitation fluences. As before, for a laser repetition rate of 2 MHz, a zoomed view of the phasor plot is shown in order to compare the positions of the calculated phasors easily with the biexponential decay observed for low laser repetition rates in the last section, again visualized by the turquoise colored line. The tolerance interval of the fitted biexponential decay is again visualized by the red and black lines corresponding to the lines with minimum and maximum slope within the fitted parameters. The grey circles on the universal semicircle are part of the ruler of lifetimes and show the phasors corresponding to the values 0.5 ns and 1 ns counterclockwise.

Notably, the phasors corresponding to a laser repetition rate of 8 MHz do not lie on the straight line corresponding to the biexponential decay but have a small deviation, see Fig. 5.9. For the phasor corresponding to the excitation fluence of $1 \cdot 10^{13}$ photons/(pulse·cm^2), visualized by the green circle symbol, the error bar overlaps with the turquoise colored line corresponding to the biexponential decay obtained for low laser repetition rates with contributing lifetimes of 730 ps and 50 ps. So, the underlying kinetics is also biexponential.
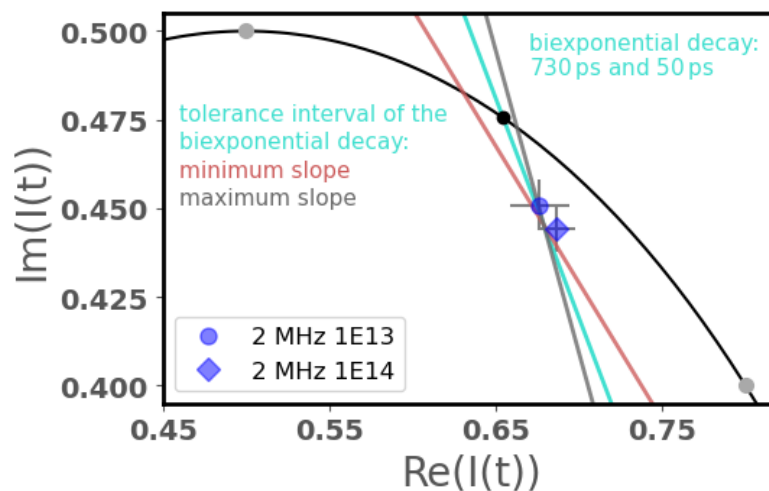
Figure 5.9.: Phasor plot for fluorescence transients measured at a laser repetition rate of 8 MHz: The phasors corresponding to the excitation parameter combinations 8 MHz and 1E13 and 8 MHz and 1E14 are shown. The excitation fluence is coded by different symbols (1e14: diamond, 1e13: circle). The biexponential decay obtained for low laser repetition rates (compare Fig. 5.7) is shown as a straight line in turquoise color. The lines in red and black color represent the lines of minimum and maximum slope within the fitted parameters and thus visualize the tolerance interval of the linear fit yielding the biexponential decay for low laser repetition rates. The grey circles correspond counterclockwise to the values 0.5 ns and 1 ns on the ruler of lifetimes. For detailed description see text.

In contrast, the phasor corresponding to an excitation photon fluence of $1 \cdot 10^{14}$ photons/(pulse·cm^2) is clearly separated from the turquoise colored line, see green diamond symbol Fig. 5.9. Moreover, it lies also clearly separated from tolerance interval of the biexponential kinetics, visualized by the red and black lines within the phasor plot. Hence, a biexponential kinetics is not sufficient and the underlying kinetics has most probably an additional contributing lifetime component, resulting in a triexponential kinetics, as already indicated in the qualitative analysis above. For the analysis of this triexponential kinetics it is assumed that the biexponential kinetics observed for low laser repetition rates is preserved when the laser repetition rate is increased to 8 MHz. Therefore, the biexponential decay is expanded to a triexponential decay by adding a third, yet unknown lifetime component while keeping the two lifetime components of the biexponential kinetics fixed. The algorithm for the calculation of such a triexponential kinetics is introduced and outlined in detail in Section 4.5.3. The results of the calculations, such as the values of the third lifetime component and the fractional contributions of all three contributing lifetime components,

are summarized in Table 5.4 for the different excitation parameter combinations.

excitation parameters	f_{730}	f_{50}	τ_{third} [ps]	f_{third}
8 MHz and 1E13	0.92	0.08		
8 MHz and 1E14	0.78	0.06	490	0.16

Table 5.4.: Calculated third lifetime component and fractional contributions of the contributing lifetimes for the fluorescence kinetics at a laser repetition rate of 8 MHz

High laser repetition rate: 80 MHz

For the highest laser repetition rate of 80 MHz, a situation with multiple electronic excitations within the LH2 complex may occur. Due to the short time interval of only 12.5 ns between the excitation laser pulses, it is highly probable that an LH2 complex still carries a triplet excitation resulting from the prior excitation laser pulse, as already mentioned in Section 5.1. Thus, a complex situation of both, singlet excitations as well as triplet excitations within the LH2 complex is possible.

The phasors corresponding to the fluorescence transients measured for different excitation fluences and a laser repetition rate of 80 MHz are shown in Fig. 5.10. As before, for the laser repetition rates 2 MHz and 8 MHz, a zoomed view of the phasor plot is shown to compare the positions of the calculated phasors with the biexponential decay that was analyzed for low laser repetition rates. The biexponential kinetics with the contributing lifetimes of 730 ps and 50 ps corresponding to a low number of excitations within the LH2 complex is again visualized by the turquoise colored line. The tolerance interval of the fitted biexponential decay is also again visualized by the red and black lines corresponding to the lines with minimum and maximum slope within the fitted parameters. The grey dots on the universal semicircle are part of the ruler of lifetimes and show the phasors corresponding to the values 0.5 ns and 1 ns counterclockwise.
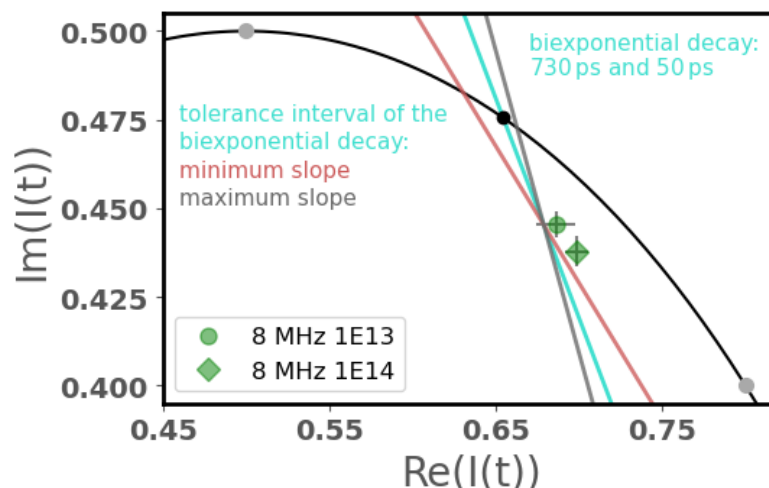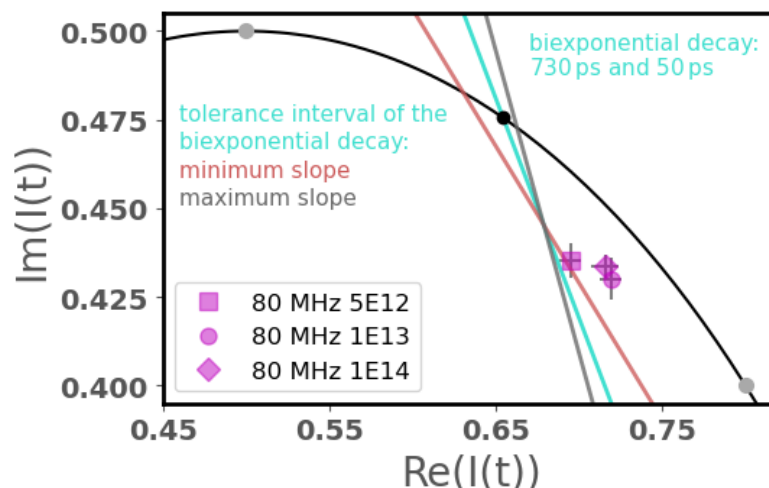
Figure 5.10.: Phasor plots for fluorescence transients measured at 80 MHz: *The phasors corresponding to the excitation parameter combinations 80 MHz and 5E12, 80 MHz and 1E13 and 80 MHz and 1E14 are shown. The excitation fluence is coded by different symbols (5E12: square, 1E13: circle, 1E14: diamond). Additionally, the biexponential kinetics obtained for low laser repetition rates (compare Fig. 5.7) is shown as a straight line in turquoise color. The lines in red and black color represent the lines of minimum and maximum slope within the fitted parameters nd visualize the tolerance interval of the linear fit. The grey circles correspond counterclockwise to the values 0.5 ns and 1 ns on the ruler of lifetimes. For detailed description see text.*

The square symbol of the phasor corresponding to the smallest excitation fluence of $5 \cdot 10^{12}$ photons/(pulse·cm^2) lies close to the turquoise colored line representing the biexponential kinetics with the contributing lifetimes of 730 ps and 50 ps obtained for low laser repetition rates, see Fig. 5.10. Moreover, it overlaps with the red line visualizing the tolerance interval of the biexponential fit. Thus, its underlying kinetics is assumed to be biexponential. In contrast, the phasors of the other two excitation fluences clearly do not lie within or close to the tolerance interval of the fitted biexponential decay obtained for low laser repetition rates. The deviation from the turquoise colored line representing the biexponential decay is the more pronounced for increasing excitation fluence and is significantly larger than for the excitation fluences $1 \cdot 10^{13}$ and $1 \cdot 10^{14}$ photons/(pulse·cm^2) at lower laser repetition rates, compare Fig. 5.8 and Fig. 5.9. Thus, a triexponential kinetics can be expected. In analogy to the considerations above for 8 MHz, it is assumed that the biexponential kinetics observed for low laser repetition rates is preserved when increasing the laser repetition rate to 80 MHz.

Hence, analogously to the calculations for medium laser repetition rates in the

previous section, the third contributing lifetime component as well as the relative fractional intensity contributions of the lifetime components can be calculated according to Section 4.5.3. The resulting values are summarized in Table 5.5 for the different excitation fluences and a laser repetition rate of 80 MHz.

excitation parameters	f_{730}	f_{50}	τ_{third} [ps]	f_{third}
80 MHz and 5E12	0.90	0.1		
80 MHz and 1E13	0.63	0.05	500	0.33
80 MHz and 1E14	0.6	0.05	520	0.35

Table 5.5.: Calculated third lifetime component and fractional contributions of all three lifetime components for the fluorescence kinetics at a laser repetition rate of 80 MHz

For the higher excitation photon fluences of $1 \cdot 10^{13}$ photons/(pulse·cm^2) and $1 \cdot 10^{14}$ photons/(pulse·cm^2) a triexponential kinetics is revealed by phasor analysis, whereas for the lowest excitation fluence of $5 \cdot 10^{12}$ photons/(pulse·cm^2) a biexponential kinetics is observed. Notably, the value of the third contributing lifetime component increases from 500 ps to 520 ps with increasing excitation fluence. The corresponding fractional contributions of the third lifetime component are in the same order of magnitude of 30 %, which is well above the respective value found for the triexponential kinetics at 8 MHz before.

Variation of the excitation fluence

The analysis of the detected fluorescence transients above focused on the influence of the laser repetition rates, determining the temporal separation between the excitation laser pulses. Nevertheless, the analysis also included some information about the influence of the excitation fluence. The excitation fluence is defined as the number of photons that arrives at the sample per pulse and area. Thus, it determines the number of excitations that are created within the LH2 complex per excitation pulse. For all laser repetition rates a significant shift of the phasor positions can be seen upon variation of the excitation fluences, compare Fig. E.1 as well as Figures 5.8-5.10. Especially for higher laser repetition rates, such as 2 MHz, 8 MHz and 80 MHz, the phasors corresponding to high excitation fluences of $1 \cdot 10^{14}$ photons/(pulse·cm^2) tend to shift towards shorter lifetimes clockwise along the universal semicircle. Thus, a variation of the excitation photon fluences, resulting in a variation of the number of electronic

excitations created within the LH2 complex per excitation laser pulse, strongly influences the observed fluorescence kinetics.

5.2.3. Summary of the fluorescence kinetics of isolated B830 complexes observed for excitation of BChl *a*

The fluorescence transients of isolated LH2 complexes from *Mch. purpuratum* in detergent-solution were measured for different combinations of the excitation fluence and the laser repetition rate for excitation of the BChl *a* molecules at 790 nm and analyzed. A first inspection of the fluorescence transients by eye indicates a monoexponential kinetics as reported previously in literature for isolated LH2 complexes of various other species of bacteria [1, 2]. A more detailed analysis of the observed fluorescence transients was then performed using the phasor approach, as introduced in detail in Chapter 4. The special strength of the phasor approach is, that this method allows for the analysis of the fluorescence kinetics without any a priori knowledge or assumption. A first qualitative analysis using the phasor approach surprisingly revealed a multiexponential kinetics for all measured fluorescence transients of isolated LH2 complexes from *Marichromatium purpuratum*. In order to determine the distinct values of the contributing lifetimes and their fractional contributions of this multiexponential kinetics, a quantitative analysis of the phasors calculated from the measured fluorescence transients was performed.

Considering the fact that a well-aimed variation of excitation parameters, namely a variation of the laser repetition rate as well as the excitation photon fluence, may result in different situations of electronic excitations within an LH2 complex a global biexponential kinetics, which is the most simple case of a multiexponetial kinetics, is not sufficient for a consistent description of the entire data set of phasors. Thus, the excitation situation corresponding to the most unperturbed fluorescence response, avoiding any annihilation and quenching effects as best as possible, which corresponds to the fluorescence transients measured at low laser repetition rates was chosen as a starting point for the further analysis. For low laser repetition rates of 0.05 MHz and 0.5 MHz a biexponential kinetics was observed. The contributing lifetime components were identified to amount to the values of 730 ps and 50 ps which have on average the fractional contributions of 0.93 and 0.07, respectively. When increasing the laser repetition rate

to 2 MHz still a biexponential kinetics was found, but turning to 8 MHz and finally to 80 MHz the occurrence of a third lifetime component was observed for the higher excitation fluences. In order to resolve that triexponential kinetics it was assumed that the biexponential kinetics corresponding to the most simple situation of excitations within the LH2 complex is always included in the triexponential kinetics. So, the biexponential decay observed for low laser repetition rates was expanded by adding a further lifetime component and the third contributing lifetime component as well as the fractional contributions of all three lifetime components were calculated. Thus, in total a mixed multiexponential kinetics consists of a mixing of either of two or three exponentials was revealed for the measured data set.

The calculated values for the contributing lifetime components and their fractional contributions are summarized in Table 5.6 as a function of the excitation photon fluence and the laser repetition rate. The accuracy of the number values of the fractional contributions is ± 0.03.

laser repetition rate (MHz)	excitation fluence $\frac{photons}{pulse \cdot cm^2}$		
	$5 \cdot 10^{12}$	$1 \cdot 10^{13}$	$1 \cdot 10^{14}$
0.05			730 ps (0.94)
			50 ps (0.06)
0.5		730 ps (0.92)	730 ps (0.94)
		50 ps (0.08)	50 ps (0.06)
2		730 ps (0.94)	730 ps (0.92)
		50 ps (0.06)	50 ps (0.08)
8		730 ps (0.92)	730 ps (0.78)
		50 ps (0.08)	50 ps (0.06)
			490 ps (0.16)
80	730 ps (0.90)	730 ps (0.63)	730 ps (0.60)
	50 ps (0.1)	50 ps (0.05)	50 ps (0.05)
		500 ps (0.33)	520 ps (0.35)

Table 5.6.: Calculated lifetime components and their fractional contributions for the multiexponential kinetics of isolated LH2 complexes from Marichromatium purpuratum upon excitation of bacteriochlorophyll pigments at different excitation parameter combinations

In analogy to previous tabular arrangements in this thesis, different columns

correspond to different excitation fluences (increasing from left to right) and different rows correspond to different laser repetition rates (increasing from top to bottom). For each measured fluorescence transient the calculated contributing lifetime components of the multiexponential kinetics are shown. The fractional contributions of the lifetime components are represented in brackets. For the triexponential kinetics found at 8 MHz and 80 MHz it can be seen in Table 5.6 that the third lifetime component is in the order of 500 ps for all parameter combinations of the excitation fluence and the laser repetition rate. Moreover, significant changes of the fractional contributions of the distinct lifetimes can be seen upon variation of the excitation parameters. In order to investigate and also visualize these changes of the fractional contributions in more detail, the fractional contributions are plotted in Fig. 5.11 as a function of the excitation density, defined as the product of the laser repetition rate and the excitation fluence.
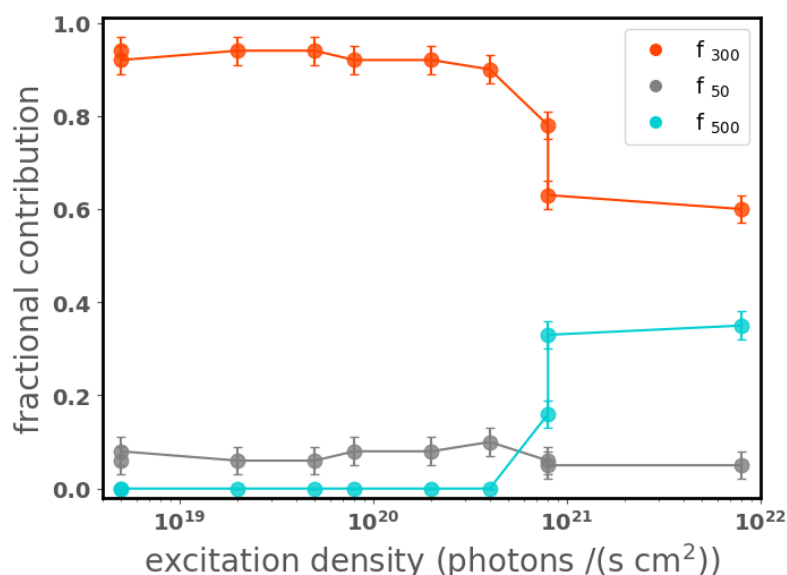
Figure 5.11.: Changes of the fractional contributions for the multiexponential kinetics with either two or three exponentials (visualization of Table 5.6): The fractional contributions of the three lifetime components are plotted as a function of the excitation density. In order to allow for comparison biexponential kinetics are represented with a third lifetime component with a fractional contribution equal to zero. The excitation density is defined as the product of the laser repetition rate and the excitation fluence. For details see text.

The different excitation parameter combinations of the laser repetition rate and the excitation fluence for which fluorescence transients were detected in the

experiments correspond to different values of the excitation density. As the product of a laser repetition rate of 8 MHz and an excitation fluence of $1 \cdot 10^{14}$ photons/(pulse·cm^2) yields the same value as the product of 80 MHz and an exitation fluence of $1 \cdot 10^{13}$ photons/(pulse·cm^2), the resulting excitation density shows two entries for each of the fractional contributions at a value of $8 \cdot 10^{20}$ photons/(s·cm^2).

Notably, the fractional contribution f_{50} of the shortest lifetime component of 50 ps, which is included in the kinetics of all fluorescence transients, is in the same order of magnitude for all excitation parameter combinations and shows no significant changes within the limits of accuracy. In contrast, the fractional contributions of the other two contributing lifetimes, f_{730} and f_{500}, show variations for the different excitation parameter combinations. Whereas the fractional contribution f_{730} is almost constant within the limits of accuracy up to an excitation density of $3 \cdot 10^{20}$ photons/(s ·cm^2) and decreases then tremendously. It can be clearly recognized from Table 5.6 as well as Fig. 5.11 that the 500 ps lifetime component only appears at laser repetition rates of 8 MHz and higher. The fractional contribution of this third lifetime component, f_{500}, increases up to more than 0.3 when changing from a laser repetition rate from 8 MHz to 80 MHz, which corresponds to a reduction of the temporal separation between the excitation laser pulses by a factor of 10. Concomitantly the fractional contribution f_{730} of the longest lifetime component of 730 ps decreases analogously from more than 90% to 60% upon increasing the laser repetition rate.

5.3. Excitation into the carotenoid absorption band in the VIS

In addition to the experiments using the absorption properties of the bacteriochlorophyll pigments within the B830 LH2 complex *Mch. purpuratum*, outlined in detail in the previous section, also further experiments are conducted taking advantage of the light-harvesting properties of the carotenoid pigments as well a the highly efficient carotenoid-to-bacteriochlorophyll energy transfer within LH2. These experiments of time-resolved spectroscopy using the technique of time-correlated single photon counting (TCSPC) are performed on isolated B830 LH2 complexes in detergent solution as a function of the excitation fluence and

the laser repetition rate. Two different excitation laser wavelength, 485 nm and 560 nm, both resonant with the pronounced carotenoid absorption band in the absorption spectrum of the LH2 complex from *Mch. purpuratum*, see Fig. 5.1, were used for the experiments. For experimental details see Chapter 3: Materials and Methods.

5.3.1. Excitation into the carotenoid absorption band: excitation wavelength 485 nm

For the experiments using an excitation laser wavelength of 485 nm the excitation fluence is varied over more than one order of magnitude from $5 \cdot 10^{12}$, $1 \cdot 10^{13}$, $5 \cdot 10^{13}$ to $1 \cdot 10^{14}$ photons/(pulse·cm^2). As mentioned before sometimes these values for excitation fluences are denoted as '5E12', '1E13', '5E13' and '1E14' without naming the units of photons per pulse and squared centimeters for reasons of abbreviation and smoother reading. The laser repetition rate is varied over three orders of magnitude ranging from 0.5 MHz, 2 MHz, 8 MHz, 20 MHz to 40 MHz, corresponding to temporal separations between two successive laser pulses of 2 μs, 500 ns, 125 ns, 50 ns and 25 ns, respectively. Table 5.7 shows the parameter combinations for which experiments with an excitation wavelength of 485 nm are performed.

laser repetition rate (MHz)	excitation fluence $\frac{photons}{pulse \cdot cm^2}$			
	$5 \cdot 10^{12}$	$1 \cdot 10^{13}$	$5 \cdot 10^{13}$	$1 \cdot 10^{14}$
0.5	-	-	+	+
2	-	+	+	+
8	+	+	+	+
20	+	+	+	+
40	+	+	+	+

***Table 5.7.: Variation of the excitation parameters for an excitation wavelength of 485 nm:** Time-resolved experiments are performed for all combinations of excitation parameters shown. For the different parameter situations the experiment gave a either a good signal (+) or a weak signal(-). For details see text.*

For excitation parameter combinations labeled with a minus sign in Table 5.7 only a very weak signal, showing almost no fluorescence emission, is detected by

the confocal microscope. For excitation parameter combinations labeled with a plus sign, results with good signal-to-noise ratio are obtained. These parameter combinations, highlighted in green color in the table, are used to analyze the fluorescence kinetics of the isolated B830 LH2 complexes upon excitation of the carotenoid pigments.

Observed fluorescence kinetics

The fluorescence transients measured for the excitation parameter combinations labeled in green in Table 5.7 all feature a similar shape[6]. Exemplarily the fluorescence transient for the excitation parameter combination of a laser repetition rate of 2 MHz and an excitation photon fluence of $1 \cdot 10^{14}$ photons/(pulse·cm^2), resulting from excitation of the carotenoid molecules at 485 nm, is shown in Fig. 5.12.
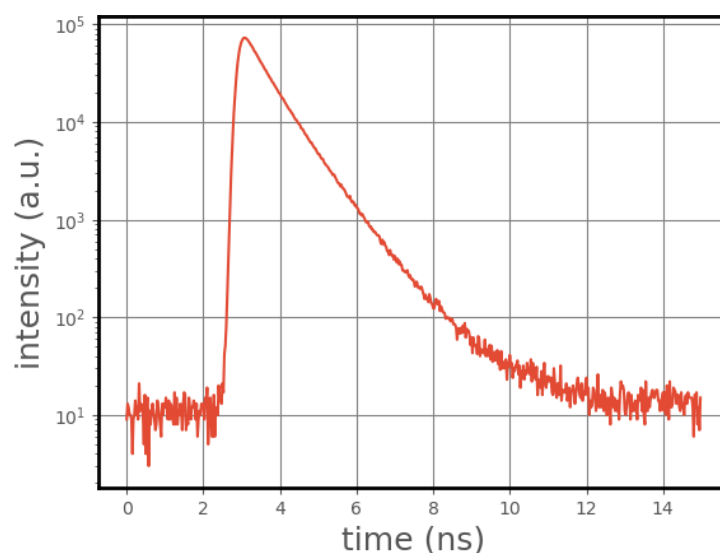
Figure 5.12.: Fluorescence transient of detergent-isolated LH2 complexes from Mch. purpuratum resulting from excitation into the carotenoid absorption band at 485 nm *The fluorescence transient corresponding to the excitation parameter combination of 2 MHz laser repetition rate and an excitation fluence of $1 \cdot 10^{14}$ photons/(pulse·cm^2) is shown in semi-logarithmic scaling. For detailed description see text.*

The almost linear shape[7] of the fluorescence decay curve in semi-logarithmic

---

[6]A table showing all the measured fluorescence transient for an excitation wavelength of 485 nm, similar to Fig. 5.3, is given in Appendix E.2.

[7]Considering the fact that the FWHM of the IRF was 264 ps at this excitation wavelength, see Chapter Material and Methods, the shape of the transient is considered as linear.

scaling indicates a monoexponential kinetics as reported for isolated LH2 complexes of several other species of light harvesting purple bacteria [1, 2] in the literature before. A more detailed analysis of the measured fluorescence transients using the phasor approach is given below.

Analysis of the observed fluorescence kinetics using the phasor approach

The measured fluorescence transients resulting from excitation of carotenoid molecules at 485 nm were analyzed using the phasor approach as this was done for data resulting from excitation of bacterichlorophylls before. All phasors shown in the following are calculated according to the procedure of phasor calculation outlined in detail in Chapter 4 and visualized in the flow chart in Fig. 4.9. Thus, all phasors are already corrected for background fluorescence and the influence of the IRF. The harmonic number of the Fourier transformation used for the calculation of the phasor coordinates is chosen to $n = 5$. A ruler of lifetimes, counterclockwise featuring the lifetime values of 0 ns, 0.1 ns, 0.2 ns, 0.5 ns, 1 ns, 2 ns, 5 ns and 10 ns, will be shown in all phasor plots from now on in order to allow for orientation along the universal semicircle. For reasons of clarity only the grey dots will be shown, without labels.

The <u>commentaries</u> given for phasor plots in Section 5.2 remain valid:

- All frequencies named in the following analysis of the fluorescence transient using the phasor approach and the accompanying figures refer to the laser repetition rates of the experiments and do <u>not</u> correspond to the transformation frequencies ω at which the phasor coordinates were calculated from the measured fluorescence transients.

- All phasors shown afterwards were calculated from the measured data and thus are expected to have an uncertainty in their position within the phasor plot. Thus, phasors are shown with corresponding error bars when necessary. The estimation of uncertainties for the phasor positions within the phasor plot is given in detail in Appendix C.

In the following, first, a qualitative analysis of the phasors corresponding to the measured fluorescence transient is given. Next, a quantitative analysis using the phasor approach is performed.

Qualitative analysis

The phasor plot featuring the phasors corresponding to the measured fluorescence transients is shown in Fig. 5.13 and allows for a first qualitative analysis of the underlying kinetics. In the zoomed view of the phasor plot it is clearly visible that all phasors lie inside the universal semicircle. Thus, the kinetics underlying the phasors calculated from the measured fluorescence transients is a multiexponential kinetics.
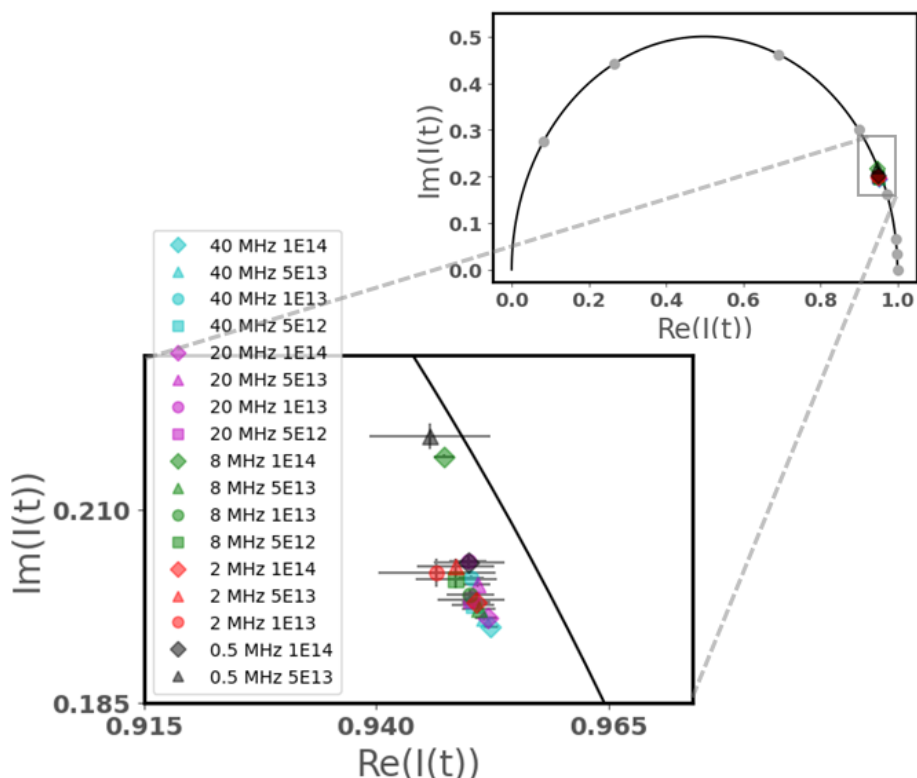
***Figure 5.13.: Phasor plot for fluorescence transients of LH2 Mch. purpuratum resulting from excitation into the carotenoid absorption band at 485 nm** The phasors corresponding to fluorescence transients measured at different excitation parameter combinations of excitation photon fluence and laser repetition rate are shown in a phasor plot. Both, a total view as well as a zoomed view are shown. The excitation fluence is coded by different symbols (5E12: square, 1E13: circle, 5E13: triangle, 1E14: diamond), different laser repetition rates are coded by color. The grey circles on the universal semicircle correspond counterclockwise to the values 0 ns, 0.1 ns, 0.2 ns, 0.5 ns, 1 ns, 2 ns, 5 ns and 10 ns on the ruler of lifetimes. For detailed description see text.*

Quantitative analysis

From the first qualitative analysis of the phasors a multiexponential kinetics is indicated. Thus, as the simplest case of a multiexponential kinetics a global biexponential decay might be taken into consideration. However, as discussed in detail in Section 5.2 the assumption of a gobal biexponential will not allow for a consistent description of the entire data set. Namely, it was the aim of the experiments to experimentally probe different situation of electronic excitations within the LH2 complex, resulting in different fluorescence responses in order to investigate the kinetics of electronic excitations and thus the electronic structure of the B830 LH2 complex of *Mch. purpuratum*. Consequently, a global biexponential kinetics that does not take into account the different situations of electronic excitations within the LH2 complex is not suitable. Thus, in analogy to the procedure of analysis of the fluorescence kinetics resulting from excitation of the bacteriochlorophylls, a more detailed analysis has to be performed:

First, the situation corresponding to a low number of excitations within the LH2 complex is considered. This situation occurs for low laser repetition rates, such as 0.5 MHz and 2 MHz, which were the lowest possible laser repetition rates for experiments featuring an excitation wavelength of 485 nm. Due to the temporal separation of the excitation laser pulses of 2 μs and 500 ns, respectively, the measured fluorescence transients are expected to represent the fluorescence kinetics corresponding to excitations resulting from only one excitation laser pulse and thus the most 'pure' fluorescence response. Assuming a biexponential kinetics for low laser repetition rates and evaluation of the calculated phasors as described in detail in Section 4.5.1, yields fluorescence lifetime values of 750 ps (+ 123 /- 26) ps and 11 ps (+ 320 /- 179) ps [8]. In the following these two lifetime components are referred to as 750 ps and 10 ps, which is valid with respect to the uncertainty interval. The linear fit to the phasors revealing that biexponential kinetics is visualized as turquoise colored line in Fig. 5.14. Contributing lifetime components are given by intersections of the turquoise colored line with the universal semicircle.

---

[8]The asymmetric values of the uncertainty of the lifetime components is due to the nonlinear scaling of the ruler of lifetimes along the universal semicircle, see also Appendix C
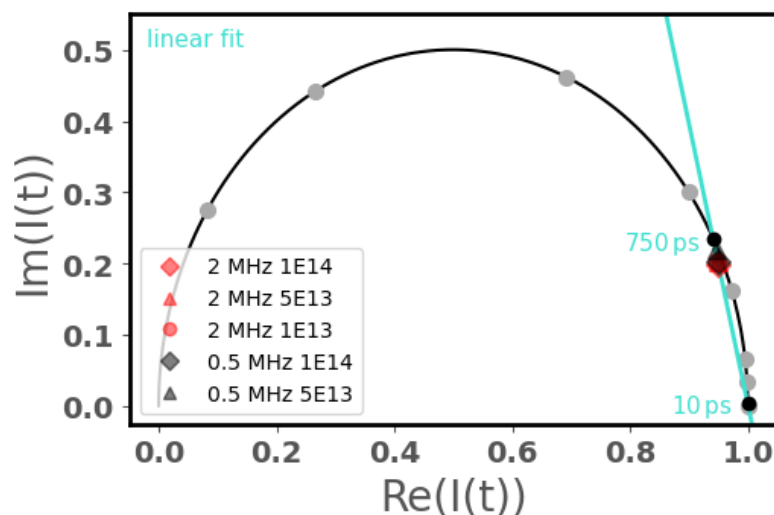
Figure 5.14.: Phasor plot of the biexponential kinetics at low laser repetition rates for excitation of carotenoid molecuels at 485 nm *The phasors corresponding to the fluorescence transients measured at 0.5 MHz and 2 MHz are shown. The laser repetition rate is coded by color, the excitation fluence is coded by different symbols. The turquoise colored line visualizes the biexponential decay resulting from the linear fit, the black circles correspond to the intersections with the universal semicircle giving the two contributing lifetime components. Along the universal semicircle a ruler of lifetimes counterclockwise featuring the values 0 ns, 0.1 ns, 0.2 ns, 0.5 ns, 1 ns, 2 ns, 5 ns and 10 ns is shown (grey circles). For detailed description see text.*

Next, the influence of an increase of the laser repetition rate on the observed fluorescence transients and thus the measured fluorescence kinetics is analyzed for the laser repetition rates 8 MHz, 20 MHz and 40 MHz. An increase of the laser repetition rates correspond to smaller temporal separations of the excitation laser pulses and more complex situations of electronic excitations within the B830 LH2 complex of *Mch. purpuratum* may occur, possibly resulting in a more complex fluorescence response. In Fig. 5.15 the phasors corresponding to the fluorescence transients measured at laser repetition rates 8 MHz, 20 MHz and 40 MHz are shown. In order to allow for comparison with the biexponential kinetics observed for low laser repetition rates, this biexponential kinetics is visualized as turquoise colored line, as before in Fig. 5.14. The tolerance interval of the biexponential kinetics is visualized by the red and black lines representing the lines of minimum and maximum slope, respectively, as obtained from fitting of the kinetics for low laser repetition rates.
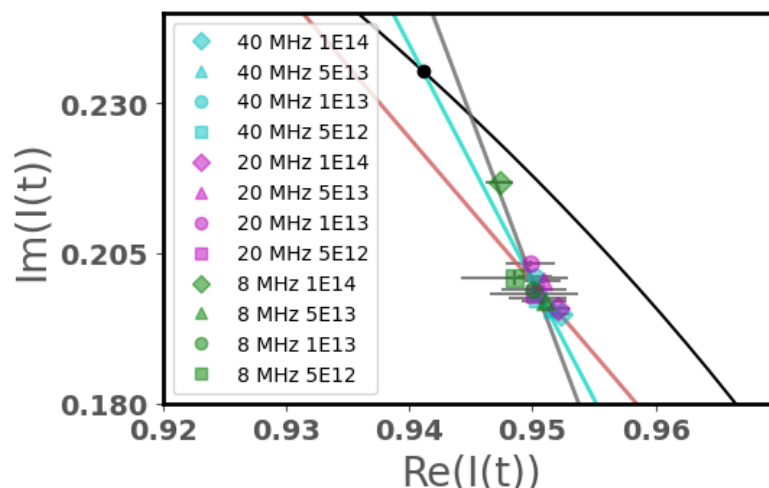
Figure 5.15.: Phasors corresponding to fluorescence transients at laser repetition rates 8 MHz, 20 MHz and 40 MHz resulting from excitation into the carotenoid absorption band at 485 nm The phasors calculated from the measured fluorescence transients are shown for different excitation fluences at laser repetition rates of 8 MHz, 20 MHz and 40 MHz. The excitation fluence is coded by different symbols, different laser reptition rates are coded by color. Additionally, the biexponential kinetics obtained for low laser repetition rates (compare Fig. 5.14) is visualized as a straight line in turquoise color. The lines in red and black color represent the lines of minimum and maximum slope and visualize the tolerance interval of the biexponential kinetics. For detailed description see text.

As can be clearly seen in Fig. 5.15, the phasors calculated from the measured fluorescence transients agree well with the biexponential kinetics with lifetime components of 750 ps and 10 ps obtained for low laser repetition rates. All the phasor, coding different laser repetition rates by color and different excitation fluences by symbol, overlap with the turquoise colored line representing the biexponential kinetics itself or with the tolerance interval of that biexponential kinetics, spanned by the red and black lines of minimum and maximum slope, respectively. Thus, the biexponential kinetics observed for low laser repetition rates allows for description of the fluorescence kinetics of the B830 LH2 complex upon excitation of carotenoids at 485 nm for all excitation parameter combinations of laser repetition rate and excitation fluence.

According to the procedure outlined before in Section 4.5.1 the fractional contributions of both lifetimes components are determined and summarized in Table 5.8 as a function of the excitation parameters, laser repetition rate and excitation fluence. Different rows correspond to different laser repetition rates

increasing from top to bottom, different columns correspond to different excitation fluences increasing from left to right. The accuracy of the number values of the fractional contributions is ±0.02.

laser repetition	excitation fluence $\frac{photons}{pulse \cdot cm^2}$			
rate (MHz)	$5 \cdot 10^{12}$	$1 \cdot 10^{13}$	$5 \cdot 10^{13}$	$1 \cdot 10^{14}$
0.5			750 ps (0.93)	750 ps (0.86)
			10 ps (0.07)	10 ps (0.14)
2		750 ps (0.86)	750 ps (0.86)	750 ps (0.84)
		10 ps (0.14)	10 ps (0.14)	10 ps (0.16)
8	750 ps (0.85)	750 ps (0.84)	750 ps (0.83)	750 ps (0.92)
	10 ps (0.15)	10 ps (0.16)	10 ps (0.17)	10 ps (0.08)
20	750 ps (0.84)	750 ps (0.86)	750 ps (0.85)	750 ps (0.83)
	10 ps (0.16)	10 ps (0.14)	10 ps (0.15)	10 ps (0.17)
40	750 ps (0.84)	750 ps (0.85)	750 ps (0.83)	750 ps (0.82)
	10 ps (0.16)	10 ps (0.15)	10 ps (0.17)	10 ps (0.18)

Table 5.8.: Calculated lifetime components and their fractional contributions for a biexponential kinetics of isolated B830 LH2 complexes upon excitation at 485 nm into the carotenoid absorption band

Notably, although slight changes of the fractional contributions are observed within the table, no clear significant trend is observed for either increasing laser repetition rate nor increasing excitation fluence. On average the fractional contributions of the lifetime component 750 ps and 10 ps amount to 85% and 15%, respectively.

5.3.2. Excitation into the carotenoid absorption band: excitation wavelength 560 nm

For the experiments using an excitation laser wavelength of 560 nm the excitation fluence is varied over more than one order of magnitude from $5 \cdot 10^{12}$, $1 \cdot 10^{13}$, $5 \cdot 10^{13}$ to $1 \cdot 10^{14}$ photons/(pulse·cm²). As mentioned before these values for excitation fluences are denoted as '5E12', '1E13', '5E13' and '1E14' sometimes in the following without naming the units of photons per pulse and squared centimeters for reasons of abbreviation and smoother reading. The laser repetition rate

is varied over three orders of magnitude ranging from 0.5 MHz, 1 MHz, 2 MHz, 8 MHz, 20 MHz to 40 MHz, corresponding to temporal separations between two successive laser pulses of 2 μs, 1 μs, 500 ns, 125 ns, 50 ns and 25 ns, respectively. Table 5.9 summarizes the parameter combinations for which experiments with an excitation wavelength of 560 nm were performed.

laser repetition	excitation fluence $\frac{photons}{pulse \cdot cm^2}$			
rate (MHz)	$5 \cdot 10^{12}$	$1 \cdot 10^{13}$	$5 \cdot 10^{13}$	$1 \cdot 10^{14}$
0.5	-	-	+	+
1	-	+	+	+
2	-	+	+	+
8	+	+	+	+
20	+	+	+	+
40	+	+	+	+

Table 5.9.: Variation of the excitation parameters for an excitation wavelength of 560 nm: Time-resolved experiments are performed for all combinations of excitation parameters shown. For the different parameter situations the experiment gave a either a good signal (+) or a weak signal(-). For details see text.

For excitation parameter combinations labeled with a minus sign in Table 5.9 only a very weak signal, showing almost no fluorescence emission, is detected by the confocal microscope. For excitation parameter combinations labeled with a plus sign, results with good signal-to-noise ratio are obtained. These parameter combinations, highlighted in green color in the table, are used to analyze the fluorescence kinetics of the isolated B830 LH2 complexes upon excitation of the carotenoid pigments at 560 nm.

Observed fluorescence kinetics

The fluorescence transients measured for the excitation parameter combinations labeled in green in Table 5.9 all feature a similar shape[9]. As an example the fluorescence transient for the excitation parameter combination of a laser repetition rate of 8 MHz and an excitation photon fluence of $1 \cdot 10^{14}$ photons/(pulse·cm^2), resulting from excitation of the carotenoid molecules at 560 nm, is shown in Fig. 5.16.

---

[9]A table showing all the measured fluorescence transient for an excitation wavelength of 560 nm, similar to Fig. 5.3, is given in Appendix E.3.
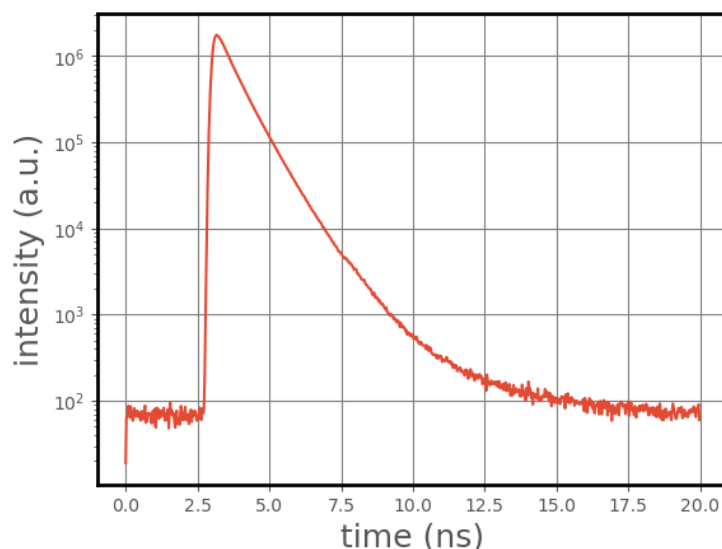
Figure 5.16.: Fluorescence transient of detergent-isolated LH2 complexes from Mch. purpuratum resulting from excitation into the carotenoid absorption band at 560 nm *The fluorescence transient corresponding to the excitation parameter combination of 8 MHz laser repetition rate and an excitation fluence of $1 \cdot 10^{14}$ photons/(pulse·cm^2) is shown in semi-logarithmic scaling. For detailed description see text.*

The mostly linear shape[10] of the fluorescence decay curve in semi-logarithmic scaling indicates a monoexponential kinetics as reported for isolated LH2 complexes of several other species of light harvesting purple bacteria [1, 2] in the literature before. A more detailed analysis of the measured fluorescence transients and its underlying kinetics is given below by using the phasor approach.

Analysis of the observed fluorescence kinetics using the phasor approach

The measured fluorescence transients resulting from excitation of carotenoid molecules at 560 nm were analyzed using the phasor approach as this was done for data resulting from excitation of at wavelenghts 790 nm and 485 nm before. All phasors shown in the following are calculated according to the procedure of phasor calculation outlined in detail before, see Chapter 4. Thus, all phasors are already finally corrected including corrections for background fluorescence and the influence of the IRF. The harmonic number of the Fourier transformation

---

[10]Considering the fact that the FWHM of the IRF was 168 ps at this excitation wavelength, see Chapter Material and Methods, the shape of the transient is considered as linear.

used for the calculation of the phasor coordinates is chosen to $n = 5$. A ruler of lifetimes, counterclockwise featuring the lifetime values of 0 ns, 0.1 ns, 0.2 ns, 0.5 ns, 1 ns, 2 ns, 5 ns and 10 ns, will be shown in all phasor plots from now on in order to allow for orientation along the universal semicircle. For reasons of clarity only the grey dots will be shown, without labels.

The commentaries given for phasor plots in Section 5.2 remain valid:

- All frequencies named in the following analysis of the fluorescence transient using the phasor approach and the accompanying figures refer to the laser repetition rates of the experiments and do not correspond to the transformation frequencies ω at which the phasor coordinates were calculated from the measured fluorescence transients.

- All phasors shown afterwards were calculated from the measured data and thus are expected to have an uncertainty in their position within the phasor plot. Thus, phasors are shown with corresponding error bars when necessary. The estimation of uncertainties for the phasor positions within the phasor plot is given in detail in Appendix C.

Below, first a qualitative analysis of the phasors corresponding to the measured fluorescence transient is given. Then, a quantitative analysis using the phasor approach is performed.

Qualitative analysis

A phasor plot featuring the phasors calculated from all the measured fluorescence transients resulting from an excitation wavelength of 560 nm is shown in Fig. 5.17 and allows for a first qualitative analysis of the underlying kinetics. Whereas the non-zoomed view of the phasor plot might inidcate that all the phasor lie on the universal semicircle, in the zoomed view of the phasor plot in Fig. 5.17 it is clearly visible that all the phasors corresponding to the measured fluorescence transients lie inside the universal semicircle, thus indicating a multiexponential kinetics.
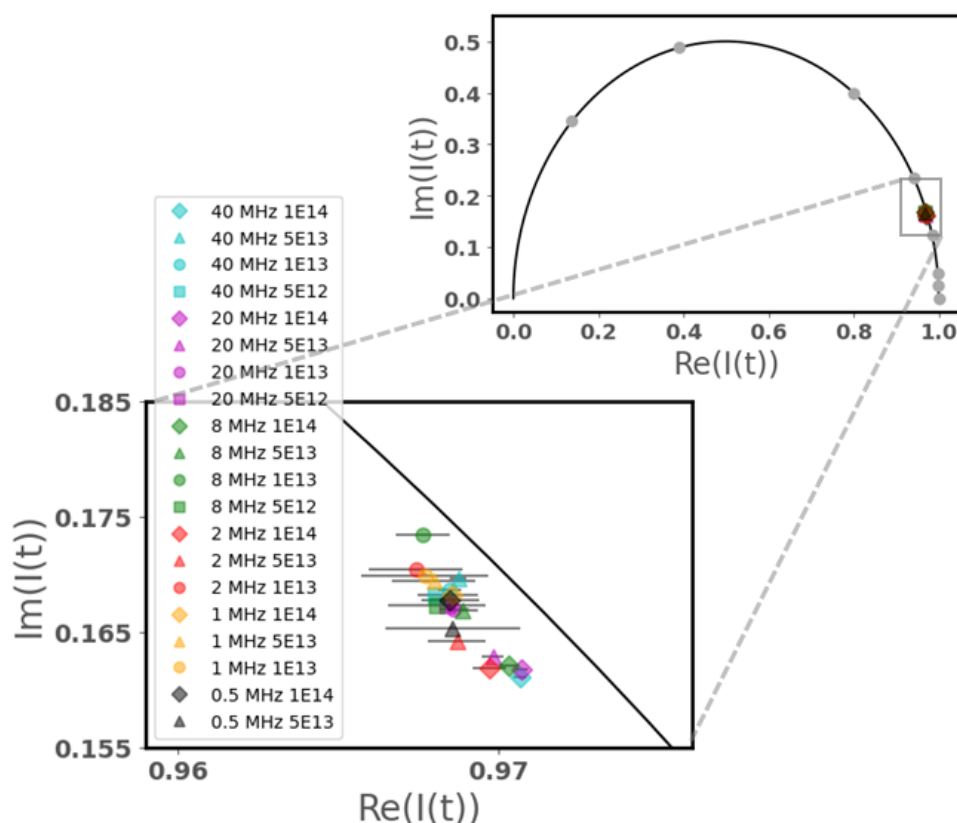
Figure 5.17.: Phasor plot for fluorescence transients of LH2 Mch. purpuratum resulting from excitation into the carotenoid absorption band at 560 nm *The phasors corresponding to fluorescence transients measured at different excitation parameter combinations of excitation photon fluence and laser repetition rate are shown in a phasor plot. Both, a total view as well as a zoomed view are shown. The excitation fluence is coded by different symbols (5E12: square, 1E13: circle, 5E13: triangle, 1E14: diamond), different laser repetition rates are coded by color. The grey circles on the universal semicircle correspond counterclockwise to the values 0 ns, 0.1 ns, 0.2 ns, 0.5 ns, 1 ns, 2 ns, 5 ns and 10 ns on the ruler of lifetimes. For detailed description see text.*

Quantitative analysis

Now, a quantitative analysis of the phasors is performed. In analogy to the rgumentation as well as the procedure of phasor evaluation for excitation wavelengths, first, the fluorescene kinetics for low excitation conditions is analyzed. This situation of excitation is achieved by low laser reptition rates, such as 0.5 MHz and 1 MHz, which were the lowest possible laser repetition rates for experiments performed with an excitation wavelength of 560 nm. For these laser repetition rates, the temporal separation of the excitation laser pulses amount to $2\,\mu$s and $1\,\mu$s, respectively. Thus, the measured fluorescence transients are

expected to represent the fluorescence kinetics corresponding to excitations resulting from only one excitation laser pulse. Assuming a biexponential kinetics for low laser repetition rates and evaluation of the corresponding phasors as described before, see Section 4.5.1, reveals contributing fluorescence lifetime values of 759 ps (+ 200 /- 17) ps and 71 ps (+ 320 /- 179) ps [11]. In the following these two lifetime components are referred to as 760 ps and 70 ps, which is valid with respect to the uncertainty interval. The linear fit to the phasors revealing that biexponential kinetics is visualized as turquoise colored line in Fig. 5.18. The contributing lifetime components are given by the intersections of the turquoise colored line with the universal semicircle.
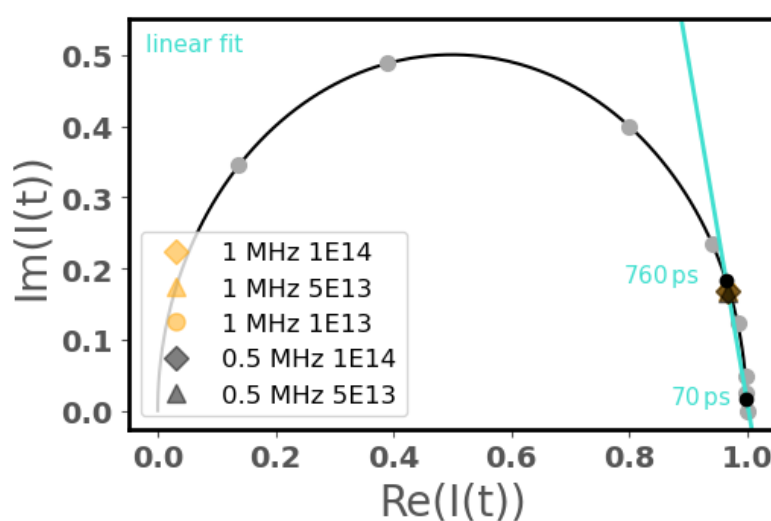
Figure 5.18.: Phasor plot of the biexponential kinetics at low laser repetition rates for excitation of carotenoid molecuels at 560 nm The phasors corresponding to the fluorescence transients measured at 0.5 MHz and 1 MHz are shown. The laser repetition rate is coded by color, the excitation fluence is coded by different symbols. The turquoise colored line visualizes the biexponential decay resulting from the linear fit, the black circles correspond to their intersections with the universal semicircle giving the two contributing lifetime components of 760 ps and 70 ps. Along the universal semicircle a ruler of lifetimes counterclockwise featuring the values 0 ns, 0.1 ns, 0.2 ns, 0.5 ns, 1 ns, 2 ns, 5 ns and 10 ns is shown (grey circles). For detailed description see text.

Next, the influence of an increase of the laser repetition rate on the kinetics underlying the observed fluorescence transients is analyzed for the laser repetition rates 2 MHz, 8 MHz, 20 MHz and 40 MHz. An increase of the laser repetition rates correspond to a smaller temporal separation of the excitation laser pulses

---

[11]The asymmetric values of the uncertainty of the lifetime components is due to the nonlinear scaling of the ruler of lifetimes along the universal semicircle, see also Appendix C

and thus a more complex situation of electronic excitations may occur within the B830 LH2 complex of *Mch. purpuratum*. In Fig. 5.19 the phasors corresponding to the fluorescence transients measured at laser repetition rates 2 MHz, 8 MHz, 20 MHz and 40 MHz are shown. Different laser repetition rates are coded by color, different excitation photon fluences are coded by symbol. In order to allow for comparison with the biexponential kinetics that is resolved for low laser repetition rates, this biexponential kinetics is visualized as turquoise colored line, as before in Fig. 5.18. The tolerance interval of the biexponential kinetics is visualized as red and black lines representing the lines of minimum and maximum slope, respectively, as obtained from fitting of the kinetics for low laser repetition rates.
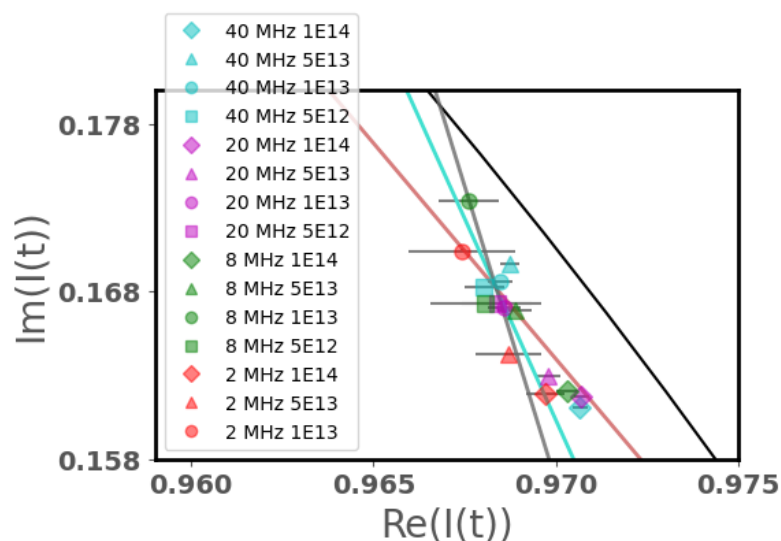
Figure 5.19.: Phasors corresponding to fluorescence transients at laser repetition rates 2 MHz, 8 MHz, 20 MHz and 40 MHz resulting from excitation into the carotenoid absorption band at 560 nm The phasors calculated from the measured fluorescence transients are shown for different excitation fluences at laser repetition rates of 8 MHz, 20 MHz and 40 MHz. The excitation fluence is coded by different symbols, different laser reptition rates are coded by color. Additionally, the biexponential kinetics obtained for low laser repetition rates (compare Fig. 5.14) is visualized as a straight line in turquoise color. The lines in red and black color represent the lines of minimum and maximum slope and visualize the tolerance interval of the biexponential kinetics. For detailed description see text.

In Fig. 5.19 it is clearly visible that all the phasors calculated from the measured fluorescence transients agree well with the biexponential kinetics with lifetime components of 760 ps and 70 ps obtained for low laser repetition rates. All the

phasor, coding different laser repetition rates by color and different excitation fluences by symbol, overlap with the turquoise colored line representing the biexponential kinetics itself or with the tolerance interval of that biexponential kinetics, spanned by the red and black lines of minimum and maximum slope, respectively. Thus, the biexponential kinetics observed for low laser repetition rates allows for description of the fluorescence kinetics of the B830 LH2 complex upon excitation of carotenoids at 560 nm for all excitation parameter combinations of laser repetition rate and excitation fluence.

Now the fractional contributions of both lifetimes components are determined according to the procedure outlined before in Section 4.5.1 and summarized in Table 5.8 as a function of the excitation parameters, namely the laser repetition rate and the excitation photon fluence. As before, different rows correspond to different laser repetition rates increasing from top to bottom, different columns correspond to different excitation fluences increasing from left to right. The accuracy of the number values of the fractional contributions is ± 0.02.

laser repetition rate (MHz)	excitation fluence $\frac{photons}{pulse \cdot cm^2}$			
	$5 \cdot 10^{12}$	$1 \cdot 10^{13}$	$5 \cdot 10^{13}$	$1 \cdot 10^{14}$
0.5			760 ps (0.89) 70 ps (0.11)	760 ps (0.91) 70 ps (0.09)
1		760 ps (0.92) 70 ps (0.08)	760 ps (0.92) 70 ps (0.08)	760 ps (0.91) 70 ps (0.09)
2		760 ps (0.92) 70 ps (0.08)	760 ps (0.89) 70 ps (0.11)	760 ps (0.87) 70 ps (0.13)
8	760 ps (0.9) 70 ps (0.1)	760 ps (0.94) 70 ps (0.06)	760 ps (0.9) 70 ps (0.1)	760 ps (0.87) 70 ps (0.13)
20	760 ps (0.9) 70 ps (0.1)	760 ps (0.9) 70 ps (0.1)	760 ps (0.88) 70 ps (0.12)	760 ps (0.87) 70 ps (0.13)
40	760 ps (0.91) 70 ps (0.09)	760 ps (0.91) 70 ps (0.09)	760 ps (0.92) 70 ps (0.08)	760 ps (0.87) 70 ps (0.13)

Table 5.10.: Calculated lifetime components and their fractional contributions for a biexponential kinetics of isolated LH2 complexes from Marichromatium purpuratum upon excitation at 560 nm in the carotenoid absorption band

Notably, the fractional contributions show only minor changes and no clear

trend is observed for an increase of either the laser repetition rate nor of the excitation fluence. The on average fractional contributions of the lifetime component 760 ps and 70 ps amount to 90% and 10%, respectively.

5.3.3. Summary of the fluorescence kinetics of isolated B830 complexes observed for excitation of carotenoids

The fluorescence transients of detergent-isolated LH2 complexes from *Mch. purpuratum* were measured for different combinations of the excitation fluence and the laser repetition rate upon excitation into the carotenoid absorption band. Experiments were performed for two excitation wavelength, 485 nm and 560 nm, both resonant with the carotenoid absorption band of the B830 LH2 complex, compare Fig. 5.1. Although a first inspection of the measured fluorescence transients by eye indicates a monoexponential kinetics, a detailed analysis using the phasor approach revealed a multiexponential kinetics. In order to determine the distinct values of the contributing lifetimes and their fractional contributions a quantitative analysis of the phasors calculated from the measured fluorescence transients was performed.

Following the considerations regarding the influence of a variation of the excitation conditions on the situation of electronic excitations into the B830 LH2 complex outlined before for excitation into the BChl *a* absorption band, the argument in the analysis of the fluorescence kinetics resulting from excitation of carotenoids is analogous. Thus, first, the fluorescence kinetics corresponding to low excitation conditions, realized by low laser repetition rates, was analyzed. Afterwards, this newly identified kinetics is kept fixed and it was tested whether this kinetics was sufficient for increasing excitation conditions, namely higher laser repetition rates.

For both excitation wavelengths into the carotenoid absorption band a biexponential kinetics was identified for low laser repetition rates. For an excitation wavelength of 485 nm lifetime components of 750 ps and 10 ps were resolved, for excitation at 560 nm the contributing lifetime components were identified to amount to 760 ps and 70 ps. The on average fractional contributions of the longer lifetime component in the order of 750 ps amounts to 85% and 90% for the excitation wavelengths 485 nm and 560 nm, respectively. Although slight dif-

ferences between lifetime values of the biexponential kinetics were observed for the two excitation wavelength, compare Tables 5.8 and 5.10, they feature in general the same trend of one longer lifetime component in the order of 750 ps and a second lifetime component amounting to a value smaller than 100 ps, thus almost one order of magnitude smaller. Notably, for both excitation wavelengths the phasor analysis revealed that no third lifetime component is observed and the fluorescence transients at all excitation conditions suffice this biexponential kinetics.

5.4. Summary of the observed fluorescence kinetics of isolated B830 complexes

Time-resolved experiment on detergent-isolated LH2 complexes from *Marichromatium purpuratum* were performed for both, excitation of bacteriochlorophyll pigments as well as carotenoids. A detailed phasor analysis revealed a complex multiexponential kinetics, which is in contrast to the monoexponential kinetics reported for isolated LH2 complexes of various species before [1, 2]. A summary of the lifetime components observed for the distinct excitation situations of the B830 LH2 complex of *Marichromatium purpuratum* investigated in this thesis is given in Table 5.11.

excitation of	lifetime components		
pigments	1st	2nd	3rd
BChl *a* exc 790 nm	730 ps	50 ps	500 ps
Carotenoid exc 485 nm	750 ps	10 ps	none
exc 560 nm	760 ps	70 ps	none

Table 5.11.: Summary of the observed multiexponential kinetics of isolated LH2 complexes from Marichromatium purpuratum

Overall, the observed fluorescence kinetics of LH2 from *Marichromatium purpuratum* is a biexponential kinetics with one lifetime component in the order of about 750 ps and one second lifetime component below 100 ps. Whereas for excitation of bacteriochlorophylls a third lifetime component in the order of about

500 ps is observed for high excitation density, corresponding to high laser repetition rates, no such third lifetime component is observed upon excitation of carotenoid pigments within LH2.

6. Discussion of the observed multiexponential kinetics of isolated LH2 complexes of *Marichromatium purpuratum*

In order to investigate the kinetics of electronic excitations within the B830 LH2 complex of *Mch. purpuratum* and thus its electronic structure, time-resolved spectroscopy was performed for excitation of either bacteriochlorophyll pigments or carotenoid pigments, with varying excitation parameters. Namely, the excitation parameters laser repetition rate and excitation fluence were varied. The obtained fluorescence transients were analyzed by means of the phasor approach in the last chapter.

In contrast to the previously reported monoexponential fluorescence kinetics of electronic excitations in LH2 complexes of various species of purple bacteria [1, 2, 4] and thus unexpectedly, a multiexponential kinetics of the fluorescence emission is observed for the B830 LH2 complex of *Mch. purpuratum* for all excitation conditions. Whereas a biexponential kinetics was identified in the detected fluorescence emission for all excitation conditions, either for excitation of bacteriochlorophylls (BChls) in the NIR or upon excitation of carotenoid pigments in the VIS, an additional appearing third lifetime component was only observed for excitation of BChls in the NIR at high excitation densities, compare Tables 5.6 and 5.11 as well as Fig. 5.11.

From these finding two main aspects or questions arise for the discussion given below: First, identification of the three fluorescence lifetime components. What is the molecular origin of the two or three, respectively, observed lifetime components in fluorescence emission? Second, why is the third lifetime compo-

nent only observed for excitation of BChls but is not observed for excitation of carotenoid pigments? In the following these two major aspects will be addressed in detail and finally an energy level scheme for the B830 LH2 complex of *Mch. purpuratum* will be proposed.

6.1. B830 LH2 complex: a mixed multiexponential kinetics

Phasor analysis of the experimentally obtained fluorescence transients revealed a multiexponential kinetics for the B830 LH2 complex from *Mch. purpuratum*, either upon excitation of BChl *a* pigments in the NIR or upon excitation of carotenoids by visible laser light. This is highly unexpected, since before monoexponential fluorescence kinetics were reported in literature for LH2 complexes of various species of photosynthetic purple bacteria [1, 2, 3, 4].

Now, for the LH2 complex of *Mch. purpuratum* a biexponential kinetics with lifetime components of 730 ps and 50 ps was identified for all excitation parameter combinations upon excitation of BChls. For excitation of carotenoid pigments within the LH2 complex similar values of the lifetime components, namely 750 ps and 760 ps for the longer lifetime and 10 ps and 70 ps for the fast lifetime component, were obtained. In summary, the observed fluorescence kinetics of LH2 from *Marichromatium purpuratum* is a biexponential kinetics featuring one lifetime component in the order of about 750 ps and one second lifetime component below 100 ps. The fractional intensity contributions of these two lifetime components approximately amount to 90% for the longer lifetime component of about 750 ps and 10% for the short lifetime of below 100 ps, almost independently of the excitation wavelength. No significant difference in the ratio of fractional intensity contributions is observed upon excitation of BChls or excitation of carotenoids.

In addition to this biexponential kinetics, for excitation of the bacteriochlorophyll pigments within the LH2 complex, a third lifetime component amounting to a value of about 500 ps is appearing for high excitation densities. The fractional contributions of this third lifetime component and the long lifetime component of the always observed biexponential kinetics behave in the opposite

way. In fact, the fractional contribution of the 750 ps lifetime component decreases as the third lifetime component appears in the overall kinetics. Thus, the overall complex multiexponential kinetics features in summary up to three lifetime components: one short lifetime component amounting to a value of below 100 ps, one long lifetime component in the order of about 750 ps and one third lifetime component of about 500 ps.

Turning over to the identification of the three observed lifetime components, the long lifetime component in the order of about 750 ps appears to be the most simple to identify. In literature monoexponential kinetics with a fluorescence lifetime in the order of 1 ns were reported for the detergent-isolated LH2 complexes of several species of purple bacteria [1, 2, 3, 4]. In fact, the lifetime component of about 750 ps observed for the detergent-isolated LH2 complex of *Mch. purpuratum* is quenched with respect to this value but is still in the same order of magnitude. Hence, this lifetime component is identified as resulting from the fluorescence emission of the B830 LH2 complex.

Regarding the identification of the other two lifetime components, the fast lifetime component of below 100 ps and the third lifetime component of about 500 ps, observed only for high excitation densities and excitation of bacteriochlorophyll pigments, more complex considerations are required. Thus, in the following the possibility of the occurrence of excitation annihilation processes in the B830 LH2 complex of *Mch. purpuratum* is discussed.

6.2. Excitation annihilation processes within the B830 LH2 complex

In a first approach, an energy level scheme for the B830 LH2 complex was proposed before in analogy to the 'standard' LH2 complex of *Rps. acidophila*, see Section 5.1. A refined energy level scheme now taking into account that the 750 ps lifetime component was just identified as resulting from fluorescence emission of the B830 LH2 complex is shown in Fig. 6.1. As before, the excited states of the three groups of pigments, the B800 BChl *a* molecules, the B830 BChl *a* molecules and the Car molecules, are shown as single energy levels. The singlet excitation levels of the B800 and the B830 ring are denoted as ^{1}B800* and ^{1}B830*, respec-

tively, and the singlet excitation level of carotenoids is denoted as ^{1}Car*. The triplet state of the Car molecules is referred to as ^{3}Car*. Both, excitation of bacteriochlorophyll pigments as well as excitation of carotenoids within the LH2 complex is considered, visualized by arrows of red color. From Fig. 6.1 it can be clearly seen that due to the highly efficient energy transfer from carotenoid pigments to bacteriochlorophyll pigments within the LH2 complex, on a timescale of a few picoseconds and below [100, 96], excitation of either of the two pigments results in excitation of the B830 BChl *a* pigments. Then, either emission of fluorescence may occur by relaxation of the ^{1}B830* state to the ground state or alternatively a triplet excitation of the carotenoids may be created within about 10 ns [53, 76].

As the energy transfer processes both from carotenoid to bacteriochlorophyll as well as between B800 BChls and B830 BChls occur on timescales faster than the temporal resolution of the experiments in this thesis, it is feasible to focus on the the singlet excited state of the B830 BChl *a* molecules and the triplet excitations within the LH2 complex in the following discussion concerning the identification of observed lifetime components in the emission of LH2 from *Mch. purpuratum*.
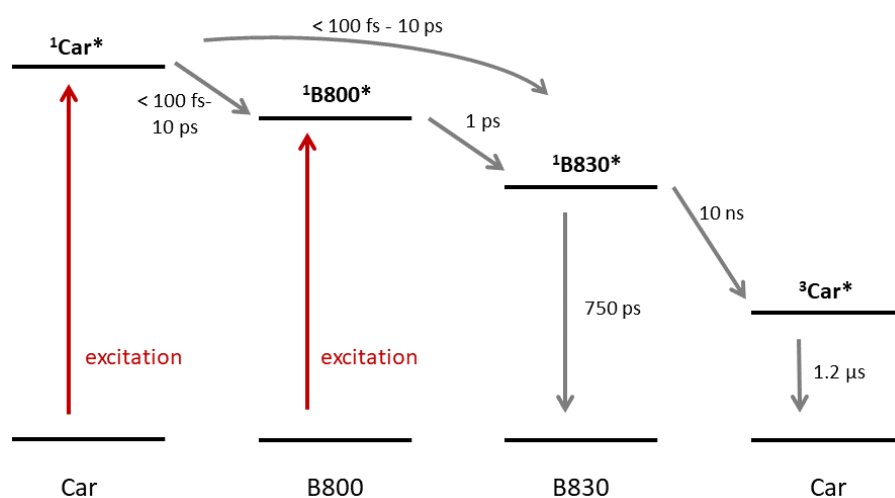
Figure 6.1.: Simplified energy level scheme of the B830 LH2 complex: *The excited states of the carotenoid pigments as well as the bacteriochlorophylls are shown as single energy levels. The singlet excitation levels of the B800 and the B830 ring are denoted as* ^{1}*B800* and* ^{1}*B830*, respectively. The singlet excited states of the Car molecules are denoted as* ^{1}*Car*, triplet states of the carotenoids are referred to as* ^{3}*Car*. Absorption of excitation light, either by carotenoids or bacteriochlorophylls is depicted by red arrows, downhill transitions between the distinct energy levels are depicted as grey arrows. For details see text.*

From the pre-experimental considerations on the investigation of the electronic structure of the B830 LH2 complex by probing different situations of electronic excitations via variation of the excitation parameters, see Section 5.1 for details, it is clear and even expected that excitation annihilation processes might occur within the B830 LH2 complex of *Mch. purpuratum*. In general three types of excitation annihilation processes might occur within the LH2 complex of purple bacteria: singlet-singlet annihilation (SSA), singlet-triplet annihilation (STA) and triplet-triplet annhilation (TTA), compare also Sections 2.3 and 5.1. First, the process of SSA is discussed with respect to the performed experiments and the observed lifetime components. Then, the excitation annihilation processes, involving triplet excitations, namely triplet-triplet annihilation and singlet-triplet annihilation are taken into account within the discussion.

Singlet-singlet annihilation (SSA)

The process of singlet-singlet annihilation (SSA) is reported to occur in LH2 complexes of photosynthetic bacteria for excitation fluences of and above $8 \cdot 10^{14}$ photons/(pulse·cm^2) [61]. Fluences above this reported threshold value are necessary in order to create more than one singlet excitation per LH2 complex. The value of the highest excitation fluence used for the experiments in this thesis is $1 \cdot 10^{14}$ photons/(pulse·cm^2), which is significantly smaller than the reported threshold value by almost one order of magnitude. Thus, SSA is highly unlikely to occur for the experiments in this thesis.

However, even if SSA could not be excluded to occur in the experiments performed at the highest excitation photon fluence, all the observed lifetime components were identified for all excitation parameter combinations of laser repetition rate and excitation fluence, even for excitation fluences almost two orders of magnitude smaller than the documented threshold value for the onset of SSA. Moreover, the process of SSA is reported to occur on a subpicosecond timescale [61], which is far below the temporal resolution of the experiments discussed here. Thus, this process cannot be resolved by the experiments either. Hence, SSA can be neglected in the further analysis of the observed fluorescence transients and the contributing fluorescence lifetime components.

Triplet-triplet annihilation (TTA)

For the occurrence of triplet-triplet annihilation processes multiple triplet excitations within one LH2 complex are required. However, triplet excitations within the LH2 complex are known to be highly immobile and localized on one of the carotenoid molecules within the LH2 complex [63, 65]. Thus, the occurrence of TTA implies at least two, but preferably an even higher number of triplet excitations within one LH2 complex in order to allow for two triplet excitations being close enough to each other for annihilation. The situation of multiple triplet excitations within one LH2 complex corresponds either to a situation that several carotenoid molecules within one LH2 complex carry one triplet each (resulting from a previous excitation laser pulse) or alternatively to a situation that one carotenoid molecule carries two triplet excitations. As pointed out before in Chapter 2, the triplet state populated within the LH2 complex is either the triplet state of the bacteriochlorophyll (BChl) pigments featuring a lifetime of about $70\,\mu$s [53, 54] or is alternatively the triplet state of the carotenoid pigment, which has a lifetime in the order of microseconds depending on the respective carotenoid incorporated in the LH2 complex [57]. Hence, a countable triplet population within one LH2 complex is only expected to occur for high laser repetition rates, especially in combination with high excitation fluences.

The fact that the long fluorescence lifetime component of about $750\,$ps as well as the small fluorescence lifetime component amounting to a value below $100\,$ps, were observed and identified for all excitation parameter combinations of laser repetition rate and excitation fluence, even for low laser repetition rates where the situation of multiple triplet excitations is highly unlikely if not impossible, already indicates that TTA most probably does not have to be considered in the discussion and identification of these lifetime components. Only the third lifetime component of about $500\,$ps was observed for excitation parameter combinations of high laser repetition rate and high excitation photon fluence, when BChl$\,a$ pigments were excited. Moreover, one has to keep in mind that TTA is a process reducing the number of triplets within an LH2 complex and thus a process without involvement of singlet excitations that result in fluorescence emission of the LH2 complex. Hence, in the further discussion concerning the identification of observed lifetime components in fluorescence emission of the B830 LH2 complex TTA can be neglected.

Singlet-triplet annihilation (STA)

The process of singlet-triplet annihilation (STA) is possible to occur, when an LH2 ring still carries a triplet excitation resulting from the previous pulse when the next pulse arrives and new singlet excitations are created. Thus, obviously both, the temporal separation of the excitation pulses which is determined by the laser repetition rate and the excitation fluence, determining the number of excitations which are created per excitation laser pulse, are expected to influence the occurrence of such annihilation processes. The newly created singlet excitations, which are known to at least partially delocalize over the B850 ring[1] of BChl *a* molecules within the LH2 complex [1, 48, 49, 50, 51], are highly mobile along the pigment ring within the LH2 complex [45] and thus can easily find a rather immobile and localized triplet excitation [63, 65] resulting from the previous excitation laser pulse to annihilate with. Considering all this, the occurrence of STA within an LH2 complex seems much more likely than the occurrence of TTA. The process of STA reduces the number of singlet excitations, which corresponds to the number of states from which fluorescence emission might occur, whereas in contrast TTA reduces the number of triplet excitations but has no influence on fluorescence emission.

The fact, that the third lifetime component in the order of 500 ps is observed for high excitation densities, resulting from the combination of high laser repetition rate and high excitation photon fluence, is a hint for a possible correlation with STA processes. Moreover, the inverse behavior of the fractional contributions of the 500 ps lifetime component and the 750 ps lifetime component, which was recently attributed to the fluorescence emission of the B830 LH2 complex, gives rise to the assumption of the involvement of STA annihilation processes. Next, the process of STA is considered in detail in the discussion of the origin of 500 ps lifetime component, which is only observed upon excitation of BChl *a* pigments in the NIR.

---

[1]Of course, for the B830 LH2 complex of *Mch. purpuratum* this refers to the B830 ring.

6.3. Origin of the third lifetime component observed for excitation of BChl *a*

Considering the discussion of excitation annihilation processes occurring in the LH2 complex of *Mch. purpuratum* in the previous section, singlet-triplet annihilation (STA) seems to be a likely candidate for originating in the 500 ps lifetime component. The process of STA effectively reduces the number of singlet excitations and thus directly influences the observable fluorescence emission. In Section 5.2.3 significant changes of the fractional intensity contributions of the three lifetime components were described for excitation of BChl *a* within the B830 LH2 complex, see Fig. 5.11. The observed inverse behavior of the fractional contributions f_{730} and f_{500} of the 730 ps lifetime component and the 500 ps lifetime component, respectively, clearly indicate that the process resulting in the 500 ps lifetime component correlates with a quenching of the fluorescence emission, as the 730 ps lifetime component was just identified as the fluorescence lifetime of the B830 LH2 complex[2].

In order to analyze and discuss the observed changes of the fractional contributions in more detail the fractional contributions of the three lifetime components are visualized as a function of the laser repetition rate for the excitation fluences $1 \cdot 10^{13}$ photons/(pulse·cm^2) and $1 \cdot 10^{14}$ photons/(pulse·cm^2) in Fig. 6.2. The fractional contributions of the three contributing lifetimes are coded by color.

It is clearly seen for both excitation fluences that the fractional contribution f_{50} of the smallest lifetime component of 50 ps is almost constant and below 0.1 for all laser repetition rates. The fractional contributions of the other two contributing lifetimes are significantly influenced by an increase of the laser repetition rate. For the excitation fluence of $1 \cdot 10^{13}$ photons/(pulse·cm^2) the fractional contributions f_{730} and f_{500} decrease and increase, respectively, for the laser repetition rate of 80 MHz. Whereas the fractional contribution f_{730} of the longest lifetime component of 730 ps drops by almost 30% from 0.92 to 0.63, the 500 ps lifetime component appears with a fractional contribution f_{500} of 0.33.

---

[2]Although in the general description of the multiexponential kinetics the longest lifetime component was denoted to amount to about 750 ps, here the value of 730 ps is used as this section here directly refers to the experiments for excitation of the bacteriochlorophylls.
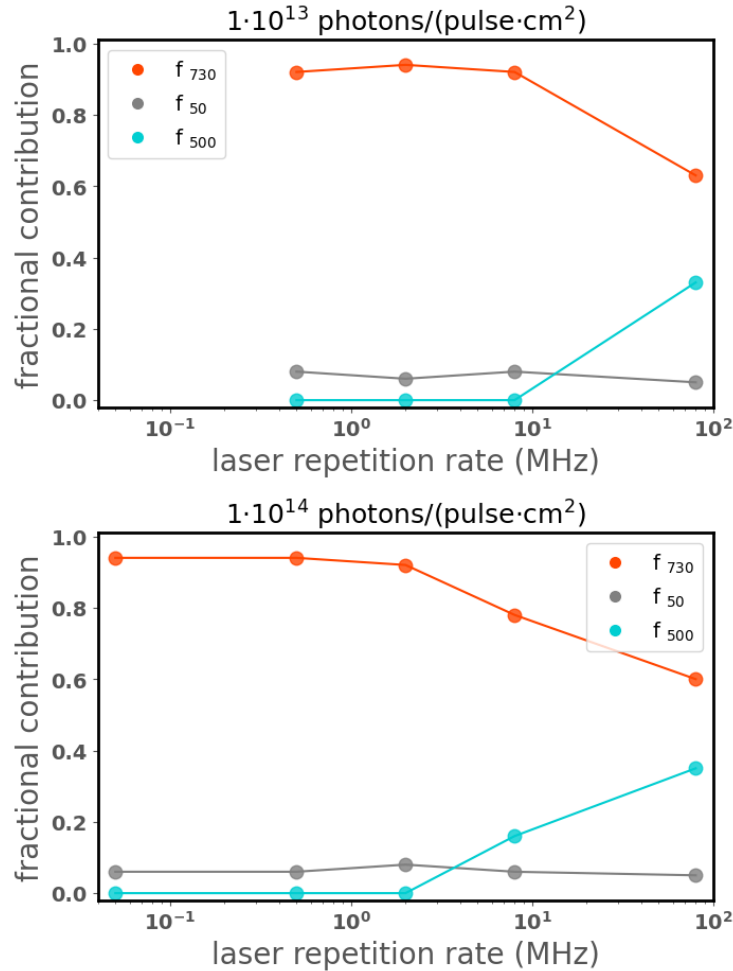
Figure 6.2.: Fractional intensity contributions of the distinct lifetime components of the multiexponential kinetics observed for excitation of bacteriochlorophylls: *The fractional contributions of the up to three contributing lifetimes, respectively, are shown as a function of the laser repetition rate for the excitation fluences $1 \cdot 10^{13}$ photons/(pulse·cm^2) and $1 \cdot 10^{14}$ photons/(pulse·cm^2). Data values are taken from Table 5.6, for biexponential kinetics a fractional contribution amounting to zero is visualized for the third lifetime component. The connecting lines serve as a guide to the eye. For details see text.*

For the excitation fluence of $1 \cdot 10^{14}$ photons/(pulse·cm^2) overall a similar behaviour of the fractional contributions f_{730} and f_{500} can be seen. In contrast to the lower excitation fluence, here the decrease of f_{730} and the concomitant increase of f_{500} appears already for the laser repetition rate of 8 MHz. Thus, f_{730} decreases from 0.92 down to 0.6 and f_{500} rises up to a fractional contribution of 0.35 for a laser repetition rate of 80 MHz. Thus, from Fig.6.2 it can be clearly seen that predominantly the laser repetition rate influences the changes of the

fractional contributions of two of the three contributing lifetimes of the multiexponential kinetics, giving additional evidence that the process of STA is involved.

Hence, summarizing the considerations above, the third lifetime component amounting to about 500 ps is attributed to the occurrence of STA processes within the LH2 complex of *Mch. purpuratum* and identified as corresponding to the fluorescence of those LH2 complexes within the investigated ensemble of LH2 complexes. Considering the fact that the 730 ps lifetime component was attributed to the fluorescence lifetime of the B830 LH2 complex, $k_{fluo} = (730\,ps)^{-1}$, and moreover that the 500 ps presumably reflects the fluorescence emission quenched by occurrence of STA, $k_{fluo,quench} = k_{fluo} + k_{STA} = (500\,ps)^{-1}$, the rate for quenching via STA can be determined, $k_{STA} = 6.3 \cdot 10^8\,s^{-1}$. This value is larger than the previously reported value for the rate of STA-quenching within LH2 [3], which was also speculated to give a lower boundary for the value of the rate for STA in LH2 complexes, but still in the same order of magnitude.

Moreover, the value reported in the literature refers to LH2 complexes of *Rps. acidophila*, whereas in this thesis detergent-isolated LH2 complexes of *Mch. purpuratum* are studied. From the recently published structure of the B830 LH2 it is known that this LH2 complex hosts two carotenoid pigments per apoprotein pair, thus offering double the number of possible host positions for triplet excitations within the LH2 complex with respect to the LH2 complexes of other species of purple bacteria[3]. Hence, this allows to speculate that in the LH2 complex of *Mch. purpuratum* for a singlet excitation it is presumably easier to find a nearby triplet excitation to annihilate with , in consequence resulting not only in a more efficient quenching via STA but likely also reflected by a significantly higher rate of singlet-triplet annihilation for this species of purple bacteria.

---

[3]Of course this strictly refers only to the limited number of LH2 complex whose molecular structures have been resolved at high resolution [22, 24, 23].

6.4. Origin of the fast lifetime component below 100 ps observed for all excitation conditions

Whereas the lifetime component of about 750 ps was attributed to the fluorescence lifetime of the B830 LH2 complex and the lifetime component of about 500 ps observed exclusively for excitation of BChl a was just attributed to the fluorescence lifetime under the involvement of singlet-triplet annihilation processes, in contrast, the origin of the fast lifetime component amounting to a value of below 100 ps has not been discussed yet. This lifetime component is observed for excitation of bacteriochlorophylls as well as for excitation of carotenoid pigments within the LH2 complex. Moreover, it was shown that its fractional intensity contribution is neither affected by the laser repetition rate nor the excitation photon fluence of the experiments, compare Sections 5.2.3 and 5.3.3. Thus, it can be excluded that the fast lifetime component amounting to a value of below 100 ps results from any quenching effects due to excitation annihilation processes within the LH2 complex. In consequence, it must originate from another emissive state within the energy level scheme of the LH2 complex.

From the experiments performed upon excitations of bacteriochlorophyll pigments it follows that this additional emissive state, named X for the moment, is proposed to lie in the vicinity of the singlet excited states of the B800 and B830 manifold within the LH2 complex and may either be populated via the B800 BChl a molecules or those arranged in the B830 ring of bacteriochlorophyll pigments. An involvement of the carotenoid pigments in the population pathway of state X can be excluded for two reasons: First, if it was the case that carotenoid pigments were involved in the population of state X, the emission of state X could not or only hardly be observed upon excitation of bacteriochlorophyll pigments. However, emission from state X is observed in the experiments using excitation of bacterichlorophyll pigments in this thesis, thus there is no indication of an involvement of carotenoid pigments in the population of state X. Moreover, the second reason for disregarding the carotenoid pigments in the further discussion of the population pathway of state X is that no significant increase of the fractional contribution of the fast lifetime component, which was attributed to the emission of state X, was observed with respect to the experiments performed upon excitation of bacteriochlorophylls. However, a significant increase of the fractional contribution would have been expected for

excitation of carotenoids when the carotenoid pigments were directly involved in the population pathway of state *X*. Next, the two possible population pathways for the newly introduced state *X* via the two pools of bacteriochlorophyll pigments within the LH2 complex, B800 and B830, are discussed.

Assuming that the population of state *X* occurs via the B830 manifold of bacteriochlorophyll pigments corresponds to an additional relaxation channel of the singlet excitations in the ^{1}B830* state, thus competing with the radiative relaxation channel resulting in fluorescence emission. Hence, this population pathway for state *X* would result in a decrease of the observed fluorescence lifetime, in a similar manner as discussed in the previous section for quenching of the fluorescence lifetime due to annihilation effects. However, this is not the case in the experiments. There, the small fluorescence lifetime of below 100 ps is observed in addition to the fluorescence lifetime of about 750 ps. In consequence, a population of state *X* via the B830 BChl *a* molecules can be excluded to occur.

The second possibility for the population of the newly introduced state *X* is a population pathway via the B800 bacteriochlorophyll manifold. This pathway for the flow of energy to state *X* is in accordance with the experimental observations that the two fluorescence lifetimes attributed to state *X* and attributed to the fluorescence emission of the B830 BChl *a* pigments are observed simultaneously. Hence, a population of the newly introduced state *X* via the B800 bacteriochlorophyll pigments in the LH2 complex of *Mch. purpuratum* can be assumed. An energy level scheme for the B830 LH2 complex including now the new introduced emissive state *X*, as expected from a general analogy to the 'standard' LH2 complex of *Rps. acidophila*, is shown in Fig. 6.3.

Although the population pathway of the newly introduced emissive state *X* was just considered, the molecular origin of this state remains still an open question. In the following, two possible explanations are discussed. Thus, either low lying excited states of the carotenoid pigments within the LH2 complex or alternatively excitonic states with a certain admixture of a charge-transfer character within the LH2 complex might be the origin of the newly introduced state *X* attributed to the observed fast lifetime component in fluorescence emission.
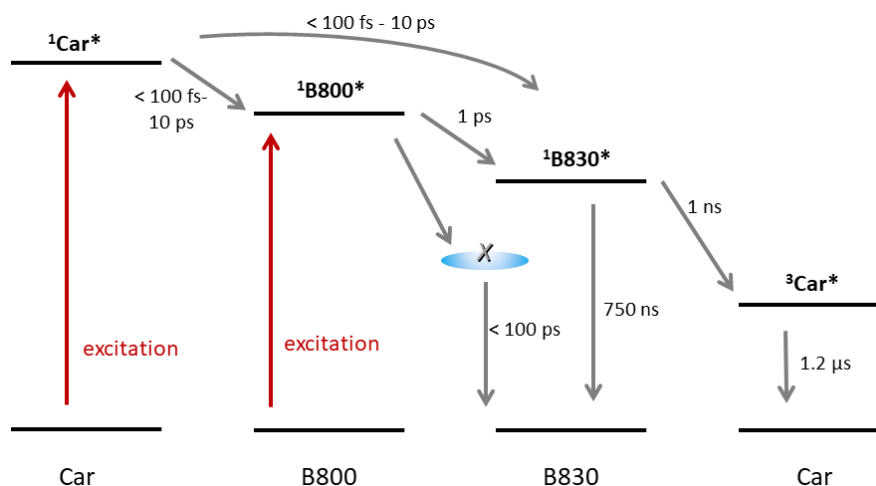
Figure 6.3.: Proposal of an additional emissive state within the energy level scheme of LH2 of Mch. purpuratum: The energy level scheme of the LH2 complex of Mch. purpuratum is visualized as expected from the analogy to 'standard' LH2 from Rps. acidophila. The excited states of the carotenoid pigments as well as the bacteriochlorophylls are shown as single energy levels. The singlet excitation levels of the B800 and the B830 ring are denoted as ^{1}B800 and ^{1}B830*, respectively. The singlet excited states of the Car molecules are denoted as ^{1}Car*, triplet states of the carotenoids are referred to as ^{3}Car*. A new emissive state denoted as X is visualized, lying in close vicinity to the singlet excited states of the B800 and B830 ring, respectively. The population of state X via the B800 pigments is indicated. For details see text.*

6.4.1. Carotenoid excited states in the B830 LH2 complex

The photophysics of carotenoids is complex and still a matter of ongoing research and discussion[4] [73, 133, 134, 135, 136, 137]. In the current understanding of the excited states of carotenoids low lying excited states, such as an intramolecular charge-transfer (ICT) state within the carotenoid, lying in the vicinity of and below the S_1 state of carotenoids may occur for distinct carotenoid molecules [73, 133, 138, 139]. The first singlet excited state S_1 of carotenoids is not optically accessible by absorption of excitation laser light [133, 140, 134, 135, 73] and thus is only populated via internal conversion processes within a carotenoid molecule. It is well known and also proven by experiments that the S_1 state is involved in the highly efficient energy transfer from carotenoids to bacteriochlorophyll pigments within LH2 complexes, both in general [75, 77] as well as especially for the case of the LH2 complex of *Mch. purpuratum* [100, 96].

---

[4]In Appendix A a brief summary of the current concensus on the photophysics of carotenoids is given.

Thus, by consequence the S_1 state of carotenoids clearly has to lie above the excited states of the two pools of bacteriochlorophyll pigments within the LH2 complex, B800 and B830, in order to allow for energy transfer, whereas a lower lying excited state such as an ICT state might lie below S_1 and thus possibly even below the excited state of the B800 ring or the B830 ring of bacteriochlorophyll molecules. Hence, such an ICT state of carotenoid might in principle be the origin of the newly introduced state *X* in the B830 LH2 complex of *Mch. purpuratum*. However, although such ICT states are often observed for the group of carbonyl-carotenoids, carotenoids featuring a carbonyl side chain, and the carotenoid okenone incorporated in the LH2 complex of *Mch. purpuratum* belongs to the group of carbonyl carotenoids, see structure formal in Fig. 2.19 as well as Appendix A, there is no indication that okenone features such a low lying state in its manifold of excited states [141].

Moreover, if it was the case that the new state *X* in the energy level scheme of LH2 from *Mch. purpuratum* would be a low lying excited state of carotenoid, the fractional contribution of the fast lifetime component attributed to state *X* should significant increase for excitation of the carotenoid pigments. This would be expected due to internal conversion processes within the carotenoid molecule, populating state *X* in addition to the population pathway via the B800 BChl *a* molecules that was identified above. However, such an increase of the fractional contribution of the fast lifetime component is not observed in the experiments for excitation of either carotenoids or bacteriochlorophyll pigments. In contrast, similar fractional contributions of about 10% of the fast lifetime component of below 100 ps were observed, independently of the excitation wavelength. In conclusion, from the current point of view it can be likely excluded that a low lying state of carotenoid is the origin of the newly introduced state *X* in the energy level scheme of B830 LH2 complex of *Mch. purpuratum*.

6.4.2. Charge-transfer states in the B830 LH2 complex

The photophysics of the 'standard' LH2 complex strongly depends on the two rings of BChl *a* molecules within the LH2 ring, named the B800 ring and the B850 ring[5], as introduced in detail in Chapter 2. Those two rings of pigments, named

---

[5]Of course, for the B830 LH2 complex of *Mch. purpuratum* this refers to the B830 ring.

after their respective absorption bands in the NIR wavelength range, mainly determine the electronic excitations within the LH2 complex and thus their kinetics. Whereas the B800 ring consists of rather weakly coupled BChl *a* molecules, by contrast the B850 ring comprises twice the number of BChl *a* molecules in close proximity resulting in strong coupling between the individual pigments [36]. Excitation energy, either resulting from direct excitation or by energy transfer from the B800 ring, is known to delocalize along the ring at least over parts of the B850 ring [51, 1]. This delocalization of excitation energy in the excited state of the B850 ring is often referred to as Frenkel exciton, as it can be effectively described using the model of molecular excitons introduced by Frenkel in 1931 [142], and is in detail calculated [36] and discussed theoretically in the literature numerous times [143, 144, 15].

Moreover, due to the tight packing of pigments and the resulting strong coupling between the individual BChl *a* molecules, the delocalization of excitation energy can be affected by this coupling. Thus, the "asymmetry of the electron density in the excited state may become larger, and the excited state may, in these conditions exhibit charge-transfer character" [145] which corresponds to a mixing of the electronically excited states and charge-transfer states (CT) resulting in so called mixed exciton charge-transfer states (ex-CT). Pure charge transfer states feature in general a nonzero static dipole moment and a transition dipole moment of zero [8] and due to the latter fact these states are optically forbidden and cannot be optically excited from the ground state. Hence, these CT states are sometimes also referred to as dark states. However, mixing of the electronically excited states with CT states results in a finite transition-dipole moment of the resultant mixed exciton charge-transfer state and thus in principle allows for emission of fluorescence from these states by coupling to the electronic ground state.

The occurrence of mixed exciton CT states in the LH2 complex of purple bacteria was indicated by means of Stark spectroscopy experiments in the 1990s [146, 147]. In order to account for the high values observed for the difference dipole moment $\Delta\mu$ between the ground state and the excited state as well as for the corresponding difference polarizabilities $\Delta\alpha$, these studies proposed a mixing of the lowest excited state with CT states between the neighboring, densely packed BChl *a* molecules within the B850 ring to explain their results. Since

141

then, and especially within the last decade, the occurrence of mixed exciton CT states within the LH2 complex of purple bacteria and moreover their influence on the spectroscopic properties have come more and more into the focus of current research, both theoretically as well as experimentally. Thus, the occurrence of low-energy CT states on adjacent BChl *a* molecules, resulting from the close proximity and the strong overlap of the tetrapyrrole rings in the dimerized B850 molecules, was proposed to explain exciton-self trapping and in particular strong electron-phonon coupling within the LH2 complex of *Rps. acidophila* by mixing of those CT states with the excited states [148]. Results from quantum chemical simulations indicated the occurrence of mixed exciton CT states for the 'standard' LH2 complex of *Rps. acidophila* as well as for the blue-shifted low-light spectral variant with absorption bands at 800 nm and 820 nm, respectively [149].

In 2016 Ferretti and coworkers reported on the occurence of a dark state in two types of LH2 complexes of *Rps. palustris*, one wild-type LH2 complex with 'standard' absorption bands a 800 nm and 850 nm, respectively, and one genetically modified mutant LH2 complex, with only one absorption band located at 810 nm [8]. From two-dimensional electronic spectroscopy (2DES) a low-lying mixed exciton CT state was identified for both types of LH2 complexes, the wild-type LH2 complex as well as for the mutant LH2 complex. In both cases this mixed exciton CT state was found to be populated from the B800 ring of BChl *a* molecules within 50 - 65 fs [8]. For the mutant LH2 complex of *Rps. palustris* strong quenching of the fluorescence emission with respect to the wild-type LH2 complex was observed, indicated by a significant decrease of the fluorescence lifetime. This strong quenching was attributed to the occurrence of the newly found mixed exciton CT state. From time-resolved spectroscopy the lifetime of the mixed exciton CT state was determined to be 70 ps [8].

Moreover, in recent studies mixed exciton CT states were found to play a significant role in the spectral tuning of LH2 complexes of purple bacteria. In fact, both the spectral position of the absorption bands [6, 150] as well as the width of the absorption bands was found to be influenced by the involvement of mixed exciton CT states in the photophysics of the LH2 complex [151]. Very recently, such mixed exciton CT states were reported to at least influence or even mediate the energy transfer between the two rings of BChl *a* molecules within the LH2 complex, namely the B800 ring and the B850 ring [152]. In recent years several

review articles emphasized the occurrence and importance of the mixed exciton CT states in the LH2 complexes of purple bacteria for various purposes and tried to figure out what is known about their general role in bacterial photosynthesis [153, 154, 155].

Finally, from all what is known about the occurrence and involvement of mixed exciton CT states within LH2 complexes of purple bacteria up to the present, there is profound indication that such mixed exciton CT states may also occur in the B830 LH2 complex of *Mch. purpuratum* investigated in this thesis. Thus, in analogy to the findings of Ferretti et al. [8] that reported a biexponential kinetics with lifetime components of 700 ps and 70 ps for a genetically modified mutant LH2 complex of *Rps. palustris*, the biexponential kinetics observed for the B830 LH2 complex of *Mch. purpuratum* within this thesis is likely attributed to the occurrence of a mixed exciton CT state. Hence, the significant shortening of the 750 ps fluorescence lifetime component for the LH2 complex of *Mch.purpuratum* with respect to the in general reported fluorescence lifetime of approximately 1 ns for LH2 complexes of other species of purple bacteria [1, 2] is in accordance with the literature [8] and thus allows the assumption of the occurrence of a mixed exciton CT state in the B830 LH2 complex. The observed fast lifetime component of below 100 ps in the multiexponential fluorescence kinetics of the LH2 complex of *Mch.purpuratum* is thus tentatively identified as the lifetime of the mixed exciton CT state, in analogy to Ferretti et al. [8].

6.5. Proposal of an energy level scheme of the B830 LH2 complex

The identification of the up to three lifetimes in the observed multiexponential fluorescence kinetics, see previous sections, now allows for the proposal of an energy level scheme for the B830 LH2 complex of *Mch. purpuratum*. The energy level scheme proposed here is based on the general building principle of bacterial light-harvesting complexes as spherical arrangements of pigments embedded into a protein scaffold and thus features analogy to the current understanding of the energy level scheme of LH2 complexes such as the 'standard' LH2 complex from *Rps. acidophila*, compare Section 2.3, and considers in addition the experimental findings for the B830 LH2 complex of *Mch. purpuratum* in

this thesis.

The proposed energy level scheme is shown in Fig. 6.4 and the time constants of the distinct steps in the flow of energy within the propsed energy level scheme are summarized in Table 6.1. Most of the time constants directly refer to the LH2 complex of *Mch. purpuratum*, either from literature or the experiments of this thesis. However, although a few of the time constants refer to other species of photosynthetic purple bacteria, it is reasonable to use their number values in the construction of the energy level scheme of *Mch. purpuratum* because according to the current knowledge about the photophysics of light-harvesting complexes of purple bacteria different species in fact may show some variations in the time constants of the energy transfer processes but these are always in the same order of magnitude.

transition process	time constant	species	reference
energy transfer Car-BChl	100 fs ($S_2 \rightarrow$ B830) 0.5 ps ($S_1 \rightarrow$ B800) 5 ps ($S_1 \rightarrow$ B830)	*Mch. purpuratum*	[100]
energy transfer B800-B830	$\leq$ 1 ps	*Rba. sphaeroides*	[45, 47]
internal conversion within Car ($S_1 \rightarrow S_2$)	$\leq$ 300 fs	*Mch. purpuratum*	[73, 100, 156]
population of state *CT* via B800	$\leq$ 100 fs	*Rps. palustris*	[8]
lifetime of state *CT*	$\leq$ 100 ps	*Mch. purpuratum*	this thesis
B830 lifetime	$\approx$ 750 ps	*Mch. purpuratum*	this thesis
ISC in B830	10 ns	*Rba. sphaeroides*	[53]
B830 triplet lifetime	70 μs	*Rba. sphaeroides*	[53, 54]
triplet-triplet energy transfer (B830$\rightarrow$Car)	$\leq$ 1 ns	*Mch. purpuratum*	[57]
Car triplet lifetime	1.2 μs	*Mch. purpuratum*	[57]

Table 6.1.: Time constants of the energy transfer processes within the energy level scheme of the LH2 complex of Mch. prupuratum in Fig. 6.4

Upon excitation of the B800 bacteriochlorophyll pigments within the B830 LH2 complex of *Mch. purpuratum* the flow of energy may either follow the highly efficient excitation energy transfer to the B830 bacteriochlorophyll pigments, within

about 1 ps [47], or alternatively may follow the newly identified relaxation pathway populating a mixed-exciton charge-transfer state *CT* within about 100 fs [8], see Fig. 6.4.
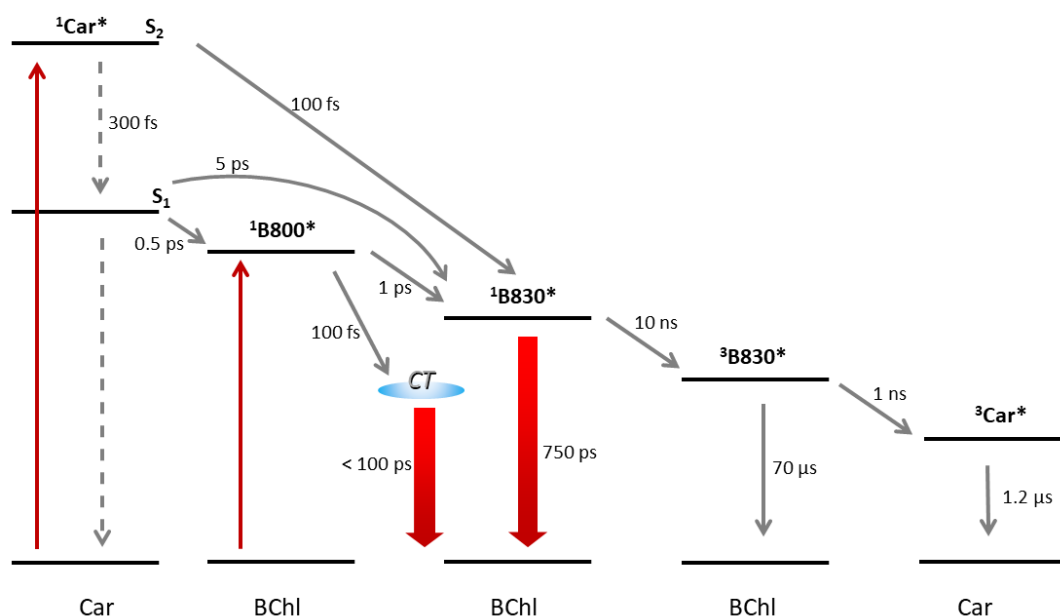
Figure 6.4.: Energy level scheme of the B830 LH2 complex derived from the observed multiexponential fluorescence kinetics: The energy level scheme of the B830 LH2 complex is shown, the different pathways of the downhill flow of energy are indicated by arrows. The excited states of the three groups of pigments, the B800 BChl a molecules, the B830 BChl a molecules and the Car molecules, are shown as single energy levels. The singlet excitation levels of the B800 and the B830 ring are denoted as ^{1}B800 and ^{1}B830*, respectively. In analogy the second singlet excited states S_2 of the Car molecules are denoted as ^{1}Car* and the triplet states of the Car molecules are referred to as ^{3}Car*. The newly proposed mixed-exciton charge-transfer state is denoted as CT. Absorption of excitation light either by the carotenoid pigments or bacteriochlorophylls is depicted by thin red arrows, fluorescence emission is indicated by thick red arrows and downhill transitions between the distinct energy levels are depicted as grey arrows. An overview of the values of the transition times including references is given in Table 6.1. For details see text.*

Both possible pathways result in fluorescence emission, with lifetimes of below 100 ps and about 750 ps, respectively, as seen from the experiments of this thesis. When excitation energy is transferred to the B830 BChl *a* manifold of pigments, bacteriochlorophyll triplet excitations of the B830 molecules are formed via inter-system crossing within 10 ns [53, 76]. Those triplet excitations of the B830 bacteriochlorophyll pigments may either relax to the ground state within 70 μs [53, 54] or may result in carotenoid triplet excitations via triplet-triplet en-

ergy transfer. For *Mch. purpuratum* triplet-triplet excitation energy transfer from bacteriochlorophylls to carotenoids is reported to occur highly efficient on a timescale of 1 ns [57], the resulting carotenoid triplets of okenone have a lifetime of $1.2\,\mu$s [57].

Absorption of excitation light by the carotenoid pigments results in excitation of the S_2 state of the carotenoid molecules, see Fig. 6.4, because the lower lying first excited singlet state S_1 is optically forbidden[6]. Then either direct energy transfer to the B830 bacteriochlorophyll pigments within about 100 fs may occur [100] or alternative internal conversion processes may result in population of the S_1 of the carotenoid on similar timescales [73, 100, 156]. From S_1 singlet energy transfer to both pools of bacteriochlorophyll pigments may occur [100], resulting in population of either the B800 or the B830 pigments within the LH2 complex of *Mch. purpuratum*. From there on the excitation energy may follow the same intra-complex energy pathways in the energy cascade as described above for excitation of BChl pigments.

The energy level scheme proposed above for the B830 LH2 complex of *Mch. purpuratum* considers the two lifetime components observed in the fluorescence experiments but yet the question why a third lifetime component attributed to singlet-triplet annihilation is only observed upon excitation of bacteriochlorophylls in the experiments remains unsolved. However, based on the proposed energy level scheme the next section will discuss this experimental finding and will discuss the origin of this effect.

6.6. Origin of the difference in the observed kinetics for excitation of BChl *a* or carotenoid molecules

Whereas the possible origin of the up to three lifetime components identified in the fluorescence kinetics was discussed in detail in the previous sections of this chapter, the reason for the remarkable difference in the kinetics either for excitation of bacteriochlorophylls or carotenoid pigments, namely that for excita-

---

[6]An overview of the photophysics of carotenoids in general is given in Appendix A.

tion of carotenoids no third lifetime component was observed, remains an open question. The third lifetime component of about 500 ps, which was exclusively observed for excitation of bacteriochlorophyll pigments, has yet been attributed to the occurrence of singlet-triplet annihilation events. Thus, the fact that this lifetime component was not observed for excitation of carotenoid pigments leads to the conclusion that no singlet-triplet annihilation may occur for excitation of carotenoids. Moreover, this may only be the case when no triplet excitations are available for such annihilation processes because singlet excitations are created by each excitation laser pulse. However, from the just proposed energy level scheme of the LH2 complex of *Mch. purpuratum*, see Fig. 6.4, it is clear that triplets will be generated upon excitation of either of the pigments. Hence, the question arises which mechanism results in the fact that no triplets are available for singlet-triplet annihilation upon excitation of carotenoid pigments.

Within the possible excitation annihilation processes discussed before, only one process has an influence on the number of triplet excitations within the LH2 comlex: triplet-triplet annihilation (TTA). However, carotenoid triplet excitations within an LH2 complex of purple bacteria are reported to be localized on one carotenoids molecules and can be assumed as almost immobile [63, 64, 65]. Triplet-triplet interactions are known to rely on the short-range exchange interaction, which requires overlap of the electronic wavefunctions of the two triplet excitations (Dexter mechanism of energy transfer) [68, 157]. Hence, in order to allow for the criterion of wavefunction overlap for the occurrence of TTA, either a very high number of carotenoid triplet excitations within the LH2 complex is necessary such that neighboring pigment molecules might carry a triplet excitation or alternatively two triplet excitations have to be located on the same carotenoid molecule.

The recently published structure of the B830 LH2 complex of *Mch. purpuratum* [96] allows for determination of the interpigment distances within the LH2 complex. In Fig. 6.5 one apoprotein pair acting as the basic building block of the LH2 complex is shown in order to visualize the tight packing of pigments within the LH2 complex of *Mch. purpuratum*. The intermolecular distance between Car1 and the closest B830 BChl *a* molecule, visualized in green and red color, respectively, amounts to 6.3 Å. The distance between Car2, visualized in blue color, and the B800 BChl *a* pigment, visualized in yellow color, is 3.7 Å and the closest

spatial separation of the two carotenoid molecules, visualized in green and blue color, amounts to 4.5 Å. All these values are below 10Å, which is, as a rule of thumb, the maximum separation that allows for triplet-triplet exchange interaction [68, 158, 159]. Hence, from this point of view the occurrence of TTA either between triplets located on adjacent carotenoid pigments or between neighboring BChl *a* and carotenoid pigments can be assumed to be possible.
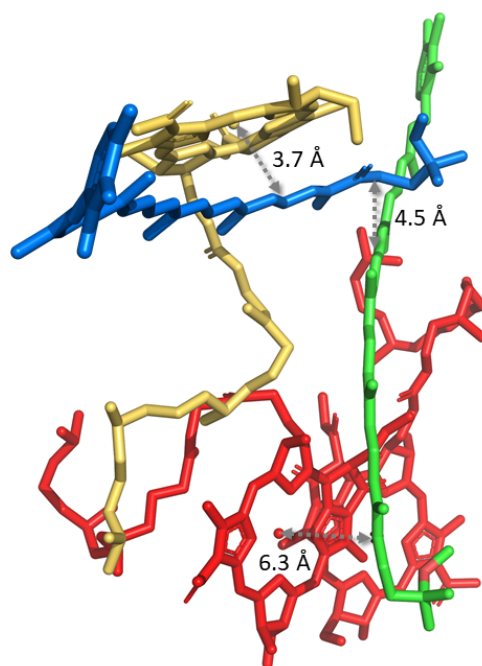
Figure 6.5.: Tight packing of bacteriochlorophyll and carotenoid pigments within the LH2 complex of Mch. purpuratum: *The pigment arrangement in the basic bulding block of the LH2 complex is visualized, as known from the CryoEm structure [96]. The color code is chosen as before, BChl a molecules of the B800 and the B830 ring are visualized in yellow and red, respectively. The two carotenoid pigments of okenone, Car1 and Car2, are shown in green and blue color, respectively, coding their different molecular orientations within the LH2 complex. Intramolecular distances are indicated by dashed arrows. The rendering of the molecular arrangement of the pigments as well as the measurement of the intermolecular distances was done with PyMOL (Schrödinger). For details see text.*

The assumption that the observed difference in the kinetics upon excitation of bacteriochlorophyll or carotenoid pigments is due to the occurrence of TTA within the LH2 complex is appealing and even supported by the fact, that the molecular arrangement of pigments within the LH2 complex of *Mch. purpuratum* would allow for the occurrence of TTA. However, it is yet still speculative because triplet excitations are created upon excitation of either of the pigments,

bacteriochlorophylls as well as carotenoids, compare previous section and Fig 6.4. In order to elucidate the situation of triplet excitations in the LH2 complex, resulting from excitation of either of the pigments, next, a detailed look on the flow of energy within the LH2 complex will be given, first for excitation of bacteriochlorophyll pigments, then for excitation of carotenoids.

In Fig. 6.6 the flow of energy within the LH2 complex of *Mch. purpuratum* upon excitation of bacteriochlorophylls is visualized, according to the recently developed energy level scheme that was proposed in the previous section. In addition to the energy transfer times of the distinct transfer steps within the energy level scheme, also the relative flow of energy is indicated according to the quantum yields of the transfer steps. The values of the quantum yields were calculated from the ratio of transfer rates, each given by the inverse of the distinct transfer time.
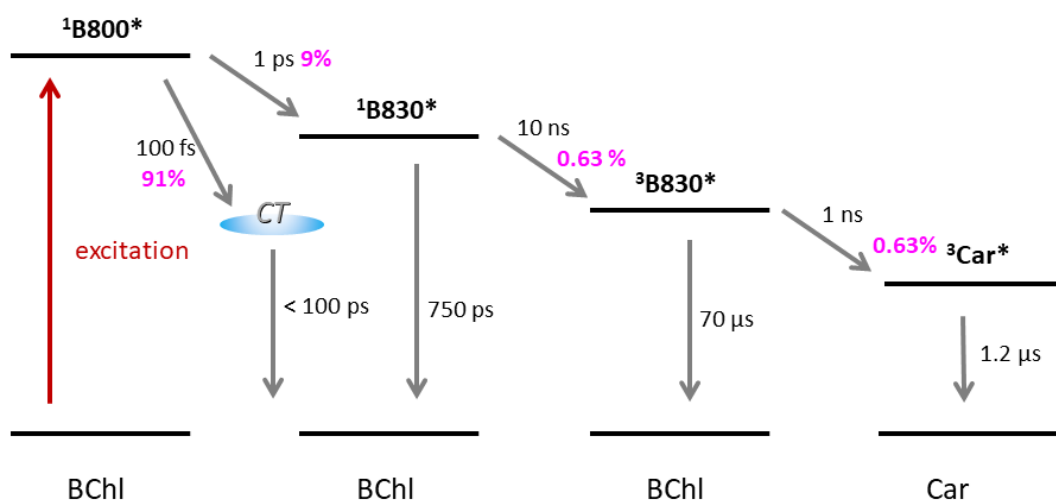
Figure 6.6.: Flow of energy within the LH2 complex of Mch. purpuratum upon excitation of bacteriochlorophylls:The energy level scheme of the LH2 complex of Mch. purpuratum is shown for excitation of bacteriochlorophylls, including the pathways of the downhill flow of energy. The excited states of the three groups of pigments, the B800 BChl a molecules, the B830 BChl a molecules and the Car molecules, are shown as single energy levels as before. Besides the values of the characteristic timescales of the energy transfer steps, in addition also the values of the quantum yields of the distinct energy transfer process are given in magenta color. Those percentage values refer to the initially excited state and thus denote the relative population of the respective excited states. For details see text.

From Fig. 6.6 it is clear, that after absorption of excitation laser light by the B800

bacteriochlorophyll molecules, only 9 % of the energy is transferred to the B830 BChl a molecules and 91 % result in population of the newly identified state CT. When excitation energy is located on the B830 BChl pigments, it may either relax into the ground state within 750 ps or alternatively a bacteriochlorophyll triplet may be generated within 10 ns. This bacteriochlorophyll triplet will then either relax within a lifetime of 70 μs or alternatively be transferred to an adjacent carotenoid molecule multiple orders of magnitude faster, within about 1 ns. In consequence, the quantum yield for the generation of carotenoid triplet excitations upon excitation of bacteriochlorophyll pigments within the LH2 complex, is calculated to amount to only 0.63 %.

Next, the flow of energy is considered for excitation of carotenoid pigments within the LH2 complex of *Mch. purpuratum*. In analogy to the situation just described, the flow of energy is visualized for excitation of carotenoid pigments in Fig. 6.7. For each transition the distinct transfer time as well as the relative flow of energy is indicated, according the quantum yields of the distinct transition steps. As before, the values of the quantum yields were calculated from the ratio of transfer rates, each given by the inverse of the distinct transfer time.

Upon excitation of the carotenoid pigments about 75% of energy are transferred to the B830 pool of bacteriochlorophyll pigments and 25% are transferred to the S_1 state of the carotenoids via internal conversion processes, whereas triplet generation within the carotenoid molecules is almost negligible. From the S_1 state most of the energy (22.7%) is transferred to the B800 bacteriochlorophylls where only a small fraction is transferred to the B830 pigments. In total Fig. 6.7 visualizes nicely that for excitation of the carotenoid pigments about 75% of the excitation energy bypasses the B800 state and thus also the newly identified mixed-exciton charge transfer state CT. Hence, due to the quantum yield of intersystem crossing in BChl a as well as the highly efficient triplet-triplet energy transfer within the LH2 complex of *Mch. purpuratum*, the overall triplet generation yield upon excitation of carotenoid pigments within the B830 LH2 complex amounts to 5.5%.

As outlined above the triplet generation quantum yields either for excitation of bacteriochlorophylls (0.63%) and for excitation of carotenoids (5.5%) differ in about one order of magnitude. Hence, these significantly different quantum

yields of triplet formation support the idea outlined above that upon excitation of either the bacteriochlorophyll pigments or the carotenoid molecules significantly different situations of triplet excitations within the LH2 complex of *Mch. purpuratum* occur, giving rise to the occurrence of TTA for excitation of the carotenoid pigments. In consequence, resulting in the fact that for excitation of carotenoids in the B830 LH2 complex no triplets are available for the occurrence of singlet-triplet annihilation (STA).
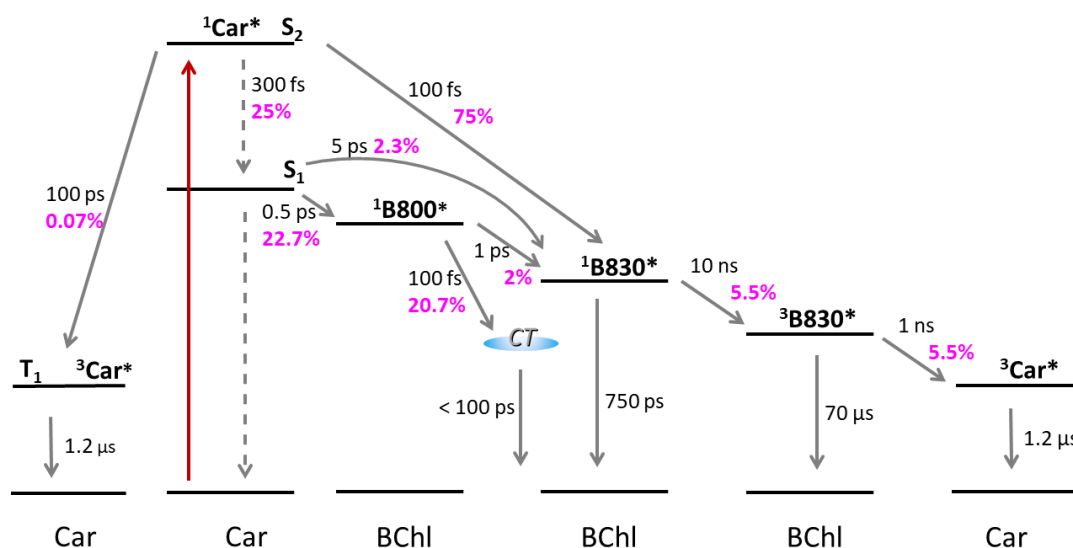
Figure 6.7.: Flow of energy within the LH2 complex of Mch. purpuratum upon excitation of carotenoids: The energy level scheme of the LH2 complex of Mch. purpuratum is shown for excitation of carotenoid pigments, including the pathways of the downhill flow of energy. The excited states of the three groups of pigments, the B800 BChl a molecules, the B830 BChl a molecules and the Car molecules, are shown as single energy levels as before. Besides the values of the characteristic timescales of the energy transfer steps, in addition also the values of the quantum yields of the distinct energy transfer process are given in magenta color. Those percentage values refer to the initially excited state and thus denote the relative population of the respective excited states. For details see text.

The trend of a fundamental different situation of triplet excitations in the LH2 complex of *Mch. purpuratum* upon excitation of bacteriochlorophylls or carotenoids is further validated by considering the exemplary situation of one single LH2 complex excited by a series of laser pulses and calculating the resulting triplet population[7]. In dependence of the ratio of the temporal separation of the laser pulses with respect to the carotenoid triplet lifetime of 1.2 μs [57] a steady

---

[7]The details of the calculation are given in Appendix F.

state triplet population accumulates within the LH2 complex after a few hundred laser pulses. In Fig. 6.8 the evolution curves of the triplet population within the LH2 complex of *Mch. purpuratum* are shown for excitation of bacteriochlorophylls as well as for excitation of carotenoids at the highest excitation density, given by the product of the laser repetition rate and the excitation photon fluence, thus corresponding to the situation of the maximum number of triplets in the experiments.

(a) excitation of bacteriochlorophylls   *(b) excitation of carotenoids*
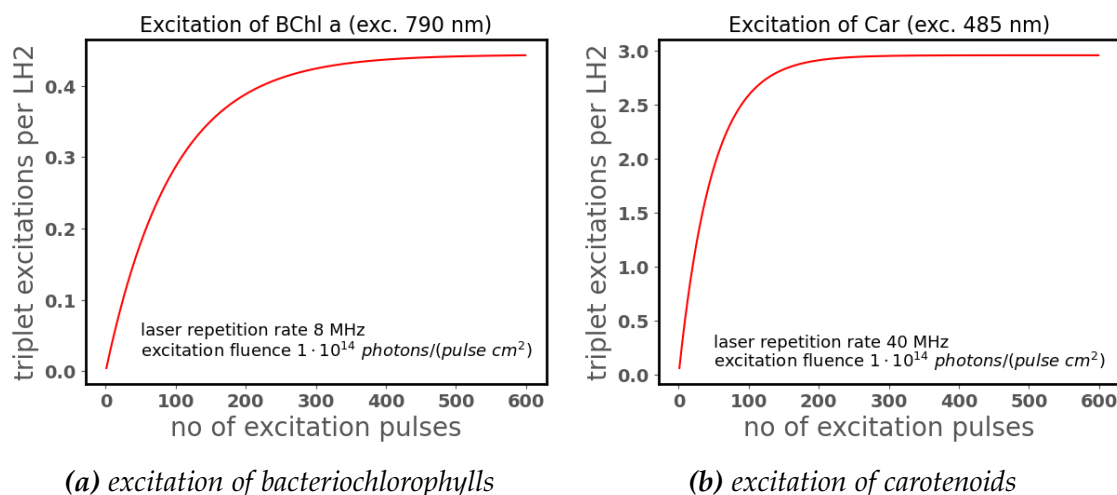
Figure 6.8.: Triplet population evolution curves: *Calculated evolution of the number of triplet excitations in the LH2 complex of Mch. purpuratum is shown as a function of the number of excitation laser pulses for a fluence of $1 \cdot 10^{14}$ photons/$(pulse \cdot cm^2)$ for excitation of bacteriochlorphylls at 790 nm (a) at a laser repetition rate of 80 MHz and for excitation of carotenoid pigments (b) at a laser repetition rate of 40 MHz. For details see text.*

For excitation of bacteriochlorophylls a steady state population of 0.44 triplets per LH2 complex is reached within about 500 excitation laser pulses, corresponding to $6.25\,\mu$s, see Fig. 6.8a. In contrast, for excitation of the carotenoid pigments a steady state triplet population of 2.96 triplets per LH2 complex is reached within about $5\,\mu$s corresponding to 500 excitation pulses, see Fig. 6.8b. Both saturation times are short with respect to the integration times of the experiments of 60 ms and 120 s for excitation of bacteriochlorophyll and carotenoid pigments, respectively, see Chapter 3, and thus reflect the situation of the experiments well. As already indicated by the significantly different quantum yields of triplet generation upon excitation of either of the two pigments, the calculated steady state triplet population for excitation of the carotenoid pigments exceeds the value obtained for excitation of bacteriochlorphylls by almost one order of

magnitude.

Considering the fact that the steady state triplet populations calculated above reflect the expectation value of a Poisson distribution, the probability that an LH2 complex carries one, two or multiple triplet excitations can be calculated[8]. Hence, for excitation of bacteriochlorophylls the probability that an LH2 complex carries one triplet excitation is 28%, whereas the accumulated probability that an LH2 complex carries two or more triplet excitations is only about 7%. In contrast, the situation for considering excitation of the carotenoid pigments appears fundamentally different. Whereas the probability that an LH2 complex carries one triplet excitation amounts to 15%, the probability that an LH2 complex carries up to 5 triplet excitations accumulates to 62%. Considering in addition that two triplet excitations have to be located on adjacent carotenoid molecules then allows for estimation of the probability that TTA may occur in the LH2 complex of *Mch. purpuratum* to values of 1.3 % for excitation of bacteriochlorophylls and 15.7 % for excitation of the carotenoid pigments, respectively. Hence, these estimations[9] corroborate the interpretation that excitation of either of the two pigments, bacteriochlorophylls or carotenoids, result in fundamentally different situations of triplet excitations within the LH2 complex such that upon excitation of the carotenoid pigments the occurrence of TTA is very likely and thus results in the fact that almost no triplet excitations are available for singlet-triplet annihilation processes.

In summary, besides the fact that the heptameric symmetry of the B830 LH2 complex of *Mch. purpuratum* already results in overall smaller interpigment distances in comparison to LH2 complexes from other species of purple bacteria [96], in addition the peculiarity that in the molecular structure of LH2 complex each apoprotein pair features two carotenoid molecules of okenone promotes this effect. In total, both aspects highly favor the occurrence of TTA in the B830 LH2 complex of *Mch. purpuratum*, especially for high numbers of triplet excita-

---

[8]The detailed calculation is outlined in Appendix F.

[9]In order to allow for simplicity the estimation of the triplet populations outlined here does not yet consider that there is indication that the two carotenoid molecules within the B830 LH2 complex, Car1 and Car2, feature slightly different energy transfer behavior to the two pools of bacteriochlorphyll pigments within the LH2 complex, B800 and B830 [100]. Nonetheless, the trend of a fundamental different situation of triplet excitations upon excitation of either of the two pigments, bacteriochlorphylls or carotenoids, is clearly visible and a more detailed calculation would result in only minor changes of the number values.

tions. Overall it appears to be the fact that the specialty of its molecular structure in combination with the newly proposed, additional emissive state *CT* within the electronic structure of the LH2 complex of *Mch. purpuratum* both together result in the fact that no lifetime component indicating the occurrence of STA is observed in the experiments upon excitation of the carotenoid pigments.

6.7. Summary of the discussion of the observed kinetics of the B830 LH2 complex

The multiexponential kinetics which was revealed by phasor analysis of the experimental fluorescence transients of the LH2 complex of *Mch. purpuratum* was discussed regarding different aspects. Mainly two central questions were to answer: First, what is the molecular origin of the up to three lifetime components identified in fluorescence emission? And second, why is the third lifetime component only observed for excitation of BChls but is not observed for excitation of carotenoid pigments?

The first aspect of the identification of the up to three lifetime components of the fluorescence emission was addressed. Regarding the biexponential kinetics which was observed for all excitation densities, given by the product of the laser repetition rate and the excitation photon fluence, and irrespective of the excitation of bacteriochlorophylls or carotenoid pigments, an influence of excitation annihilation processes could be ruled out. In consequence, the longer lifetime component of about 750 ps was identified as the fluorescence lifetime of the B830 pool of bacteriochlorophyll pigments and the fast lifetime component of below 100 ps was attributed to the fluorescence emission of another emissive state within the energy level scheme of the LH2 complex. In analogy to previous findings of a biexponential decay for an LH2 complex featuring lifetime components of 700 ps and 70 ps [8], the additional emissive state resulting in the fast lifetime component identified in the experiments on the B830 LH2 complex of *Mch. purpuratum* in this thesis is proposed to be a mixed exciton charge-transfer state *CT*. The appearance of such mixed exciton charge-transfer states in bacterial LH2 complexes and their involvement in the spectroscopic properties are under discussion in the literature since the 1990s, see Section 6.4.2.

Concerning the aspect of a third lifetime component observed exclusively for excitation of the bacteriochlorophyll pigments for high excitation densities, it was discussed that this lifetime component of about 500 ps can be attributed to the occurrence of singlet-triplet annihilation (STA) within the LH2 complex of *Mch. purpuratum*. Calculating the rate of singlet-triplet annihilation from the experiments in this thesis results in a value of $k_{STA} = 6.3 \cdot 10^8 \, s^{-1}$, which is higher than but still in the same order of magnitude of previously reported values for LH2 complexes from different species of purple bacteria [3]. However, the increased value for the LH2 complex of *Mch. purpuratum* might reflect the specialty of its molecular structure, featuring two carotenoids per apoprotein pair, thus likely resulting in a higher number of possible triplet excitations.

Finally, the discussion of the up to three lifetime components resolved in the experiments allowed for the formulation of an energy level scheme for the B830 LH2 complex of *Mch. purpuratum*, reflecting its electronic structure, see Section 6.5.

The second main aspect addressed in the discussion was the difference in the observed fluorescence kinetics upon excitation of either the bacteriochlorophylls or the carotenoid pigments. Whereas for excitation of bacteriochlorophylls a third lifetime component attributed to the occurrence of singlet-triplet annihilation was identified in the overall multiexponential fluorescence kinetics, no such lifetime component was identified for excitation of carotenoids. Singlet excitations are created within the LH2 complex by every excitation laser pulse by absorption of photons, hence the non-occurrence of singlet-triplet annihilation processes, which is indicated by the absence of a third lifetime component, must result from a lack of triplet excitations. Considering the possibility of excitation annihilation processes, triplet-triplet annihilation (TTA) is the only mechanism that influences the number of triplets within the LH2 complex.

Using the newly constructed energy level scheme of the LH2 complex of *Mch. purpuratum* as a starting point it is clear that the generation of triplets and thus the situation of triplet excitations within the LH2 complex are fundamentally different whether the bacteriochlorophyll pigments or the carotenoids are excited. Moreover, from the recently published molecular structure [96] there is

155

profound indication from the small interpigment distances that TTA might occur within the LH2 complex of *Mch. purpuratum*. Hence, on the basis of these two aspects and in addition an estimation of the triplet excitations within an LH2 complex as a function of the excitation conditions, determined by laser repetition rate and excitation photon fluence, the missing of a lifetime component indicating the occurrence of STA in the experiments for excitation of the carotenoids pigments of this thesis can be attributed to the occurrence of TTA in the LH2 complex very likely.

In order to test the energy level scheme of the B830 LH2 complex of *Mch. purpuratum* proposed within this section, next dynamic Monte-Carlo simulations will be performed.

7. Modelling of electronic excitations in isolated LH2 complexes of *Mch. purpuratum*

In order to test the simplified energy level scheme shown in Fig. 6.4 numerical simulations using the Dynamic Monte Carlo (DMC) method are performed. The use of the DMC method to perform numerical simulations of the kinetics of a multichromophoric system, such as bacterial light-harvesting complexes, is a widely known principle [3, 69, 160, 161] and the DMC algorithm is well described in the literature [162, 163, 164].

Below, a rate model based on the energy level scheme of the B830 LH2 complex of *Mch. purpuratum* is developed for excitation of bacteriochlorophylls. The resulting simulated fluorescence transients are compared with the experimentally obtained fluorescence transients for testing of the energy level scheme that was derived from the observed multiexponential kinetics. In addition also a phasor analysis is performed for the simulated data in order to investigate the underlying kinetics.

7.1. A model for electronic excitations in the LH2 complex upon excitation of bacteriochlorophylls

In references [3, 69] a rate model was developed by Pflock and coworkers to describe the kinetics of isolated LH2 complexes of *Rps. acidophila* [3] and clusters of such LH2 complexes [69]. In order to allow for comparison of the rate models a similar color code and similar graphical representation is chosen in the following development of a rate model for the isolated B830 LH2 complex of

157

Mch. purpuratum.

Starting point of the rate model for the simulation of the fluorescence kinetics of the B830 LH2 complex is a simplified energy level scheme shown on the left hand side of Fig. 7.1, which is mostly identical to Fig. 6.4. The only difference is the relaxation of the excitation energy via the newly proposed mixed exciton *CT* state, which is depicted as a one-step relaxation process as outlined below.
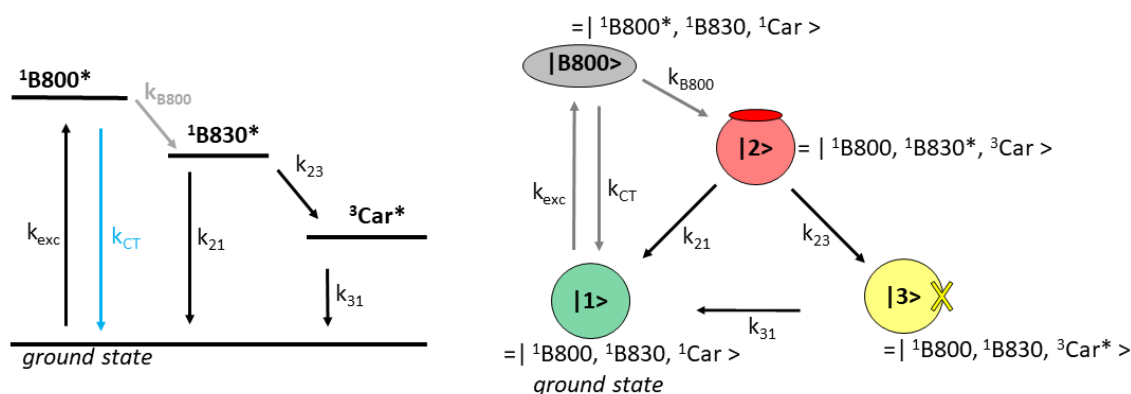
Figure 7.1.: Electronic excitations within the B830 LH2 complex of Mch. purpuratum: *On the left hand side a simplified energy level scheme is shown. The excited states of the three groups of pigments, the B800 BChl a molecules, the B830 BChl a molecules and the Car molecules, are shown as single energy levels. The singlet excitation levels of the B800 and the B830 ring are denoted as ^{1}B800* and ^{1}B830*, respectively. The triplet states of the Car molecules is referred to as ^{3}Car*. The relaxation of energy from the ^{1}B800* state into the ground state via the newly proposed CT state is shown as a single step (light blue arrow). On the right hand side a pictorial representation of the different electronic states of the B830 LH2 complex of Mch. purpuratum including the possible transitions between those states is shown. Different electronic states of the B830 LH2 complex are coded by color, the small ellipses and crosses attached to the big colored circle representing the LH2 complex visualize singlet and triplet excitations within the LH2 complex, respectively. For details see text.*

Absorption of the excitation laser light at a wavelength of 790 nm results in excitation of the B800 BChl *a* molecules as already explained in detail earlier. Then, alternatively relaxation of the excitation energy into the newly identified mixed exciton charge-transfer state *CT* or energy transfer to the B830 BChl *a* molecules can occur, compare also Fig. 6.4. As the population of the state *CT* happens within approximately 60 fs [8], which is much faster than the temporal resolution of the experiments in this thesis, for modelling of the electronic excitations within the LH2 complex the relaxation of energy via the *CT* state is simplified

into a one-step relaxation process in the following with a single rate k_{CT}, given by the inverse of the lifetime of the mixed-exciton *CT* state, $k_{CT} = (50\,ps)^{-1}$. The other energy transfer processes within the LH2 complex are identical to those discussed in detail in Section 6.5, compare also Fig. 6.4. The transfer rates are renamed in analogy to the right hand side of Fig. 7.1, following the principle that the subscript of the specific rate k_{ij} refers to the transition from the starting state i to the final state j.

On the right hand side of Fig. 7.1 a pictorial representation of the different electronic states of the B830 LH2 complex and the transitions between these states are shown. An LH2 complex in the electronic ground state is represented as a circle of green color. This state is denoted as state $|1\rangle = |^1B800,^1B830,^1Car\rangle$ as both, the BChl *a* molecules in the two groups of molecules, B800 and B830, as well as the Car molecules within the LH2 complex, are in the ground state and do not carry any excitation. Absorption of excitation light of a wavelength of 790 nm is represented by the rate k_{exc} and results in the excited state $^1B800^*$ of the B800 BChl *a* molecules, depicted as grey ellipse and denoted as $|B800\rangle = |^1B800^*,^1B830,^1Car\rangle$. In analogy to the energy level scheme on the left, relaxation of the energy of the $|B800\rangle$ state into the ground state can occur via the newly identified *CT* state as represented by the rate $k_{CT} = (50\,ps)^{-1}$ or alternatively the energy of the $|B800\rangle$ state can be transferred to the excited state $^1B830^*$ of the B830 BChl *a* molecules with the rate $k_{B800} = (1\,ps)^{-1}$ [47]. An LH2 ring carrying a $^1B830^*$ state is represented as a red circle with an additional red ellipse to visualize the $^1B830^*$ state. This state is denoted as $|2\rangle = |^1B800,^1B830^*,^1Car\rangle$ as it carries one excitation in the $^1B830^*$ state while the B800 BChl *a* molecules and the Car molecules are in the ground state. From state $|2\rangle$ either relaxation into the ground state $|1\rangle$ can occur, corresponding to fluorescence emission, as depicted by the rate $k_{21} = (730\,ps)^{-1}$ given by the fluorescence lifetime of the B830 bacteriochlorophylls from the experiments of this thesis, or intersystem crossing can lead to the formation of a triplet excitation on the carotenoid molecules. An LH2 complex which carries a triplet excitation $^3Car^*$ of the carotenoid molecules but no excitation of the B800 and B830 BChl *a* molecules is denoted as state $|3\rangle = |^1B800,^1B830,^3Car^*\rangle$ and is depicted as a yellow circle with a yellow cross to represent the triplet excitation. Thus, the rate of intersystem crossing is named k_{23}. Finally, relaxation of the triplet excitation into the ground state can occur as transition from state $|3\rangle$ to state

|1> which is represented by the rate k_{31}. The values of the rates $k_{23} = (20\,ns)^{-1}$ and $k_{31} = (1.2\,\mu s)^{-1}$ are taken from the literature [53, 57].

In order to account for the occurrence of excitation annihilation processes within the LH2 complex of *Mch. purpuratum* multiple excitations on one LH2 ring have to be considered. Hence, the excitation of an LH2 complex yet carrying an electronic excitation has to be included in the model. In principle, both states, state |2> as well as state |3> of the LH2 complex, shown in red and yellow color respectively in Fig. 7.1, could be re-excited. However, from the laser repetition rates in the experiments of this thesis and the corresponding temporal separation of the excitation laser pulses it is clear that in principle only LH2 complexes carrying a triplet excitation will be re-excited[1]. Thus, in order to allow for re-excitation of LH2 complexes resulting in multiple excitations on one LH2 complex the simplified pictorial representation on the right hand side of Fig. 7.1 is expanded to a larger rate model now representing also multiple electronic excitations per LH2 complex and allowing for excitation annihilation processes as shown in Fig. 7.2.
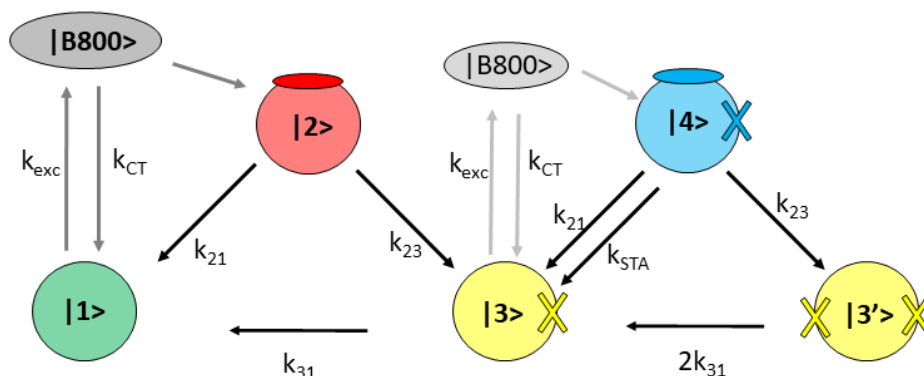
Figure 7.2.: Pictorial representation of the transitions between electronic states of an isolated B830 LH2 complex of Mch. purpuratum: The different electronic states of the B830 LH2 complex of Mch. purpuratum and the possible transitions between these states are shown. Different electronic states of the B830 LH2 complex are coded by color, the small ellipses and crosses attached to the big colored circle representing the LH2 complex visualize singlet and triplet excitations within the LH2 complex, respectively. The excitation process of the LH2 complex via the B800 ring of BChl a molecules is visualized in grey color as before on the right hand side of Fig. 7.1. For details see text.

---

[1]An entire model considering all possible re-excitations is outlined in Appendix G.1.

As pointed out above, absorption of excitation light results in the creation of a singlet excitation within the ring of B830 BChl *a* molecules of the B830 LH2 complex. This transition from the electronic ground state |1> , depicted as a green circle, to state |2> corresponding to an LH2 complex carrying a singlet excitation within the ring of B830 BChl *a* molecules, depicted in red color, always happens via the |B800> state, visualized in grey. In order to allow for a simplified visualization the excitation process of the LH2 complex resulting in the creation of a singlet excitation within the B830 ring BChl *a* molecules is always visualized in pale grey color whenever an additional singlet excitation is created. Hence all the pale grey ellipses denoted as |B800> in Fig. 7.2 refer to excitation processes of the LH2 complex.

When an LH2 complex in state |3>, already carrying a triplet excitation of the carotenoid molecules and depicted in yellow color, is excited again, this results in the formation of a new singlet excitation of the B830 BChl *a* molecules. Such an LH2 ring which carries one singlet excitation and one triplet excitation is depicted in Fig. 7.2 as a blue circle hosting a blue ellipse representing the singlet excitation ^{1}B830* of the B830 molecules and hosting a blue cross representing the triplet excitation ^{3}Car*. The resulting state is denoted as state |4>=|^{1}B800,^{1}B830*,^{3}Car*>. Now, starting from state |4> several transitions are possible. One possible pathway is the transition to state |3>, represented by a yellow circle with one yellow cross, either upon radiative relaxation under emission of fluorescence with a rate $k_{43} = k_{21}$ or by the occurrence of singlet-triplet annihilation (STA) with a rate $k_{STA} = 6.3 \cdot 10^8 \, s^{-1}$, which was identified from the experiments as outlined in Section 6.3. Alternatively, also intersystem crossing can take place with the rate k_{23} resulting in an electronic state of the LH2 complex which carries two triplet excitations, represented as a yellow circle with two yellow crosses, and which is denoted as state |3'>=|^{1}B800,^{1}B830,^{3}Car*,^{3}Car*>. The transition from state |3'> to state |3> happens nonradiative with a rate $k_{3'3} = 2 k_{31}$, as both tripet excitation are assumed to decay independently.

Finally, using the model depicted in Fig. 7.2 only a few transition rates, some taken from the experiments and some from the literature, are needed to allow for modelling of electronic excitations within the B830 LH2 complex of *Mch. purpuratum*. Simulations using this model soon showed a saturation in population of the double triplet state |3'>. Thus, the model outlined above and depicted

in Fig. 7.2 is not sufficient for qualitative modelling of the observed kinetics due to the observed saturation effect. So the rate model needs to be expanded to higher triplet states, such that an LH2 complex can carry multiple triplet excitations, in order to avoid saturation effects in the numerical simulations. Due to the recently published structural information of the B830 LH2 complex of *Mch. purpuratum* [96] that reports a heptameric ring structure, see also Section 2.5.1, the rate model in Fig. 7.2 is expanded in order to allow for up to seven triplets per LH2 complex[2], as shown in Fig. 7.3. In order to focus on the expansion of the rate model the excitation pathway of the B830 LH2 complex via the B800 BChl *a* molecules, which was discussed in detail before, is now only depicted schematically in pale grey color for reasons of better visualization.
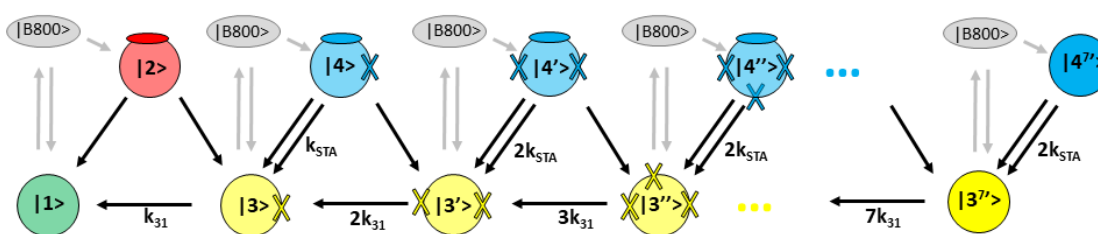
Figure 7.3.: Expanded pictorial representation of the transitions between electronic states of an isolated B830 LH2 complex of Mch. purpuratum: *The different electronic states of the B830 LH2 complex of Mch. purpuratum and the possible transitions between these states are shown. Different electronic states of the B830 LH2 complex are coded by color, the small ellipses and crosses attached to the big colored circle representing the LH2 complex visualize singlet and triplet excitations within the LH2 complex, respectively. The excitation process of the LH2 complex via the B800 ring of BChl a molecules is visualized in grey color as before in Figures 7.1 and 7.2. For details see text.*

In order to allow for easier identification of the different electronic states of the LH2 complex in the expanded model, in analogy to the smaller model an LH2 complex carrying no singlet excitation but any number of triplet excitations is always represented by a yellow circle and an LH2 complex carrying one singlet excitation plus any number of triplet excitations is always represented by a blue circle. On the right end of Fig. 7.3 the states corresponding to an LH2 complex carrying seven triplet excitations, one in each subunit of the LH2 complex, and either none or one singlet excitations on the B830 bacteriochlorophyll *a*

---

[2]Although the structure of the B830 LH2 complex features two carotenoid molecules per apoprotein subunit of the LH2 complex, here, in order to keep the model as simple as possible only one carotenoid triplet per apoprotein pair is assumed.

molecules are shown as filled circles of yellow and blue color, respectively. For reasons of simplicity and visualization, these states corresponding to electronic states of the LH2 complex carrying seven triplets, the number of triplets are not visualized by crosses anymore. The naming of those higher triplet states is $|3^{7'}\rangle$ and $|4^{7'}\rangle$ in analogy to the nomenclature of the states $|3\rangle$ and $|4\rangle$ featuring a superscript number to indicate the number of triplet excitations.

Concerning the transitions between the different electronic states of the LH2 complex, the black arrows indicate the transitions as outlined in detail above for the smaller rate mode. The transition rates are mostly adapted from the smaller rate model shown in Fig. 7.2 with only one exception: The rate for the triplet relaxation is assumed to depend on the number of triplets carried by one LH2 complex as triplets are assumed to decay independently. Thus, the triplet relaxation rates between the electronic states that only contain triplet excitations are build according to the following principle: $k_{3'3} = 2\,k_{31}$, $k_{3''3'} = 3\,k_{31}$ and so on, which is also shown in Fig. 7.3.

7.2. Simulated fluorescence transients of the B830 LH2 complex for excitation of bacteriochlorophylls

In order to test the energy level scheme that was deduced from the measured fluorescence transients, numerical simulations were performed in collaboration with Dr. Johannes Förster, University of Bayreuth[3]. For these simulations the expanded rate model developed in this thesis and outlined above, compare Fig. 7.3, was used and a dynamic Monte Carlo (DMC) algorithm was implemented by Dr. Johannes Förster.

In Table 7.1 the input values of the transition rates of the expanded rate model that is used for the DMC simulations of the fluorescence kinetics of the B830 LH2 complex of *Mch. purpuratum* are summarized. Among all of the rates for the

---

[3]The development of the rate model on basis of the experiments of this thesis was done by Inga Elvers. The computational implementation of the rate model for the numerical DMC simulations was done by Dr. Johannes Förster. Analysis and evaluation of the simulated transients was done by Inga Elvers.

simulations, the rate k_{exc} for the excitation of the LH2 complex by absorption of laser light is calculated from the excitation photon fluence per pulse and squared centimeter, J_{exc}, and the absorption cross section $\sigma_{790\,nm}$ of the LH2 complex at the excitation wavelength of 790 nm for each simulation. The absorption cross section $\sigma_{790\,nm}$ of the LH2 complex at the excitation wavelength of 790 nm was determined[4] to $\sigma_{790\,nm} = 4.6 \cdot 10^{-15} cm^2$.

transition rate	values [s^{-1}]	reference
k_{exc}	$= J_{exc}\,\sigma_{790\,nm}$	
k_{CT}	$1.96 \cdot 10^{10}$	this thesis
k_{B800}	$1 \cdot 10^{12}$	[47]
k_{21}	$1.37 \cdot 10^9$	this thesis
k_{23}	$5 \cdot 10^7$	[53]
k_{31}	$8.3 \cdot 10^5$	[57]
k_{STA}	$6.3 \cdot 10^8$	this thesis

Table 7.1.: Input values of the transition rates for the numerical simulations

For each of the excitation parameter combinations of the excitation fluence and the laser repetition rate for which experiments were performed, also numerical simulations were performed. In order to allow for comparison, in Fig. 7.4 the normalized fluorescence transients obtained experimentally from the streak camera measurements and those resulting from the DMC simulations are shown as a function of the experimental parameters. Analogously to previous tabular arrangements in this thesis, the different columns in Fig. 7.4 correspond to different excitation photon fluences and different rows correspond to different laser repetition rates. For each of the excitation parameter combinations the experimentally obtained fluorescence transient, denoted as *Decay*, and the simulated fluorescence transient that was convoluted with the experimental IRF for reasons of comparability, denoted as *Simulation*, are shown both normalized in one plot. Below each of the plots, the corresponding residual visualizes the difference of the experimental curve and the simulated curve.

---

[4]From the extinction of one B850 BChl *a* molecule in the 'standard' LH2 complex of $184 \cdot 10^3$ L/(mol· cm) [165], the extinction of the B830 BChl *a* molecules in the LH2 complex of *Mch. purpuratum* is approximated by $\epsilon_{830} = 14 \cdot 184 \cdot 10^3\ L/(mol \cdot cm) = 2.6 \cdot 10^6\ L/(mol \cdot cm)$. Thus, scaling with the relative absorption at 790 nm (0.46 with respect to the B830 peak) yields $\epsilon_{790\,nm} = 1.2 \cdot 10^6\ L/(mol \cdot cm)$. The absorption cross section can be obtained by the conversion $\sigma_{790\,nm} = ln(10) \cdot \epsilon_{790\,nm}/N_A$, with N_A being Avogadro's number.
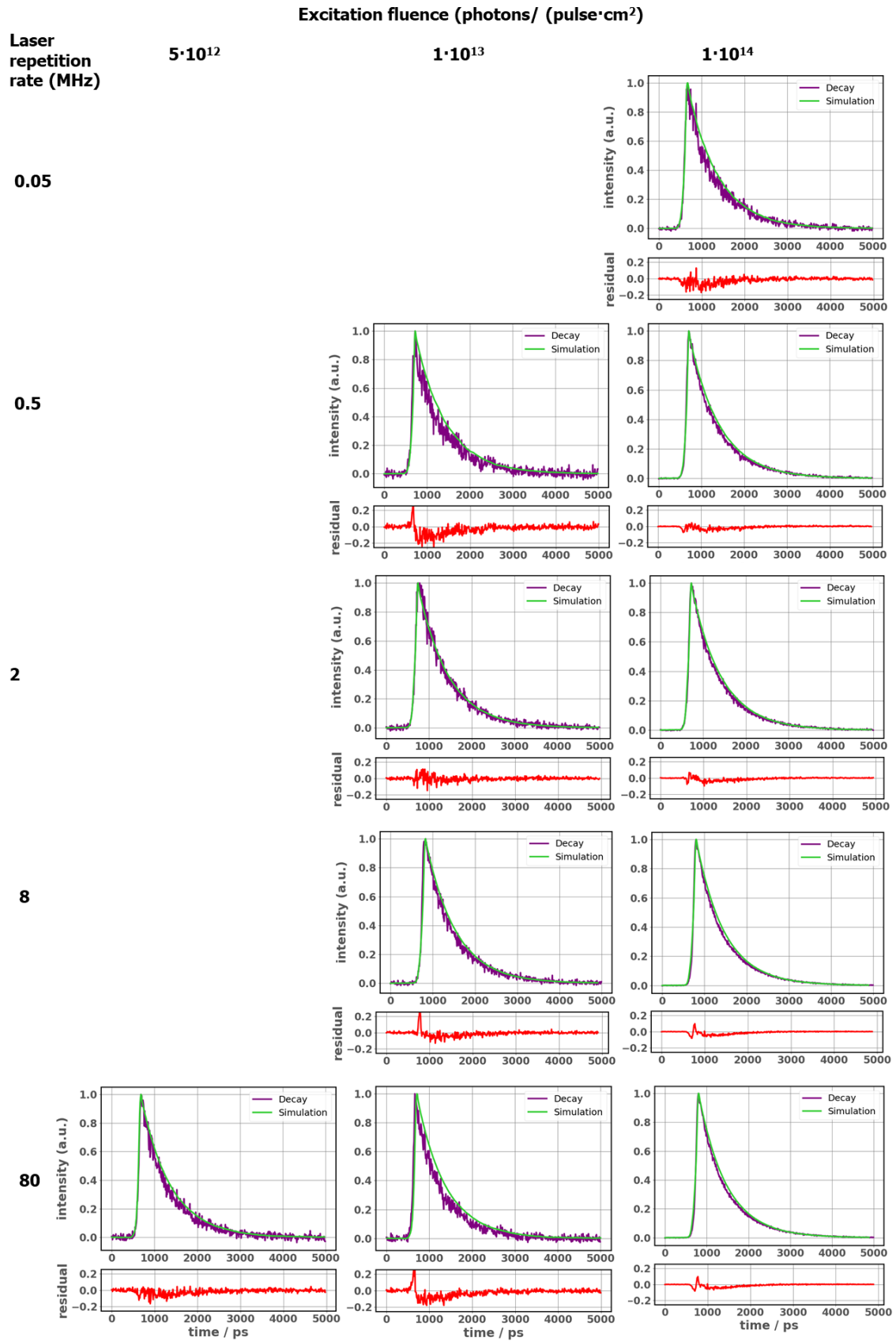
Figure 7.4.: Comparison of experimental and simulated fluorescence transients: For details see text.

The comparison of the simulated fluorescence transients and those obtained experimentally in Fig. 7.4 shows qualitative good agreement of the two curves for almost all of the excitation parameter combinations. The pronounced fluctuations of the otherwise mostly flat residuals located around the maximum intensity of the transient curves can be attributed to the noise of the measured fluorescence signal. The positive peaking signal of the residual observed for some excitation parameter combinations and occurring at the almost instantaneous rise of the fluorescence signal is attributed to the fact that the simulated fluorescence transient was convoluted with the experimentally obtained IRF.

Besides the qualitative good agreement of the simulated fluorescence transients and those resulting from the experiments, see Fig. 7.4, next the kinetics of the simulated fluorescence transients are analyzed. In analogy to the evaluation of the experimentally obtained fluorescence transients the phasor approach is applied to the fluorescence transients resulting from the DMC simulations and a phasor analysis is performed. Thus, first a biexponential kinetics is assumed for low laser repetition rates and then it is checked whether the phasors corresponding to fluorescence transients of higher excitation densities, given by the product of the laser repetition rate and the excitation photon fluence, correspond to this biexponential kinetics or whether an additional lifetime component is needed[5].

For low laser repetition rates a biexponential kinetics with lifetime components of 712 (+ 19/- 8) ps and 216 (+ 152/- 117) ps is identified[6]. The lifetime component of about 730 ps of the experimentally observed kinetics for excitation of bacteriochlorophylls is nicely reproduced. Although the fast lifetime component, amounting to 216 ps for the simulated transients, appears to be significantly lager than the experimentally obtained value of 50 ps, considering the confidence intervals of both values shows that both lifetime values agree within the limits of their uncertainty and correspond to a fast lifetime of below 100 ps. Hence, the biexponential kinetics observed for low laser repetition rates in the experiments is reproduced by the DMC simulations. The results of a phasor analysis for all simulated fluorescence transients are summarized in Table 7.2 as a function of the excitation parameters. Different columns correspond to

---

[5]The detailed phasor analysis is outlined in Appendix G.2.
[6]The asymmetric values of the uncertainty of the lifetime components is due to the nonlinear scaling of the ruler of lifetimes along the universal semicircle, see also Appendix C.

different excitation fluences, increasing from left to right, and different rows correspond to different laser repetition rates, increasing from top to bottom.

laser repetition rate (MHz)	excitation fluence $\frac{photons}{pulse \cdot cm^2}$		
	$5 \cdot 10^{12}$	$1 \cdot 10^{13}$	$1 \cdot 10^{14}$
0.05			712 ps (0.94)
			216 ps (0.06)
0.5		712 ps (0.95)	712 ps (0.95)
		216 ps (0.05)	216 ps (0.05)
2		712 ps (0.95)	712 ps (0.92)
		216 ps (0.05)	216 ps (0.08)
8		712 ps (0.94)	712 ps (0.83)
		216 ps (0.06)	216 ps (0.05)
			437 ps (0.12)
80	712 ps (0.92)	712 ps (0.81)	712 ps (0.28)
	216 ps (0.08)	216 ps (0.05)	216 ps (0.02)
		464 ps (0.14)	455 ps (0.71)

Table 7.2.: Lifetime components and their fractional contributions for the multi-exponential kinetics of simulated fluorescence transients considering excitation of bacteriochlorophyll pigments

The biexponential kinetics with lifetime components of 712 ps and 216 ps shows similar fractional contributions for almost all excitation parameter combinations in Table 7.2. The average of the fractional contributions amounts to 0.93 and 0.07, respectively, which is in excellent agreement with the experiments, compare Section 5.2.3. For high laser repetition rates in combination with high excitation fluence, a third lifetime component in the order of 450 ps is identified in the phasor analysis. This value is in the same order of magnitude as the values of the third lifetime components of the experiments, compare Section 5.2.3 and especially Table 5.6. Whereas the fractional contributions for the excitation parameter combinations of 8 MHz and an excitation fluence of $1 \cdot 10^{14}$ photons/(pulse·cm^2) agrees well with the values resulting from the analysis of the experiments, for the highest laser repetition rate of 80 MHz a significant difference of the fractional contributions is observed for the excitation fluences $1 \cdot 10^{13}$ photons/(pulse·cm^2) and $1 \cdot 10^{14}$ photons/(pulse·cm^2) with respect to the experimental data, compare Table 5.6.

For the current simulation the value of the singlet-triplet annihilation rate k_{STA} was determined from the lifetimes resulting from phasor analysis of the experiments, compare Section 6.3. There it was already mentioned that this value is slightly higher than the value of $1.3 \cdot 10^8\, s^{-1}$ reported before for the LH2 complex of *Rps. acidophila* [3]. Hence, in the following two refinement approaches for the simulations are presented considering alternative values for the singlet-triplet annihilation rate k_{STA}.

7.3. Refinement approaches of the DMC simulations by variation of k_{STA}

For the DMC simulations described above a value of $6.3 \cdot 10^8\, s^{-1}$ was used for the singlet-triplet annilihation rate k_{STA} as determined from the experiments of this thesis. Next, two alternative simulations will be considered, refinement 1, using the value of $1.3 \cdot 10^8\, s^{-1}$ reported for STA in LH2 complexes of *Rps. acidophila* [3], and a second refinement using a value of $2 \cdot 10^9\, s^{-1}$ determined from simulations of LH2 complexes of *Rps. acidophila* [69].

Refinement 1: smaller k_{STA}

The rate model used for the simulations in this first refinement is identical to the model outlined before in detail in Section 7.1. Also the number values of the transitions rates are in principle identical with only one exception, which is the rate for singlet-triplet annihilation k_{STA}, which now amounts to $1.3 \cdot 10^8\, s^{-1}$ and is taken from [3].

The refined simulations with a smaller value for k_{STA} reproduce the experimental fluorescence transients well as it can be see in the tabular overview in Fig. G.4 in Appendix G.3. Only for the highest excitation density resulting from the combination of a laser repetition rate of 80 MHz and an excitation fluence of $1 \cdot 10^{14}$ photons/(pulse·cm^2) a difference of the refined simulated curve with respect to the basic simulation is observable, see Fig. 7.5. The experimental observed fluorescence transient is plotted in purple and denoted as *Decay*, whereas the simulated transient is shown in green color for the basic simulations using the experimentally determined value for k_{STA}, denoted as *Simulation*. In blue color

the fluorescence transient resulting from the refined simulations using a smaller value of $k_{STA} = 1.3 \cdot 10^8 \, s^{-1}$ is shown. As it can be clearly seen, the refined simulated transient decays slightly slower than both, the fluorescence transient from the basic simulation as well as the experimental *Decay* curve in Fig. 7.5.

Figure 7.5.: Comparison of experimental and simulated fluorescence transients for different values of k_{STA} in the simulations: For the excitation parameter combination of a laser repetition rate of 80 MHz and an excitation fluence of $1 \cdot 10^{14}$ photons/(pulse·cm^2), both the experimental and the simulated normalized fluorescence transients for k_{STA} determined from the experiments as well as for a smaller value of k_{STA} are shown. For details see text.

However, as the overall agreement of the simulated curves and the experimental fluorescence transients is good, a phasor analysis is performed[7]. As before, a biexponential kinetics is assumed for low laser repetition rates and by phasor analysis the lifetime components of 723 (+ 53/- 14) ps and 325 (+ 183/- 148) ps [8] are identified. Whereas the longer lifetime component is good reproduced with respect to the experiments, where a value of about 730 ps was observed, the fast lifetime component of about 50 ps seen in the experiments upon excitation of bacteriochlorophylls is not reproduced by the simulations. Instead a much longer lifetime of 325 ps appears in the refined simulations. A third lifetime component could not be identified at all from phasor analysis of the simulated transients.

---

[7]The details of this phasor analysis are outlined in Appendix G.3.

[8]The asymmetric values of the uncertainty of the lifetime components is due to the nonlinear scaling of the ruler of lifetimes along the universal semicircle, see also Appendix C.

Thus, in total using a smaller value for the singlet-annihilation rate k_{STA} does not result in a significant improvement of the numeric DMC simulations of the fluorescence kinetics of the LH2 complex of *Mch. purpuratum* with respect to the basic simulation using a value of k_{STA} obtained from the experiments in this thesis, see Section 7.2. Next, an alternative refinement using a higher value for k_{STA} in the DMC simulations is tested.

Refinement 2: higher k_{STA}

In the second refinement of the simulations the rate model used for the simulations is identical to the model outlined before in detail in Section 7.1. Also the number values of the transition rates are in principle identical with only one exception, namely the rate for singlet-triplet annihilation k_{STA} that is now increased to $2 \cdot 10^9 \, s^{-1}$ in accordance to a value reported before for simulations on LH2 complexes from *Rps. acidophila* [69].

The refined simulations now using a higher value for the singlet-triplet annihilation rate k_{STA} reproduce the experimental fluorescence transients overall well, as it can be see in the tabular overview in Fig. G.7 in Appendix G.3, with only one exception. For the highest excitation density resulting from the combination of a laser repetition rate of 80 MHz and an excitation fluence of $1 \cdot 10^{14}$ photons/(pulse·cm^2) a significant difference of the refined simulated curve with respect to the basic simulation is observable, see Fig. 7.6. The experimental observed fluorescence transient is plotted in purple and denoted as *Decay*, whereas the simulated transient from the basic simulations, denoted as *Simulation*, and the refined simulations using a higher value of $k_{STA} = 2 \cdot 10^9 \, s^{-1}$ are shown in green color and blue color, respectively. It can be clearly seen, that the refined simulated transient considering a higher value of k_{STA} decays significantly faster than both, the fluorescence transient from the basic simulation as well as the experimental *Decay* curve.

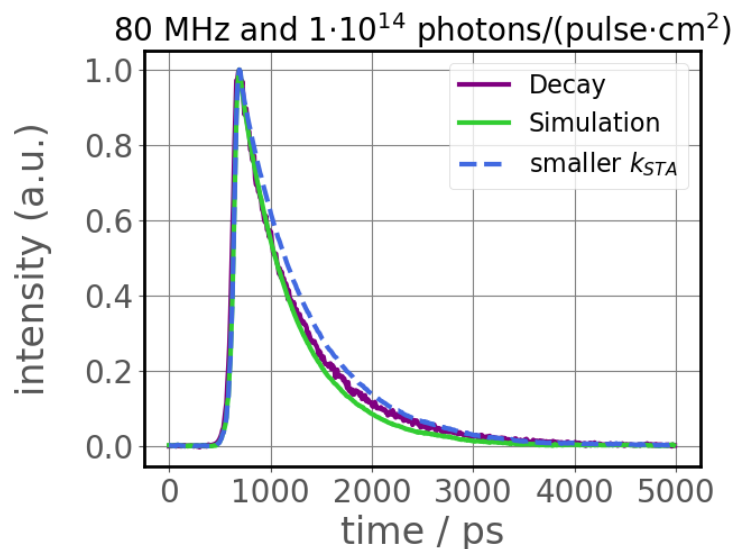However, besides this one exception the overall agreement of the simulated curves and the experimental fluorescence transients is good and a phasor analysis is performed[9]. A biexponential kinetics is assumed for low laser repetition

---

[9]The details of this phasor analysis are outlined in Appendix G.3.

rates and the phasor analysis yields lifetime components of 703 (+ 4/- 3) ps and 99 (+ 71/- 61) ps [10]. Notably, these two lifetime components reproduce the lifetime values of 730 ps and 50 ps determined from the experiments relatively well, considering to the tolerance intervals of the distinct values. The quantitative phasor analysis[11] is summarized in Table G.2 in Appendix G.3. A biexpoential kinetics with on average fractional contributions of 0.96 and 0.04 for the lifetime components of 703 ps and 99 ps, respectively, is observed, which is in good agreement with the experiments.
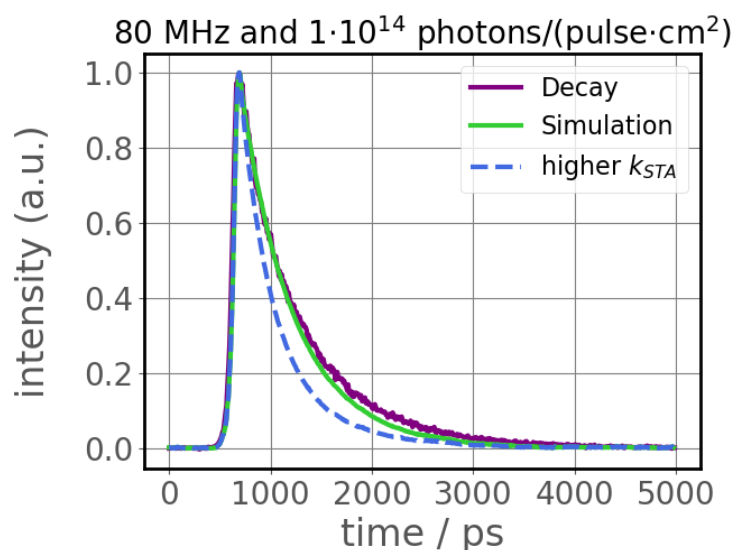
Figure 7.6.: Comparison of experimental and simulated fluorescence transients for different values of k_{STA} in the simulations: For the excitation parameter combination of a laser repetition rate of 80 MHz and an excitation fluence of $1 \cdot 10^{14}$ photons/(pulse·cm²), both the experimental and the simulated normalized fluorescence transients for k_{STA} determined from the experiments as well as for a higher value of k_{STA} are shown. For details see text.

Moreover, a triexponential kinetics was revealed to be necessary for the combination of high excitation densities, namely for the excitation parameter combinations of 8 MHz and an excitation fluence of $1 \cdot 10^{14}$ photons/(pulse·cm²) as well as for the combinations 80 MHz and $1 \cdot 10^{13}$ photons/(pulse·cm²), and 80 MHz and $1 \cdot 10^{14}$ photons/(pulse·cm²). The third lifetime components for these excitation parameter combinations were identified to amount to 304 ps, 420 ps and 455 ps with fractional contributions of 9%, 10% and 61%, respectively. Notably

---

[10]The asymmetric values of the uncertainty of the lifetime components is due to the nonlinear scaling of the ruler of lifetimes along the universal semicircle, see also Appendix C.

[11]The details of this phasor analysis are given in Appendix G.3.

the lifetime values are smaller than the values of about $500\,ps$ observed in the phasor analysis of the experiments and also the fractional contributions do not correspond to the experimental findings. In summary, the refinement of using a higher value for the singlet-triplet annihilation rate k_{STA} does not result in an improvement of the DMC simulations with respect to the basic simulation outlined above in Section 7.2.

7.4. Summary of the DMC simulations and outlook on possible further refinements

Starting point for the modelling of electronic excitations in isolated B830 LH2 complexes of *Mch. purpuratum* was the finding of an unexpected multiexponential fluorescence kinetics that was revealed by phasor analysis in Chapter 5. Discussion of the origin of the up to three lifetime components then allowed for the proposal of an energy level scheme for the B830 LH2 complex, see Chapter 6 and especially Section 6.5. Subsequently, in order to test this proposed energy level scheme a rate model was developed on basis of this energy level scheme, in order to allow for the performance of numerical simulations of the excitation kinetics within the B830 LH2 complex by means of a dynamic Monte Carlo (DMC) algorithm.

First, a simulation taking into account all the kinetic information from the experiments, such as considering the evaluation of all up to three lifetime components observed in the experiments, was performed. This basis simulation used a value of $6.3 \cdot 10^8\,s^{-1}$ for the singlet-annihilation rate k_{STA}. Overall, both the fluorescence transients as well as the kinetics of the experiments were reproduced by this basis simulation in good quality. Comparison of the experimental and simulated fluorescence transients showed only minor deviations, which are mostly attributed to noise of the experimental data. Concerning the kinetic evaluation of the DMC simulations by a phasor analysis, see Section 7.2, all three lifetime components observed in the experiments were reproduced and also the fractional contributions showed good agreement with the experimental kinetics, except for the highest excitation density, corresponding to the highest laser repetition rate of $80\,MHz$ at highest excitation fluence of $1 \cdot 10^{14}$ photons/(pulse·cm^2).

172

When the value of the singlet-triplet annihilation rate k_{STA} was determined from the experimental data it was mentioned that this value is larger than the value previously reported for the 'standard' LH2 complex from *Rps. acidophila* [3]. Hence, it was tested whether a variation of the value for the singlet-triplet annihilation rate k_{STA} influences the results of the DMC simulations significantly. As a first refinement, a smaller value for k_{STA} was tested and this showed only minor influence on the shape of the fluorescence transients but a significant change of the underlying kinetics was observed. Neither was the biexponential kinetics observed for low laser repetition rates in the experiments fully reproduced, nor could a third lifetime component be identified for high excitation densities. So in a second refinement, a larger value of the singlet-triplet annihilation rate k_{STA} was used, as proposed from simulations of LH2 complex from *Rps. acidophila* [69]. This refined simulation showed overall good agreement of the fluorescence transients and the experimental decay curves, except for the combination of the highest laser repetition rate of 80 MHz and the highest excitation fluence of $1 \cdot 10^{14}$ photons/(pulse·cm^2). Evaluation of the kinetics of the simulated transients by phasor analysis then revealed that the multiexponential kinetics observed in the experiments was overall well reproduced with two major exceptions: First, the value of the third lifetime component was identified to be smaller in this refined simulations with respect to both, the experimental kinetics as well as to the kinetics of the basis simulation using the experimentally obtained value for k_{STA}. Second, although the fractional contributions of the distinct lifetimes were reproduced well within the entire data set, for the highest laser repetition rate a mismatch with respect to the values resulting from the phasor analysis of the experiments was observed for the excitation fluences of $1 \cdot 10^{13}$ photons/(pulse·cm^2) and $1 \cdot 10^{14}$ photons/(pulse·cm^2).

In summary, no significant improvement of the DMC simulations was achieved by variation of the singlet-triplet annihilation rate k_{STA}. The best overall agreement of the simulations and the experimental data regarding both, the shapes of the fluorescence transients and also the fluorescence kinetics, was observed for the basis DMC simulation considering the entire experimentally observed kinetic information. Hence, as the only discrepancy between simulations and experiments concerns the fractional intensity contribution of one excitation parameter combination within the entire data set, whereas all other kinetic properties are reproduced in good accordance, this basis simulation successfully confirms

173

the proposed energy level scheme for the LH2 complexes of *Mch. purpuratum*.

A detailed analysis of the entire simulation data revealed, that the observed discrepancy between experiment and simulation for the highest excitation density is likely due to a high number of triplets within the DMC simulations for these excitation conditions, see Appendix G.4. Nonetheless, although some additional refinements of the basis simulation presented here might be needed, the rate model presented for the DMC simulations in this thesis appears to be a promising candidate with regard to simulating the situation of electronic excitations within the LH2 complexes of *Mch. purpuratum* upon excitation of the bacteriochlorphyll pigments. However, both, a further refinement of the DMC simulations presented here as well as an adaption of the rate model for the simulation of the excitation of carotenoids pigments, goes beyond the scope of this thesis and moreover, gives space for additional considerations and investigations possibly resulting a complete separate thesis for itself.

8. Summary and Outlook

Detergent-isolated LH2 complexes of the purple bacterium *Marichromatium purpuratum* were studied in detergent solution (20 mM HEPES, 0.1% LDAO, pH 7.8) by time-resolved spectroscopy as a function of the excitation parameters, such as the excitation photon fluence and the laser repetition rate. Both, excitation of the incorporated bacteriochlorphyll pigments as well as excitation of carotenoid pigments was investigated. The aim of the time-resolved experiments was to investigate the fluorescence kinetics of the light-harvesting complexes and thus to investigate the kinetics of electronic excitations within the B830 LH2 complex of *Mch. purpuratum*.

The fluorescence transients of isolated LH2 complexes of *Mch. purpuratum* in detergent-solution were analyzed using the phasor approach for each of the different combinations of the excitation fluence and the laser repetition rate, and for excitation of either of the two pigments, bacteriochlorophylls or carotenoids, respectively. The phasor approach was originally formulated for fluorescence lifetime measurements in the frequency domain and was now adapted to lifetime measurements in the time domain. Recognizing the specific features of the fluorescence transients that were extracted from time-resolved measurements, here a procedure for the calculation of the phasor coordinates was developed including all necessary corrections, such as background correction and correction for the influence of the instrument response (IRF) function. The special strength of the phasor approach is that it allows for the analysis of the fluorescence kinetics without any *a priori* knowledge or assumption. Thus, the phasor approach allows for both a qualitative as well as quantitative analysis of the recorded fluorescence transients taking only into account the measured raw data and without making any assumption of the underlying kinetics as it is done for the 'traditional' fitting approach often seen in literature.

Whereas first inspection of the observed fluorescence transients indicated a mo-

noexponential kinetics, a more detailed analysis using the phasor approach revealed a multiexponential kinetics for all measured fluorescence transients of the isolated LH2 complexes of *Mch. purpuratum*. For excitation of bacteriochlorophyll pigments in the near-infrared (NIR) wavelength range, a global biexponential kinetics with lifetime components of 730 ps and 50 ps was revealed. In addition a third lifetime component of about 500 ps was observed in phasor analysis for high excitation densities, corresponding to the combination of high excitation fluence and high laser repetition rate. Upon excitation of the carotenoid pigments in the visible wavelength (VIS) range a biexponential kinetics featuring one lifetime component in the order of 750 ps and one faster lifetime of or below 100 ps was identified, hence showing almost the same biexponential kinetics as for bacteriochlorophyll excitation. Notably, no third lifetime component was observed for excitation of the carotenoid pigments.

The long fluorescence lifetime component of about 750 ps observed in the experiments is significantly quenched with respect to the usually reported fluorescence lifetime in the order of 1 ns for isolated LH2 complexes of various species of purple bacteria [1, 2, 3, 4]. Nonetheless, this lifetime component is attributed to the fluorescence emission of the B830 bacteriochlorophyll pigments within the LH2 complex of *Mch. prupuratum*. The fast lifetime component of below 100 ps which is observed for all excitation conditions is tentatively attributed to the occurrence of a yet not known or resolved mixed exciton charge-transfer (CT) state within the B830 LH2 complex of *Mch. purpuratum*. The occurrence of such mixed exciton CT states in bacterial LH2 complexes is under discussion since years [5, 6, 7] and is in accordance with the observed shortening of B830 fluorescence lifetime [8]. The third lifetime component observed exclusively for excitation of bacteriochlorophyll pigment at high excitation densities is attributed to the occurrence of singlet-triplet annihilation (STA) processes.

The identification of the different lifetime components in the multiexponential kinetics finally allowed for the evolution and proposal of an energy level scheme for the B830 LH2 complex of *Mch. purpuratum*. From this proposal of an energy level scheme, the origin of the difference in the observed fluorescence kinetics upon excitation of bacteriochlorophylls or carotenoids was discussed. Thus, the different flow of energy within the LH2 complex upon excitation of the different pigments results in fundamental different situations such that most likely the

occurrence of triplet-triplet annihilation results in the difference of the observed fluorescence kinetics.

In order to test the energy level scheme proposed for the LH2 complex of *Mch. purpuratum* numerical simulations using a dynamic Monte Carlo algorithm were performed, using a rate model based on the newly developed energy level scheme. A comparison of the fluorescence transients obtained experimentally and those resulting from the simulations showed an overall good agreement. Phasor analysis of the simulated fluorescence transients revealed that the multiexponential kinetics seen in the experiments was reproduced correctly with respect to the up to three lifetime components. Also the fractional contributions of the distinct lifetime components were well reproduced, with the only exception for the highest laser repetition rate. There, although the lifetime components were reproduced correctly the fractional contribution did not reproduce the experimental data. A variation of the value for the singlet-triplet annihilation rate was not observed to result in an improvement of the numerical simulations. Overall, the experimentally observed kinetics was reproduced well by the numerical simulations for excitation of the bacteriochlorophyll pigments and thus confirms the developed energy level for the LH2 complex of *Mch. purpuratum*. Hence, the proposed energy level for the B830 LH2 complex of *Mch. purpuratum* including the occurrence of a newly identified emissive state, tentatively attributed to a mixed exciton charge-transfer state, can be assumed to be valid. In summary, a consistent model for the description of the experimental findings was presented.

The investigation of the fluorescence kinetics of isolated LH2 complexes of *Mch. purpuratum* in detergent-solution in this thesis gave new insights into the electronic structure of this light-harvesting complex. Due to the recently published structure of the B830 LH2 complex [96] the molecular arrangement of the light-harvesting pigments was included in the discussion of the experimental findings. However, the energetic position as well as the molecular origin of the newly proposed mixed exciton charge-transfer state within this LH2 complex are yet not resolved. Thus, the work presented here might be an interesting starting point for future work on the B830 LH2 complex of *Mch. purpuratum*, such as single-molecule spectroscopy (SMS) or two dimensional spectroscopy on isolated B830 LH2 complexes. Both experimental techniques would allow for a more pre-

cise investigation of the B830 LH2 complex, owing the potential to resolve the origin of this feature of the electronic structure of the B830 LH2 complex of *Mch. purpuratum* and thus continuing the pathway of this thesis.

A. The photophysics of carotenoids

The electronic excited states of carotenoids and thus their photophysics are matter of ongoing research since decades and still under debate until now [73, 133, 134, 135, 136, 137]. Here, the current scientific consensus on the excited states of carotenoids is summarized in order to allow for their basic understanding.

A.1. Excited states of carotenoids

Besides bacteriochlorophylls the most important natural pigments of bacterial light harvesting are carotenoids. The naming carotenoids refers to a group of molecules featuring a conjugated backbone of alternating single (C-C) and double (C=C) bonds as the main motif to which different functional groups may be attached. Depending on the length of the conjugated carbon backbone, given by the number of alternating single and double bonds, and the type of the functional group as well as their position along the conjugated backbone, different carotenoids are distinguished [73].

Exemplary a few carotenoids typically incorporated in bacterial peripheral light-harvesting complexes (LH2) are visualized in Fig. A.1 with their molecular structures and their corresponding absorption spectra. The molecular structures of the carotenoids rhodopin glucoside, spheroidene and okenone which are incorporated in the LH2 complexes of *Rps. acidophila*, *Rba. spheroides* and *Marichromatium purpuratum*, respectively, shown from top to bottom, clearly allow for identification of the elongated conjugated backbone and the individual attached sidegroups characterizing the distinct carotenoid. Moreover, all three carotenoids feature a broad absorption spectrum in the visible wavelength range, ranging mostly between 400 nm and 500 nm, which makes carotenoids ideal counterparts to the bacteriochlorophyll pigments in the light harvesting machinery of

photosynthetic bacteria.
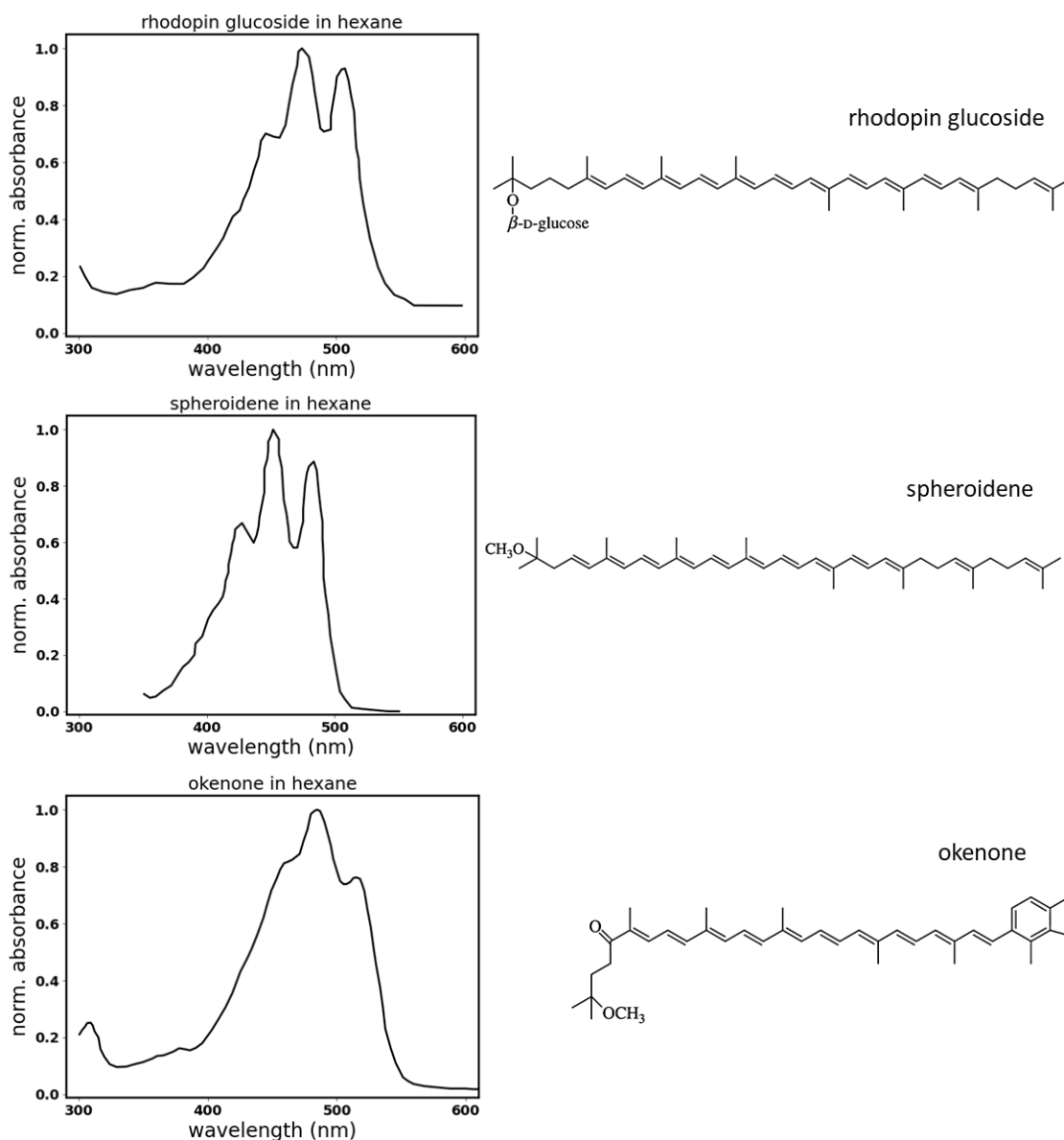
Figure A.1.: Photophysics of carotenoids: *The molecular structure formulas and the characteristic absorption spectra are shown for rhodopin glucoside (top) the carotenoid in the 'standard' LH2 complex from Rps. acidophila, spheroidene (middle) the carotenoid in the LH2 complex from Rba. spheroides, and okenone (bottom) the carotenoid incorporated in the LH2 complex from Marichromatium purpuratum. All absorption spectra refer to carotenoid molecules in hexane solution and were normalized to the maximum of the absorption spectrum in order to allow for comparison. Absorption data was taken from [36, 166, 141]. For details see text.*

The electronic excited states of carotenoids can in general be understood using the three state model known for linear polyenes, resulting from both, spectro-

scopic investigations as well as symmetry considerations [73, 140, 133]. This approach originates in the structural similarity of carotenoids and linear polyenes, which only feature the conjugated backbone of carotenoids without any functional groups attached, and moreover the assumption that the spectroscopic properties are mainly determined by the conjugated backbone of the molecules. Thus, the three singlet excited states of carotenoids are named S_0, S_1 and S_2 and refer to the electronic ground state as well as the first and second excited state, respectively, as visualized in Fig. A.2.
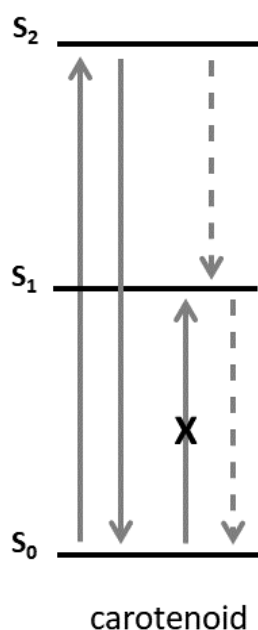
Figure A.2.: Singlet excited states of carotenoids: The scientific consensus of singlet excited states of carotenoids is visualized. The electronic ground state is denoted as S_0, the first and second excited singlet states are denoted as S_1 and S_2, respectively. Transitions between the electronic states are visualized by arrows. Solid lines correspond to allowed transitions due to absorption or emission of a photon. Non-radiative downhill transitions are visualized as arrows with dotted lines. Arrows marked with an bold X correspond to forbidden transitions. For details see text.

Due to the molecular symmetry of the conjugated backbone the transition between the electronic ground state S_0 and the first excited state S_1 is symmetry forbidden for linear polyenes, the model system for carotenoid molecules, and thus is not allowed for one-photon absorption processes [133]. Although carotenoids show less molecular symmetry than their ideal counterparts due to the attachment of functional groups, the optical darkness of the $S_0 \rightarrow S_1$ transition is commonly accepted [140, 134]. Hence, the lowest optically allowed transition

from the ground states is the $S_0 \rightarrow S_2$ transition into the second excited state S_2. This transition corresponds to the characteristic absorption bands of carotenoids in the visible region of the electromagnetic spectrum, compare Fig. A.1. [135, 73, 133]

For carotenoids typically incorporated in bacterial light harvesting complexes, featuring 9 - 11 conjugated double bonds along their carbon backbone [73, 56], the excitation energy resulting from the absorption of a photon may relax via two alternative pathways. It may either relax from S_2 non-radiatively to the S_1 state or can alternatively relax from S_2 radiatively into the ground state S_0 under emission of fluorescence, compare Fig. A.2. Fluorescence from the S_1 state is generally not observed for these carotenoids [167].

Besides the above described and most generally accepted three state model of the singlet excited states of carotenoids a multiple number of other excited states is at least proposed and partially experimentally proven to occur in carotenoids [133, 73]. The resulting manifold of excited states of carotenoids will be outlined below.

A.1.1. The manifold of singlet excited states of carotenoids

At least three additional excited states are proposed to lie lie in the vicinity of the three singlet excited states of carotenoids S_0, S_1 and S_2 [133]. In Fig. A.3 an energy level scheme illustrating the manifold of singlet excited states of carotenoid molecules is visualized. As outlined above, absorption of light in the visible wavelength range results in excitation of the second excited state S_2. Then, besides population of the first excited state S_1 via internal conversion, also the dark states S_X or S^* may alternatively be populated via non-radiative internal conversion processes.

The singlet excited state S_X was reported to be formed intermediately in the non-radiative internal conversion process of the second excited state S_2 decays, thus finally resulting in the first excited state S_1 [168]. Moreover, from two-dimensional electronic spectroscopy (2DES) an involvement of the intermediate S_X state in the energy flow and energy transfer from carotenoids to bacteriochlorophylls in bacterial light harvesting complexes was proposed [169].

Alternatively, also the intermediate state S^* might be populated by non-radiative, internal conversion processes from S_2, see Fig. A.3. However, especially when carotenoids incorporated into bacterial light harvesting complexes, the intermediate dark state S^* is proposed to be a precursor of the carotenoid triplet state [133, 170, 75].
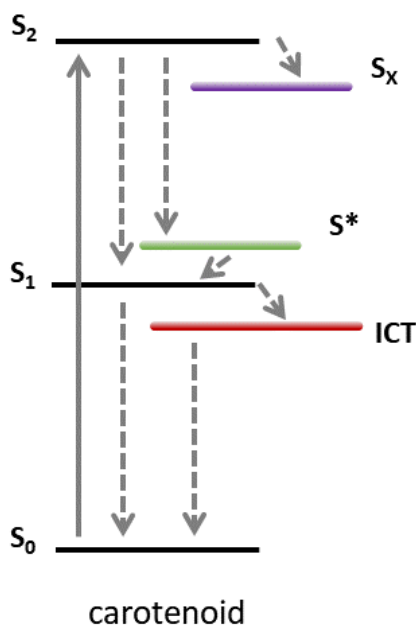
Figure A.3.: Manifold of singlet excited states of carotenoids: *An energy level scheme illustrating current concensus on the manifold of singlet excited states is shown. Absorption of light (solid arrow) results in excitation of the S_2 state, then downhill relaxations (dashed arrows) results in population the distinct singlet excited states S_X, S^*, S_1 and ICT. Adapted from [135]. For details see text.*

A distinct group of carotenoids, the so called carbonyl cyarotenoids featuring a carbonyl sidegroup attached to their conjugated backbone, feature the possibility of forming and additional, third, dark singlet excited state named *ICT* [73, 133, 138, 139]. This naming refers to the formation of an intramolecular charge transfer states (ICT) and such states are reported to lie energetically close to or below the first excited state S_1. However, although carbonyl carotenoids may feature such ICT states in their manifold of excited states, not all of them show spectroscopic signatures of such ICT states indicating their occurrence, such as the carotenoid okenone incorporated in the LH2 complex of *Marichromatium purpuratum* where no indication of an ICT state is observed [141].

A.1.2. Triplet excited states

Besides the manifold of singlet excited states carotenoids also feature triplet excited states in their overall landscape of electronically excited states. As isolated molecules in solution carotenoids are reported to feature almost negligible triplet populations due to intersystem crossing yields far below 1% [53, 171, 172, 173]. However, triplet excited states of carotenoids play a crucial role when carotenoids are embedded in bacterial pigment-protein antenna complexes, such as the bacterial LH1 and LH2 complexes, where the carotenoid triplet states in involved in the photoprotective role of carotenoids [72, 58, 60, 59].

B. Calculations for chapter 4: 'The Phasor Approach'

B.1. The two basic relations of phase fluorometry

A simple two-level system as shown in Fig. 4.2 represents a single exponential fluorescence decay with lifetime τ and is described by the differential equation

$$\frac{dN}{dt} = -k \cdot N + E(t) = -\frac{1}{\tau} \cdot N + E(t) \tag{B.1}$$

with the decay rate k defined as the inverse lifetime. As the fluorescence emission F(t) is proportional to the population of the excited state N this equation is also valid for F(t) instead of N.

$$\frac{d}{dt}F(t) = -k \cdot F(t) + E(t) = -\frac{1}{\tau} \cdot F(t) + E(t) \tag{B.2}$$

Using the definitions of the modulated excitation in the frequency domain

$$E(t) = E_0 + E\ sin(\omega t) \tag{B.3}$$

and the resulting modulated fluorescence emission

$$F(t) = F_0 + F\ sin(\omega t - \phi) \tag{B.4}$$

with the modulation frequency ω and the phase shift ϕ one obtains from equation B.2:

$$F\ cos(\omega t - \phi)\ \omega = -k\ F_0 - k\ F\ sin(\omega t - \phi) + E_0 + E\ sin(\omega t) \tag{B.5}$$

Because this holds at any time, both, the constant terms as well as the time dependent terms containing $cos(\omega t)$ and $sin(\omega t)$ must be equal independently.

From the time independent terms of equation B.5 it follows

$$\frac{E_0}{F_0} = k = \frac{1}{\tau} \tag{B.6}$$

which allows to calculate the fluorescence lifetime from the static, unmodulated amplitudes of excitation and emission.

Using the trigonometric identities

$$sin(x \pm y) = sin(x)cos(y) \pm cos(x)sin(y) \tag{B.7}$$
$$cos(x \pm y) = cos(x)cos(y) \mp sin(x)sin(y) \tag{B.8}$$

the time dependent parts of equation B.5 can be written as

$$F\ [cos(\omega t)cos(\phi) + sin(\omega t)sin(\phi)]\ \omega =$$
$$- k\ F\ [sin(\omega t)cos(\phi) - cos(\omega t)sin(\phi)] + E\ sin(\omega t) \tag{B.9}$$

As already pointed out this is valid at any time. Thus, one obtains for nulling of the cosine coefficients

$$F\ cos(\phi)\ \omega = k\ F\ sin(\phi) \tag{B.10}$$

By reformulation and using the definition of k = $1/\tau$ this gives the **first basic relation of phase fluorometry**

$$\boxed{\frac{\omega}{k} = \frac{sin(\phi)}{cos(\phi)} = tan(\phi) = \omega\ \tau} \tag{B.11}$$

Nulling the sine coefficients yields

$$F\ sin(\phi)\ \omega = -k\ cos(\phi) + E \tag{B.12}$$

Multiplication on both sides with $cos(\phi)$ leads to

$$F\ sin(\phi)\ cos(\phi)\ \omega = -k\ cos^2(\phi) + E\ cos(\phi) \tag{B.13}$$

Division on both sides by E and using equation B.11 for substitution of ω leads

to

$$\frac{F}{E} \, sin(\phi) \, cos(\phi) \frac{tan(\phi)}{\tau} = -k \, \frac{F}{E} \, cos^2(\phi) + cos(\phi) \tag{B.14}$$

Using the definition of $tan(\phi) = \frac{sin(\phi)}{cos(\phi)}$ and $k = \frac{1}{\tau}$ one obtains

$$\frac{F}{E} \, sin^2(\phi) \, \frac{1}{\tau} = -\frac{1}{\tau} \frac{F}{E} \, cos^2(\phi) + cos(\phi) \tag{B.15}$$

and

$$\frac{F}{E} \, sin^2(\phi) \, \frac{1}{\tau} + \frac{1}{\tau} \frac{F}{E} \, cos^2(\phi) = cos(\phi) \tag{B.16}$$

which, by using $sin^2(x) + cos^2(x) = 1$, can be simplified to

$$\frac{F}{E} \, \frac{1}{\tau} \left[sin^2(\phi) + cos^2(\phi) \right] = \frac{F}{E} \, \frac{1}{\tau} = cos(\phi) \tag{B.17}$$

Using equation B.6 the **second basic relation of phase fluorometry** is obtained

$$\boxed{\frac{F}{E} \frac{E_0}{F_0} = m = cos(\phi)} \tag{B.18}$$

relating the cosine of the phase shift ϕ and the modulation ratio m. Using equation B.11 and the trigonometric identity $cos(x) = \frac{1}{\sqrt{1+tan^2(x)}}$ this can be reformulated as

$$\boxed{m = cos(\phi) = \frac{1}{\sqrt{1 + \omega^2 \tau^2}}} \tag{B.19}$$

B.2. Calculation of the Fourier transform for a measured decay given by a convolution of the IRF and the pure decay F

The measured fluorescence decay D mathematically corresponds to a convolution of the IRF and the pure fluorescence decay F

$$D = IRF * F \tag{B.20}$$

For measurements in the time domain the phasor coordinates G and S are defined as the real and imaginary parts of the area normalized Fourier transformed

measured decay D. Thus $G[D]$ and $S[D]$ can be written as

$$G[D] = Re(\ \mathcal{F}\{D\}\ ) = Re(\ \mathcal{F}\{IRF * F\}\ ) \qquad \text{(B.21)}$$

$$S[D] = Im(\ \mathcal{F}\{D\}\ ) = Im(\ \mathcal{F}\{IRF * F\}\ ) \qquad \text{(B.22)}$$

According to the convolution theorem the Fourier transform of a convolution of two functions, exemplarily called f and g, is given by a product of their individual Fourier transforms:

$$\mathcal{F}\{f * g\} = \mathcal{F}\{f\} \cdot \mathcal{F}\{g\} \qquad \text{(B.23)}$$

Using the convolution theorem $G[D]$ and $S[D]$ can be rewritten as

$$G[D] = Re(\ \mathcal{F}\{D\}\ ) = Re(\ \mathcal{F}\{IRF * F\}\ ) = Re(\ \mathcal{F}\{IRF\} \cdot \mathcal{F}\{F\}\ ) \qquad \text{(B.24)}$$

$$S[D] = Im(\ \mathcal{F}\{D\}\ ) = Im(\ \mathcal{F}\{IRF * F\}\ ) = Im(\ \mathcal{F}\{IRF\} \cdot \mathcal{F}\{F\}\ ) \qquad \text{(B.25)}$$

The Fourier transforms of the IRF and the pure fluorescence decay F in general follow the relation

$$\mathcal{F}\{IRF\} = Re(\ \mathcal{F}\{IRF\}\ ) + i\ Im(\ \mathcal{F}\{IRF\}\ ) = G[IRF] + i\ S[IRF] \qquad \text{(B.26)}$$

$$\mathcal{F}\{F\} = Re(\ \mathcal{F}\{F\}\ ) + i\ Im(\ \mathcal{F}\{F\}\ ) = G[F] + i\ S[F] \qquad \text{(B.27)}$$

Thus, the product of the Fourier transform of the IRF and the Fourier transform of the pure decay F can be written as

$$
\begin{aligned}
\mathcal{F}\{IRF\} \cdot \mathcal{F}\{F\} &= [G[IRF] + i\ S[IRF]] \cdot [G[F] + i\ S[F]] \\
&= G[IRF]\ G[F] + G[IRF]\ i\ S[F] + i\ S[IRF]\ G[F] + i\ S[IRF]\ i\ S[F] \\
&= G[IRF]\ G[F] + G[IRF]\ i\ S[F] + i\ S[IRF]\ G[F] + i^2\ S[IRF]\ S[F] \\
&= G[IRF]\ G[F] + iG[IRF]\ S[F] + i\ S[IRF]\ G[F] - S[IRF]\ S[F] \quad \text{(B.28)}
\end{aligned}
$$

Finally, for $G[D]$ and $S[D]$ follows from their definition as real and imaginary parts of the Fourier transform, respectively,

$$G[D] = Re(\ \mathcal{F}\{IRF\} \cdot \mathcal{F}\{F\}\ ) = G[IRF]\ G[F] - S[IRF]\ S[F] \qquad \text{(B.29)}$$

$$S[D] = Im(\ \mathcal{F}\{IRF\} \cdot \mathcal{F}\{F\}\ ) = G[IRF]\ S[F] + S[IRF]\ G[F] \qquad \text{(B.30)}$$

B.3. Calculation of the phasor correction for the influence of the IRF

According to equation 4.30 in Section 4.3.3 the phasor of the pure fluorescence decay F can be written as

$$\begin{bmatrix} G[F] \\ S[F] \end{bmatrix} = \frac{1}{m_{IRF}} \begin{bmatrix} cos(\phi_{IRF}) & sin(\phi_{IRF}) \\ -sin(\phi_{IRF}) & cos(\phi_{IRF}) \end{bmatrix} \begin{bmatrix} G[D] \\ S[D] \end{bmatrix} \tag{B.31}$$

By using the basic definition of the phasor coordinates G and S for the terms of the measured decay D as $G[D] = m_D \cdot cos(\phi_D)$ and $S[D] = m_D \cdot sin(\phi_D)$ this can be reformulated as

$$\begin{bmatrix} G[F] \\ S[F] \end{bmatrix} = \frac{1}{m_{IRF}} \begin{bmatrix} cos(\phi_{IRF}) & sin(\phi_{IRF}) \\ -sin(\phi_{IRF}) & cos(\phi_{IRF}) \end{bmatrix} \begin{bmatrix} G[D] \\ S[D] \end{bmatrix} \tag{B.32}$$

$$= \frac{m_D}{m_{IRF}} \begin{bmatrix} cos(\phi_{IRF}) & sin(\phi_{IRF}) \\ -sin(\phi_{IRF}) & cos(\phi_{IRF}) \end{bmatrix} \begin{bmatrix} cos(\phi_D) \\ sin(\phi_D) \end{bmatrix} \tag{B.33}$$

$$= \frac{m_D}{m_{IRF}} \begin{bmatrix} cos(\phi_{IRF})cos(\phi_D) + sin(\phi_{IRF})sin(\phi_D) \\ -sin(\phi_{IRF})cos(\phi_D) + cos(\phi_{IRF})sin(\phi_D) \end{bmatrix} \tag{B.34}$$

Leaving the matrix formulation leads to separate equations for the phasor coordinates $G[F]$ and $S[F]$ of the pure fluorescence decay F

$$G[F] = \frac{m_D}{m_{IRF}} [cos(\phi_{IRF})cos(\phi_D) + sin(\phi_{IRF})sin(\phi_D)] \tag{B.35}$$

$$S[F] = \frac{m_D}{m_{IRF}} [cos(\phi_{IRF})sin(\phi_D) - sin(\phi_{IRF})cos(\phi_D)] \tag{B.36}$$

and using the trigonometric identities

$$sin(x \pm y) = sin(x)cos(y) \pm cos(x)sin(y) \tag{B.37}$$
$$cos(x \pm y) = cos(x)cos(y) \mp sin(x)sin(y) \tag{B.38}$$

the phasor coordinates $G[F]$ and $S[F]$ can be written as

$$G[F] = \frac{m_D}{m_{IRF}} cos(\phi_{IRF} - \phi_D) \tag{B.39}$$

$$S[F] = \frac{m_D}{m_{IRF}} sin(\phi_D - \phi_{IRF}) \tag{B.40}$$

Using the symmetry of the cosine function, $G[F]$ can be rewritten as

$$G[F] = \frac{m_D}{m_{IRF}} \cos(\phi_D - \phi_{IRF}) \tag{B.41}$$

Thus, one can define the phase shift ϕ_F and the modulation ratio m_F of the pure decay F by calculation from the phase shifts and modulation ratios of the measured decay D and the IRF

$$\phi_F = \phi_D - \phi_{IRF} \tag{B.42}$$

and

$$m_F = \frac{m_D}{m_{IRF}} \tag{B.43}$$

This finally allows writing the phasor coordinates $G[F]$ and $S[F]$ of the pure fluorescence decay F as

$$G[F] = m_F \cos(\phi_D) \tag{B.44}$$

$$S[F] = m_F \sin(\phi_D) \tag{B.45}$$

B.4. Calculation of the third lifetime component for a triexponential decay resulting from the expansion of a biexponential decay

From the calculations in Section 4.5.3 the phasor coordinate S_C of the yet unknown phasor C, is accessible by

$$S_C = \frac{A_{ABC} \, S_P - A_\alpha \, S_A - A_\beta \, S_B}{A_\gamma} \tag{B.46}$$

Using the relation $A_{ABC} = A_\alpha + A_\beta + A_\gamma$ allows rewriting as

$$S_C = \frac{(A_\alpha + A_\beta + A_\gamma) \, S_P - A_\alpha \, S_A - A_\beta \, S_B}{A_\gamma} \tag{B.47}$$

$$= \frac{A_\alpha \, S_P + A_\beta \, S_P + A_\gamma \, S_P - A_\alpha \, S_A - A_\beta \, S_B}{A_\gamma} \tag{B.48}$$

$$= \frac{A_\alpha \, (S_P - S_A) + A_\beta \, (S_P - S_B)}{A_\gamma} + S_P \tag{B.49}$$

Defining the values S_{PA} and S_{PB} as differences of phasor coordinates

$$S_{PA} = (S_P - S_A) \tag{B.50}$$

and

$$S_{PB} = (S_P - S_B) \tag{B.51}$$

allows rewriting of equation B.49 as

$$S_C = \frac{A_\alpha (S_{PA}) + A_\beta (S_{PB})}{A_\gamma} + S_P \tag{B.52}$$

As outlined previously at the beginning of Section 4.5.3, for the phasor P it is assumed that the two contributing lifetimes τ_1 and τ_2 as well as the ratio R of their fractional contributions is maintained when expanding the expected bi-exponential to a triexponential decay. In general, a phasor corresponding to a triexponential decay lies within a triangle spanned by the phasors of the contributing lifetime components τ_1, τ_2 and τ_3 as visualized in Fig. B.1.
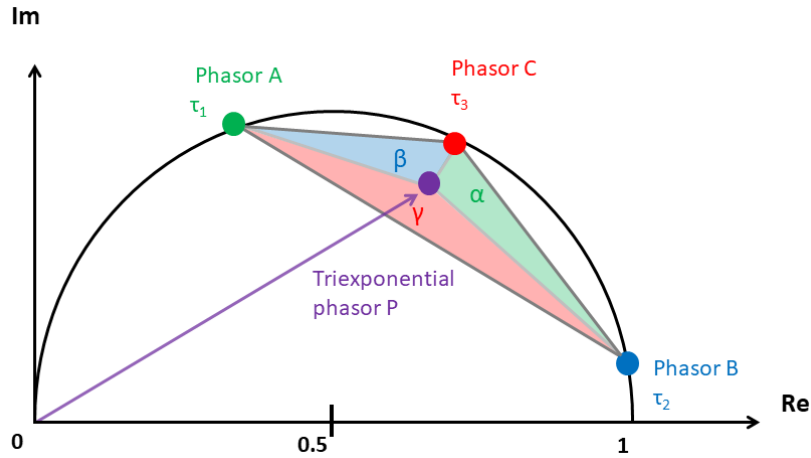
Figure B.1.: Triexponential phasor lying within a triangle: *A phasor (purple circle) corresponding to a triexponential decay lies within a triangle ABC. The triangle is spanned by the phasors A, B and C (green, blue and red colored circles, respectively) corresponding to the contributing lifetimes τ_1, τ_2 and τ_3. The phasor P divides the total area of the big triangle ABC into smaller triangles α, β and γ, colored in green, blue and red, respectively. For detailed description see text.*

The fractional contributions of the three lifetime components τ_1, τ_2 and τ_3 are given by the partial fractions of the smaller triangles α, β and γ with respect to the big triangle ABC. Thus, it follows that the ratio R of the fractional contri-

butions of the two contributing lifetimes components τ_1, τ_2, adapted from the biexponential decay, is now given by the ratio of the areas A_α and A_β of the smaller triangles α and β

$$R = \frac{A_\alpha}{A_\beta} \tag{B.53}$$

This allows reformulation of equation B.52

$$S_C = \frac{R\, A_\beta\, S_{PA} + A_\beta\, S_{PB}}{A_\gamma} + S_P \tag{B.54}$$

$$= A_\beta \frac{R\, S_{PA} + S_{PB}}{A_\gamma} + S_P \tag{B.55}$$

$$= A_\beta\, u_0 + S_P \tag{B.56}$$

with

$$u_0 = \frac{R\, S_{PA} + S_{PB}}{A_\gamma} \tag{B.57}$$

From the situation of the phasor P, as shown in Fig. B.2, it is clear that both, the phasor coordinates G and S of the phasors A and B as well as the area A_γ of the small triangle γ, which is given by the phasors A, B and P, are known.
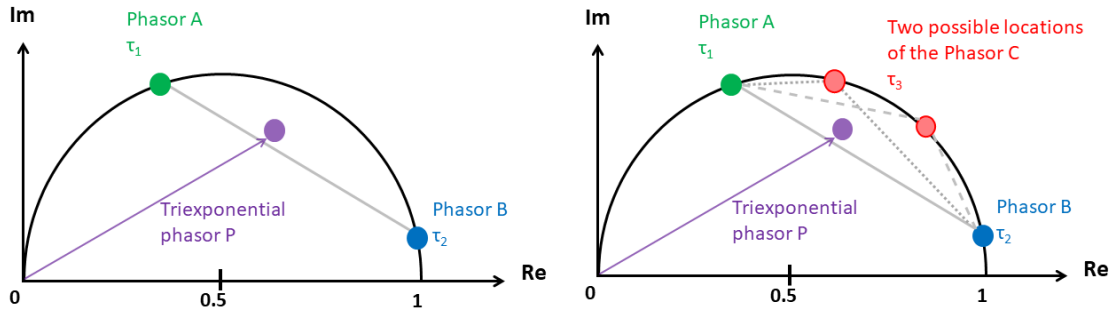
Figure B.2.: Phasor of a triexponential decay expanded from a biexponential decay: On the left hand side a purple colored phasor clearly lies apart from the straight line (shown in grey) defining all possible locations of the biexponential decay with contributing lifetime components τ_1 and τ_2 represented by the phasors A and B, shown in green and blue, respectively. Thus, this phasor has to be described by a triexponential decay. On the right hand side two possible locations of the phasor C, representing the third, yet unknown contributing lifetime component τ_3, are illustrated in red. The triangles connecting the phasors C with the phasors A and B are illustrated as dotted and dashed lines, respectively. For detailed description see text.

The area A_γ of the triangle γ can be calculated using the cross product as out-

lined in Section 4.5.2

$$A_\gamma = 0.5\,|\overrightarrow{AB} \times \overrightarrow{AP}| = 0.5\,(G_{BA}\,S_{PA} - S_{BA}\,G_{PA}) \tag{B.58}$$

Thus, u_0 can be written as

$$u_0 = \frac{R\,S_{PA} + S_{PB}}{0.5\,(G_{BA}\,S_{PA} - S_{BA}\,G_{PA})} \tag{B.59}$$

Thus, when A_β in equation B.52 is known, the phasor coordinate S_C can be calculated. The area A_β of the triangle β can be calculated by means of the cross product

$$A_\beta = 0.5\,|\overrightarrow{AP} \times \overrightarrow{AC}| = 0.5\,(G_{PA}\,S_{CA} - S_{PA}\,G_{CA}) \tag{B.60}$$

The appearing values G_{PA}, S_{CA}, S_{PA} and G_{CA} are defined as the differences of the corresponding phasor coordinates analogously to equations B.50 and B.51 . This allows reformulation of equation B.56 as

$$S_C = 0.5\,(G_{PA}\,S_{CA} - S_{PA}\,G_{CA})\,u_0 + S_P \tag{B.61}$$

$$= 0.5\,(G_{PA}\,S_C - G_{PA}\,S_A - S_{PA}\,G_C + S_{PA}\,G_A)\,u_0 + S_P \tag{B.62}$$

This equation contains both coordinates of the yet unknown phasor C. Recognizing that the phasor C has to lie on the universal semicircle per definition and thus its phasor coordinates fulfill the relation $S = \sqrt{G(1-G)}$, one obtains an equation only containing the phasor coordinate G_C

$$\sqrt{G_C(1-G_C)} =$$
$$0.5\,(G_{PA}\,\sqrt{G_C(1-G_C)} - G_{PA}\,S_A - S_{PA}\,G_C + S_{PA}\,G_A)\,u_0 + S_P \tag{B.63}$$

Sorting of terms yields

$$-0.5\,G_{PA}\,S_A\,u_0 + 0.5\,S_{PA}\,G_A\,u_0 + S_P =$$
$$(1 - 0.5\,G_{PA}\,u_0)\,\sqrt{G_C(1-G_C)} + (0.5\,S_{PA}\,u_0)\,G_C \tag{B.64}$$

Introduction of the abbreviations u_1, u_2 and u_3 given by

$$u_1 = -0.5\,G_{PA}\,S_A\,u_0 + 0.5\,S_{PA}\,G_A\,u_0 + S_P \tag{B.65}$$

$$u_2 = (1 - 0.5\, G_{PA}\, u_0) \tag{B.66}$$

$$u_3 = (0.5\, S_{PA}\, u_0) \tag{B.67}$$

simplifies equation B.64 to

$$u_1 = u_2 \sqrt{G_C(1 - G_C)} + u_3\, G_C \tag{B.68}$$

This can be easily transformed into a quadratic equation for the phasor coordinate G_C

$$(u_3^2 + u_2^2)\, G_C^2 + (-2u_1u_3 - u_2^2)\, G_C + u_1^2 = 0 \tag{B.69}$$

Solving this equation, one finally obtains the following relation for calculation of the phasor coordinate G_C:

$$G_{C_{1,2}} = \frac{-(-2u_1u_3 - u_2^2) \pm \sqrt{(-2u_1u_3 - u_2^2)^2 - 4(u_3^2 + u_2^2)\,u_1^2}}{2\,(u_3^2 + u_2^2)} \tag{B.70}$$

C. Estimation of errors within the phasor analysis

As phasors are calculated from measured fluorescence transients their positions within the phasor plot are affected by the uncertainties of the underlying measurements. Thus, the phasor positions within the phasor plot have some uncertainty which can be visualized by error bars. In the following, an estimation for the errors of the phasor positions as well as the resulting effects of those errors in the analysis of phasors are discussed.

C.1. Accuracy of phasor positions within the phasor plot

As already outlined in Chapter 4 the measured fluorescence decay from which the phasor positions are calculated features a discrete character and corresponds to a histogram of measured fluorescence intensities. The entry of each histogram bin corresponds to the number of photons counted by the streak camera within the respective temporal bin of the histogram. In photon-counting mode of the streak camera, which was used for all measurements of this thesis, the process of photon counting is known to follow Poisson statistics [174].

The calculation of the phasors from the measured fluorescence transients, as outlined in detail in Chapter 4, is performed by calculation of the discrete and normalized Fourier transform D_n of the intensity histogram that approximates the measured fluorescence decay curve:

$$D_{\mathrm{n}} = \frac{\sum_{k=0}^{N_{\mathrm{bins}}-1} N_k \, \exp^{i n \omega (k+\frac{1}{2}) \frac{T}{N_{\mathrm{bins}}}}}{\sum_{k=0}^{N_{\mathrm{bins}}-1} N_k} \tag{C.1}$$

The summation runs over k counting the bins of the intensity histogram within

the discrete Fourier transform. N_k is the fluorescence intensity for the kth bin of the histogram in units of photon counts and N_{bins} is the total number of bins of the intensity histogram, as before in Chapter 4. n is the harmonic number of the transformation and the transformation frequency ω is defined as

$$\omega = \frac{2\pi}{T} \tag{C.2}$$

with T being the finite temporal length of the detection window.

The phasor coordinates G and S are given by

$$G(\omega) = Re(\ D_n\ ) \tag{C.3}$$

$$S(\omega) = Im(\ D_n\ ) \tag{C.4}$$

as the real and imaginary parts of the discrete and normalized Fourier transform D_n of the intensity histogram approximating the measured fluorescence decay curve.

Turning now to the question of the error of the phasor positions, defined by the phasor coordinates, it is quite clear that N_k as the fluorescence intensity for the kth bin of the histogram in units of photon counts is the only value within the calculation of the phasor coordinates that is affected by an uncertainty due to the measurement. Thus, focusing on the k-dependency of D_n, in brevity D_n can be written as

$$
\begin{aligned}
D_{\mathrm{n}} &= \frac{\sum_{k=0}^{N_{\mathrm{bins}}-1} N_k\ \exp(k)}{\sum_{k=0}^{N_{\mathrm{bins}}-1} N_k} \\
&= \frac{N_0\ \exp(0)}{\sum_{k=0}^{N_{\mathrm{bins}}-1} N_k} + \frac{N_1\ \exp(1)}{\sum_{k=0}^{N_{\mathrm{bins}}-1} N_k} + ... + \frac{N_{bins-1}\ \exp(bins-1)}{\sum_{k=0}^{N_{\mathrm{bins}}-1} N_k} \\
&= \frac{1}{\sum_{k=0}^{N_{\mathrm{bins}}-1} N_k} \Big(N_0\ \exp(0) + N_1\ \exp(1) + ... + N_{bins-1}\ \exp(bins-1) \Big)
\end{aligned}
\tag{C.5}
$$

with $exp(k)$ summarizing the broad exponential factor for simplicity to a simple dependency on the index k of bins of the intensity histogram.

From the general principle of the propagation of uncertainties it is known that

196

the error of a function $f(x_1, x_2, x_3)$ that depends on multiple variables x_1, x_2, x_3 is given by

$$err_{f(x_1,x_2,x_3)} = \sqrt{\sum_{i=1}^{3}\left(\frac{d}{dx_i}f(x_1,x_2,x_3)\right)^2 \cdot err_{x_i}{}^2} \qquad (C.6)$$

with err_{x_i} being the error of the i-th variable x_i.

Adapting this to the discrete and normalized Fourier transform D_n and its k-dependency it follows that for each k of the summation the derivative $\frac{d}{dN_k}D_n$ has to be calculated. From equation C.5 it follows that each summand of D_n has the same shape. Thus, exemplarily the derivative $\frac{d}{dN_0}D_n$ of the first summand is given by

$$\frac{d}{dN_0} = \frac{exp(0)\left(\sum_{k=0}^{N_{\text{bins}}-1}N_k\right) - \left(\sum_{k=0}^{N_{\text{bins}}-1}N_k\,exp(k)\right)}{\left(\sum_{k=0}^{N_{\text{bins}}-1}N_k\right)^2} \qquad (C.7)$$

In analogy to equation C.6 then the error of D_n can be written as

$$err_{D_n} = \sqrt{\sum_{p=0}^{N_{\text{bins}}-1}\left(\frac{exp(p)\left(\sum_{k=0}^{N_{\text{bins}}-1}N_k\right) - \left(\sum_{k=0}^{N_{\text{bins}}-1}N_k\,exp(k)\right)}{\left(\sum_{k=0}^{N_{\text{bins}}-1}N_k\right)^2}\right)^2 \cdot err_{N_p}{}^2}$$

$$(C.8)$$

with index p running over all bins of the histogram and $err_{N_p} = \sqrt{N_p}$ resulting from the Poission statistics of the photon-counting mode.

Finally, the uncertainty of the phasor position are calculated as

$$err_G = Re(\,err_{D_n}\,) \qquad (C.9)$$

$$err_S = Im(\,err_{D_n}\,) \qquad (C.10)$$

and can be visualized as error bars in the phasor plot. In Fig. C.1 a group of phasors is exemplary show within the phasor plot, including error bars representing the uncertainties err_G and err_S of their phasor positions, respectively.
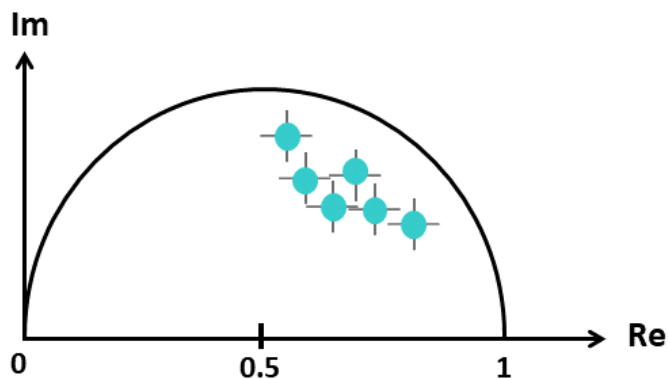
Figure C.1.: The uncertainty of phasor positions within the phasor plot: *A group of phasors is shown within the phasor plot (cyan colored circles). The uncertainties err_G and err_S of their phasor coordinates, resulting from the measured data, are visualized by error bars of grey color. For details see text.*

C.2. Biexponential decays: The accuracy of a linear fit to multiple phasors

Performing phasor analysis, the phasor coordinates resulting in the phasors position within the phasor plot are used for investigating the underlying fluorescence kinetics. As pointed out in the section before, the phasors positions within the phasor plot feature some uncertainty which has to be considered when working with the phasors.

In Section 4.5 the principle of performing a linear fit through a cloud of phasors for revealing the underlying biexponential decay was presented and discussed in detail. For recognizing the uncertainties of the phasor positions in both phasor coordinates performing a least-square linear fit is not sufficient. Instead an orthogonal distance regression (ODR) linear fit has to be performed for taking into account the errors of both phasor coordinates in the process of revealing the biexponential kinetics [121, 131]. In Fig. C.2 a group of phasors with their respective error bars is shown in a phasor plot. The grey line is the fitted line obtained by an ODR fit through the group of phasors taking into account the uncertainty of the phasor positions and represents the biexponential decay. The contributing lifetime components τ_1 and τ_2 are obtained by calculating the intersections of the fitted line with the universal semicircle, as already introduced in Chapter 4.
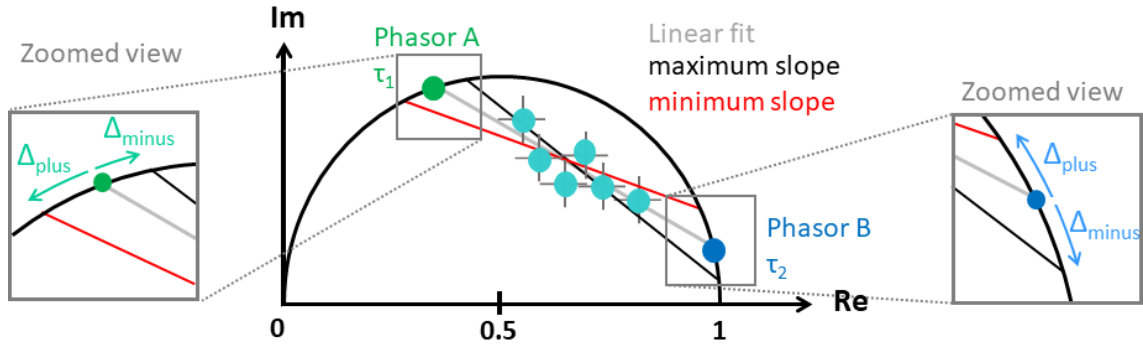
Figure C.2.: Resolving a biexponential decay by linear fitting: By performing a orthogonal distance regression (ODR) linear fit through the group of phasors, the underlying biexponential decay can be resolved. The phasors are shown with error bars representing the uncertainties of the phasor positions within the phasor plot. The intersections of the fitted line with the universal semicircle represent the contributing lifetimes of the biexponential decay. The grey line through the group of phasors corresponds to the linear fit, representing the best parameters. The two lines of red and black color correspond to the lines of minimum and maximum slope, respectively, calculated from the fit parameters and their corresponding uncertainties. Thus, they allow for visualization of the uncertainty the linear fit. The two zoomed views of the phasors A and B illustrate the uncertainties Δ_{plus} and Δ_{minus} of the respective lifetime components τ_1 and τ_2 resulting from the uncertainty of the linear fit through the group of phasors. For details see text.

The ODR fitting routine for performing the linear fit[1] does not only give the best parameters of the linear fit but also the uncertainties of these best parameters. From the uncertainties finally, the errors of the two contributing lifetimes of the biexponential decay can be estimated. This is done by calculating the straight lines with the minimum and the maximum slope from the fit parameters and their corresponding uncertainties that go through the cloud of scattered phasors within the limits of their error bars. These two straight lines of minimum and maximum slope are represented in red and black color, respectively, in Fig. C.2. The respective intersections of the two lines with the universal semicircle then allow for calculation of the corresponding lifetime components. Thus, the uncertainties of the two contributing lifetime components of the biexponential kinetics underlying the cloud of scattered phasors can be estimated, as visualized in the zoomed views of the phasors A and B in Fig. C.2. From the nonlinearity of the scaling of the ruler of lifetimes along the universal semicircle, as introduced in Chapter 4, in general the obtained uncertainties of the contributing lifetime components are asymmetric. Thus, as visualized in the zoomed views in Fig. C.2

---

[1]In this thesis the ODR package of Python was used. For details concerning this package see [175].

each of the lifetime components τ_1 and τ_2 features two uncertainties, Δ_{plus} and Δ_{minus}, of their lifetime values. Especially for the region of low lifetimes on the ruler of lifetimes, even small deviations of the lines with minimum and maximum slope from the fitted line corresponding to the best parameters can result in enormous values for the uncertainties of the calculated lifetime component as the scaling values of the ruler of lifetimes are lying very dense there.

D. The strength of the phasor approach

As outlined before in Section 4.6 it is one strength of the phasor approach and moreover the phasor analysis to resolve multiexponential kinetics featuring at least one lifetime component contribution only to a very small fraction. This appendix will emphasize this strength of the phasor approach.

D.1. From fractional contributions to relative amplitudes of a multiexponential decay

When analyzing fluorescence decay curves often a mathematical description such as a decay function is needed, in order to allow further analysis of the observed fluorescence kinetics. In general, a multiexponential decay can be mathematically written as a sum of exponentials

$$I(t) \; = \; \sum_i x_i \, exp[-\frac{t}{\tau_i}] \tag{D.1}$$

The pre-exponential coefficients x_i within the sum correspond to the relative amplitudes ($\sum_i x_i = 1$) of the different exponentials of the multiexponential decay with lifetime components τ_i .

Following the 'traditional' pathway of analyzing a measured fluorescence decay by using the fitting routine, both, the amplitudes as well as the lifetime components, are known such that the mathematical decay function according to equation D.1 can be easily named. In contrast, using the phasor approach for the analysis of a measured fluorescence decay as outlined above, only the values of the contributing lifetime components τ_i of the multiexponential decay and their fractional contributions f_i are known, see also Sections 4.5.1-4.5.3.

For a multiexponential decay according to equation D.1 the fractional contributions f_i can be calculated from the relative amplitudes x_i and the lifetime components τ_i as [127, 107]

$$f_i = \frac{x_i \, \tau_i}{\sum_i x_i \, \tau_i} \tag{D.2}$$

They correspond to the relative intensity contributions of the lifetime components τ_i to the total measured fluorescence intensity, given by the area below the fluorescence decay curve. In contrast, the relative amplitudes x_i are in principle a mathematical construction in order to allow for a mathematical description and writing of a decay function for the measured fluorescence decay. The assignment of the relative amplitudes to certain physical meanings is in general non-trivial, as the distinct experimental situation as well as the excited fluorescent sample has to be taken into account [107]. However, from equation D.2 it follows that vice versa the relative amplitudes x_i can be calculated from the fractional contributions f_i. This is done by solving a homogeneous linear system of equations for the relative amplitudes x_i and recognizing moreover the fact, that both, relative amplitudes as well as fractional contributions, are normalized: $\sum_i x_i = 1$ and $\sum_i f_i = 1$. Hence, also for measured fluorescence decay curves analyzed with the phasor approach, in principle a mathematical decay function according to equation D.1 can be named.

In the analysis and the discussion of measured fluorescence decay curves often the relative amplitudes of the distinct lifetime components are discussed in terms of relative contributions of a multiexponential decay. However, in order to allow for drawing generally valid conclusions instead the fractional contributions of the lifetime components should be taken into account, as they correspond to the relative contributions to the total fluorescence intensity. In order to illustrate that the two parameters, the relative amplitudes and the fractional contributions of the distinct lifetime components, respectively, may differ significantly for different values of the lifetime components, two exemplary cases of a biexponential decay are compared in Table D.1. Example decay 1 features two lifetime components in the same order of magnitude, 850 ps and 1100 ps, whereas example decay 2 features two lifetime components of different orders of magnitude, 850 ps and 50 ps. Both example decays have equal relative amplitudes of the contributing lifetime components amounting to 0.5, as can be seen in Table D.1.

	Example decay 1		Example decay 2	
lifetime values	850 ps	1100 ps	850 ps	50 ps
relative amplitudes	0.5	0.5	0.5	0.5
fractional contributions	0.44	0.56	0.94	0.06

Table D.1.: Illustration of the differences between relative amplitudes and fractional contributions for two example decays with different contributing lifetime components

From the calculated fractional contributions of the different lifetime components it can be clearly seen that these values differ significantly for the two exemplary cases. For example decay 1, featuring two lifetime component in the same order of magnitude, the values of the fractional contributions are almost equal to the values of the relative amplitudes. Thus, the conclusion drawn from either considering the relative amplitudes or alternatively the fractional contributions are almost identical. In contrast, a tremendous difference between the values of the relative amplitudes and the fractional contributions is observed for the second exemplary considered decay, featuring contributing lifetime components that different by an order of magnitude. Hence, it can be easily seen that in this case it makes a significant difference which of the parameters is considered in the analysis and discussion of a fluorescence decay.

In conclusion, in order to allow for drawing generally valid conclusions from the analysis of a measured fluorescence decay, irrespective of the number of lifetime components and their distinct lifetime values, the fractional contributions of the distinct lifetime components to the total measured fluorescence intensity should be considered in the discussion of the observed fluorescence kinetics.

D.2. The strength of phasor analysis

As outlined above, the phasor approach gives direct access to the contributing lifetime components as well as to their fractional contributions to the total fluorescence intensity of a measured fluorescence decay. It allows the resolution of contributing lifetime components that are not visible from the shape of the fluorescence decay curve and thus often not recognized via the 'traditional' fitting pathway. In order to illustrate this strength of phasor analysis, we consider two exemplary cases of a biexponential decay in the following. First, the case

of two contributing lifetime components that differ by an order of magnitude (950 ps and 100 ps) is discussed. Afterwards, a second biexponential decay with contributing lifetime components in the same order of magnitude (950 ps and 1500 ps) is considered.

In Fig. D.1 the simulated decay curves of a biexponential decay with lifetime components of 950 ps and 100 ps are shown on the left hand side for different combinations of the relative amplitudes. On the right hand side the corresponding phasors are shown in a phasor plot.
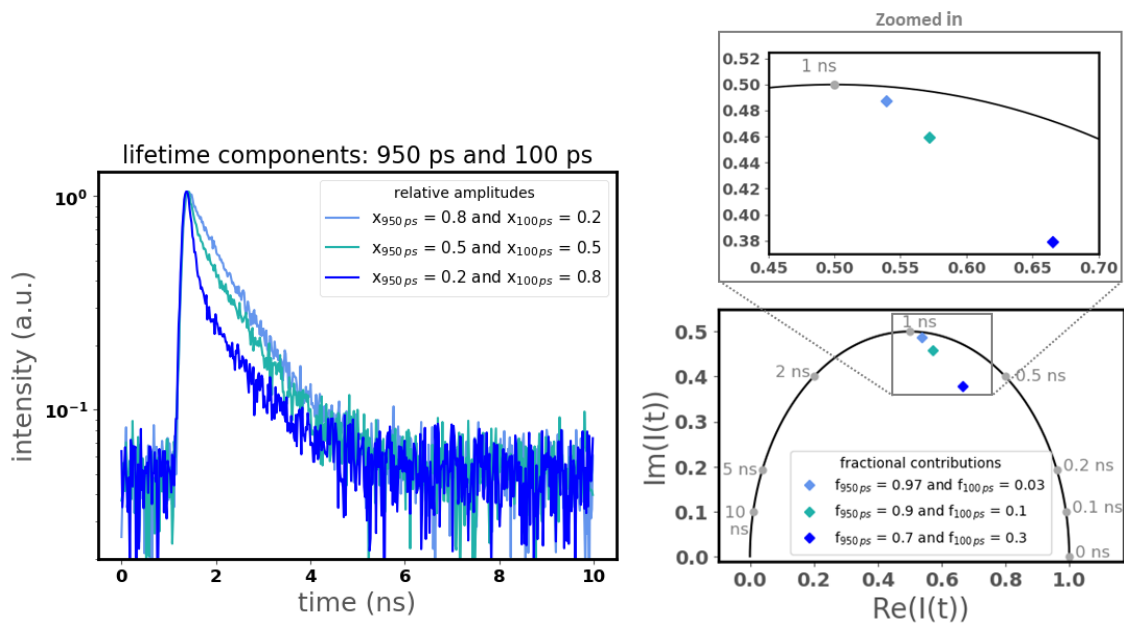

Figure D.1.: A biexponential decay with contributing lifetime components that differ by an order of magnitude: On the left hand side the simulated normalized decay curves of a biexponential decay with lifetime components of 950 ps and 100 ps are shown in a half logarithmic scaling for different combinations of the relative amplitudes x_i. On the right hand side the corresponding phasors are shown within a phasor plot. A zoomed view of the phasors is given above. In order to allow for orientation within the phasor plot a ruler of lifetimes is shown in grey color along the universal semicircle. Different combinations of the relative amplitudes of the lifetime components are shown color coded. For details see text.

From the semi-log plot of the simulated[1] decay curves on the left hand side it can be easily seen that the dark blue curve, corresponding to a relative amplitude of

---

[1]Decay curves were simulated according to Equation D.1 and convoluted with a gaussian IRF function. In order to allow for comparison with measured decay curves signal noise was included in the simulations.

0.8 for the smaller lifetime component of 100 ps, easily allows for visible identification of a biexponential decay. The other two decay curves that correspond to other combinations of the relative amplitudes of the lifetime components, shown in cyan and light blue color, respectively, do not allow for visual identification of a second contributing exponential as they have almost linear shapes. In contrast, the phasor plot on the right hand side of Fig. D.1 clearly allows for identification of non-monoexponential kinetics from the corresponding phasors by their positions within the phasor plot. The phasors corresponding to the different exemplary considered biexponential decays are all located within the universal semicircle, thus indicating a multiexponential kinetics. Hence, the phasor approach and using it for the analysis of measured fluorescence decay curves allows for resolution of a small lifetime component even when it has only a small amplitude in the decay function and thus has only a small fractional contribution to the total fluorescence intensity.

The second example mentioned above is a biexponential decay featuring two lifetime components in the same order of magnitude. In similar manner as before in Fig. D.1, the simulated decay curves of a biexponential decay with lifetime components of 950 ps and 1500 ps as well as their corresponding phasors are shown in Fig. D.2. On the left hand side the normalized simulated decay curves are shown for different combinations of the relative amplitudes, coded by color. All three decay curves have an almost linear shape within the semi-log plot and thus do not allow for clear visual identification of a second contributing lifetime component. On the right hand side the phasors corresponding to the different simulated decay curves are shown in a phasor plot. As can be seen especially in the zoomed view of the phasors in Fig. D.2, all three phasors lie close to but inside the universal semicircle. Their phasor positions clearly indicate a non-monoexponential kinetics which was not directly visible from the decay curves themselves. Thus, performing phasor analysis allows for resolution of a biexponential decay even when the contributing lifetime components are in the same order of magnitude.
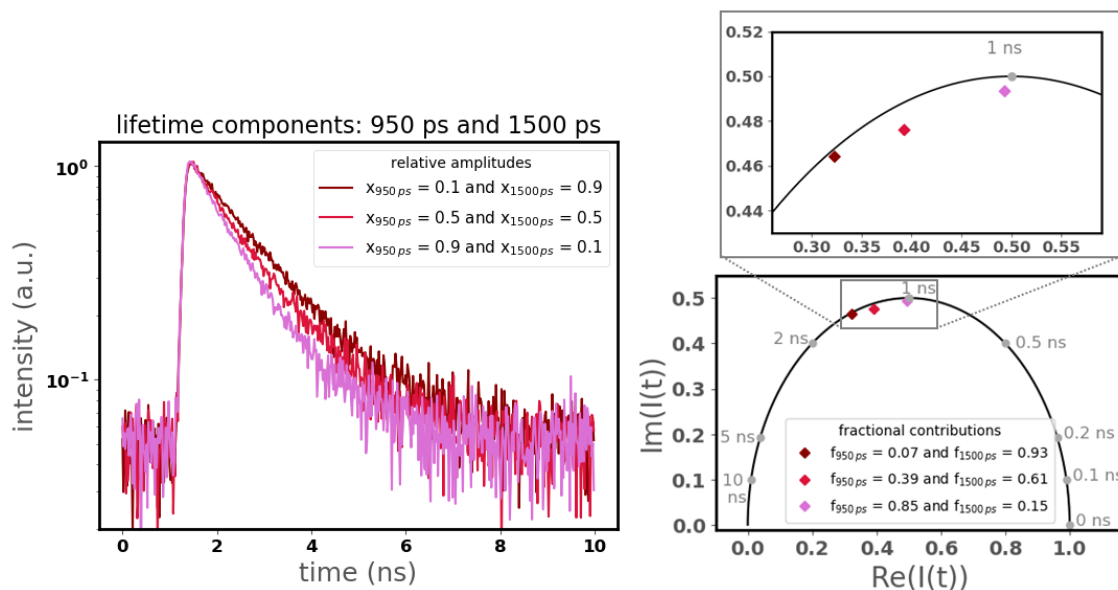
***Figure D.2.: A biexponential decay with contributing lifetime components in the
same order of magnitude:*** *On the left hand side the simulated normalized decay curves
of a biexponential decay with lifetime components of 950 ps and 1500 ps are shown in
a half logarithmic scaling for different combinations of the relative amplitudes x_i. On
the right hand side the phasors corresponding to the simulated decay curves are shown
within a phasor plot. A zoomed view of the phasors is given above. In order to allow for
orientation within the phasor plot a ruler of lifetimes is shown in grey color along the
universal semicircle. Different combinations of the relative contributions of the lifetime
components are shown color coded. For details see text.*

In conclusion, using the phasor approach for analysis of measured fluorescence
lifetime data allows for identification of multiexponential kinetics without any
apriori knowledge of the underlying kinetics or any implication given by the
visual shape of the fluorescence decay curve. Simply, from the position of a
phasor within the phasor plot the underlying kinetics, given by the contribution
lifetime components as well as their fractional contributions, is revealed.

E. Supplementary information for chapter 5: 'Fluorescence kinetics of isolated B830 LH2 complexes of *Marichromatium purpuratum*'

E.1. Inhomogeneity of the fluorescence kinetics within the datatset of isolated B830 LH2 complexes upon excitation at 790 nm

In Fig. E.1 the phasors of all measured fluorescence transients upon excitation at 790 nm are shown within one phasor plot. Error bars are shown for visualization of the uncertainty of the phasor positions. For low laser repetition rates the phasors corresponding to the measured fluorescence transients show overlapping uncertainties of their phasor positions, whereas for increasing laser repetition rate and increasing excitation fluence a significant shift of the phasor positions is observed. Moreover, the phasors of the whole data set optically seem to align on a straight line and thus giving rise to the assumption of a biexponential decay. Performing a linear fit through the cloud of phasors of the whole data set, as shown in Fig. E.1, yields a biexponential decay with the contributing lifetime components of 885 ps (+ 66/- 49) ps and 478 ps (+ 31/- 36) ps [1]. The fractional contributions that were calculated from the phasors positions are summarized in Table E.1 for different combinations of the excitation parameters, the laser repetition rate and the excitation photon fluence.

---

[1] The asymmetric values of the uncertainty of the lifetime components is due to the nonlinear scaling of the ruler of lifetimes along the universal semicircle, see also appendix C.
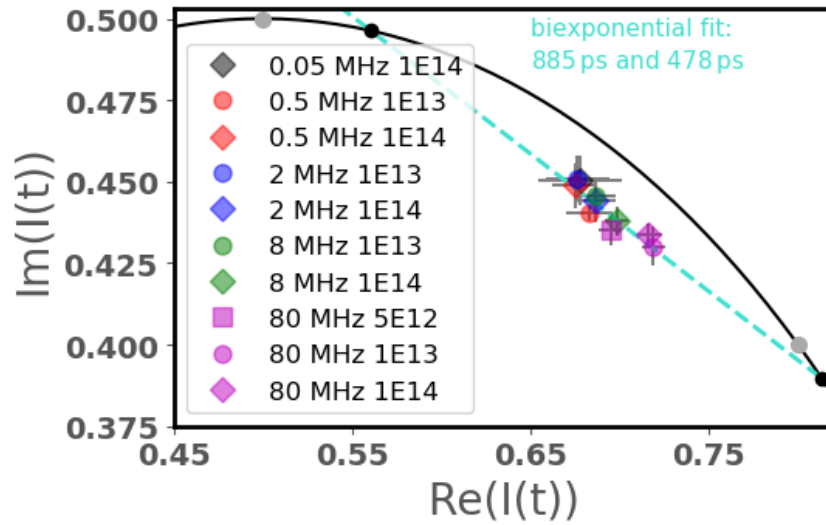
Figure E.1.: Comparison of phasor positions in the phasor plot: *The phasors corresponding to the measured fluorescence transients are shown in a zoomed view of a phasor plot. The turquoise colored line represents the biexponential kinetics resulting from the linear fit through the cloud of phasors. The black dots visualize their intersections with the universal semicircle, corresponding to the phasors of the contributing lifetime components. The two grey dots on the universal semicircle counterclockwise correspond to the values of 0.5 ns and 1 ns on the ruler of lifetimes. Different laser repetition rates are coded in color, different excitation fluences are coded by symbol. For details see text.*

laser repetition rate (MHz)	excitation fluence $\frac{photons}{pulses \cdot cm^2}$		
	$5 \cdot 10^{12}$	$1 \cdot 10^{13}$	$1 \cdot 10^{14}$
0.05			885 ps (0.54)
			478 ps (0.46)
0.5		885 ps (0.51)	885 ps (0.55)
		478 ps (0.49)	478 ps (0.45)
2		885 ps (0.55)	885 ps (0.50)
		478 ps (0.45)	478 ps (0.50)
8		885 ps (0.51)	885 ps (0.45)
		478 ps (0.49)	478 ps (0.55)
80	885 ps (0.45)	885 ps (0.37)	885 ps (0.39)
	478 ps (0.55)	478 ps (0.63)	478 ps (0.61)

Table E.1.: Calculated lifetime components and their fractional contributions for a global biexponential kinetics of isolated LH2 complexes from Marichromatium purpuratum at different excitation parameter combinations

For laser repetition rates below 80 MHz it is clearly seen that the two contribut-

ing lifetime components of 885 ps and 478 ps of the biexponential decay show an almost equal contribution to the observed fluorescence transients. For a laser repetition rate of 80 MHz this changes to a more pronounced contribution of the shorter lifetime component of 478 ps of up to 63%.

In order to account for the differences in the phasor positions it is worth having a more detailed look on the biexponential decay. If the whole data set of phasors, corresponding to the measured fluorescence transients, follows a biexponential kinetics, every category of laser repetition rates, namely low, medium and high laser repetition rates, respectively, should show almost the same two contributing lifetime components. This can be easily tested by calculating the two contributing lifetimes τ_{long} and τ_{short} of the supposed biexponential decay for each of the categories of laser repetition rates. The results for the contributing lifetime components of the supposed biexponential decay together with their corresponding uncertainties are summarized in Table E.2 for the different categories of laser repetition rates. The estimation of the uncertainties was performed as outlined in the appendix C.

category of laser repetition rates	τ_{long} [ps]	τ_{short} [ps]
low laser repetition rates	727 (+ 39/- 13)	51 (+ 215/- 140) [2]
medium laser repetition rates	788 (+ 16/- 13)	386 (+ 25/- 25)
high laser repetition rates	1300 (+ 324/- 225)	558 (+ 16/- 25)

Table E.2.: Contributing lifetimes τ_{long} and τ_{short} for a supposed biexponential kinetics at different categories of laser repetition rates

Evidently, the two contributing lifetimes τ_{long} and τ_{short} vary significantly for the different categories of laser repetition rates. Moreover, none of the different subgroups of the data set, corresponding to the different categories of laser repetition rates, shows an almost similar combination of contributing lifetime components as the global biexponential decay over the whole data set within the limits of uncertainties. As a consequence of this, it is concluded that a biexponential kinetics is not sufficient for the description of the whole data set of phasors.

---

[2]The huge values for the uncertainties with respect to the calculated value of the lifetime component is due to the nonlinear scaling of the ruler of lifetimes along the universal semicircle, see appendix C for details.

E.2. Fluorescence transients of isolated B830 LH2 complexes upon excitation of carotenoids at 485 nm

Figure E.2.: *Observed fluorescence transients of isolated B800 LH2 complexes upon excitation at 485 nm as a function of the excitation parameters: The normalized fluorescence transients of the isolated LH2 complexes of Mch. purpuratum are shown in semi-logarithmic scaling as a function of the excitation parameters. Different rows correspond to different laser repetition rates (increasing from top to bottom). Different columns correspond to different excitation fluences (increasing from left to right). For details see text.*

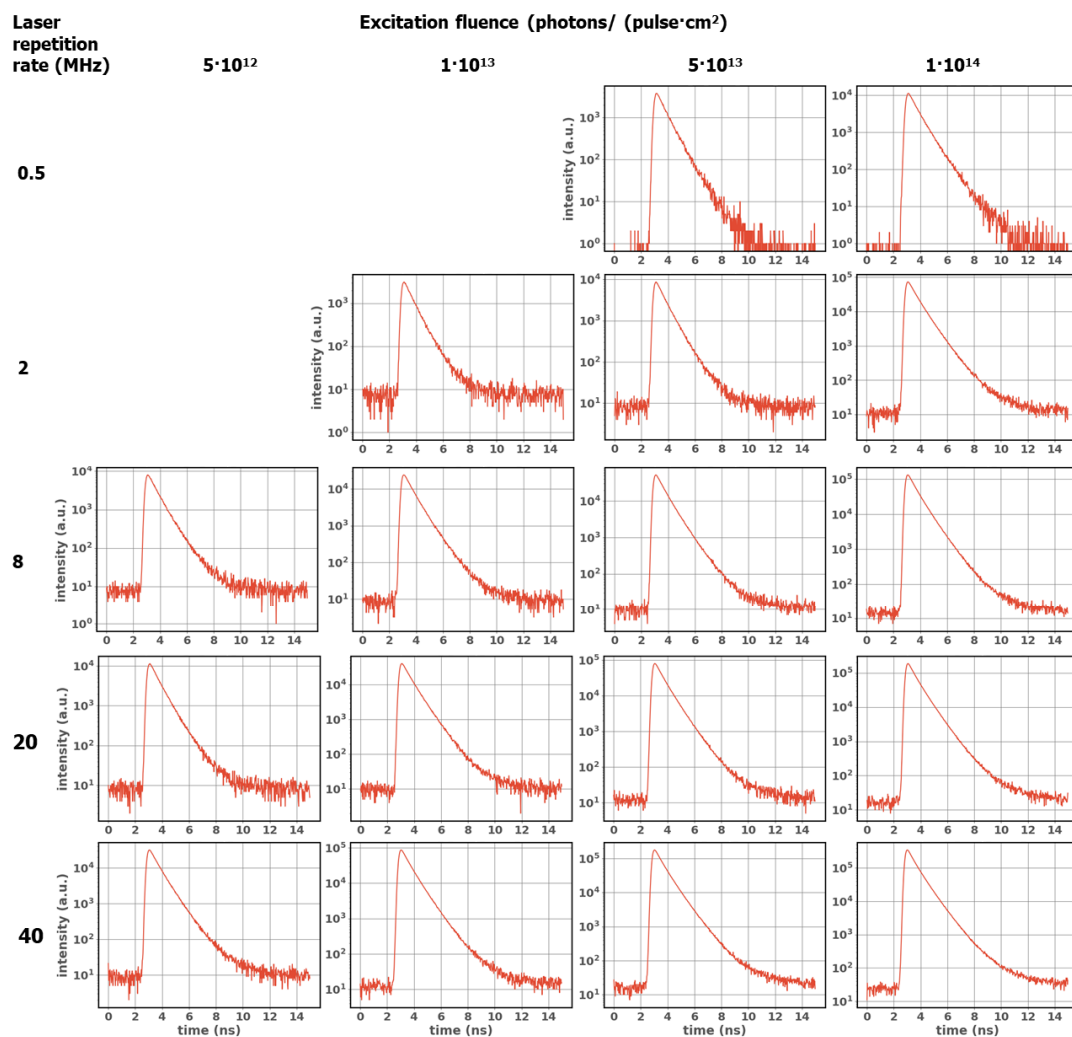# E.3. Fluorescence transients of isolated B830 LH2 complexes upon excitation of carotenoids at 560 nm
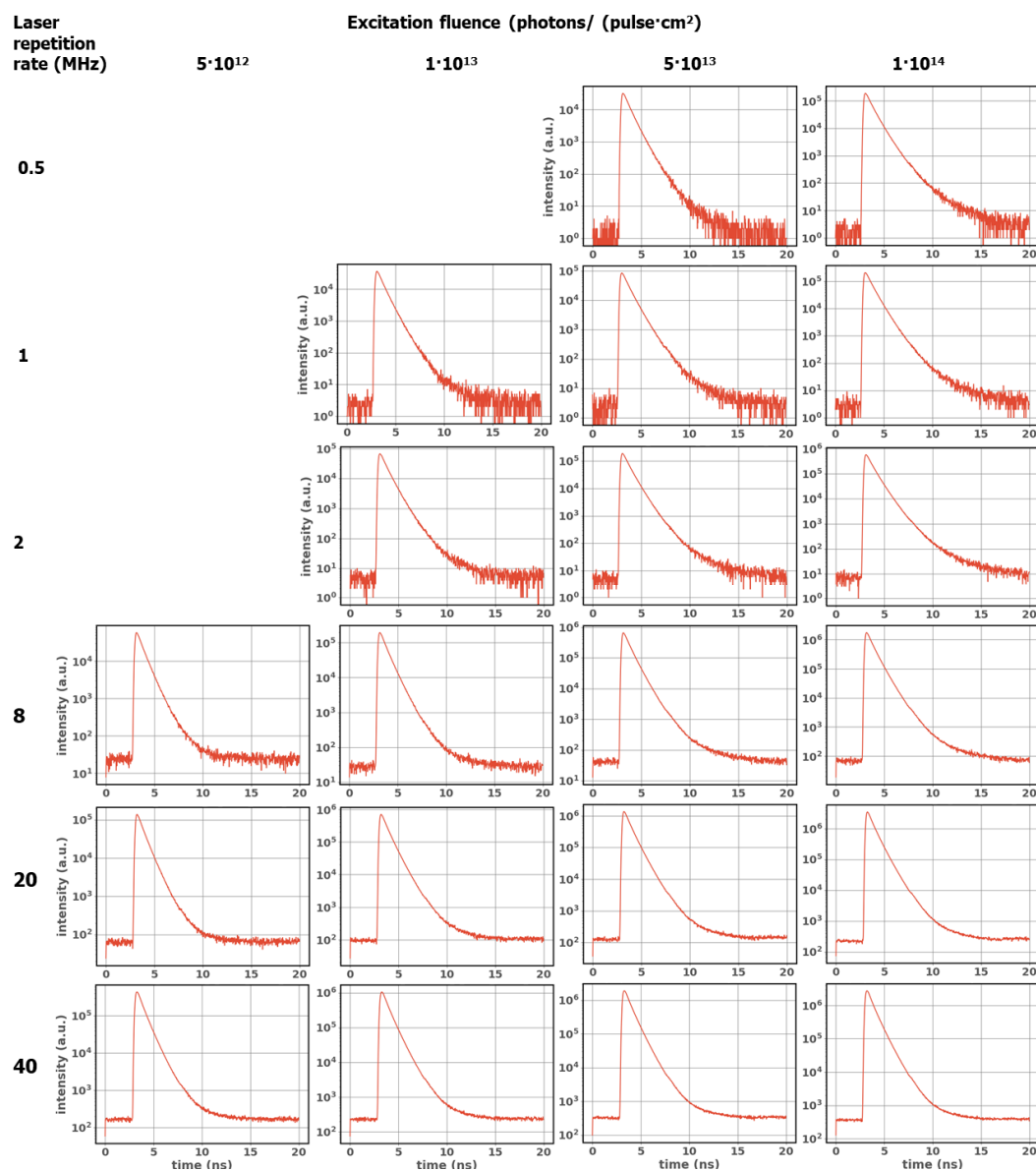
Figure E.3.: Observed fluorescence transients of isolated B800 LH2 complexes upon excitation at 560 nm as a function of the excitation parameters: *The normalized fluorescence transients of the isolated LH2 complexes of Mch. purpuratum are shown in semi-logarithmic scaling as a function of the excitation parameters. Different rows correspond to different laser repetition rates (increasing from top to bottom). Different columns correspond to different excitation fluences (increasing from left to right). For details see text.*

F. Calculation of triplet excitations

This appendix refers to the situation of triplet excitations within the LH2 complex of *Mch. purpuratum*. A single LH2 complex excited by a series of successive laser pulses is considered and the resulting triplet population within the LH2 complex is of interest.

First, the absorption cross-section of the LH2 complex for excitation of bacteriochlorophylls or carotenoid pigments, respectively, is calculated. The exctinction of one BChl a molecule in the B850 pool of pigments in the LH2 complex of *Rps. sphaeroides* is reported to amount to $184 \cdot 10^3 \frac{L}{mol \cdot cm}$ [165] . Using this value we approximate the extinction of the 14 molecules of BChl a molecules in the B830 ring of the LH2 complex of *Mch. purpuratum* as

$$\epsilon_{830} = 14 \cdot 184 \cdot 10^3 \frac{L}{mol \cdot cm} = 2.6 \cdot 10^6 \frac{L}{mol \cdot cm} \tag{F.1}$$

Scaling this number to the relative absorption at 790 nm (scaling by a factor of 0.46 with respect to 830 nm) yields $\epsilon_{790nm} = 1.2 \cdot 10^6 \frac{L}{mol \cdot cm}$ which is converted to an absorption cross-section of

$$\sigma_{790nm} = ln\,(10)\, \frac{\epsilon_{790nm}}{N_A} = 0.4 \cdot 10^{-14} cm^2 \tag{F.2}$$

where, N_A refers to Avogadro's number.
Analogously, the absorption cross-section for excitation into the carotenoids is approximated from the extinction coefficient of $134 \cdot 10^3 \frac{L}{mol \cdot cm}$ of okenone in the visible wavelength range [84, 141], which results in a value of

$$\sigma_{okenone} = 0.7 \cdot 10^{-14} cm^2 \tag{F.3}$$

Using these numbers for the absorption cross-sections we can estimate the average triplet population on a single LH2 complex as a function of the number of preceeding excitation pulses. First, we calculate the number of absorbed photons per pulse and per LH2 complex, n_{abs}, via

$$n_{abs} = \frac{P_{avg}}{h\nu} \cdot \Delta t_{rep} \cdot \frac{\sigma_{LH2}}{A_{focus}} = \frac{P_{avg}}{hc/\lambda} \cdot \Delta t_{rep} \cdot \frac{\sigma_{LH2}}{A_{focus}} \tag{F.4}$$

Here P_{avg} denotes the time-averaged power of the excitation laser, $h\nu$ refers to the photon energy at frequency ν (respectively hc/λ refers the photon energy at wavelength λ), Δt_{rep} is the temporal separation of subsequent excitation laser pulses, given by the inverse of the laser repetition rate, σ_{LH2} refers to the absorption cross-section at the particular wavelength, and A_{focus} corresponds to the size of the focus that amounted to $1.65 \cdot 10^{-6} cm^2$ for excitation at 790 nm, and to $1.91 \cdot 10^{-9} cm^2$ for excitation into the carotenoid absorption band. From these numbers we obtain the number of absorbed photons per pulse and per LH2 complex as summarized in Table F.1.

Excitation wavelength (nm)	Average laser power (W)	Excitation fluence $(photons/(pulse \cdot cm^2))$	n_{abs} absorbed photons per pulse and complex
790 nm	$0.16 \cdot 10^{-3}$	$5 \cdot 10^{12}$	0.035
	$0.6 \cdot 10^{-3}$	$1 \cdot 10^{13}$	0.073
	$6 \cdot 10^{-3}$	$1 \cdot 10^{14}$	0.73
485 nm / 560 nm	$0.16 \cdot 10^{-6}$	$5 \cdot 10^{12}$	0.055
	$0.56 \cdot 10^{-6}$	$1 \cdot 10^{13}$	0.11
	$1.56 \cdot 10^{-6}$	$5 \cdot 10^{13}$	0.55
	$5.6 \cdot 10^{-6}$	$1 \cdot 10^{14}$	1.1

Table F.1.: Calculated number of absorbed photons per pulse per complex for different excitation conditions. The averaged excitation laser power values refer to experiments performed at highest repetition rates, such as 80 MHz for excitation of bacteriochlorophylls (790 nm), and 40 MHz for excitation of carotenoids (485 nm / 560 nm.)

As discussed in Section 6.6 the triplet quantum yields $\Phi_{triplet}$ for populating the ^{3}Car* state in the LH2 complex of *Mch. purpuratum* amount to about 0.63 % for excitation into the B800 band and to about 5.5 % for excitation into the carotenoid

absorption band. Hence, after the first laser pulse the population of the ^{3}Car* state amounts to $n_1 = n_{abs} \cdot \phi_{triplet}$ and decays with a rate $k_{triplet}$=1.2 μs^{-1} to the ground state [57]. The averaged population of the ^{3}Car* triplet state prior to the second laser pulse is therefore

$$n_1 \cdot exp[-\Delta t_{rep} \cdot k_{triplet}] \tag{F.5}$$

Thus, after the second laser pulse the triplet population of the ^{3}Car* state is given by

$$n_2 = n_1 \cdot exp[-\Delta t_{rep} \cdot k_{triplet} + n_{abs} \cdot \Phi_{triplet} \tag{F.6}$$

and successive excitations lead to the accumulation of population in the ^{3}Car* state, that amounts to

$$n_i = \sum_{j=1}^{i} n_{abs}\phi_{triplet}(exp[-\Delta t_{rep} \cdot k_{triplet}])^{j-1} \tag{F.7}$$

after the i-th pulse.

Examples for the evolution of the triplet population in the LH2 complex, corresponding to the number of triplet excitations per LH2 complex, as a function of the number of excitation pulses are shown in Section 6.6 in Fig. 6.8 for excitation of both pigments at high excitation densities. The saturation time is mainly determined by the ratio of Δt_{rep}, the temporal separation of successive laser pulses, and the carotenoid triplet lifetime $\tau_{triplet}$, whereas the number of absorbed photons per pulse, see Table F.1 in combination with the value of the triplet quantum yield $\phi_{triplet}$ determines the saturation value of the steady state triplet population. An overview of the steady state triplet populations for the different combinations of the laser repetition rate and the excitation photon fluences are given in Tables F.2 and F.3 for excitation of bacteriochlorophylls and carotenoid pigments, respectively.

Laser repetition rate (MHz)	Excitation fluence $(photons/(pulse \cdot cm^2))$			Accumulation time (no. of pulses / time)
	$5 \cdot 10^{12}$	$1 \cdot 10^{13}$	$1 \cdot 10^{14}$	
0.05			0	
0.5		0	0	
2		0	0	
8		0	0.05	60 pulses / 7.5 μs
80	0	0.04	0.44	500 pulses / 6.25 μs

Table F.2.: Steady-state triplet population for excitation into the B800 manifold.

Laser repetition rate (MHz)	Excitation fluence $(photons/(pulse \cdot cm^2))$				Accumulation time (no. of pulses / time)
	$5 \cdot 10^{12}$	$1 \cdot 10^{13}$	$5 \cdot 10^{13}$	$1 \cdot 10^{14}$	
0.5			0	0	
1		0	0	0	
2		0	0	0.18	
8	0	0	0.3	0.62	60 pulses / 7.5 μs
20	0	0.15	0.74	1.49	150 pulses/ 7.5 μs
40	0.15	0.3	1.46	2.96	200 pulses/ 5 μs

Table F.3.: Steady-state triplet population for excitation into the carotenoids.

In the next step it is considered that the values of the steady state triplet populations given in the two tables above corresponds to the expectation value of a Poisson distribution. Thus, it is possible to determine the probability that an LH2 complex carries k triplets via

$$P_\lambda(k) = \frac{\lambda^k}{k!} e^{-\lambda} \tag{F.8}$$

where λ denotes the expectation value of the Poisson distribution.

In Table F.4 the situation of triplets is considered for the highest excitation density, corresponding ton the combination of highest laser repetition rate and highest excitation fluence, for excitation of bacteriochlorophylls on the left hand side and excitation of carotenoid pigments on the right hand side. For both excitation situations the probability of finding one, two, three or even four triplets

is summarized as calculated from Equation F.8. Whereas for excitation of bacteriochlorophylls the probability of finding more than one triplet excitation per LH2 ring is about 7%, for excitation of the carotenoid pigments it appears to be highly probably (62%) that multiple triplet excitations may exist on one LH2 ring.

Next, it is taken into account that triplets have to be located on adjacent carotenoids in order to allow for triplet-triplet annihilation (TTA). Thus, by considering the fraction of adjacent located triplet excitations of all possible arrangements of triplets on a ring with 14 possible triplet locations, resulting from the 14 carotenoids molecules within the B830 LH2 complex, the probabilities P(2), P(3) and P(4) reduce by factors of 0.1538, 0.4679 and 0.1043, respectively, from considerations of combinatorics. Hence, accumulating the weighted probabilities then yields the overall probabilities of 0.013 and 0.157 for finding adjacently arranged triplet excitations within the LH2 complex from *Mch. purpuratum* upon excitation of bacteriochlorophyll or carotenoid pigments, respectively.

Excitation of BChl			Excitation of Car		
$\lambda = 0.44$			$\lambda = 2.96$		
Probability of finding k triplets P(k)		Accumulated probability for adjacent triplets	Probability of finding k triplets P(k)		Accumulated probability for adjacent triplets
P(1)	0.28	0	P(1)	0.15	0
P(2)	0.06		P(2)	0.23	
P(3)	0.009	0.013	P(3)	0.22	0.157
P(4)	$1 \cdot 10^{-3}$		P(4)	0.17	

Table F.4.: Probabilities for finding different numbers of triplet excitations on an LH2 complex upon excitation of bacteriochlorphyll or carotenoid.

From considerations on TTA before, see Sections 6.2 and 6.6 it is clear that the occurrence of TTA requires triplet excitations to be located on adjacent carotenoid molecules within the LH2 complex. Hence, the probability for the occurrence of TTA is proportional to the accumulated probability values for triplets located on adjacent carotenoid molecules given in Table F.4 and thus the accumulated probabilities for adjacent triplet arrangement within an LH2 complex can be treated as an upper limit for the probability of TTA occurrence in the LH2 complex of *Mch. purpuratum*.

G. Supplementary information for chapter 7: 'Modelling of electronic excitations in isolated LH2 complexes of *Mch. purpuratum*'

This appendix gives additional information on the dynamical Monte-Carlo simulations outlined in Chapter 7. First, a rate model considering all possible re-excitations of an LH2 complex yet carring an electronic excitations is considered. Then, the additional information concerning the simulated fluorescence transients are given. Both, the basis simulation as well as the refined simulations by variation of the singlet-triplet annihilation rate are discussed for excitation of the bacteriochlorophyll pigments within the LH2 complex. Finally, the situation of triplet excitations in the basis simulations using the experimentally obtained value for the singlet-triplet annihilation rate is discussed.

G.1. A rate model considering re-excitation of an LH2 complex

A basis rate model for the electronic states of an LH2 complex upon excitation of bacteriochlorophylls was developed in Section 7.1 and is shown in Fig. 7.1. Hence, in order to consider excitation annihilation processes within the DMC simulations, the possibility of multiple excitations on one LH2 complex must be included in the simulations. Thus, the re-excitation, namely the excitation of an LH2 complex yet carrying an excitation, has to be included in the rate model for the simulations.

An expanded rate model for the excitation of an LH2 complex is presented, now including the possibility that both, either an LH2 complex in state |2> carrying a singlet excitation as well as an LH2 complex in state |3> yet carring a triplet excitation may be re-excited by another excitation laser pulse. This allows for the occurrence of multiple excitations on one LH2 complex and thus allowing for the occurrence of excitation annihilation processes. Hence, the simplified pictorial representation on the right hand side of Fig. 7.1 is expanded to a larger rate model representing now also multiple excitation on one LH2 complex, see Fig. G.1, and allows for the occurrence of excitation annihilation processes within the LH2 complex.
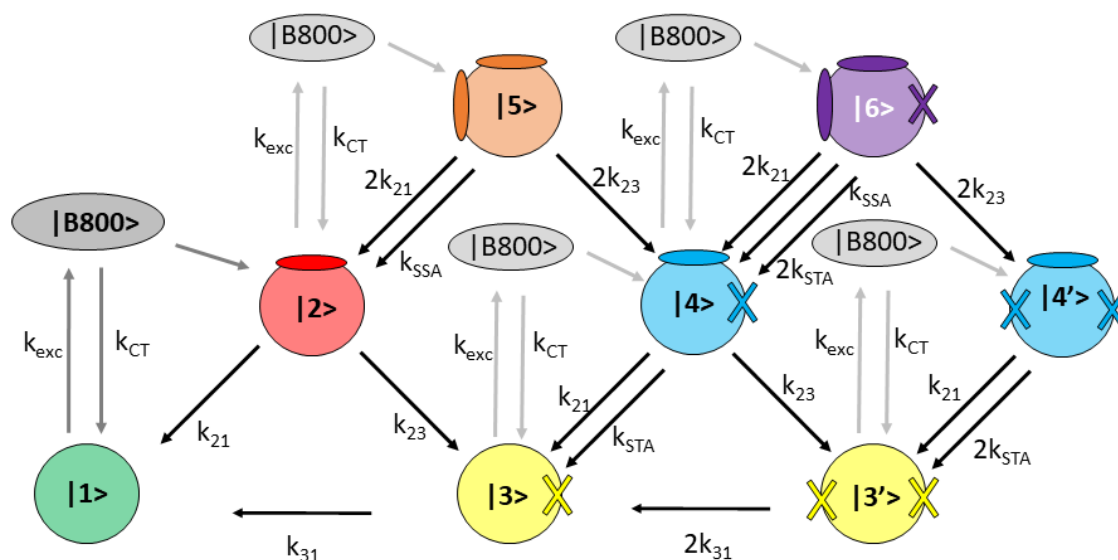

Figure G.1.: Pictorial representation of the transitions between electronic states of an isolated LH2 complex of the B830 LH2 complex of Mch. purpuratum: *The different electronic states of the B830 LH2 complex of Mch. purpuratum and the possible transitions between these states are shown. Different electronic states of the B830 LH2 complex are coded by color, the small ellipses and crosses attached to the big colored circle representing the LH2 complex visualize singlet and triplet excitations within the LH2 complex, respectively. The excitation process of the LH2 complex via the B800 ring of BChl a molecules is visualized in grey color as before on the right hand side of Fig. 7.1. For details see text.*

As pointed out before, absorption of excitation light results in the creation of a singlet excitation within the ring of B830 BChl *a* molecules of the B830 LH2 complex. This transition from the electronic ground state |1> , depicted as a green circle, to state |2> corresponding to an LH2 complex carring a singlet excitation

within the ring of B830 BChl *a* molecules, depicted in red color, always happens via the |B800> state, visualized in grey. In order to allow for a simplified visualization the excitation process of the LH2 complex resulting in the creation of a singlet excitation within the B830 ring BChl *a* molecules is always visualized in pale grey color whenever an additional singlet excitation is created. Hence all the pale grey ellipses denoted as |B800> in Fig. G.1 refer to excitation processes of the LH2 complex.

When an LH2 complex in state |2>, that carries a singlet excitation of the B830 molecules, is excited again this results in two singlet excitations of the B830 ring of BChl *a* molecules. Such an LH2 ring which carries two singlet excitations is depicted in Fig. G.1 as an orange circle with two orange ellipses representing the two excited states and is denoted as state $|5>=|^1B800,^1B830^*,^1B830^*,^3Car>$. Relaxation from state |5> to state |2> may happen under emission of fluorescence with a rate[1] $k_{52} = 2 k_{21}$ or by singlet-singlet-annhiliation (SSA) as depicted by the rate $k_{SSA} = (1 ps)^{-1}$ which is taken from literature [61]. Alternatively the energy of state |5> can be transferred to state |4> by intersystem crossing with a rate $k_{54} = 2 k_{23}$ which results in the formation of a triplet state on one of the carotenoid molecules. The resulting state $|4>=|^1B800,^1B830^*,^3Car^*>$ is represented as a blue circle hosting a blue ellipse representing the singlet excitation $^1B830^*$ of the B830 molecules and hosting a blue cross representing the triplet excitation $^3Car^*$.

Now, starting from state |4> several transitions are possible. One possible pathway is the transition to state |3>, represented by a yellow circle with one yellow cross, either upon radiative relaxation under emission of fluorescence with a rate $k_{43} = k_{21}$ or by the occurrence of singlet-triplet annihilation (STA) with a rate $k_{STA} = 6.3 \cdot 10^8 s^{-1}$, which was identified from the experiments as outlined in Section 6.3. Alternatively also intersystem crossing can take place with the rate k_{23} resulting in an electronic state of the LH2 complex which carries two triplet excitations, represented as a yellow circle with two yellow crosses, and which is denoted as state $|3'>=|^1B800,^1B830,^3Car^*,^3Car^*>$. As a third possibility, state |4> can receive another singlet excitation upon further excitation which results in an electronic state of the LH2 complex which carries two singlet

---

[1]At room temperature both excited singlet excited states of state |5> can decay independently [69].

excitations and one triplet excitation. Such an LH2 complex is depicted by a purple circle hosting two purple ellipses representing the two ^{1}B830* singlet excitations and the one ^{3}Car* triplet excitation and this state is referred to as state $|6>=|^1$B800,^{1}B830*,^{1}B830*,^{3}Car*>. For the transition from state $|6>$ to state $|4>$ there are three possibilities: radiative relaxation under emission of fluorescence with a rate $k_{64} = 2\,k_{21}$ or alternatively either SSA or STA might occur with the rates $k_{SSA,64} = k_{SSA}$ and $k_{STA,64} = 2\,k_{STA}$, respectively. Via intersystem crossing also the transition from state $|6>$ to a state $|4'>=|^1$B800,^{1}B830*,^{3}Car*,^{3}Car*> can occur with a rate $k_{64'} = 2\,k_{23}$, resulting in a electronic state of the LH2 complex that carries one singlet ^{1}B830* and two ^{3}Car* triplet excitations, represented as a blue circle hosting one blue ellipse and two blue crosses visualizing the one singlet and the two triplet excitations, respectively. The relaxation from state $|4'>$ to state $|3'>$ can occur either radiative with a rate $k_{4'3'} = k_{21}$ or by the occurrence of STA with a rate $k_{STA,4'3'} = 2\,k_{STA}$. The transition from state $|3'>$ to state $|3>$ happens nonradiative with a rate $k_{3'3} = 2\,k_{31}$.

Using the model depicted in Fig. G.1 then only a few transition rates, some taken from the experiments and some from literature, are needed to allow for modelling of the electronic excitations within the B830 LH2 complex of *Mch. purpuratum*. Such simulations showed a saturation in population of the higher triplet states, such as states $|3'>$ and $|4'>$. Hence, regarding the number of possible triplet excitations on one LH2 complex the rate model outlined above is not sufficient and has to be expanded. In addition, in the simulations the excitation of an LH2 complex in state $|2>$ was only negligibly observed in the simulations[2] and re-excitation of an LH2 complex in state $|4>$ never occurred. This finding is in accordance with the estimations on basis of the laser repetition rates in the experiments in Section 7.1 and hence it is not necessary to include the re-excitations of these two states in the rate model for the DMC simulations and a simplified rate model neglecting these re-excitations, as outlined in Section 7.1, is sufficient.

---

[2]Only 2 of 10^8 simulated excitation processes were excitations of an LH2 complex in state $|2>$.

G.2. Kinetic evaluation of the simulated fluorescence transients (basis simulation, k_{STA} from experiments)

The simulated fluorescence transients shown in Fig. 7.4 are now analyzed using the phasor approach, which was outlined in detail in Chapter 4. Hence, phasor were calculated from the simulated transients analogously to the procedure performed for the fluorescence transients obtained from the experiments. In Fig. G.2 the phasors calculated from the simulated transients are shown in a zoomed view of the phasor plot. Notably all phasor are located inside the universal semicircle, thus indicating a multiexponential kinetics. Next, a detailed phasor analysis is performed. In analogy to the procedure of phasor analysis of the experimental data, first a biexponential kinetics is assumed for the phasors corresponding to low laser repetition rates. Then it is checked whether the phasors corresponding to higher laser repetition rates correspond to this biexponential kinetics or an additional time constant is necessary for description of the underlying kinetics.
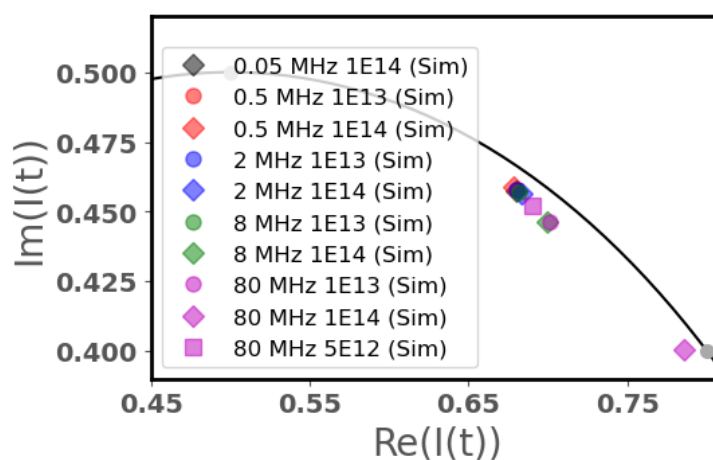
Figure G.2.: Phasor plot illustrating the phasors calculated from the simulated transients: The phasors that were calculated from the simulated fluorescence transients in Fig. 7.4 are shown in a zoomed view of the phasor plot. Different laser repetition rate are coded by color, different excitation fluence are indicated by different symbols. For details see text.

Performing a linear fit to the phasors at low laser repetition rates yields lifetime

components of $712 (+ 19/- 8)$ ps and $216 (+ 152/- 117)$ ps [3] from the intersections with the universal semicircle as can be seen in Fig. G.3a. The turquoise line corresponds to the linear fit, the lines of pale grey and pale red color visualize the tolerance interval of the linear fit and correspond to the lines of minimum and maximum slope of the fit parameters, respectively.
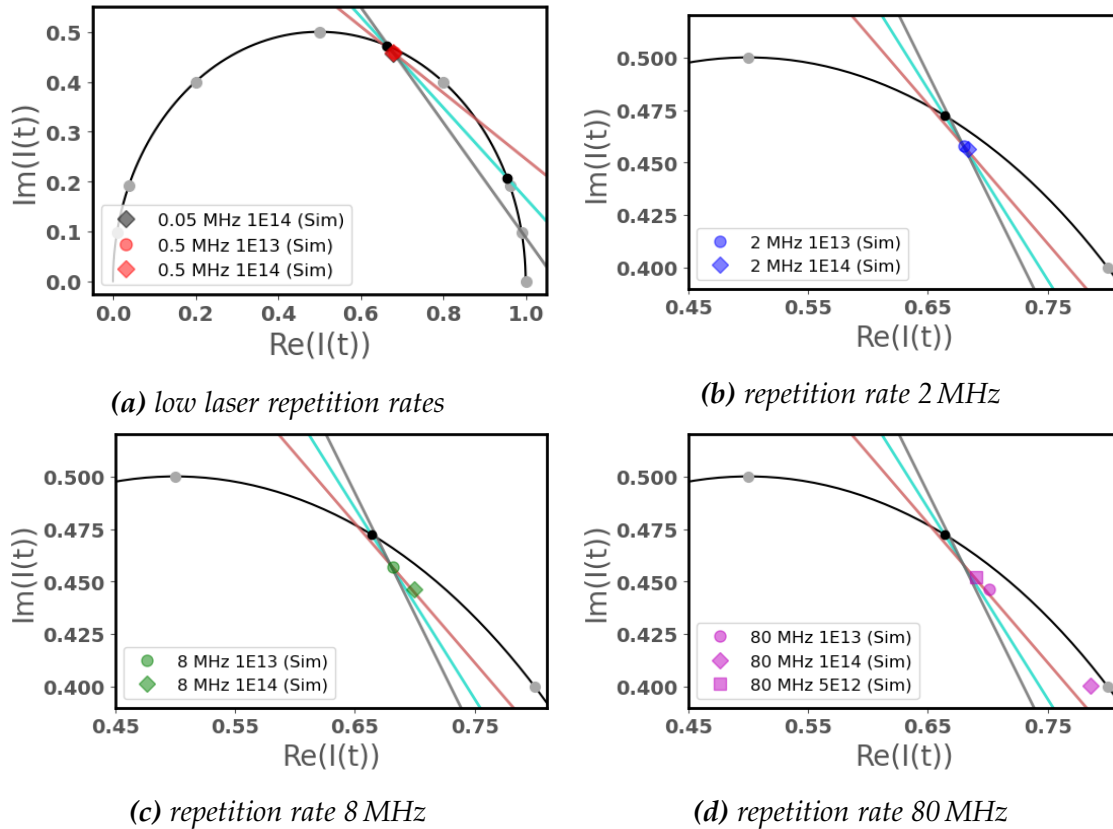

(a) low laser repetition rates

(b) repetition rate 2 MHz

(c) repetition rate 8 MHz

(d) repetition rate 80 MHz

Figure G.3.: Phasor plots for analysis of the phasor calculated from the simulated fluorescence transients: *The phasors calculated from simulate fluorescence transients shown in Fig. 7.4 are visualized in separate phasor plots for the laser repetition rates of 0.05 MHz and 0.5 MHz **(a)**, 2 MHz **(b)**, 8 MHz **(c)** and 80 MHz **(d)**, respectively. For the laser repetition rates 0.05 MHz and 0.5 MHz in **a** an non zoomed view of the phasor plot is shown including a ruler of lifetimes along the universal semicircle (grey circles) counterclockwise denoting the values 0 ns, 0.1 ns, 0.2 ns, 0.5 ns, 1 ns, 2 ns, 5 ns and 10 ns, respectively. The other subfigures **(b,c,d)** show zoomed views of the phasor plot. Different laser repetition rates are coded by color, different excitation fluence are coded by different phasor symbols. For details see text.*

Next, for the other laser repetition rates 2 MHz, 8 MHz and 80 MHz it is checked whether they correspond to this biexponential kinetics by evaluation of the pha-

---

[3]The asymmetric values of the uncertainty of the lifetime components is due to the nonlinear scaling of the ruler of lifetimes along the universal semicircle, see also appendix C.

sor positions with respect to the colored lines representing the biexponential kinetics. However this is not as easy as for the experimental data due to the fact that the uncertainty of the phasor positions is very small for the simulated transients[4]. Hence, the outer limits of the phasor symbols are used for estimation of the uncertainty of the phasor positions in the following evaluation of phasor positions. From Figures G.3c and G.3d it is visible that for a laser repetition rate of 8 MHz and an excitation fluence of $1 \cdot 10^{14}$ photons/(pulse·cm^2) a third lifetime component is likely necessary as well as for a laser repetition rate of 80 MHz and an excitation fluence of $1 \cdot 10^{13}$ photons/(pulse·cm^2) as their phasor symbols, green colored diamond in Fig. G.3c and magenta colored circle symbol in G.3d, only touch the red line within the figures, thus lying almost outside the tolerance interval of the biexponential kinetics and thus indicating a likely third lifetime component.

In contrast, for the situation of a laser repetition rate of 80 MHz in combination with an excitation fluence, the corresponding phasor illustrated by a magenta colored diamond symbol in Fig. G.3d clearly lies apart from the colored lines representing the biexponential kinetics and its tolerance interval. Hence, a triexponential kinetics is necessary for this combination of excitation parameters. For all other excitation parameter combinations a biexponential kinetics is sufficient, as the phasor symbols clearly lie inside within the tolerance interval of the biexponential fit, spanned by the pale grey and pale red lines. Table G.1 summarizes the qualitative results of the phasor analysis.

laser repetition	excitation fluence $\frac{photons}{pulses \cdot cm^2}$		
rate (MHz)	$5 \cdot 10^{12}$	$1 \cdot 10^{13}$	$1 \cdot 10^{14}$
0.05			biexponential
0.5		biexponential	biexponential
2		biexponential	biexponential
8		biexponential	triexponential
80	biexponential	triexponential	triexponential

---

[4]From Fig. 7.4 it is clearly visible that the simulated transients feature a smooth shape and thus calculation of the error of the phasor positions as outlined in appendix C results in infinitesimal values for the uncertainty of the phasor position.

Table G.1.: Lifetime components and their fractional contributions for the multi-exponential kinetics of simulated fluorescence transients considering excitation of bacteriochlorophyll pigments

A quantitative overview of the biexponential or triexponential kinetics, respectively, summarizing the fluorescence lifetime components as well as their calculated fractional intensity contributions is given in Table 7.2 in Section 7.2.

G.3. Refinement approaches by variation of k_{STA}

Two refined simulations using alternative values for the singlet-annihilation rate k_{STA} but being apart of this completely identical to the basic simulation are presented.

Refinement 1: smaller k_{STA}

This refinement refers to a value of $1.3 \cdot 10^8 \, s^{-1}$ for the singlet-triplet annihilation rate k_{STA}, which was reported for LH2 complexes of *Rps. acidophila* [3].

An overview of the simulated fluorescence transients in comparison to the transients obtained in the experiments are shown in Fig. G.4. Analogously to previous tabular arrangements in this thesis, the different columns correspond to different excitation photon fluences and different rows correspond to different laser repetition rates. For each of the excitation parameter combinations the experimentally obtained fluorescence transient, denoted as *Decay*, and the simulated fluorescence transient that was convoluted with the experimental IRF for reasons of comparability, denoted as *Simulation*, are shown both normalized in one plot. Below each of the plots, the corresponding residual visualizes the difference of the experimental curve and the simulated curve. Although overall good agreement of the two curves is observed, for high excitation densities small discrepancies are observed.

Figure G.4.: Comparison of experimental and simulated fluorescence transients: Refinement 1 For details see text.
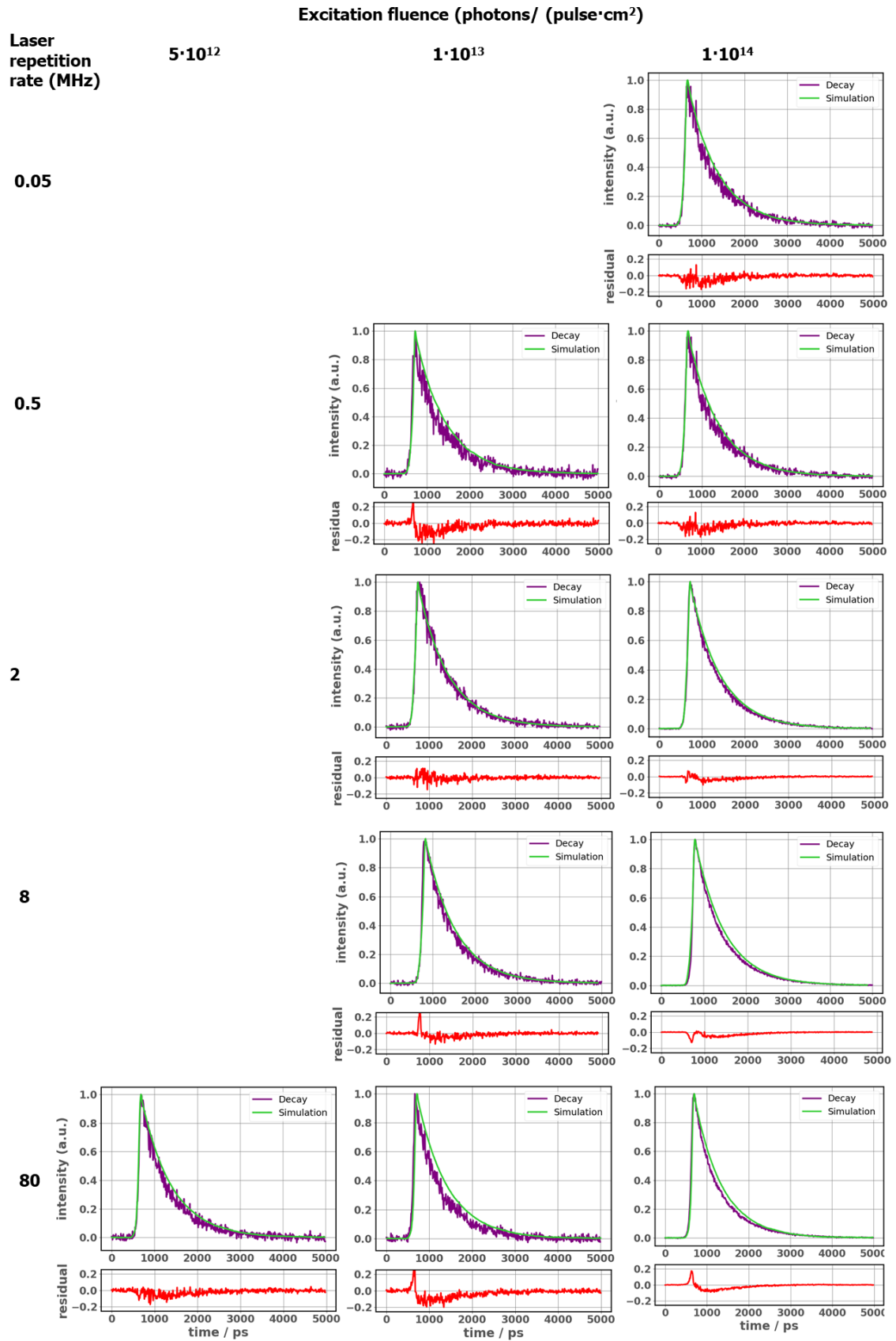
Next, a phasor analysis is performed in order to analyze the kinetics of the simulated fluorescence transients. As outlined before for the phasor analysis of the basic simulation using the experimental value for the singlet-triplet annihilation rate, the phasors were calculated from the simulated transients and the position of the phasors within the phasor plot is analyzed. Notably all phasor are located inside the universal semicircle, thus indicating a multiexponential kinetics.
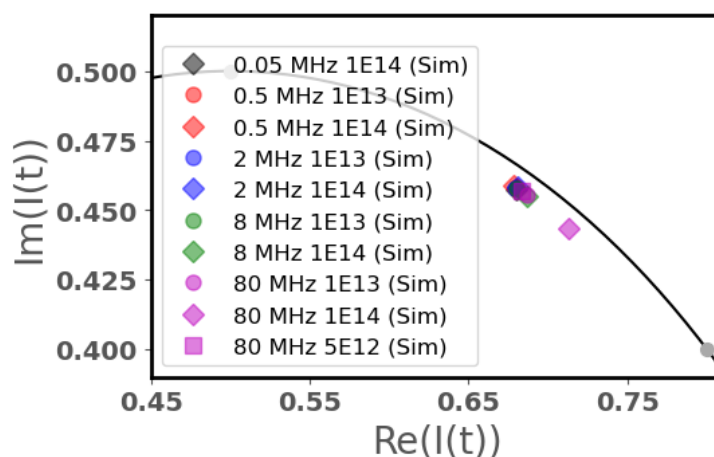

Figure G.5.: Phasor plot illustrating the phasors calculated from the simulated transients: *The phasors that were calculated from the simulated fluorescence transients in Fig. G.4 are shown in a zoomed view of the phasor plot. Different laser repetition rate are coded by color, different excitation fluence are indicated by different symbols. For details see text.*

Now, a detailed phasor analysis is performed. In analogy to the procedure of phasor analysis of the experimental data, first a biexponential kinetics is assumed for the phasors corresponding to low laser repetition rates. Then it is checked whether the phasors corresponding to higher laser repetition rates correspond to this biexponential kinetics or an additional time constant is necessary for description of the underlying kinetics.

Performing a linear fit to the phasors at low laser repetition rates yields lifetime components of 723 (+ 53/- 14) ps and 325 (+ 183/- 148) ps [5] from the intersections with the universal semicircle as can be seen in Fig. G.6a. The turquoise line corresponds to the linear fit, the lines of pale grey and pale red color visualize the tolerance interval of the linear fit and correspond to the lines of minimum

---

[5]The asymmetric values of the uncertainty of the lifetime components is due to the nonlinear scaling of the ruler of lifetimes along the universal semicircle, see also appendix C.

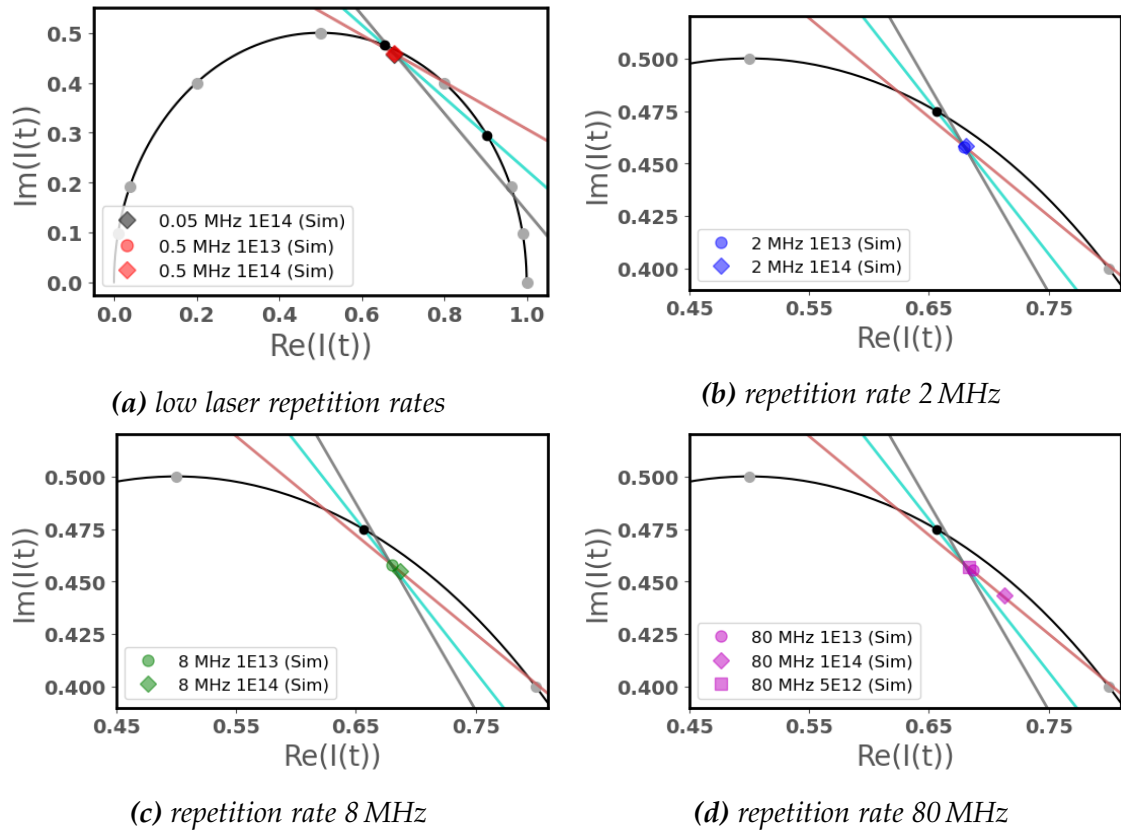and maximum slope of the fit parameters, respectively.

(a) low laser repetition rates

(b) repetition rate 2 MHz

(c) repetition rate 8 MHz

(d) repetition rate 80 MHz

***Figure G.6.: Phasor plots for analysis of the phasor calculated from the simulated fluorescence transients (Refinement 1: smaller k_{STA}:** The phasors calculated from simulate fluorescence transients shown in Fig. G.4 are visualized in separate phasor plots for the laser repetition rates of 0.05 MHz and 0.5 MHz **(a)**, 2 MHz **(b)**, 8 MHz **(c)** and 80 MHz **(d)**, respectively. For the laser repetition rates 0.05 MHz and 0.5 MHz in **(a)** a non zoomed view of the phasor plot is shown including a ruler of lifetimes along the universal semicircle (grey circles) counterclockwise denoting the values 0 ns, 0.1 ns, 0.2 ns, 0.5 ns, 1 ns, 2 ns, 5 ns and 10 ns, respectively. The other subfigures **(b,c,d)** show zoomed views of the phasor plot. Different laser repetition rates are coded by color, different excitation fluence are coded by different phasor symbols. For details see text.*

From the subfigures G.6b, G.6c and G.6d it is clearly visible that all the phasors overlap with the tolerance interval of the biexponential kinetics spanned by the colored lines[6]. Hence a bixpoential kinetics is sufficient for the entire dataset.

---

[6]As outlined before in Section G.2 the outer limits of the phasor symbols are used for estimation of the uncertainty of the phasor positions.

Refinement 2: higher k_{STA}

This refinement refers to a higher value for the singlet-triplet annihilation rate k_{STA} and for the simulations a value of $2 \cdot 10^9 \, s^{-1}$ was used, as reported by simulations on LH2 complexes from *Rps. acidophila* before [69].

In Fig. G.7 an overview of the simulated fluorescence transients is given in comparison to the transients obtained in the experiments. In analogy to previous tabular arrangements in this thesis, the different columns correspond to different excitation photon fluences and different rows correspond to different laser repetition rates. For each of the excitation parameter combinations the experimentally obtained fluorescence transient, denoted as *Decay*, and the simulated fluorescence transient that was convoluted with the experimental IRF for reasons of comparability, denoted as *Simulation*, are shown both normalized in one plot. Below each of the plots, the corresponding residual visualizes the difference of the experimental curve and the simulated curve. Overall good agreement of the two curves is observed except for the excitation parameter combination of highest laser repetition rate of 80 MHz and highest excitation fluence of $1 \cdot 10^{14}$ photons/(pulse·cm^2). There the simulated fluorescence transients decays much faster than the experimental curve.

Next, a detailed phasor analysis is performed in order to investigate the kinetics of the simulated transients. First a biexponential kinetics is assumed for the phasors corresponding to low laser repetition rates in analogy to the phasor analysis of the experimental data. Then in the second step it is checked whether the phasors corresponding to higher laser repetition rates correspond to this biexponential kinetics or an additional time constant is necessary for description of the underlying kinetics.
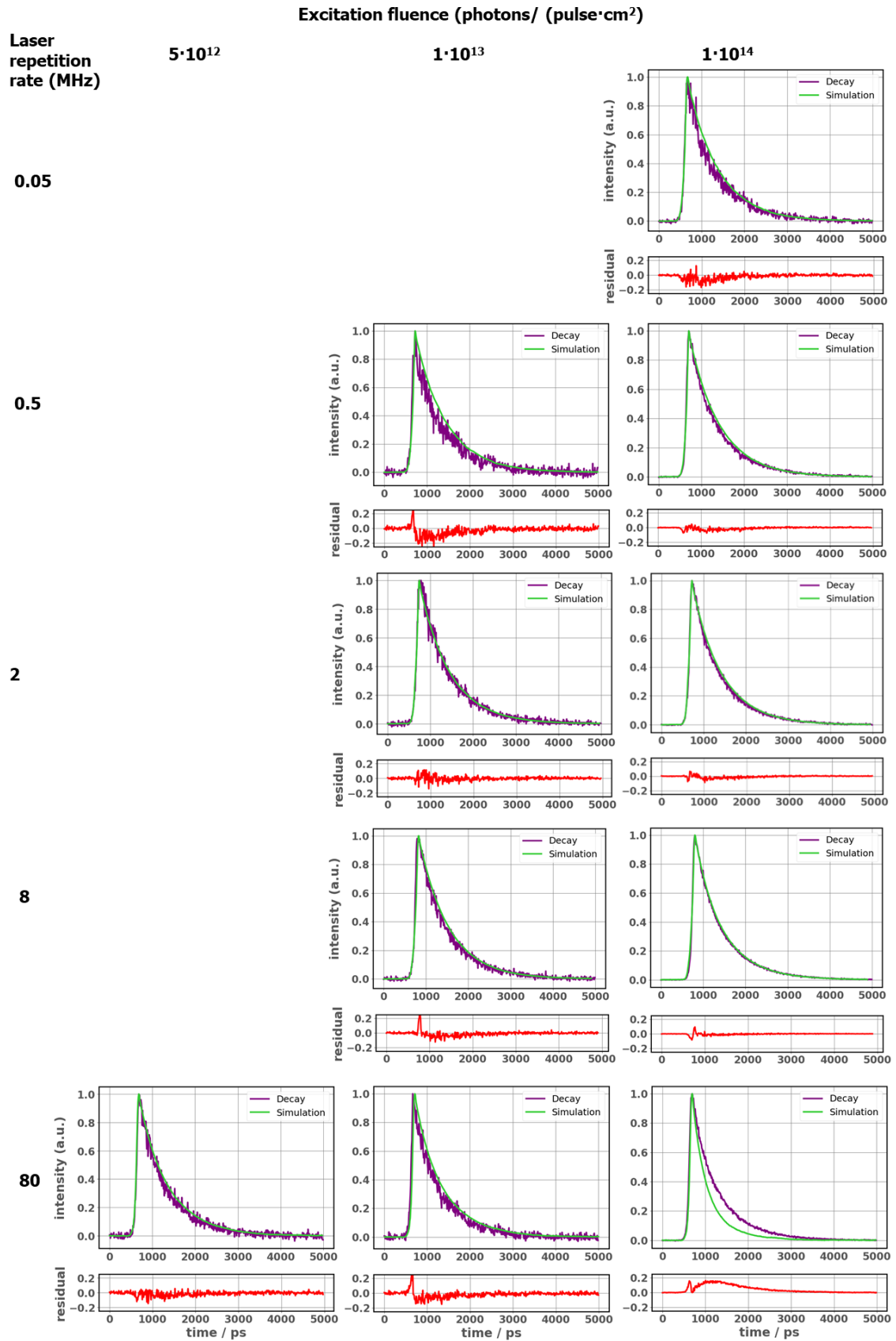
Figure G.7.: Comparison of experimental and simulated fluorescence transients: Refinement 2 For details see text.

231

In a first qualitative analysis, all the phasors calculated from the simulated transients are visualized within one phasor plot, see Fig. G.8. As all phasor are clearly located within the universal semicircle a multiexponential kinetics is indicated.
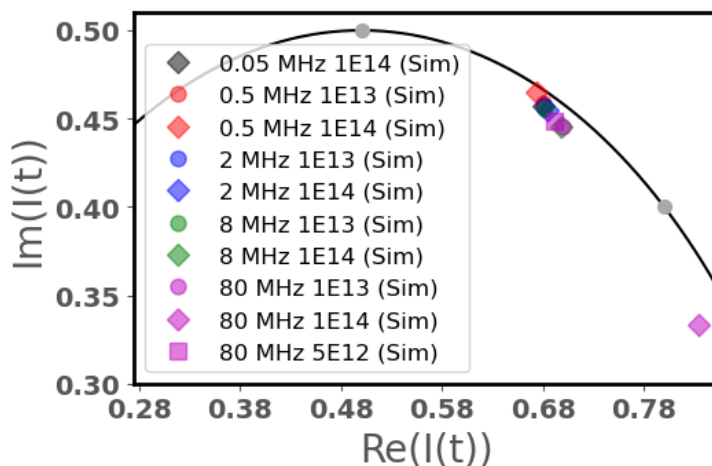

Figure G.8.: Phasor plot illustrating the phasors calculated from the simulated transients: The phasors that were calculated from the simulated fluorescence transients in Fig. G.7 are shown in a zoomed view of the phasor plot. Different laser repetition rate are coded by color, different excitation fluence are indicated by different symbols. For details see text.

Next, a quantitative phasor analysis is given. Performing a linear fit to the phasors corresponding to simulations at low laser repetition rates yields lifetime components of 703 (+ 4/- 3) ps and 99 (+ 71/- 61) ps [7] as can be seen in Fig. G.6a. The turquoise line corresponds to the linear fit and its intersections with the universal semicircle give the phasors of the lifetime components.The two lines of pale grey and pale red color visualize the tolerance interval of the linear fit and correspond to the lines of minimum and maximum slope of the fit parameters, respectively. The subfigures G.6b, G.6c and G.6d allow for a detailed analysis of the kinetics of the distinct phasors at higher laser repetition rates.

---

[7]The asymmetric values of the uncertainty of the lifetime components is due to the nonlinear scaling of the ruler of lifetimes along the universal semicircle, see also appendix C.
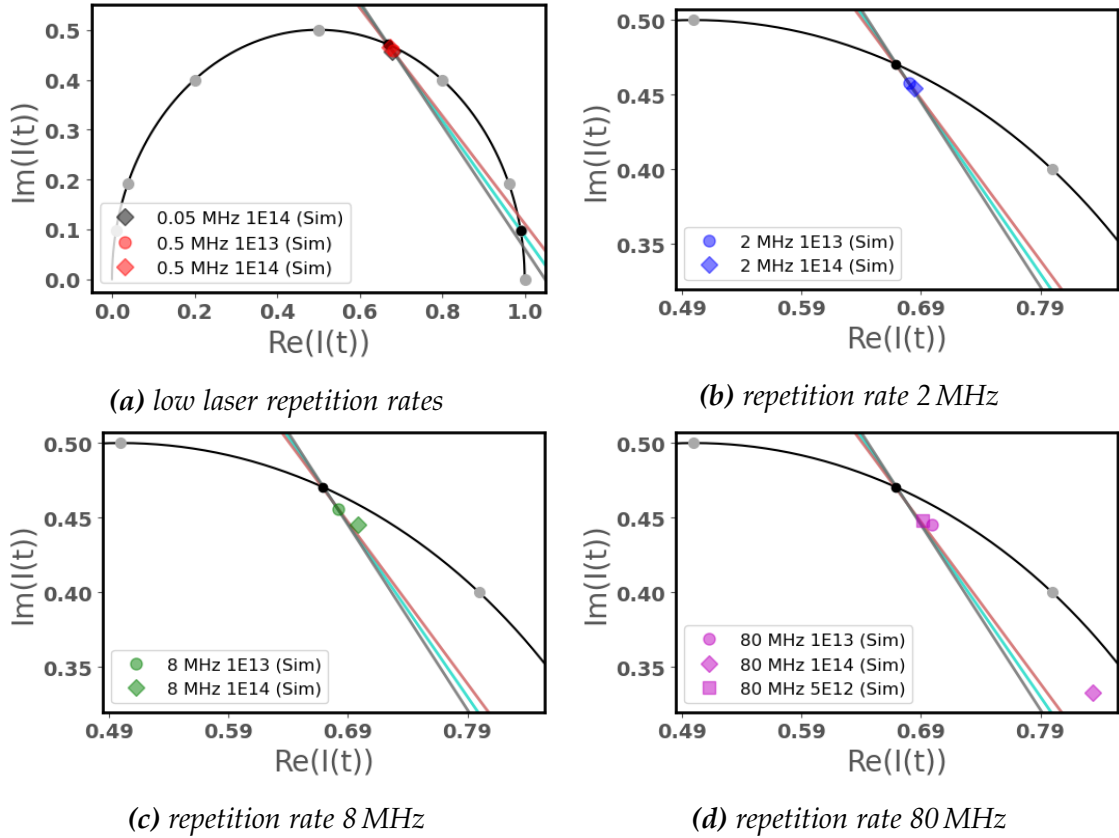
(a) low laser repetition rates

(b) repetition rate 2 MHz

(c) repetition rate 8 MHz

(d) repetition rate 80 MHz

***Figure G.9.: Phasor plots for analysis of the phasor calculated from the simulated fluorescence transients (Refinement 2: larger k_{STA}:** The phasors calculated from simulate fluorescence transients shown in Fig. G.4 are visualized in separate phasor plots for the laser repetition rates of 0.05 MHz and 0.5 MHz **(a)**, 2 MHz **(b)**, 8 MHz **(c)** and 80 MHz **(d)**, respectively. For the laser repetition rates 0.05 MHz and 0.5 MHz in **(a)** a non zoomed view of the phasor plot is shown including a ruler of lifetimes along the universal semicircle (grey circles) counterclockwise denoting the values 0 ns, 0.1 ns, 0.2 ns, 0.5 ns, 1 ns, 2 ns, 5 ns and 10 ns, respectively. The other subfigures **(b,c,d)** show zoomed views of the phasor plot. Different laser repetition rates are coded by color, different excitation fluence are coded by different phasor symbols. For details see text.*

For 2 MHz all phasors overlap with the tolerance interval of the biexponential kinetics[8], whereas for laser repetition rates of 8 MHz and 80 MHz a third lifetime component is necessary, namely for the excitation parameter combinations of 8 MHz and an excitation fluence of $1 \cdot 10^{14}$ photons/(pulse· cm^2), 8 MHz and an excitation fluence of $1 \cdot 10^{14}$ photons/(pulse·cm^2), 80 MHz and an excitation fluence of $1 \cdot 10^{13}$ photons/(pulse·cm^2) as well as for a laser repetition rate of 80 MHz and an excitation fluence of $1 \cdot 10^{14}$ photons/(pulse· cm^2).

---

[8]As outlined before in Section G.2 the outer limits of the phasor symbols are used for estimation of the uncertainty of the phasor positions.

The quantitative results of a phasor analysis for all simulated fluorescence transients are summarized in Table G.2 as a function of the excitation parameters. Different columns correspond to different excitation fluences, increasing from left to right, and different rows correspond to different laser repetition rates, increasing from top to bottom. The fractional contributions of the distinct lifetime components are given in brackets.

laser repetition rate (MHz)	excitation fluence $\frac{photons}{pulses \cdot cm^2}$		
	$5 \cdot 10^{12}$	$1 \cdot 10^{13}$	$1 \cdot 10^{14}$
0.05			703 ps (0.97) 99 ps (0.03)
0.5		703 ps (0.97) 99 ps (0.03)	703 ps (0.99) 99 ps (0.01)
2		703 ps (0.97) 99 ps (0.03)	703 ps (0.96) 99 ps (0.04)
8		703 ps (0.96) 99 ps (0.04)	703 ps (0.88) 99 ps (0.04) 394 ps (0.09)
80	703 ps (0.94) 99 ps (0.06)	703 ps (0.86) 99 ps (0.04) 420 ps (0.1)	703 ps (0.37) 99 ps (0.02) 455 ps (0.61)

Table G.2.: Lifetime components and their fractional contributions for the multiexponential kinetics of simulated fluorescence transients considering a singlet-triplet annihilation rate of $2 \cdot 10^9 \, s^{-1}$

G.4. Triplet excitations in the basis simulation (k_{STA} from experiments)

In order to investigate the disagreement of the kinetics of the basis simulations with respect to the experiment for the highest laser repetition rate and high excitation fluence, as outlined above, it is helpful to have a look at the contribution of triplet states within the DMC simulations. Fig. G.10 shows the fractional triplet occurrence obtained from the DMC simulation data as a function of the laser

repetition rate and the excitation fluence for the excitation parameter combinations of the experiments. The dashed lines in Fig. G.10 serve as a guide to the eye and connect the data points of equal excitation fluence. The fractional triplet population counts all electronic states corresponding to LH2 complexes carrying at least one triplet excitation.
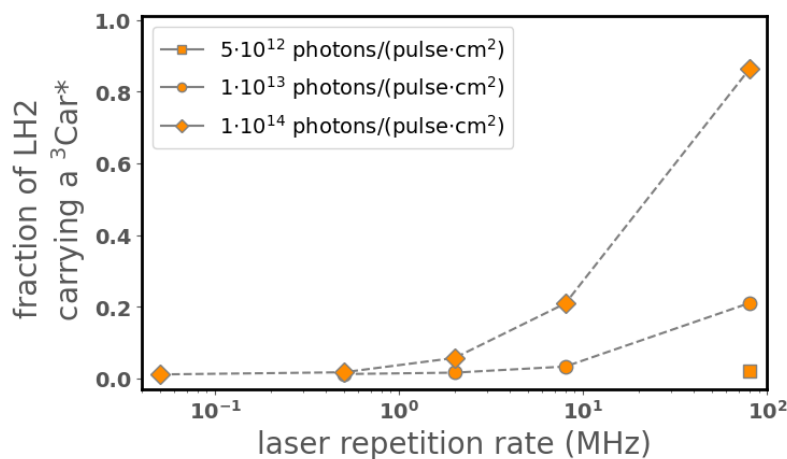

Figure G.10.: Fractional triplet population within the B830 LH2 complex of Mch. purpuratum resulting from the DMC simulations: The fraction of LH2 complexes carrying at least one triplet excitation ^{3}Car* appearing in the DMC simulations as a function of the laser repetition rate. The dashed lines serve as a guide to the eye and connect the data points of equal excitation fluence. For details see text.

For low laser repetition rates, such as 0.05 MHz and 0.5 MHz, the fractional triplet population is almost zero. Regarding the excitation photon fluence of $1 \cdot 10^{13}$ photons/(pulse·cm^2), see circle symbols in Fig. G.10, the triplet population remains that low except for the highest laser repetition rate of 80 MHz, where it rises up to 0.2. In contrast, for the highest excitation fluence of $1 \cdot 10^{14}$ photons/(pulse·cm^2) a significant influence of the laser repetition rate on the fractional triplet population is observed. Thus, as can be seen in the diamond symbols in Fig. G.10, the fractional triplet population rises tremendously up to 86 % for a laser repetition rate of 80 MHz. This massive accumulation of triplet states most likely results from the small temporal separation of only 12.5 ns between the excitation laser pulses. Actually, the observance of high triplet populations resulting from the DMC simulations at excitation parameter combinations of higher laser repetition rate, such as 8 MHz and 80 MHz, and excitation fluences equal to and above $1 \cdot 10^{13}$ photons/(pulse·cm^2), supports the identification of the third lifetime component within the discussion of the multiexpo-

nential kinetics, as outlined in Section 6.3. In fact, this third lifetime component, which was attributed to the occurrence of STA processes in Section 6.3, is only observed for excitation parameter combinations that show high triplet populations in Fig. G.10. However, the observed tremendous fractional population of triplet states of 86 % for the highest laser repetition rate of 80 MHz and the highest excitation fluence within the DMC simulation has to be considered when discussing the observed discrepancy between the kinetics corresponding to the simulations and those corresponding to the experiments.

In Section 7.1, where the expanded rate model used for the DMC simulations was developed, it was argued that the expansion of the rate model to higher triplet states, namely to allow that an LH2 complex might carry a multiple number of triplet excitations, is necessary in order to avoid a saturation of the excitation in the electronic state of the LH2 complex, carrying the highest number of triplet excitations within the simulation. Thus, it has to be checked whether this might be the case for the expanded rate model that is used for the simulations and thus might be a possible explanation for the observed high fractional triplet population in Fig. G.10.

In addition, the data of the DMC simulations allows for evaluation of the relative occurrence of electronic states corresponding to LH2 complexes that carry triplet excitations. A summary of this evaluation is given in Table G.3. Depending on the number of triplet excitations that is carried by an LH2 complex, the entries of the table are denote as 1T if there is only one triplet excitation, 2T for two triplet excitations and so on. In round brackets the fractional occurrences are shown. As can be seen in Table G.3, for low laser repetition rates, if any triplet excitation occurs, only electronic states corresponding to LH2 complexes that carry one triplet excitation appear. With increasing laser repetition rate also higher numbers of triplet excitations carried by an LH2 complex appear within the DMC simulations but mostly with an occurrence of or below 10%. Remarkably, for the excitation parameter combination of 80 MHz laser repetition rate and an excitation fluence of $1 \cdot 10^{14}$ photons/(pulse·cm^2) even LH2 complexes carrying up to five triplet excitations appear within the DMC simulation. However, the maximum possible number of seven triplet excitations on one LH2 complex is not observed. Thus, any saturation effects of the rate model developed above and used for the DMC simulations can be excluded to play a role in the observed

discrepancies between the measured and simulated fluorescence transients.

laser repetition rate (MHz)	excitation fluence $\frac{photons}{pulses \cdot cm^2}$		
	$5 \cdot 10^{12}$	$1 \cdot 10^{13}$	$1 \cdot 10^{14}$
0.05			1T
0.5		1T	1T
2		1T	1T (0.99) 2T (0.01)
8		1T (0.99) 2T (0.01)	1T (0.92) 2T (0.08)
80	1T (0.95) 2T (0.05)	1T (0.91) 2T (0.09)	1T (0.37) 2T (0.32) 3T (0.19) 4T (0.08) 5T (0.02)

Table G.3.: Relative triplet population of electronic states corresponding to LH2 complexes carrying different numbers of triplet excitations resulting from the DMC simulations: The entries of the table are denote 1T if there is only one triplet excitation, 2T for two triplet excitations and so on. In round brackets the fractional occurrence is given.

In summary, the analysis of the triplet populations given above clearly indicates that the expanded rate model used for the simulations is applicable as no saturation effect of triplet excitations occurs. Nevertheless, the expanded rate model used for the DMC simulations leads to high fractional triplet populations and moreover to observance of the population of electronic states corresponding to LH2 complexes that carry multiple triplet states, see Table G.3.

9. Bibliography

[1] René Monshouwer, Malin Abrahamsson, Frank van Mourik, and Rienk van Grondelle, *Superradiance and Exciton Delocalization in Bacterial Photosynthetic Light-Harvesting Systems*, The Journal of Physical Chemistry B **101** (1997), no. 37, 7241–7248.

[2] Tobias J Pflock, Manuela Dezi, Giovanni Venturoli, Richard J Cogdell, Jürgen Köhler, and Silke Oellerich, *Comparison of the fluorescence kinetics of detergent-solubilized and membrane-reconstituted LH2 complexes from Rps. acidophila and Rb. sphaeroides*, Photosynthesis Research **95** (2008), no. 2-3, 291–298.

[3] Tobias J. Pflock, Silke Oellerich, June Southall, Richard J. Cogdell, G. Matthias Ullmann, and Jürgen Köhler, *The Electronically Excited States of LH2 Complexes from Rhodopseudomonas acidophila Strain 10050 Studied by Time-Resolved Spectroscopy and Dynamic Monte Carlo Simulations. I. Isolated, Non-Interacting LH2 Complexes*, The Journal of Physical Chemistry B **115** (2011), no. 28, 8813–8820.

[4] Martin A. Bopp, Yiwei Jia, Liangquan Li, Richard J. Cogdell, and Robin M. Hochstrasser, *Fluorescence and photobleaching dynamics of single light-harvesting complexes*, Proceedings of the National Academy of Sciences **94** (1997), no. 20, 10630–10635.

[5] Md Wahadoszamen, Iris Margalit, Anjue Mane Ara, Rienk Van Grondelle, and Dror Noy, *The role of charge-transfer states in energy transfer and dissipation within natural and artificial bacteriochlorophyll proteins*, Nature Communications **5** (2014), 1–8.

[6] Michele Nottoli, Sandro Jurinovich, Lorenzo Cupellini, Alastair T Gardiner, Richard J Cogdell, and Benedetta Mennucci, *The role of charge-transfer states in the spectral tuning of antenna complexes of purple bacteria*, Photosynthesis Research **137** (2018), no. 2, 215–226.

[7] Lorenzo Cupellini, Sandro Jurinovich, Marco Campetella, Stefano Caprasecca, Ciro A. Guido, Sharon M. Kelly, Alastair T. Gardiner, Richard Cogdell, and Benedetta Mennucci, *An ab initio description of the excitonic properties of LH2 and their temperature dependence*, Journal of Physical Chemistry B **120** (2016), no. 44, 11348–11359.

[8] Marco Ferretti, Ruud Hendrikx, Elisabet Romero, June Southall, Richard J. Cogdell, Vladimir I. Novoderezhkin, Gregory D. Scholes, and Rienk van Grondelle, *Dark States in the Light-Harvesting complex 2 Revealed by Two-dimensional Electronic Spectroscopy*, Scientific Reports **6** (2016), no. 1, 20834.

[9] United Nations, *Energy Statistics Pocketbook 2020*, 2020.

[10] Celestino Creatore, Alex W Chin, Michael A Parker, and Stephen Emmott, *Emergent models for artificial light-harvesting*, Frontiers in Materials **2** (2015), no. 6.

[11] Yanbin Wang, Hideo Ohkita, Hiroaki Benten, and Shinzaburo Ito, *Efficient exciton harvesting through long-range energy transfer*, ChemPhysChem **16** (2015), no. 6, 1263–1267.

[12] Arash Takshi, Houman Yaghoubi, Tete Tevi, and Sara Bakhshi, *Photoactive supercapacitors for solar energy harvesting and storage*, Journal of Power Sources **275** (2015), 621–626.

[13] Gregory D. Scholes, Tihana Mirkovic, Daniel B. Turner, Francesca Fassioli, and Andreas Buchleitner, *Solar light harvesting by energy transfer: From ecology to coherence*, Energy and Environmental Science **5** (2012), no. 11, 9374–9393.

[14] Gregory D Scholes, Graham R Fleming, Alexandra Olaya-Castro, and Rienk Van Grondelle, *Lessons from nature about solar light harvesting*, Nature Chemistry **3** (2011), no. 10, 763–774.

[15] Tihana Mirkovic, Evgeny E. Ostroumov, Jessica M. Anna, Rienk Van Grondelle, Govindjee, and Gregory D. Scholes, *Light absorption and energy transfer in the antenna complexes of photosynthetic organisms*, Chemical Reviews **117** (2017), no. 2, 249–293.

[16] G S Schlau-Cohen, *Principles of light harvesting from single photosynthetic complexes*, Interface Focus **5** (2015), no. 3, 1–6.

240

[17] Christopher J Law, Aleksander W Roszak, June Southall, Alastair T Gardiner, Neil W Isaacs, and Richard J Cogdell, *The structure and function of bacterial light-harvesting complexes*, Molecular Membrane Biology **21** (2004), no. 3, 183–191.

[18] Lars Olof Björn, *The Measurement of Light*, Photobiology, Springer New York, New York, NY, 2015, pp. 37–49.

[19] Svetlana Bahatyrova, Raoul N Frese, C Alistair Siebert, John D Olsen, Kees O van der Werf, Rienk van Grondelle, Robert A Niederman, Per A Bullough, Cees Otto, and C Neil Hunter, *The native architecture of a photosynthetic membrane*, Nature **430** (2004), no. 7003, 1058–1062.

[20] Simon Scheuring and James N Sturgis, *Atomic force microscopy of the bacterial photosynthetic apparatus: plain pictures of an elaborate machinery*, Photosynthesis Research **102** (2009), no. 2-3, 197–211.

[21] Thomas Walz, Stuart J Jamieson, Claire M Bowers, Per A Bullough, and C Neil Hunter, *Projection structures of three photosynthetic complexes from Rhodobacter sphaeroides: LH2 at 6 Å, LH1 and RC-LH1 at 25 Å*, J. Mol. Bio. **282** (1998), 833–845.

[22] G. McDermott, S. M. Prince, A. A. Freer, A. M. Hawthornthwaite-Lawless, M. Z. Papiz, R. J. Cogdell, and N. W. Isaacs, *Crystal structure of an integral membrane light-harvesting complex from photosynthetic bacteria*, 1995, pp. 517–521.

[23] Juergen Koepke, Xiche Hu, Cornelia Muenke, Klaus Schulten, and Hartmut Michel, *The crystal structure of the light-harvesting complex II (B800–850) from Rhodospirillum molischianum*, Structure **4** (1996), no. 5, 581–597.

[24] Miroslav Z Papiz, Steve M Prince, Tina Howard, Richard J Cogdell, and Neil W Isaacs, *The Structure and Thermal Motion of the B800–850 LH2 Complex from Rps.acidophila at 2.0ÅResolution and 100K: New Structural Features and Functionally Relevant Motions*, Journal of Molecular Biology **326** (2003), no. 5, 1523–1538.

[25] Andrew Gall and Bruno Robert, *Characterization of the Different Peripheral Light-Harvesting Complexes from High- and Low-Light Grown Cells from Rhodopseudomonas palustris †*, Biochemistry **38** (1999), no. 16, 5185–5190.

[26] Tatas H.P. Brotosudarmo, Ralf Kunz, Paul Böhm, Alastair T. Gardiner, Vladimíra Moulisová, Richard J. Cogdell, and Jürgen Köhler, *Single-Molecule Spectroscopy Reveals that Individual Low-Light LH2 Complexes from Rhodopseudomonas palustris 2.1.6. Have a Heterogeneous Polypeptide Composition*, Biophysical Journal **97** (2009), no. 5, 1491–1500.

[27] Suman Ranjit, Leonel Malacrida, David M. Jameson, and Enrico Gratton, *Fit-free analysis of fluorescence lifetime imaging data using the phasor approach*, Nature Protocols **13** (2018), no. 9, 1979–2004.

[28] Gregorio Weber, *Resolution of the fluorescence lifetimes in a heterogeneous system by phase and modulation measurements*, Journal of Physical Chemistry **85** (1981), no. 8, 949–953.

[29] Joan L Slonczewski and John W Forster, *Microbiology: An Evolving Science*, 3 ed., W. W. Norton & Company, 2013.

[30] T Pullerits, K J Visscher, S Hess, V Sundström, A Freiberg, K Timpmann, and R van Grondelle, *Energy transfer in the inhomogeneously broadened core antenna of purple bacteria: a simultaneous fit of low-intensity picosecond absorption and fluorescence kinetics*, Biophysical Journal **66** (1994), no. 1, 236–248.

[31] S. Hess, M. Chachisvilis, K. Timpmann, M. R. Jones, G. J.S. Fowler, C. N. Hunter, and V. Sundström, *Temporally and spectrally resolved subpicosecond energy transfer within the peripheral antenna complex (LH2) and from LH2 to the core antenna complex in photosynthetic purple bacteria*, Proceedings of the National Academy of Sciences of the United States of America **92** (1995), no. 26, 12333–12337.

[32] V Nagarajan and W W Parson, *Excitation Energy Transfer between the B850 and B875 Antenna Complexes of Rhodobacter sphaeroides*, Biochemistry **36** (1997), no. 8, 2300–2306.

[33] K J Visscher, H Bergström, V Sundström, C N Hunter, and R Van Grondelle, *Temperature dependence of energy transfer from the long wavelength antenna BChl-896 to the reaction center in Rhodospirillum rubrum, Rhodobacter sphaeroides (w.t. and M21 mutant) from 77 to 177K, studied by picosecond absorption spectroscopy*, Photosynthesis Research **22** (1989), no. 3, 211–217.

[34] H Bergström, R van Grondelle, and V Sundström, *Characterization of excitation energy trapping in photosynthetic purple bacteria at 77 K*, FEBS Letters **250** (1989), no. 2, 503–508.

[35] Arvi Freiberg, James P. Allen, Jo Ann C. Williams, and Neal W. Woodbury, *Energy trapping and detrapping by wild type and mutant reaction centers of purple non-sulfur bacteria*, Photosynthesis Research **48** (1996), no. 1-2, 309–319.

[36] Richard J. Cogdell, Andrew Gall, and Jürgen Köhler, *The architecture and function of the light-harvesting apparatus of purple bacteria: From single molecules to in vivo membranes*, Quarterly Reviews of Biophysics **39** (2006), no. 3, 227–324.

[37] H P Lang and C N Hunter, *The relationship between carotenoid biosynthesis and the assembly of the light-harvesting LH2 complex in Rhodobacter sphaeroides*, Biochemical Journal **298** (1994), no. 1, 197–205.

[38] Andrew Gall, Sarah Henry, Shinichi Takaichi, Bruno Robert, and Richard J Cogdell, *Preferential Incorporation of Coloured-carotenoids Occurs in the LH2 Complexes From Non-sulphur Purple Bacteria Under Carotenoid-limiting Conditions*, Photosynthesis Research **86** (2005), no. 1-2, 25–35.

[39] Richard J. Cogdell, Neil W. Isaacs, Tina D. Howard, Karen McLuskey, Niall J. Fraser, and Stephen M. Prince, *How Photosynthetic Bacteria Harvest Solar Energy*, Journal of Bacteriology **181** (1999), no. 13, 3869–3879.

[40] B Robert, Richard Cogdell, and R Van Grondelle, *The Light-Harvesting System of Purple Bacteria*, Light-Harvesting Antennas in Photosynthesis (Beverley R Green and William W Parson, eds.), Advances in Photosynthesis and Respiration, vol. 13, Springer Netherlands, Dordrecht, 2003, pp. 169–194.

[41] Clemens Hofmann, Martijn Ketelaars, Michio Matsushita, Hartmut Michel, Thijs J Aartsma, and Jürgen Köhler, *Single-Molecule Study of the Electronic Couplings in a Circular Array of Molecules: Light-Harvesting-2 Complex from Rhodospirillum Molischianum*, Physical Review Letters **90** (2003), no. 1, 13004.

[42] Y C Cheng and R J Silbey, *Coherence in the B800 Ring of Purple Bacteria LH2*, Physical Review Letters **96** (2006), no. 2, 28103.

[43] Kenneth Sauer, Richard J Cogdell, Steve M Prince, Andy Freer, Neil W Isaacs, and Hugo Scheer, *Structure-Based Calculations of the Optical Spectra of the LH2 Bacteriochlorophyll-Protein Complex from Rhodopseudomonas acidophila*, Photochemistry and Photobiology **64** (1996), no. 3, 564–576.

[44] Villy Sundström, Tõnu Pullerits, and Rienk Van Grondelle, *Photosynthetic light-harvesting: Reconciling dynamics and structure of purple bacterial LH2 reveals function of photosynthetic unit*, Journal of Physical Chemistry B **103** (1999), no. 13, 2327–2346.

[45] Ralph Jimenez, Srivatsan N Dikshit, Stephen E Bradforth, and Graham R Fleming, *Electronic excitation transfer in the LH2 complex of Rhodobacter sphaeroides*, Journal of Physical Chemistry **100** (1996), no. 16, 6825–6834.

[46] C. De Caro, R. W. Visschers, R. Van Grondelle, and S. Völker, *Inter- and intraband energy transfer in LH2-antenna complexes of purple bacteria. A fluorescence line-narrowing and hole-burning study*, Journal of Physical Chemistry **98** (1994), no. 41, 10584–10590.

[47] A P Shreve, J K Trautman, Harry A Frank, T G Owens, and A C Albrecht, *Femtosecond energy-transfer processes in the B800–850 light-harvesting complex of Rhodobacter sphaeroides 2.4.1*, Biochimica et Biophysica Acta (BBA) - Bioenergetics **1058** (1991), no. 2, 280–288.

[48] Mirianas Chachisvilis, Oliver Kühn, Tõnu Pullerits, and Villy Sundström, *Excitons in Photosynthetic Purple Bacteria: Wavelike Motion or Incoherent Hopping?*, The Journal of Physical Chemistry B **101** (1997), no. 37, 7275–7283.

[49] M. Dahlbom, T. Pullerits, S. Mukamel, and V. Sundström, *Exciton delocalization in the B850 light-harvesting complex: Comparison of different measures*, Journal of Physical Chemistry B **105** (2001), no. 23, 5515–5524.

[50] Ana Damjanović, Ioan Kosztin, Ulrich Kleinekathöfer, and Klaus Schulten, *Excitons in a photosynthetic light-harvesting system: A combined molecular dynamics, quantum chemistry, and polaron model study*, Physical Review E **65** (2002), no. 3, 31919.

[51] D Leupold, H Stiel, K Teuchner, F Nowak, W Sandner, B Ücker, and H Scheer, *Size enhancement of transition dipoles to one- and two-exciton bands*

in a photosynthetic antenna, Physical Review Letters **77** (1996), no. 22, 4675–4678.

[52] L. D. Book, A. E. Ostafin, N. Ponomarenko, J. R. Norris, S. Mukamel, and N. F. Scherer, *Time-Dependent Exciton Delocalization Size in the B850 Band of Purple Bacterial LH2*, Springer Series in Chemical Physics, vol. 66, 2001, pp. 659–661.

[53] Teresa G Monger, Richard J Cogdell, and William W Parson, *Triplet states of bacteriochlorophyll and carotenoids in chromatophores of photosynthetic bacteria*, Biochimica et Biophysica Acta (BBA) - Bioenergetics **449** (1976), no. 1, 136–153.

[54] Roya Farhoosh, Veeradej Chynwat, Ronald Gebhard, Johan Lugtenburg, and Harry A. Frank, *Triplet energy transfer between bacteriochlorophyll and carotenoids in B850 light-harvesting complexes of Rhodobacter sphaeroides R-26.1*, Photosynthesis Research **42** (1994), no. 2, 157–166.

[55] Daisuke Kosumi, Tomoko Horibe, Mitsuru Sugisaki, Richard J. Cogdell, and Hideki Hashimoto, *Photoprotection Mechanism of Light-Harvesting Antenna Complex from Purple Bacteria*, The Journal of Physical Chemistry B **120** (2016), no. 5, 951–956.

[56] Dariusz M Niedzwiedzki, Preston L Dilbeck, Qun Tang, Elizabeth C Martin, David F Bocian, C Neil Hunter, and Dewey Holten, *New insights into the photochemistry of carotenoid spheroidenone in light-harvesting complex 2 from the purple bacterium Rhodobacter sphaeroides*, Photosynthesis Research **131** (2017), no. 3, 291–304.

[57] Robert Bittl, Eberhard Schlodder, Irene Geisenheimer, Wolfgang Lubitz, and Richard J Cogdell, *Transient EPR and Absorption Studies of Carotenoid Triplet Formation in Purple Bacterial Antenna Complexes*, The Journal of Physical Chemistry B **105** (2001), no. 23, 5525–5535.

[58] Richard J. Cogdell and Harry A. Frank, *How carotenoids function in photosynthetic bacteria*, BBA Reviews On Bioenergetics **895** (1987), no. 2, 63–79.

[59] Harry A Frank and Richard J Cogdell, *Carotenoids in Photosynthesis*, Photochemistry and Photobiology **63** (1996), no. 3, 257–264.

[60] Niall J. Fraser, Hideki Hashimoto, and Richard J. Cogdell, *Carotenoids and bacterial photosynthesis: The story so far...*, Photosynthesis Research **70** (2001), no. 3, 249–256.

[61] G Trinkunas, Jennifer L Herek, Tomáš Polívka, Villy Sundström, and T Pullerits, *Exciton delocalization probed by excitation annihilation in the light-harvesting atenna LH2*, Physical Review Letters **86** (2001), no. 18, 4167–4170.

[62] Leonas Valkunas, Vladas Liuolia, and Arvi Freiberg, *Picosecond processes in chromatophores at various excitation intensities*, Photosynthesis Research **27** (1991), no. 2, 83–95.

[63] A Angerhofer, F Bornhäuser, A Gall, and R.J. Cogdell, *Optical and optically detected magnetic resonance investigation on purple photosynthetic bacterial antenna complexes*, Chemical Physics **194** (1995), no. 2-3, 259–274.

[64] Andrew Gall, Rudi Berera, Maxime T.A. Alexandre, Andrew A. Pascal, Luc Bordes, Maria M. Mendes-Pinto, Sandra Andrianambinintsoa, Katerina V. Stoitchkova, Alessandro Marin, Leonas Valkunas, Peter Horton, John T.M. Kennis, Rienk van Grondelle, Alexander Ruban, and Bruno Robert, *Molecular Adaptation of Photoprotection: Triplet States in Light-Harvesting Proteins*, Biophysical Journal **101** (2011), no. 4, 934–942.

[65] Alexandre Maxime and Rienk Van, *Time-Resolved FTIR Difference Spectroscopy Reveals the Structure and Dynamics of Carotenoid and Chlorophyll Triplets in Photosynthetic Light-Harvesting Complexes*, Infrared Spectroscopy - Life and Biomedical Sciences (2012).

[66] Volkhard May, *Kinetic theory of exciton-exciton annihilation*, Journal of Chemical Physics **140** (2014), no. 5, 0–10.

[67] Th. Förster, *Zwischenmolekulare Energiewanderung und Fluoreszenz*, Annalen der Physik **437** (1948), no. 1-2, 55–75.

[68] D L Dexter, *A Theory of Sensitized Luminescence in Solids*, The Journal of Chemical Physics **21** (1953), no. 5, 836–850.

[69] Tobias J Pflock, Silke Oellerich, Lisa Krapf, June Southall, Richard J Cogdell, G Matthias Ullmann, and Jürgen Köhler, *The electronically excited states of LH2 complexes from Rhodopseudomonas acidophila Strain 10050 studied*

by time-resolved spectroscopy and dynamic Monte Carlo simulations. II. Homo-arrays of LH2 complexes reconstituted into phospholipid model membranes, Journal of Physical Chemistry B **115** (2011), no. 28, 8821–8831.

[70] J. Michael Gruber, Jevgenij Chmeliov, Tjaart P.J. Krüger, Leonas Valkunas, and Rienk Van Grondelle, *Singlet-triplet annihilation in single LHCII complexes*, Physical Chemistry Chemical Physics **17** (2015), no. 30, 19844–19853.

[71] Andy Freer, Steve Prince, Ken Sauer, Miroslav Papiz, Anna Hawthornthwaite-Lawless, Gerry McDermott, Richard J Cogdell, and Neil W Isaacs, *Pigment-pigment interactions and energy transfer in the antenna complex of the photosynthetic bacterium Rhodopseudomonas acidophila*, Structure **4** (1996), no. 4, 449–462.

[72] Richard J Cogdell, Tina D Howard, Robert Bittl, Erberhard Schlodder, Irene Geisenheimer, and Wolfgang Lubitz, *How carotenoids protect bacterial photosynthesis*, Philosophical Transactions of the Royal Society of London. Series B: Biological Sciences **355** (2000), no. 1402, 1345–1349.

[73] Tomáč Polívka and Villy Sundström, *Ultrafast dynamics of carotenoid excited states-from solution to natural and artificial systems*, Chemical Reviews **104** (2004), no. 4, 2021–2071.

[74] Hong Cong, Dariusz M Niedzwiedzki, George N Gibson, Amy M LaFountain, Rhiannon M Kelsh, Alastair T Gardiner, Richard J Cogdell, and Harry A Frank, *Ultrafast time-resolved carotenoid to-bacteriochlorophyll energy transfer in LH2 complexes from photosynthetic bacteria*, Journal of Physical Chemistry B **112** (2008), no. 34, 10689–10703.

[75] Emmanouil Papagiannakis, John T M Kennis, Ivo H M Van Stokkum, Richard J Cogdell, and Rienk Van Grondelle, *An alternative carotenoid-to-bacteriochlorophyll energy transfer pathway in photosynthetic light harvesting*, Proceedings of the National Academy of Sciences of the United States of America **99** (2002), no. 9, 6017–6022.

[76] Richard J. Cogdell, Michael F. Hipkins, Wallace MacDonald, and T.George Truscott, *Energy transfer between the carotenoid and the bacteriochlorophyll*

within the B-800–850 light-harvesting pigment-protein complex of Rhodopseu-domonas sphaeroides, Biochimica et Biophysica Acta (BBA) - Bioenergetics **634** (1981), no. C, 191–202.

[77] Brent P Krueger, Gregory D Scholes, Ralph Jimenez, and Graham R Fleming, *Electronic excitation transfer from carotenoid to bacteriochlorophyll in the purple bacterium Rhodopseudomonas acidophila*, Journal of Physical Chemistry B **102** (1998), no. 12, 2284–2292.

[78] K McLuskey, S M Prince, Richard J Cogdell, and N W Isaacs, *The crystallographic structure of the B800-820 LH3 light-harvesting complex from the purple bacteria Rhodopseudomonas acidophila strain 7050*, Biochemistry **40** (2001), no. 30, 8783–8789.

[79] Richard J Cogdell, T D Howard, N W Isaacs, K McLuskey, and A T Gardiner, *Structural factors which control the position of the Qy absorption band of bacteriochlorophyll a in purple bacterial antenna complexes*, Photosynthesis Research **74** (2002), no. 2, 135–141.

[80] A T Gardiner, D M Niedzwiedzki, and Richard J Cogdell, *Adaptation of Rhodopseudomonas acidophila strain 7050 to growth at different light intensities: What are the benefits to changing the type of LH2?*, Faraday Discussions **207** (2018), 471–489.

[81] M H Tadros and K Waterkamp, *Multiple copies of the coding regions for the light-harvesting B800-850 alpha- and beta-polypeptides are present in the Rhodopseudomonas palustris genome.*, The EMBO Journal **8** (1989), no. 5, 1303–1308.

[82] Monier H TADROS, Eleni KATSIOU, Mark A HOON, Natalie YURKOVA, and Dipak P RAMJI, *Cloning of a new antenna gene cluster and expression analysis of the antenna gene family of Rhodopseudomonas palustris*, European Journal of Biochemistry **217** (1993), no. 3, 867–875.

[83] Alexander Löhner, Richard J Cogdell, and Jürgen Köhler, *Contribution of low-temperature singlemolecule techniques to structural issues of pigment-protein complexes from photosynthetic purple bacteria*, Journal of the Royal Society Interface **15** (2018), no. 138.

[84] Richard J Cogdell, Anna M Hawthornthwaite, Mark B Evans, Linda A Ferguson, Cheryl Kerfeld, J Philip Thornber, Frank van Mourik, and Rienk van Grondelle, *Isolation and characterisation of an unusual antenna complex from the marine purple sulphur photosynthetic bacterium Chromatium purpuratum BN5500*, BBA - Bioenergetics **1019** (1990), no. 3, 239–244.

[85] Cheryl A Kerfeld, Todd O Yeates, and J Philip Thornber, *Purification and Characterization of the Peripheral Antenna of the Purple-Sulfur Bacterium Chromatium purpuratum: Evidence of an Unusual Pigment-Protein Composition*, Biochemistry **33** (1994), no. 8, 2178–2184.

[86] Laura J Cranston, *Structural and Functional Studies of LH2 Complexes Having Unusual Spectroscopic Properties*, Ph.D. thesis, University of Glasgow, 2016.

[87] C. A. Kerfeld, J. P. Thornber, and T. O. Yeates, *Crystallization of two integral membrane pigment–protein complexes from the purple-sulfur bacterium Chromatium purpuratum*, Protein Science **2** (1993), no. 8, 1352–1355.

[88] Tatas H. P. Brotosudarmo, Aaron M. Collins, Andrew Gall, Aleksander W. Roszak, Alastair T. Gardiner, Robert E. Blankenship, and Richard J. Cogdell, *The light intensity under which cells are grown controls the type of peripheral light-harvesting complexes that are assembled in a purple photosynthetic bacterium*, Biochemical Journal **440** (2011), no. 1, 51–61.

[89] Tatas Hardo Panintingjati Brotosudarmo, Leenawaty Limantara, Heriyanto, and Monika Nur Utami Prihastyanti, *Adaptation of the Photosynthetic Unit of Purple Bacteria to Changes of Light Illumination Intensities*, Procedia Chemistry **14** (2015), no. December, 414–421.

[90] Anne Marie Carey, Kirsty Hacking, Nichola Picken, Suvi Honkanen, Sharon Kelly, Dariusz M Niedzwiedzki, Robert E Blankenship, Yuuki Shimizu, Zheng Yu Wang-Otomo, and Richard J Cogdell, *Characterisation of the LH2 spectral variants produced by the photosynthetic purple sulphur bacterium Allochromatium vinosum*, Biochimica et Biophysica Acta - Bioenergetics **1837** (2014), no. 11, 1849–1860.

[91] Alastair T Gardiner, Richard J Cogdell, and Shinichi Takaichi, *The effect of growth conditions on the light-harvesting apparatus in Rhodopseudomonas acidophila*, Photosynthesis Research **38** (1993), no. 2, 159–167.

[92] Nikki M. Magdaong, Amy M. Lafountain, Jordan A. Greco, Alastair T. Gardiner, Anne Marie Carey, Richard J. Cogdell, George N. Gibson, Robert R. Birge, and Harry A. Frank, *High efficiency light harvesting by carotenoids in the LH2 complex from photosynthetic bacteria: Unique adaptation to growth under low-light conditions*, Journal of Physical Chemistry B **118** (2014), no. 38, 11172–11189.

[93] Dariusz M Niedzwiedzki, David Bina, Nichola Picken, Suvi Honkanen, Robert E Blankenship, Dewey Holten, and Richard J Cogdell, *Spectroscopic studies of two spectral variants of light-harvesting complex 2 (LH2) from the photosynthetic purple sulfur bacterium Allochromatium vinosum*, Biochimica et Biophysica Acta - Bioenergetics **1817** (2012), no. 9, 1576–1587.

[94] Laura J. Cranston, Aleksander W. Roszak, and Richard J. Cogdell, *Crystallization and preliminary X-ray diffraction analysis of the peripheral light-harvesting complex LH2 from Marichromatium purpuratum*, Acta Crystallographica Section F Structural Biology Communications **70** (2014), no. 6, 808–813.

[95] Alastair T Gardiner, Katerina Naydenova, Pablo Castro-Hartmann, Tu C Nguyen-Phan, Christopher J Russo, Kasim Sader, C Neil Hunter, Richard J Cogdell, and Pu Qian, *Structure of the light harvesting 2 complex reveals two carotenoid energy transfer pathways in a photosynthetic bacterium*, bioRxiv (2020).

[96] ———, *The 2.4 Å cryo-EM structure of a heptameric light-harvesting 2 complex reveals two carotenoid energy transfer pathways*, Science Advances **7** (2021), no. 7, eabe4650.

[97] Dariusz M. Niedzwiedzki, Daniel J. Sandberg, Hong Cong, Megan N. Sandberg, George N. Gibson, Robert R. Birge, and Harry A. Frank, *Ultrafast time-resolved absorption spectroscopy of geometric isomers of carotenoids*, Chemical Physics **357** (2009), no. 1-3, 4–16.

[98] Richard J. Cogdell, *Carotenoids in Photosynthesis*, Philosophical Transactions of the Royal Society of London. Series B, Biological Sciences **284** (1978), no. 1002, 569–579.

[99] Richard J Cogdell, Hideki Hashimoto, and Yasushi Koyama, *Picosecond*

Raman spectroscopy of the B830 LH2 complex of Chromatium purpuratum BN 5500, Photosynthesis Research **35** (1993), no. 1, 79–85.

[100] Per Ola Andersson, Richard J Cogdell, and Tomas Gillbro, *Femtosecond dynamics of carotenoid-to-bacteriochlorophyll a energy transfer in the light-harvesting antenna complexes from the purple bacterium Chromatium purpuratum*, Chemical Physics **210** (1996), no. 1-2, 195–217.

[101] Giulio Cerullo, Cristian Manzoni, Larry Lüer, and Dario Polli, *Time-resolved methods in biophysics. 4. Broadband pump–probe spectroscopy system with sub-20 fs temporal resolution for the study of energy transfer processes in photosynthesis*, Photochem. Photobiol. Sci. **6** (2007), no. 2, 135–144.

[102] Marko Swoboda, Jörg Henig, Hsin-Mei Cheng, Dagmar Brugger, Dietmar Haltrich, Nicolas Plumeré, and Michael Schlierf, *Enzymatic Oxygen Scavenging for Photostability without pH Drop in Single-Molecule Experiments*, ACS Nano **6** (2012), no. 7, 6364–6369.

[103] Sigma Aldrich, *N,N-Dimethyldodecylamine N-oxide*.

[104] Hamamatsu Photonics K.K., *Guide to Streak Cameras*, Tech. report, 2008.

[105] Andor - an Oxfornd Instruments company, *Specifications Shamrock 163*, Tech. report.

[106] Michael (PicoQuant) Wahl, *Time-correlated single-photon counting*, Tech. report, 2014.

[107] Christiane Albrecht, *Principles of Fluorescence Spectroscopy*, vol. 390, Springer US, Boston, MA, mar 2006.

[108] Huw Fox and William Bolton, *Mathematics for engineers and technologists*, 1 ed., Butterworth Heinemann, 2002.

[109] Clay Rawlins, *Basic AC Circuits*, 2 ed., Elsevier, 2000.

[110] Ronald Bracewell, *The Fourier transform and its applications*, 1 ed., McGraw-Hill, 1965.

[111] W. Becker, *Fluorescence lifetime imaging - techniques and applications*, Journal of Microscopy **247** (2012), no. 2, 119–136.

[112] Michelle A Digman and Enrico Gratton, *Fluorescence lifetime microscopy: The Phasor Approach*, Comprehensive Biophysics, vol. 2, Elsevier Ltd., 2012, pp. 24–38.

[113] David M Jameson, Enrico Gratton, and Robert D Hall, *The Measurement and Analysis of Heterogeneous Emissions by Multifrequency Phase and Modulation Fluorometry*, Applied Spectroscopy Reviews **20** (1984), no. 1, 55–106.

[114] Shih-chu Liao, Yuansheng Sun, and Ulas Coskun, *FLIM Analysis using the Phasor Plots*, Tech. Report 0, 2014.

[115] Liliana Martelo, Alexander Fedorov, and Mário N Berberan-Santos, *Fluorescence Phasor Plots Using Time Domain Data: Effect of the Instrument Response Function*, Journal of Physical Chemistry B **119** (2015), no. 32, 10267–10274.

[116] Liliana Martelo, Alexander Fedorov, and Mario N Berberan-Santos, *Phasor Representation of Monomer-Excimer Kinetics: General Results and Application to Pyrene*, Journal of Physical Chemistry B **119** (2015), no. 48, 15023–15029.

[117] Liliana Martelo, Alexander Fedorov, and Mário N. Berberan-Santos, *Monomer-excimer mixed fluorescence decays in the phasor space*, Journal of Luminescence **192** (2017), no. June, 64–70.

[118] Mário N Berberan-Santos, *Phasor plots of luminescence decay functions*, Chemical Physics **449** (2015), 23–33.

[119] Mario N Berberan-Santos, *Probabilistic view of the luminescence phasor plot and description of the universal semicircle as the sum of two spiraling curves*, Journal of Mathematical Chemistry **53** (2015), no. 5, 1207–1219.

[120] A. LERAY, C. SPRIET, D. TRINEL, Y. USSON, and L. HÉLIOT, *Generalization of the polar representation in time domain fluorescence lifetime imaging microscopy for biological applications: practical implementation*, Journal of Microscopy **248** (2012), no. 1, 66–76.

[121] Farzad Fereidouni, Alessandro Esposito, G A Blab, and Hans C Gerritsen, *A modified phasor approach for analyzing time-gated fluorescence lifetime images*, Journal of Microscopy **244** (2011), no. 3, 248–258.

[122] Farzad Fereidouni, Dimitris Gorpas, Dinglong Ma, Hussain Fatakdawala, and Laura Marcu, *Rapid fluorescence lifetime estimation with modified phasor approach and Laguerre deconvolution: a comparative study*, Methods and applications in fluorescence **5** (2017), no. 3, 035003.

[123] Jörg Enderlein and Rainer Erdmann, *Fast fitting of multi-exponential decay curves*, Optics Communications **134** (1997), no. 1-6, 371–378.

[124] Sjef Moling, Anna Pietraszewska-Bogiel, Marten Postma, Elena Fedorova, Mark A Hink, Erik Limpens, Theodorus W J Gadell, and Ton Bisseling, *Nod factor receptors form heteromeric complexes and are essential for intracellular infection in Medicago nodules*, Plant Cell **26** (2014), no. 10, 4188–4199.

[125] Leonel Malacrida, David M Jameson, and Enrico Gratton, *A multidimensional phasor approach reveals LAURDAN photophysics in NIH-3T3 cell membranes*, Scientific Reports **7** (2017), no. 1, 1–11.

[126] Yanzhou Zhou, Long Wu, Qinruo Wang, and Yonghua Wang, *Global analysis of dynamic fluorescence anisotropy by a polarized phasor approach*, Journal of Fluorescence **21** (2011), no. 1, 11–15.

[127] Henryk Szmacinski, Vladimir Toshchakov, and Joseph R. Lakowicz, *Application of phasor plot and autofluorescence correction for study of heterogeneous cell population*, Journal of Biomedical Optics **19** (2014), no. 4, 046017.

[128] Glen I. Redford and Robert M. Clegg, *Polar plot representation for frequency-domain analysis of fluorescence lifetimes*, Journal of Fluorescence **15** (2005), no. 5, 805–815.

[129] Fred S. Wouters and Alessandro Esposito, *Quantitative analysis of fluorescence lifetime imaging made easy*, HFSP Journal **2** (2008), no. 1, 7–11.

[130] A. H. A. Clayton, Q. S. Hanley, and P. J. Verveer, *Graphical representation and multicomponent analysis of single-frequency fluorescence lifetime imaging microscopy data*, Journal of Microscopy **213** (2004), no. 1, 1–5.

[131] Farzad Fereidouni, *Multi-spectral lifetime imaging : methods and applications*, Ph.D. thesis, Universiteit Utrecht, 2013.

[132] Chiara Stringari, Amanda Cinquin, Olivier Cinquin, Michelle A. Digman, Peter J. Donovan, and Enrico Gratton, *Phasor approach to fluorescence lifetime*

microscopy distinguishes different metabolic states of germ cells in a live tissue, Proceedings of the National Academy of Sciences of the United States of America **108** (2011), no. 33, 13582–13587.

[133] Hideki Hashimoto, Chiasa Uragami, Nao Yukihira, Alastair T Gardiner, and Richard J Cogdell, *Understanding/unravelling carotenoid excited singlet states*, Journal of the Royal Society Interface **15** (2018), no. 141.

[134] Leszek Fiedor, Alina Dudkowiak, and Mariusz Pilch, *The origin of the dark S1 state in carotenoids: A comprehensive model*, Journal of the Royal Society Interface **16** (2019), no. 158.

[135] Tomáš Polívka and Harry A Frank, *Molecular Factors Controlling Photosynthetic Light Harvesting by Carotenoids*, Accounts of Chemical Research **43** (2010), no. 8, 1125–1134.

[136] Tomáš Polívka and Villy Sundström, *Dark excited states of carotenoids: Consensus and controversy*, Chemical Physics Letters **477** (2009), no. 1-3, 1–11.

[137] Manuel J. Llansola-Portoles, Andrew A. Pascal, and Bruno Robert, *Electronic and vibrational properties of carotenoids: from in vitro to in vivo*, Journal of The Royal Society Interface **14** (2017), no. 135, 20170504.

[138] Pavel Chábera, Marcel Fuciman, Petr Híbek, and Tomá Polívka, *Effect of carotenoid structure on excited-state dynamics of carbonyl carotenoids*, Physical Chemistry Chemical Physics **11** (2009), no. 39, 8795–8803.

[139] Miriam M. Enriquez, Marcel Fuciman, Amy M. Lafountain, Nicole L. Wagner, Robert R. Birge, and Harry A. Frank, *The intramolecular charge transfer state in carbonyl-containing polyenes and carotenoids*, Journal of Physical Chemistry B **114** (2010), no. 38, 12416–12426.

[140] Leszek Fiedor, Heriyanto, Joanna Fiedor, and Mariusz Pilch, *Effects of Molecular Symmetry on the Electronic Transitions in Carotenoids*, Journal of Physical Chemistry Letters **7** (2016), no. 10, 1821–1829.

[141] Dariusz M Niedzwiedzki and Laura J Cranston, *Excited state lifetimes and energies of okenone and chlorobactene, exemplary keto and non-keto aryl carotenoids*, Physical Chemistry Chemical Physics **17** (2015), no. 20, 13245–13256.

[142] J. Frenkel, *On the transformation of light into heat in solids. i*, Physical Review **37** (1931), no. 1, 17–44.

[143] Gregory D Scholes, *Insights into Excitons Confined to Nanoscale Systems: Electron–Hole Interaction, Binding Energy, and Photodissociation*, ACS Nano **2** (2008), no. 3, 523–537.

[144] GREGORY D. SCHOLES and GARRY RUMBLES, *Excitons in nanoscale systems*, Materials for Sustainable Energy, vol. 5, Co-Published with Macmillan Publishers Ltd, UK, oct 2010, pp. 12–25.

[145] Bruno Robert, *Spectroscopic Properties of Antenna Complexes from Purple Bacteria*, The Purple Phototrophic Bacteria (C Neil Hunter, Fevzi Daldal, Marion C Thurnauer, and J Thomas Beatty, eds.), Springer, 2009, pp. 199–212.

[146] Thomas R Middendorf, Laura T Mazzola, Kaiqin Lao, Martin A Steffen, and Steven G Boxer, *Stark effect (electroabsorption) spectroscopy of photosynthetic reaction centers at 1.5K: Evidence that the special pair has a large excited-state polarizability*, Biochimica et Biophysica Acta (BBA) - Bioenergetics **1143** (1993), no. 2, 223–234.

[147] Lucas M P Beekman, Raoul N Frese, Gregory J S Fowler, Raphael Picorel, Richard J Cogdell, Ivo H. M. van Stokkum, C Neil Hunter, and Rienk van Grondelle, *Characterization of the Light-Harvesting Antennas of Photosynthetic Purple Bacteria by Stark Spectroscopy. 2. LH2 Complexes: Influence of the Protein Environment*, The Journal of Physical Chemistry B **101** (1997), no. 37, 7293–7301.

[148] Margus Rätsep, Mihkel Pajusalu, Juha Matti Linnanto, and Arvi Freiberg, *Subtle spectral effects accompanying the assembly of bacteriochlorophylls into cyclic light harvesting complexes revealed by high-resolution fluorescence spectroscopy*, Journal of Chemical Physics **141** (2014), no. 15.

[149] J Linnanto, A Freiberg, and J Korppi-Tommola, *Quantum Chemical Simulations of Excited-State Absorption Spectra of Photosynthetic Bacterial Reaction Center and Antenna Complexes*, The Journal of Physical Chemistry B **115** (2011), no. 18, 5536–5544.

[150] Felipe Cardoso Ramos, Michele Nottoli, Lorenzo Cupellini, and Benedetta Mennucci, *The molecular mechanisms of light adaption in light-harvesting com-*

plexes of purple bacteria revealed by a multiscale modeling, Chemical Science **10** (2019), no. 42, 9650–9662.

[151] Lorenzo Cupellini, Stefano Caprasecca, Ciro A Guido, Frank Müh, Thomas Renger, and Benedetta Mennucci, *Coupling to Charge Transfer States is the Key to Modulate the Optical Bands for Efficient Light Harvesting in Purple Bacteria*, The Journal of Physical Chemistry Letters **9** (2018), no. 23, 6892–6899.

[152] Ashley L Tong, Olivia C Fiebig, Muath Nairat, Dvir Harris, Marcel Giansily, Aurélia Chenu, James N Sturgis, and Gabriela S Schlau-Cohen, *Comparison of the Energy-Transfer Rates in Structural and Spectral Variants of the B800-850 Complex from Purple Bacteria*, The journal of physical chemistry. B **124** (2020), no. 8, 1460–1469.

[153] Jeffrey R Reimers, Malgorzata Biczysko, Douglas Bruce, David F Coker, Terry J Frankcombe, Hideki Hashimoto, Jürgen Hauer, Ryszard Jankowiak, Tobias Kramer, Juha Linnanto, Fikret Mamedov, Frank Müh, Margus Rätsep, Thomas Renger, Stenbjörn Styring, Jian Wan, Zhuan Wang, Zheng-Yu Wang-Otomo, Yu-Xiang Weng, Chunhong Yang, Jian-Ping Zhang, Arvi Freiberg, and Elmars Krausz, *Challenges facing an understanding of the nature of low-energy excited states in photosynthesis*, Biochimica et Biophysica Acta (BBA) - Bioenergetics **1857** (2016), no. 9, 1627–1640.

[154] Francesco Segatta, Lorenzo Cupellini, Marco Garavelli, and Benedetta Mennucci, *Quantum Chemical Modeling of the Photoinduced Activity of Multichromophoric Biosystems*, Chemical Reviews **119** (2019), no. 16, 9361–9380.

[155] Lorenzo Cupellini, Mattia Bondanza, Michele Nottoli, and Benedetta Mennucci, *Successes & challenges in the atomistic modeling of light-harvesting and its photoregulation*, Biochimica et Biophysica Acta (BBA) - Bioenergetics **1861** (2020), no. 4, 148049.

[156] Dario Polli, Giulio Cerullo, Guglielmo Lanzani, Sandro De Silvestri, Hideki Hashimoto, and Richard J Cogdell, *Carotenoid-bacteriochlorophyll energy transfer in LH2 complexes studied with 10-fs time resolution*, Biophysical Journal **90** (2006), no. 7, 2486–2497.

[157] Alexandra Olaya-Castro and Gregory D Scholes, *Energy transfer from*

Förster–Dexter theory to quantum coherent light-harvesting, International Reviews in Physical Chemistry **30** (2011), no. 1, 49–77.

[158] Ana Damjanović, Thorsten Ritz, and Klaus Schulten, *Energy transfer between carotenoids and bacteriochlorophylls in light-harvesting complex II of purple bacteria*, Physical Review E - Statistical Physics, Plasmas, Fluids, and Related Interdisciplinary Topics **59** (1999), no. 3, 3293–3311.

[159] Rienk van Grondelle, Jan P Dekker, Tomas Gillbro, and Villy Sundstrom, *Energy transfer and trapping in photosynthesis*, Biochimica et Biophysica Acta (BBA) - Bioenergetics **1187** (1994), no. 1, 1–65.

[160] Sebastian R Beyer, Lars Müller, June Southall, Richard J Cogdell, G Matthias Ullmann, and Jürgen Köhler, *The Open, the Closed, and the Empty: Time-Resolved Fluorescence Spectroscopy and Computational Analysis of RC-LH1 Complexes from Rhodopseudomonas palustris*, The Journal of Physical Chemistry B **119** (2015), no. 4, 1362–1373.

[161] J Michael Gruber, Pavel Malý, Tjaart P J Krüger, and Rienk Van Grondelle, *From isolated light-harvesting complexes to the thylakoid membrane: A single-molecule perspective*, Nanophotonics **7** (2018), no. 1, 81–92.

[162] Daniel T Gillespie, *Exact stochastic simulation of coupled chemical reactions*, The Journal of Physical Chemistry **81** (1977), no. 25, 2340–2361.

[163] Kristen A. Fichthorn and W. H. Weinberg, *Theoretical foundations of dynamical Monte Carlo simulations*, The Journal of Chemical Physics **95** (1991), no. 2, 1090–1096.

[164] Mirco S Till, Timm Essigke, Torsten Becker, and G Matthias Ullmann, *Simulating the Proton Transfer in Gramicidin A by a Sequential Dynamical Monte Carlo Method*, The Journal of Physical Chemistry B **112** (2008), no. 42, 13401–13410.

[165] R K Clayton and B J Clayton, *B850 pigment-protein complex of Rhodopseudomonas sphaeroides: Extinction coefficients, circular dichroism, and the reversible binding of bacteriochlorophyll*, Proceedings of the National Academy of Sciences **78** (1981), no. 9, 5583–5587.

[166] Tomáš Polívka, Donatas Zigmantas, Jennifer L. Herek, Zhi He, Torbjörn Pascher, Tõnu Pullerits, Richard J. Cogdell, Harry A. Frank, and Villy

Sundström, *The Carotenoid S 1 State in LH2 Complexes from Purple Bacteria Rhodobacter s phaeroides and Rhodopseudomonas a cidophila : S 1 Energies, Dynamics, and Carotenoid Radical Formation*, The Journal of Physical Chemistry B **106** (2002), no. 42, 11016–11025.

[167] Ronald L. Christensen, *The Electronic States of Carotenoids*, The Photochemistry of Carotenoids, no. January 2004, Kluwer Academic Publishers, Dordrecht, 2006, pp. 137–159.

[168] G. Cerullo, D. Polli, G. Lanzani, S. De Silvestri, H. Hashimoto, and R.J. Cogdell, *Photosynthetic light-harvesting by carotenoids: detection of an intermediate excited state*, 2003 European Quantum Electronics Conference. EQEC 2003 (IEEE Cat No.03TH8665), vol. 298, IEEE, 2003, p. 169.

[169] Evgeny E Ostroumov, Rachel M Mulvaney, Richard J Cogdell, and Gregory D Scholes, *Broadband 2D electronic spectroscopy reveals a carotenoid dark state in purple bacteria*, Science **340** (2013), no. 6128, 52–56.

[170] Claudiu C. Gradinaru, J. T. M. Kennis, Emmanouil Papagiannakis, I. H. M. van Stokkum, Richard J. Cogdell, Graham R. Fleming, Robert A. Niederman, and R. van Grondelle, *An unusual pathway of excitation energy deactivation in carotenoids: Singlet-to-triplet conversion on an ultrafast timescale in a photosynthetic antenna*, Proceedings of the National Academy of Sciences **98** (2001), no. 5, 2364–2369.

[171] Ferdy S Rondonuwu, Tokio Taguchi, Ritsuko Fujii, Kyosuke Yokoyama, Yasushi Koyama, and Yasutaka Watanabe, *The energies and kinetics of triplet carotenoids in the LH2 antenna complexes as determined by phosphorescence spectroscopy*, Chemical Physics Letters **384** (2004), no. 4-6, 364–371.

[172] Hideki Hashimoto, Yasushi Koyama, Yoshinori Hirata, and Noboru Mataga, *S1 and T1 species of .beta.-carotene generated by direct photoexcitation from the all-trans, 9-cis, 13-cis, and 15-cis isomers as revealed by picosecond transient absorption and transient Raman spectroscopies*, The Journal of Physical Chemistry **95** (1991), no. 8, 3072–3076.

[173] Renato Bensasson, Edwin A. Dawe, Derek A. Long, and Edward J. Land, *Singlet → triplet intersystem crossing quantum yields of photosynthetic and related polyenes*, Journal of the Chemical Society, Faraday Transactions 1: Physical Chemistry in Condensed Phases **73** (1977), 1319.

[174] Hamamatsu Photonics K.K., *HPD-TA High-Performance Digital Temporal Analyzer*, Tech. report, 2015.

[175] Paul T Boggs, Richard H Byrd, Janet E Rogers, and Robert B Schnabel, *User's Reference Guide for ODRPACK Version 2 . 01 Software for Weighted Orthogonal Distance Regression*, Tech. Report June, 1992.

259

10. Acknowledgement

Basic research is somewhat like shooting an arrow up in the sky
and painting a target circle where it landed.

Grundlagenforschung ist als wenn man einen Pfeil in die Luft schießt
und dort wo er landet eine Zielscheibe malt.

Homer Burton Adkins

left, you all together create the special spirit in our labs. Always open for questions, either concerning scientific research or everyday life. I am sure to come over for a coffee and a chat when possible. Stay like this!

A group of close friends, who became friends from colleagues, partly from the former GRK 1640, sharing the nerve wracking but fascinating experience of scientific work during a PhD project. Our hours together, either in the lab or in private meetings, gave me a lot of motivation and made me laugh even when things were not evolving as expected. Thank you all for your precious time! In order to not forget anyone in a list of names, I decided not to name anyone here directly but I am sure that those people tho whom these lines refer to, know from the bottom of their heart that they are meant.

My family, Dagmar and Sören, thank you for your everlasting support and patience with me and the believe in me and my skills, even when I was in doubt. Thank you for listening to numerous ideas and approaches for the discussion of this thesis and checking my typos. Thank you for giving me rest when I was in a hurry as well as giving me motivation when I was missing it. You are the best!

Sebastian, who was a colleague and then became a friend and even more. Thank you for your patience when I am about to lose my nerve and your continuous support during the writing of this thesis. I am delighted that you came into my life and am excited to see where our journey together will take us.

Thank you all for helping me painting 'my' target circle!
Danke, dass ihr mir beim Malen 'meiner' Zielscheibe geholfen habt!

11. Statutory declaration - Eidesstattliche Erklärung

Hiermit versichere ich, Inga Elvers, an Eides statt, dass ich die vorliegende Arbeit selbstständig verfasst habe und keine anderen als die von mir angegebenen Quellen und Hilfsmittel verwendet habe.

Weiterhin erkläre ich, dass ich die Hilfe von gewerblichen Promotionsberatern bzw. -vermittlern oder ähnlichen Dienstleistern weder bisher in Anspruch genommen habe, noch künftig in Anspruch nehmen werde.

Zusätzlich erkläre ich hiermit, dass ich keinerlei frühere Promotionsversuche unternommen habe.

Bayreuth, June, 8, 2022

_____

Inga Elvers